# An experimental investigation of the trailing vortex structure and mixing characteristics of stirred vessels.

Lee, Ka-Lok Carroll

# AN EXPERIMENTAL INVESTIGATION OF THE TRAILING VORTEX STRUCTURE AND MIXING CHARACTERISTICS OF STIRRED VESSELS

KA-LOK CARROLL LEE

A thesis submitted for the degree of

Doctor of Philosophy

to the Faculty of Engineering

University of London

Department of Mechanical Engineering

King's College London

December 1995

*To my parents*

慈母手中线
游子身上衣
临行密密缝
意恐迟迟归
谁言寸草心
报得三春晖

—孟郊　游子吟

# ABSTRACT

This thesis describes an experimental investigation of the trailing vortex structure and of the mixing characteristics in a stirred vessel stirred by either one or two Rushton impellers.

Time-resolved and angle-resolved (ensemble-averages over 1° of impeller shaft revolution) measurements of the velocity variations were obtained by laser-Doppler anemometry in a vessel of 100 mm diameter stirred by either one or two Rushton impellers. From the time-resolved measurements, the auto-correlation functions, power spectra and temporal scales of the flows induced by both impeller configurations were also obtained.

The measurements show that the turbulence in the trailing vortex streams is anisotropic and the flows are strongly periodic within a region surrounding the impeller. With two Rushton impellers, the trailing vortex structure and the size of the periodic flow region is altered considerably.

The angle-resolved velocity measurements were compared with those obtained in a stirred vessel of similar geometry and of 294 mm diameter to establish the effect on vessel size. The results indicated that the flows in the two vessels are essentially similar.

In order to measure the mixing time across the whole vessel, a novel experimental technique was developed. The technique made use of temperature as a passive scalar to determine the transient temperature/concentration field in the vessel. Liquid crystal tracers were suspended in the flow and the temperature field was recorded and analysed by means of a video digital image processing system. The technique was applied to investigate the effect of impeller speed on mixing time. Both qualitative and quantitative mixing time measurements were obtained for flows agitated by one and two impellers.

The results obtained from the above investigations are analysed and their implications for related CFD predictions and process design are discussed in detail.

# ACKNOWLEDGEMENTS

It gives me great pleasure to acknowledge the assistance of a number of people during the course of the research and the preparation of this thesis. I acknowledge with gratitude the constant supervision, encouragement, guidance and valuable advice and criticism of Dr M. Yianneskis. I am obliged, for the time and knowledge generously given, to Dr K.O. Suen, who introduced me to laser Doppler anemometry, and to Dr M.J. Tindal for his encouragement and valuable advice.

My thanks go to Dr Siva Nadarajah, Dr Ricardo Gomiciaga, Mr Bernardo Vazquez and Dr Huiyu Fu from whom I have benefited through our numerous discussions. I would also like to thank all my colleagues for their support and assistance, and in particular Messrs Kieran Rutherford, David Foster and Kung Ng.

I am grateful to Messrs M. Harrington, D. Elgar, A. Heaney and P. Elsey, for their help in the construction of the experimental facilities, to Mr J. Geoffery for his help with the electronics, and to Dr J. Fendley for his advice on the graphics programmes.

I am indebted to the Commission of the European Union for the financial support provided for this work.

Finally, I would like to thank my dear wife, Sandi for her support, understanding and the delicious late-night snacks she prepared for me, above all, my parents, who encouraged me and accepted my long absence.

# CONTENTS

# LIST OF FIGURES

# LIST OF TABLES

# NOMENCLATURE

| *Roman characters* | | *Units* |
|---|---|---|
| a | A constant | - |
| A | Coefficient of the cubic anharmonicity term | - |
| $b_0$ | Diameter of the beam leaving the laser at $1/e^2$ intensity | m |
| $b_0'$ | Diameter of the expanded laser beam at $1/e^2$ intensity | m |
| $b_x$ | Diameter of the measurement volume | m |
| $b_y$ | Length of the measurement volume | m |
| B | Baffle width | m |
| c | Speed of light | m/s |
| C | Clearance of the impeller from the base of the vessel in single-impeller configuration | m |
| C1 | Clearance of the lower impeller from the base of the vessel in double-impeller configuration | m |
| C2 | Separation between the upper and the lower impellers in double-impeller configuration | m |
| C3 | Submergence of the upper impeller in double-impeller configuration | m |
| $C_D$ | Drag coefficient | - |
| d | Distance from blade tip in the impeller stream | m |
| $d_p$ | Mean diameter of seeding particles | m |
| D | Impeller diameter | m |
| E | Percentage error | - |
| E(f) | Energy spectrum (power spectral density) function calculated from resampled data | $m^2/s$ |
| E'(f) | Energy spectrum function calculated from unevenly spaced data using the Lomb method | $m^2/s$ |
| f | Frequency | Hz |
| $f_{1,2,3,4,5}$ | Focal lengths of lenses $L_{1,\ 2,\ 3,\ 4,\ 5}$ of the laser anemometers | m |

| | | |
|---|---|---|
| $f_D$ | Doppler frequency | Hz |
| $f_s$ | Frequency shift | Hz |
| $F_c$ | Instrument bandwidth of the BSA | Hz |
| Fl | Flow number | - |
| g | Acceleration due to gravity | $m/s^2$ |
| h | Impeller blade height | m |
| $h$ | CIE 1976 $u'$, $v'$ hue angle | ° |
| hue | hue computed from digitised images (0 - 255) | - |
| H | Liquid height | m |
| I | Moment of inertia of the molecules | $kgm^2$ |
| k | Turbulence kinetic energy | $m^2/s^2$ |
| K | A constant | - |
| $L_{1,2,3,4,5}$ | Lenses of the anemometers | - |
| m | Order of the diffracted laser beams | - |
| M | Number of samples | - |
| n | Number of lines on the grating | - |
| $n_p$ | Number of blades | - |
| N | Impeller rotational rate | rev/s |
| | Also impeller rotational speed | rev/min |
| $N_c$ | Number of Doppler cycles to be timed | - |
| $N_{fr}$ | Number of stationary fringes in the measurement volume | - |
| $N_g$ | Rotational speed of the grating | rev/min |
| P | Pitch length of a helix | m |
| P(f) | Normalised energy spectrum function (= $E'(f)/u'^2$) | s |
| $Q$ | Pumping capacity calculated from 360° ensemble-averaged velocity data | $m^3/s$ |
| $Q_\phi$ | Pumping capacity calculated from 1° angle-resolved velocity data | $m^3/s$ |
| r | Radial distance from the axis of the vessel | m |
| r* | Normalised radial distance (= 2r/D) | - |
| $\hat{r}$ | The average molecular direction of each layer of thermochromic liquid crystals | ° |
| r | The radial co-ordinate of the measurement volume | m |
| R | Impeller radius (= D/2) | m |
| Re | Reynolds number | - |
| $R(\tau)$ | Autocorrelation function coefficient | - |

| | | |
|---|---|---|
| R, G, B | Red, green and blue tristimulus values | - |
| *R, G, B* | Video/television RGB tristimulus values | - |
| t | $= N\, t_c\, (D/T)^2$ | - |
| | Also temperature (Equation 3.9) | °C |
| $t_b$ | Impeller blade thickness | m |
| $t_c$ | Circulation time | s |
| $t_d$ | Impeller disk thickness | m |
| *s* | CIE 1976 *u'*, *v'* saturation | - |
| T | Vessel diameter | m |
| | Also temperature (Equation 3.1) | K |
| $T_b$ | Time taken to measure $N_c$ cycles of a Doppler burst | s |
| *u', v'* | CIE 1976 *u'*, *v'* chromaticity co-ordinates | - |
| u | Fluctuating velocity component | m/s |
| u' | Axial turbulence level | m/s |
| $u'_\phi$ | Turbulence levels at blade angle $\phi$ | m/s |
| U | Instantaneous axial velocity | m/s |
| $\overline{U}$ | Axial mean velocity | m/s |
| $U_\phi$ | Instantaneous velocity at blade angle $\phi$ | m/s |
| $\overline{U}_\phi$ | Mean velocity at blade angle $\phi$ | m/s |
| $U_T$ | Terminal velocity of the seeding particles | m/s |
| v' | Radial turbulence level | m/s |
| $v'_{res}$ | Resultant turbulence level in the impeller stream | m/s |
| V | Instantaneous radial velocity | m/s |
| $V_r$ | Rotational speed $(= 2\pi N r)$ | m/s |
| $V_{tip}$ | Impeller tip speed $(= \pi N D)$ | m/s |
| $\overline{V}$ | Radial mean velocity | m/s |
| $\overline{V}_{res}$ | Resultant mean velocity in the impeller stream | m/s |
| w' | Tangential turbulence level | m/s |
| W | Impeller blade width | m |
| $\overline{W}$ | Tangential mean velocity | m/s |
| *x, y* | Relative chromaticity co-ordinates | - |
| x, y, z | Traversing directions of the anemometers | - |
| *x, y, z* | Relative tristimulus values | - |
| X, Y, Z | CIE 1931 tristimulus values | - |
| *z* | Axial co-ordinate of the measurement volume | m |

| | | |
|---|---|---|
| $z'$ | Axial distance from the impeller disk mid-section elevation | m |
| $z^*$ | Normalised axial distance (= $z'/(h/2)$) | - |
| $Z_c$ | Function of confidence level (Equations 2.16 and 2.17) | - |

| ***Greek characters*** | | ***Units*** |
|---|---|---|
| $\varepsilon$ | Rate of dissipation of kinetic energy of turbulence | $m^2/s^3$ |
| $\theta$ | The tangential co-ordinate of the measurement volume | ° |
| $\theta_m$ | Mixing time | s |
| $\bar{\theta}$ | Mean angle between successive layers of liquid crystals | ° |
| $\kappa$ | Laser beam intersection angle | ° |
| $\lambda$ | Wavelength | m |
| $\lambda_0$ | Characteristic wavelength | m |
| $\lambda^*$ | Fringe spacing in the measurement volume | m |
| $\lambda_t$ | Radial micro time scale of turbulence | ms |
| $\lambda_x$ | Radial micro length scale of turbulence | mm |
| $\Lambda_t$ | Radial integral time scale of turbulence | ms |
| $\Lambda_x$ | Radial integral length scale of turbulence | mm |
| $\mu$ | Dynamic viscosity | kg/m/s |
| $\bar{\mu}$ | Mean refractive index | - |
| $\upsilon$ | Kinematic viscosity | $m^2/s$ |
| $\rho$ | Density of fluid | $kg/m^3$ |
| $\rho_d$ | Density of the seeding particles | $kg/m^3$ |
| $\sigma_{G,F,T,I,B,L}$ | Rms broadening contributions due to velocity gradient, small scale fluctuations within the measurement volume, finite transit time, finite instrument bandwidth, Brownian motion and laser linewidth respectively | m/s |
| $\sigma_b$ | Rms due to broadening contribution | m/s |
| $\sigma_D$ | Total measured rms | m/s |

| | | |
|---|---|---|
| $\sigma_{mv}$ | Standard deviation of Gaussian intensity distribution of the measurement volume | m/s |
| $\sigma_V$ | Rms due to the flow turbulence | m/s |
| $\tau$ | Correlation time | s |
| $\phi$ | Blade angle | ° |
| $\omega_0$ | Angular frequency | rad/s |

***Subscripts***

| | |
|---|---|
| a | True ensemble quantity |
| m | Measured ensemble quantity |
| mv | Measurement volume |
| 100 | Quantity obtained in the T = 100 mm vessel |
| 294 | Quantity obtained in the T = 294 mm vessel |

***Abbreviations***

| | |
|---|---|
| A/D | Analogue to digital |
| BSA | Burst Spectrum Analyser |
| CFD | Computational Fluid Dynamics |
| CIE | Commission Internationale de l' Eclairage |
| DC | Direct current |
| FFT | Fast Fourier transform |
| LCT | Liquid crystal thermography |
| LDA | Laser-Doppler anemometry |
| LIF | Laser induced fluorescence |
| pdf | Probability density function |
| PIV | Particle image velocimetry |
| PTV | Particle tracking velocimetry |
| rms | Root mean square |
| SNR | Signal/Noise ratio |
| TTL | Transistor-transistor logic |

# CHAPTER 1

# INTRODUCTION

## 1.1 BACKGROUND

Fluid mixing processes form a significant part of the operation of a number of industries, such as, chemical, biochemical, pharmaceutical, food processing, etc. Mixing processes are usually accomplished in mechanically stirred vessels. These vessels are generally used to perform several functions, such as, blending of miscible and immiscible liquids, suspension of solid particles in liquids, dispersion of gas in liquids, and three-phase mixing processes. Since mixing consumes a significant amount of processing time, it is one of the main factors which determine the processing capacity of a plant. Furthermore, insufficient or excessive mixing may result in waste of raw materials, formation of undesirable by-products and loss of processing time and capacity.

During a mixing operation, a number of physical and transport processes can occur simultaneously and the main purpose of agitation is often to enhance such processes. Since turbulent flow conditions greatly increase the speed at which mixing is achieved, in most stirred vessels the aim is to generate a turbulent flow field by means of agitation to accelerate the momentum, mass and/or heat transfer processes.

Over the years, a great deal of effort has been placed into the optimisation of mixing processes in stirred vessels with respect to power consumption, quality of mixing, duration of process, and capital and running costs (see, for example, Benkreira, 1990). For a particular mixing system, vessels with different geometries employing a variety of impeller types have been used. However, there is no universal design of impeller or mixing vessel which can be used for all mixing applications, especially as in most vessels several functions must be performed simultaneously. As a result, the design of mixing systems has relied heavily on experience. This usually involves modifications of existing mixing systems (retrofit) for better efficiency, design of new systems based on the correlation of various parameters determined from experiments; and/or design of new impellers types. To this end, researchers have undertaken extensive experimental investigations using various techniques, for example mixing time measurements by Holmes et al (1964), flow visualisation by van't Riet and Smith (1975), power measurements by Bujalski et al (1986) and laser-Doppler anemometry (LDA) by Yianneskis et al (1987). As a result, the whole design process is labour intensive, time consuming and expensive.

An alternative approach which has been employed to optimise mixing process is mathematical modelling. Many types of models have been developed but the most advanced at present involve the solution of conservation equations subject to initial and boundary conditions: these models can provide detailed information on the three-dimensional flow fields in a mixing vessel. Computational Fluid Dynamics (CFD) is frequently used to simulate fluid flow and heat transfer problems using numerical solutions of the Navier-Stokes

equations and has become an attractive research tool due to the considerable increase in computational power and speed experienced in the last decade. However, the accuracy of such models depends partly on the initial and boundary conditions specified and validation of the predictions is often necessary. In addition, the flow fields in stirred vessels are complex and formulation of appropriate CFD models is by no means straightforward. Therefore, experimental data on the hydrodynamic behaviour of the flow in stirred vessels is required in order to understand the flow structures and to assess related predictions.

The flow fields in mixing vessels are very complex, having strongly three-dimensional characteristics with transient vortical structures which are not always well-defined and high turbulence levels in the vicinity of the impellers. When a configuration employing two or more impellers is adopted the complexity of the flow is greatly increased. Furthermore, a small change in the geometry of the vessel or the impeller may sometimes result in significant differences in the quality of mixing. Knowledge of the flow behaviour of a liquid in a mixing vessel is therefore essential not only for the optimisation of the particular process concerned, but also for the formulation of appropriate design methodologies. The Rushton impeller is one of the most common designs used in stirred vessels. This impeller induces a strong radial discharge stream and is employed in a wide range of industrial processes, as it is well suited for mixing of fluids with a wide range of viscosities. Although other impeller designs may be better suited for the mixing of particular fluids, the Rushton turbine has been studied most extensively. However, as the review of the literature given

below indicates, knowledge of the velocity and mixing characteristics of the flows generated by Rushton impeller(s) is far from complete and these were therefore selected as the subject of this thesis. A three-dimensional view of a Rushton impeller is shown in Figure 1.1 and a cross-section and plan view are shown in Figure 1.2 in order to define the various geometrical characteristics referred to in the following section.

The main findings and the techniques employed in previous experimental investigations of the flows in vessels stirred by Rushton impellers are reviewed in the following two sections, in order to formulate the objectives and methodology of the present work.

## 1.2 REVIEW OF PREVIOUS WORK

This review is primarily concerned with experimental studies on the hydrodynamics of vessels agitated by Rushton impellers in particular but also with disk-type and flat-blade impellers of similar design. Since there are numerous publications on the subject of mixing in stirred vessels, the following review is selective, but sufficiently extensive to assess the present state of knowledge on the hydrodynamics of mixing processes in stirred vessels.

Schematic representations of stirred vessels with one and two Rushton impellers are shown in Figures 1.3 (a) and (b) respectively, in order to define the various geometrical characteristics of the single- and double-impeller configurations.

### 1.2.1 FLOW STRUCTURE WITH A SINGLE RUSHTON IMPELLER

Systematic research into the flow in mixing vessels commenced in the 1950's with work by Rushton et al (1950) and by Bates et al (1963) on the determination of dimensionless numbers for various impeller and vessel geometries. Rushton et al (1950) found the power number was constant for Reynolds numbers* (Re) greater than 20000. Sachs and Rushton (1954) studied the flow in the impeller stream of a four flat-blade turbine using a photographic technique. The results showed that the radial velocity profiles in the impeller stream became less steep with increasing radius while the radial flow increased. The latter increase persisted up to a radius r = T/3 after which the radial volumetric flow decreased. Periodicity of the flow in the vicinity of the impeller was indicated by a peak value of radial velocity at an angle of 40° behind a blade.

Nagata et al (1960) found that the product of the radial distance r and the local radial velocity in the impeller stream of a disk-type turbine was constant. This follows from continuity if the tangential and axial velocities are considered to be zero.

Holmes et al (1964) used a conductivity technique to study the rate of mixing in three vessels of different sizes with a variety of Rushton impeller to vessel diameter ratios. Several peaks with decreasing amplitude were observed in the concentration-time histories obtained.

---

* The Reynolds number is defined by $Re = (\rho N D^2)/\mu$; where D is the impeller diameter, N is the impeller speed, $\rho$ is the fluid density and $\mu$ is the fluid viscosity.

It was shown that the intervals between the successive peaks were equal to the circulation time ($t_c$) in the vessel. The circulation time was defined as the time required for a fluid element to move once around the average circulation loop in the vessel. Using dimensional analysis they introduced a dimensionless group $t = N\,t_c\,(D/T)^2$ which was a function of Re and found that t was constant (= 0.85 ± 0.05) for Re > 20000. The reduction in the amplitude of the peaks in the concentration-time history characterises the dispersion of the tracer during each circulation loop (Voncken et al, 1964).

Cutter (1966) used a photographic technique to measure the mean and rms velocities in the impeller stream and concluded that both mean and rms velocities are independent of Re when they are normalised by the impeller tip speed:

$$V_{tip} = \pi\,N\,D \quad (m/s) \tag{1.1}$$

Cutter estimated that the input energy to the impeller dissipated mostly in the impeller stream.

Cooper and Wolf (1968) used a Pitot tube and a hot-wire anemometer to determine the magnitude and direction of the velocities in the impeller stream. They reported that the flow at the outer edges of the blades of height (h) less than 0.3 impeller diameters (D) is mostly tangential and becomes increasingly radial towards the centre of the blades. However, increasing h over 0.3 D resulted in a more radial flow at the outer edge of the blades and a more tangential flow at the centre of the blades. A linear relationship between the impeller speed and the

pumping capacity was found, while the pumping capacity was calculated to be proportional to $D^3$. The authors identified an optimum value of D/5 for the blade height, above which the pumping capacity did not vary significantly.

Mujumdar et al (1970) used a hot-wire anemometer to investigate the turbulence in the impeller stream of a vessel with air as the working fluid and reported that a large periodic component is present near the impeller with a time scale equal to the number of blades times the rotating speed and with an amplitude decreasing with distance away from the impeller. Mujumdar et al corrected the turbulence intensities to eliminate the effects of periodicity and showed that uncorrected values are up to five times larger than the true turbulence intensities.

Fort et al (1972) and Kratky et al (1974) modelled the discharge flow profiles from a disk-type turbine with a parabolic equation and determined pumping capacities from the curve fit. Velocity data were obtained using a five-hole Pitot tube. The discharge flow was found to be maximum at the centre of the blade and decreased rapidly at the top and bottom edges of the blade. The width of the discharge flow was considerably smaller than the height of the impeller blade. The maximum discharge velocity was almost equal to $V_{tip}$. The velocity profiles, normalised with $V_{tip}$, were found to be independent of impeller rotational speed but were dependent upon the size of the impeller. Asymmetry was observed in the profiles as the impeller was not centrally located in the vessel. DeSouza and Pike (1972) noted an angle dependency in the discharge flow. The angle of the axial spread of the

discharge flow at the top and bottom of the blade was about 20° from the horizontal.

Van't Riet and Smith (1973) identified the trailing vortices behind the impeller blades using a flow visualisation technique and 2 mm polystyrene particles as tracers. The flow of the tracer particles in the stirred vessel was recorded with video, still and cine cameras rotating synchronously with the stirrer. It was found that the axes of the vortices were horizontal and the vortices maintained their identity for at least two or three blade lengths. The importance of these vortices on the dispersion and coalescence in liquid-gas mixing was pointed out. In a later study (van't Riet and Smith, 1975) the authors attempted to measure the velocity and pressure distribution within the trailing vortices. They used a photographic technique for the velocity measurements and an impact tube (fixed to the blade) for the pressure measurements. The trajectory of a particle trapped in the vortex was photographed and it appeared as a sine wave. From the length of this trajectory and the exposure time the particle velocity was determined. Their results showed that the angular velocities in the vortex were independent of the distance along the vortex axis and depended only on Re when normalised with the impeller angular speed ($2\pi N$).

Günkel and Weber (1975) used a shielded hot-wire anemometer, rotating with the impeller and mounted in-between the blades, to measure the mean and rms velocities between two successive blades of a Rushton impeller. They also used a shielded hot-wire anemometer and a yaw tube to measure the velocities in the impeller stream. The shielded wire was claimed to allow reverse flow regions to be detected.

They used air as the working fluid, based on the justification given by Mujumdar et al (1970). The measurements between two blades indicated the existence of two pairs of vortices behind the leading blade. The first pair is the trailing vortices identified by van't Riet and Smith (1973). However, Yianneskis et al (1987) showed subsequently that there is no evidence of a second pair and it is likely that these vortices were produced due to interference of the hot-wire probe with the flow. The rms velocities measured between the blades were independent of the angular position. They measured a maximum radial mean velocity of 0.8 $V_{tip}$ near the blade tip, in agreement with Cutter (1966) and Mujumdar et al (1970). Using an energy conservation equation and assuming that no energy is dissipated within the control volume surrounding the impeller, Günkel and Weber concluded that most of the input energy is dissipated in the bulk flow. They also suggested that the flow in the impeller stream is anisotropic. It must be noted that the reliability of the data obtained by Günkel and Weber must be questioned as they obtained differences of 20% between the velocities measured with the three methods in the same location.

Komasawa et al (1974a, b) using high-speed cine photography, found turbulence intensities on the order of 30%–50% in the discharge stream of a disk-type turbine. They also found that turbulence intensities increased, but the energy dissipation decreased with radial position and concluded that the flow had to be considered three dimensional.

Van't Riet et al (1976) measured the impeller discharge flow with a stationary hot-film probe and concluded that most of the fluctuations measured originated from the periodicity of the blade passages and the

accompanying vortex structure. They termed such conditions 'pseudo-turbulence'. Because of the influence of the blades and of the vortices, van't Riet et al concluded that the real turbulence could only be measured by a probe rotating with the stirrer and that otherwise the energy dissipation values were significantly overestimated. They also observed that the vortices were broken up at the baffles and the vessel wall with genuine turbulent motions thereafter in the bulk of the vessel.

Drbohlav et al (1978a, 1978b) described the discharge flow from a disk-type turbine as a tangential cylindrical jet, though recognising that the impeller discharge actually pulsed. Following De Souza and Pike (1972), they developed a model to describe the radial velocity profile. Their approach neglected the existence of the trailing vortices and the pulsing discharge from the impeller blades. The model failed to describe the flow field near the impeller. However, the pulsation decayed with distance from the impeller, and the model provided by Drbohlav et al became more realistic as the distance from the impeller increased. Costes and Couderc (1982) measured velocities and turbulence intensities for a disk-type turbine centrally positioned in a standard configuration tank using hot-film anemometry. The velocity profiles measured at different rotational speeds were similar when normalised with $V_{tip}$. Both the radial velocity and tangential velocity maxima were about 0.77 $V_{tip}$. Turbulence intensities varied between 30% and 70%.

Reed et al (1977) used LDA to study the flow in a tank stirred by a Rushton impeller located at a clearance C = T/3. The results of this investigation revealed that the flow was highly three-dimensional. The

ring vortex below the impeller was found to be stronger than the one above the impeller. The difference in the strength of the two vortices resulted in an inclination of the impeller stream slightly upwards. Reed et al also noticed that the baffles had an extensive influence on the mean flow and emphasised the existence of strong helical vortices behind the baffles. A similar observation was made by van der Molen and van Maanen (1978) who also used LDA to measure the flow.

Van der Molen and van Maanen (1978) measured the periodic component of the velocities in the vicinity of the impeller and confirmed the existence of the trailing vortices behind the blades. They employed different impellers with two different blade/disk thickness to diameter ratios and the same impeller to vessel diameter ratio. The periodic components recorded decayed fast, reaching near-zero values at two-thirds of the radius and decaying to completely random turbulence at the wall. They also reported that the turbulence away from the impeller was isotropic. Their results showed that the peak-to-peak value of the periodic axial velocities in the vicinity of an impeller increased by a factor of 3 as the blade and disk thickness of the impeller decreased from 1.5 mm to 0.5 mm. From their results a slight increase of the above mentioned velocity with Re can be observed. The effect of vessel size on the periodic axial velocities cannot be determined from their results as the measurements were performed at different Re's.

The structure of the flow around the impeller blades and in the bulk of the vessel was quantified in detail by Yianneskis et al (1987). Employing LDA, ensemble-averaged velocity measurements were

performed over 1° and over 360° of impeller rotation. A D = T/3 and $t_b$ = 3 mm impeller was used, located at C = T/3. The influence of the ring vortices on the trailing vortices was found to be significant at about 25° behind the blade, while at an angle of 30° the trailing vortices had almost dissipated. The rms velocities measured over 1° were similar to those obtained over 360° behind the blade (due to the presence of the trailing vortex) and decreased to 25% of the 360° averages where no trailing vortices are present. The maximum value of turbulence kinetic energy ($k = 0.17\ V_{tip}^2$) was measured at 20° behind the blade. The inclination of the impeller stream to the horizontal was found to decrease with increasing impeller clearance and rotational speed. The periodicity and vortical structure of the flow in the impeller region persisted up to a radius r = 0.7 D and at r = D the vortices were broken up. A similar detailed investigation of the trailing vortices was carried out by Stoots and Calabrese (1994).

Armstrong and Ruszkowski (1988) measured maximum radial velocities of 0.72 $V_{tip}$ for a disk turbine with a small hub and 0.60 $V_{tip}$ for a similar turbine with a large hub using LDA measurements synchronised with the impeller rotation. The velocity profiles were significantly different between the two geometries. Stoots and Calabrese (1994) reported that the hub size may have a small effect on the impeller discharge flow. Measurements by Mahmoudi (1994) with two hub sizes confirmed that the effect is indeed small and differences were far smaller than those reported by Armstrong and Ruszkowski.

Wu and Patterson (1989) carried out a LDA study concerned with the influence of the trailing vortices on the velocities in the impeller

stream. The periodicity of the flow resulting from the trailing vortices was found to influence strongly the rms velocities in the impeller stream close to the impeller. The largest contribution of the flow periodicity to the total radial and tangential rms velocities occurred in the impeller disk elevation and in the vicinity of the impeller. For the axial rms velocities the maximum contribution occurred on both sides of the impeller disk at a distance ± h/4 from the impeller disk elevation. The periodicity of the flow decayed rapidly with increasing distance from the tip of the impeller. At a location $r^* = 1.08$ (where $r^* = 2r/D$) the periodicity of the flow accounted for as much as 85% of the total turbulence in terms of mean-square fluctuation velocity. This contribution decreased to 20% at $r^* = 1.5$ and the periodicity disappeared completely at $r^* = 1.9$. Wu and Patterson also reported that the random rms velocities increased with distance from the impeller tip, reaching a maximum value at around $r^* = 1.5$ and then decreasing with increasing radius.

The effect of impeller geometry on the flow field in the vicinity of the impeller was also investigated by Armstrong and Ruszkowski (1986) who employed two Rushton impellers identical in all aspects except for the blade thicknesses ($t_b$) which were 1.5 and 3 mm. They also used an identical impeller with $t_b = 1.5$ mm but with the disk diameter increased from 2D/3 to 3D/4. The LDA results obtained showed identical flow numbers for all three impellers. However, Armstrong and Ruszkowski did not mention the disk thickness of the impeller ($t_d$) they used or if there was any variation in $t_d$ among the three impellers.

The effect of vessel size on the velocities in the impeller stream and bulk flow was investigated by Nouri and Whitelaw (1990). They used two vessels with diameters T = 144 and 294 mm agitated by D = T/3 Rushton impellers. LDA measurements showed that the axial and radial velocities in the impeller stream and bulk flow exhibit no dependency on vessel size when the velocities are normalised with the tip velocity and plotted in non-dimensional co-ordinates $r^* = r/(D/2)$ and $z^* = z'/(h/2)$ (where $z' = 0$ mm in the disk elevation plane). They also found a negligible difference in velocities when a lid was used.

Kusters (1991) carried out LDA measurements in three mixing vessels of T = 102, 200 and 388 mm. Kusters reported that the mean velocity profiles when normalised with $V_{tip}$ were approximately independent of the vessel size. He also found that in the immediate vicinity of the impeller tip there was a periodic contribution to the total velocity fluctuations arising from the trailing vortices issuing from the impeller blades; and that this periodic component increased with scale-up. Kusters reported that the turbulent fluctuating velocity field was dependent on scale. Near the impeller tip the normalised turbulent velocity decreased with increase in vessel size, whereas the opposite was noted for the bulk flow in the vessel. The random turbulence was approximately isotropic. The integral length scale in the impeller discharge stream was approximately equal to the blade width while in the bulk of the vessel the integral length scale increased to approximately 2.5 times of this value.

Dyster et al (1993) studied the radial discharge flows from a Rushton impeller using LDA. They used transparent Newtonian fluids with

viscosities up to 1000 mPa s as working fluids to obtain various Re's. 360° ensemble-averaged mean and rms velocity profiles were obtained in the impeller stream. The correlation between radial mean velocity and radial distance was obtained by regression analysis and was slightly different from that reported by van der Molen and van Maanen (1978). However, the correlation between the radial rms velocity and radial distance reported was in close agreement with those noted by Wu and Patterson (1989), Nouri et al (1987a), Reed et al (1977) and Laufhütte and Mersmann (1985).

### 1.2.2 FLOW STRUCTURE WITH TWO RUSHTON IMPELLERS

Relatively few investigations have been concerned with the flow structure in vessels agitated by two Rushton impellers. Most of the investigations reported to-date have been concerned primarily with large impeller clearances and separations, where there is little or no interaction between the flows generated by individual impellers. Such studies have mainly concentrated on the power consumption characteristics (see, for example, Kuboi and Nienow, 1982).

Crozier (1989) studied the flow produced by two Rushton impellers with LDA. The impellers were located at C1 = T/3 and C2 = T. The results showed an independent behaviour of the impellers as if the mixing vessel was divided into two equal parts, each part being agitated by one impeller.

Mahmoudi and Yianneskis (1991, 1992) and Mahmoudi (1994) studied the effect of impeller spacing in double-Rushton impeller

configurations. By varying the clearance of the lower impeller (C1), the separation between the two impellers (C2), and the submergence of the upper impeller (C3), they observed three stable and four unstable flow patterns.

With the stable flow patterns either both the impellers were pumping in a horizontal direction and generating four main ring vortices or the two impeller streams were merging and forming two main ring vortices or the upper impeller was pumping horizontally and generating two main ring vortices while the lower impeller was pumping towards the bottom of the vessel and generating one main ring vortex. They termed these three stable patterns parallel, merging and diverging flow respectively. Each of the four unstable flow patterns they observed was a combination of either two or three of the stable flow patterns depending on the impeller spacings, liquid height and impeller speed.

Of the three stable flow patterns, the merging flow pattern occurred with a clearance C1 = T/3 and separation C2 = T/3: the impeller streams were inclined towards each other and merged half way between the two impellers. This flow pattern was determined to be the most desirable since it produced the lowest mixing times and power consumption.

### 1.2.3 SUMMARY

The above review has shown that a lot of information has been obtained on the flows produced by a single Rushton impeller. The flow structure in the bulk of the vessel has been relatively well established.

However, the characteristics of the flow near the impeller are not as well understood and a number of conflicting findings have been reported, for example on the extent of the flow periodicity and the isotropy of the turbulence around the impeller. A better understanding of the flows in the vicinity of the impeller is therefore required.

The flows produced in vessels stirred by two Rushton impellers have received relatively little attention. In particular, little is known about the flow structure in the vicinity of the impeller in such configurations. Clearly, when the impeller streams are parallel to each other, little change from the single Rushton characteristics might be expected. With merging and diverging flow patterns though, differences could be expected. Of these two patterns, the lower mixing time and power number of the merging flow show promise for efficient mixing and a more thorough understanding of this flow is called for.

Scaling of the mean flow and turbulence structure has been reported but the conclusions reached are far from universal and further confirmation of scale-up is required. In particular, the blade thickness must be properly scaled (Rutherford et al, 1996a) as otherwise differences in the scale-up results may be found (Kusters, 1991).

## 1.3 REVIEW OF EXPERIMENTAL TECHNIQUES

Single-phase non-reacting flow in stirred vessels can be adequately characterised through the measurement of the power consumption, velocity characteristics and mixing time. Power consumption is

normally determined with strain gauge torque measurement techniques. These are well established and the power numbers for both single and double Rushton configurations have been thoroughly determined (see, for example, Kuboi and Nienow (1982), Mahmoudi and Yianneskis (1991), Rutherford et al (1996b)). More accurate torque measurement techniques have been developed (Desoutter Ltd and King's College London, 1995), but at present cannot be used to measure the relatively low torques encountered in mixing vessel shafts.

The velocity characteristics have been measured with Pitot tubes, hot-wire anemometry and LDA. The first two techniques employ probes which disturb the flow and they may result in a wrong interpretation of the flow structure. An example of this type of error is the aforementioned finding of Günkel and Weber (1975). Costes and Couderc (1988) compared velocities obtained by hot-wire anemometry and LDA in a vessel with a Rushton impeller and reported that the LDA results were more realistic.

LDA is a non-obtrusive and accurate technique that does not require calibration and at present the most convenient technique for the measurement of velocity characteristics in stirred tanks. LDA is well suited for the measurement of the complex flows encountered around impellers and has been extensively used since its first application in a stirred tank by Reed et al (1977). Time- and angle-resolved measurements can be made with LDA and therefore the periodic structure around impeller blades can be determined. Particle image velocimetry (PIV) is also well suited for such flows, but it is still being

developed at present to improve the accuracy of the particle pair identification software.

LDA is the most convenient and accurate technique available at present and was selected for the present work. The principles of this technique and its application to mixing vessel flows are discussed in detail in Chapter 2.

In contrast to power consumption and velocity measurement techniques, there is not a universally accepted technique suitable for the accurate determination of mixing time. Schofield (1974) reviewed the techniques employed for the measurement of mixing time in stirred tanks. For liquid-liquid mixing, these can be generally classified into two groupings: Observation and transducer methods.

In observation methods, the change in the colour of the liquid contained in the tank caused by the insertion of either a dye or a reacting liquid is observed as the mixing process proceeds. In the latter case the addition of the liquid initiates a chemical reaction which results in a colour change. Large inaccuracies can be encountered with this technique which may lead to significant underestimation of the mixing time. Two advantages of these methods are that the mixing state in the whole vessel can be determined at the same time and that in some situations 'dead' or stagnation zones may be identified quickly.

The most commonly used methods of the second grouping make use of conductivity or thermocouple probes to detect the variation of the conductivity or temperature of the fluid in the vessel, respectively. This

variation is produced by introducing a small amount of a passive scalar of different conductivity or temperature.

Conductivity probes may have a non-linear response and are affected by stray currents which can bias the output voltage and result in erroneous information in the concentration-time history (Khang and Fitzgerald, 1975). A probe which was free of such currents and had a linear response was designed by Khang and Fitzgerald. However, careful calibration of this probe is necessary.

The probe volume size is important and Thyn et al (1976) investigated its effect on the measured mixing time with 14 probes of different sizes. They classified their experiments into two groups on the basis of the value of probe-to-tracer volume ratio. Depending on whether this value was greater or smaller than unity they obtained two different correlations between mixing time and probe-to-tracer volume ratio. Their probes consisted of two parallel plates and the effective probe volume was larger than the actual volume between the two plates.

The finite probe volume size which affects the spatial resolution of the measurement and the need for careful calibration taking into account the tracer volume reduce significantly the usefulness of the conductivity technique. In contrast, small and accurate temperature measuring probes are available.

However, both techniques can only measure the local concentration or temperature. In order to resolve the complex concentration or temperature distributions encountered in the three-dimensional flows

occurring in stirred vessels, it is often necessary to make measurements in a large number of locations. This can be achieved by repeating the measurement in different locations. Nevertheless, such measurements are non-simultaneous, time-consuming and the probes used, however small, will interfere with the flows.

One technique that shows promise for temperature/mixing time measurements in stirred vessels is liquid crystal thermography. This utilises the change in colour of thermochromic liquid crystals when they are subjected to different temperatures. Liquid crystals exhibit a rapid and reversible response to dynamic temperature changes over a wide range of temperatures and they are available in sheet, paint and suspension form.

A number of applications of liquid crystal thermography techniques for the measurement of wall temperature distributions in forced convection flows have been reported, for example by Cooper et al (1975), Goldstein and Timmers (1982), Akino et al (1986), Rojas et al (1987), Yianneskis (1988) and Lee and Yianneskis (1993). Other applications have included the measurement of transient temperature fluctuations on surfaces, for example, Iritani et al (1984), and in fluids, Kuriyama et al (1981) and Rhee et al (1984).

The ability to suspend liquid crystal tracers in a stirred vessel can allow temperature measurements to be obtained simultaneously across the whole vessel. This renders liquid crystal thermography a very convenient and versatile technique for the measurement of mixing time in stirred tanks, using temperature as a passive scalar. Such a

technique would not only present none of the aforementioned problems with probes, but could also offer all the advantages of observation methods together with considerably increased accuracy.

Finally, it should be noted that recently laser-induced fluorescence (LIF) techniques have been developed for mixing time measurements in stirred tanks (for example, Marquis (1995)). As an unobtrusive technique, LIF shows considerable promise but has not as yet been extensively applied for fluid mixing studies.

## 1.4 OBJECTIVES OF PRESENT INVESTIGATION

The preceding review of the published literature indicates clearly that the knowledge of the hydrodynamic behaviour of the flow in stirred vessels is far from complete. The velocity characteristics of the flows produced by the commonly-employed Rushton impeller have not been fully determined and deserved further investigation. Also, as dual-impeller systems are frequently employed in mixing practice, quantification of the degree of interaction which occurs between the flows generated by the impellers is important. A number of differences between one- and two-impeller flows have been identified but not studied in any detail and investigations reported to-date have been concerned primarily with large impeller clearances and separations, where there is little or no interaction between the flows generated by individual impellers. Such studies have mainly concentrated on the power characteristics (Kuboi and Nienow, 1982). The inconsistencies between the findings reported with respect to the effect of vessel size on

the flow characteristics (Nouri and Whitelaw (1990), Kusters (1991)) indicates that further investigation of this effect is necessary.

Furthermore, as mentioned earlier, the accuracy of CFD models can only be assessed and improved through the provision of accurate experimental data. In addition, most CFD predictions to date treated the impeller region in an approximate manner, as a rotating disk and therefore suffer from inaccuracies associated with this approximation. Although the results obtained in this way may be accurate enough for process design purposes, if the size of the region affected by the periodicity of the flow is known, it is possible to overcome the aforementioned CFD problem by specifying conditions further away from the impeller blades, at the edges of this region. Turbulence modelling could also be aided if the degree of anisotropy of the flow is determined.

In addition, the review of experimental techniques has indicated that an accurate and non-obtrusive technique for the measurement of mixing time would be useful.

Therefore, the above survey has indicated that new and/or more detailed knowledge and clarification is required in the following areas:

1. Quantification of the extent of the influence of the trailing vortex structure formed around impeller blades on the mean velocity and turbulence characteristics in vessels stirred by a single Rushton impeller.

2. Determination of the influence on the trailing vortex structure in dual-Rushton impeller systems.

3. Quantification of the degree of anisotropy in the impeller stream(s) generated by single and double impellers.

4. Assessment of scaling effects in the impeller vicinity in vessels stirred by Rushton impellers.

5. Development and application of an non-obtrusive technique utilising liquid crystal tracers for the qualitative and quantitative determination of the mixing time.

In addition, in order to improve the accuracy of the CFD predictions which often employ the k-ε turbulence model, knowledge of the local energy dissipation rate, ε is very important:

6. Determination of the integral time and length scales to enable the estimation of the dissipation rate of the kinetic energy of turbulence in the impeller stream in single- and dual-impeller systems.

## 1.5 OUTLINE OF THESIS

The remainder of this thesis is divided into six chapters. In the following chapter the design and construction of the test rig and impellers and the experimental techniques used for the investigation of

the velocity and turbulence characteristics are described. In Chapter 3, the development of a technique utilising liquid crystal tracers and temperature as a passive scalar for the determination of mixing time is described. Chapter 4 is concerned with the velocity characteristics of a vessel stirred by a single Rushton impeller, and the results obtained in the vessels stirred by two Rushton impellers are presented and discussed in Chapter 5. The mixing time measurements obtained in the vessel stirred by single and double impellers at various speeds using the liquid crystal technique developed are presented in Chapter 6, Finally, a brief overview of the research carried out is given in Chapter 7, where the findings of the investigation are summarised and recommendations for future work are made.

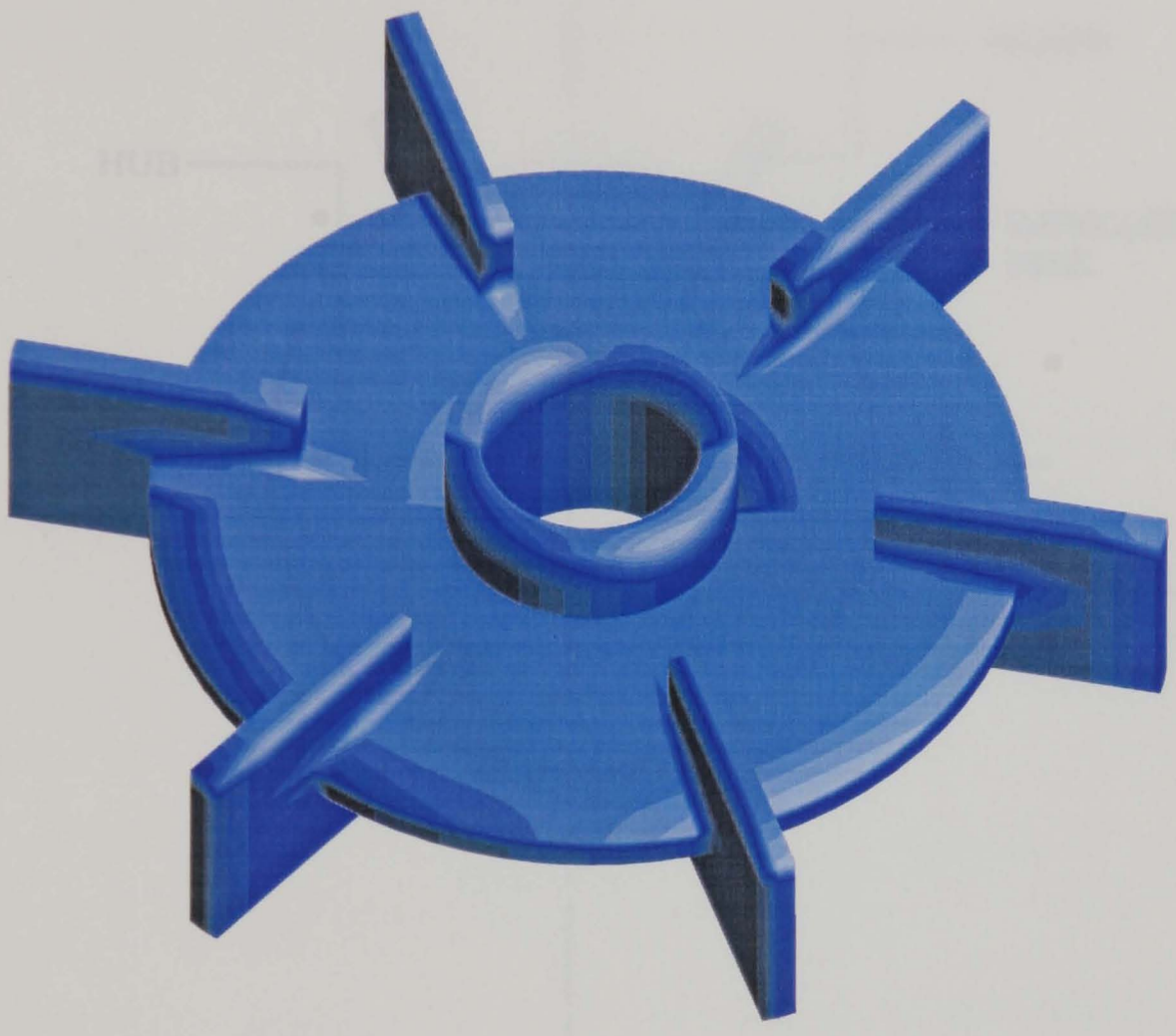

**Figure 1.1** Three-dimensional view of a Rushton impeller.

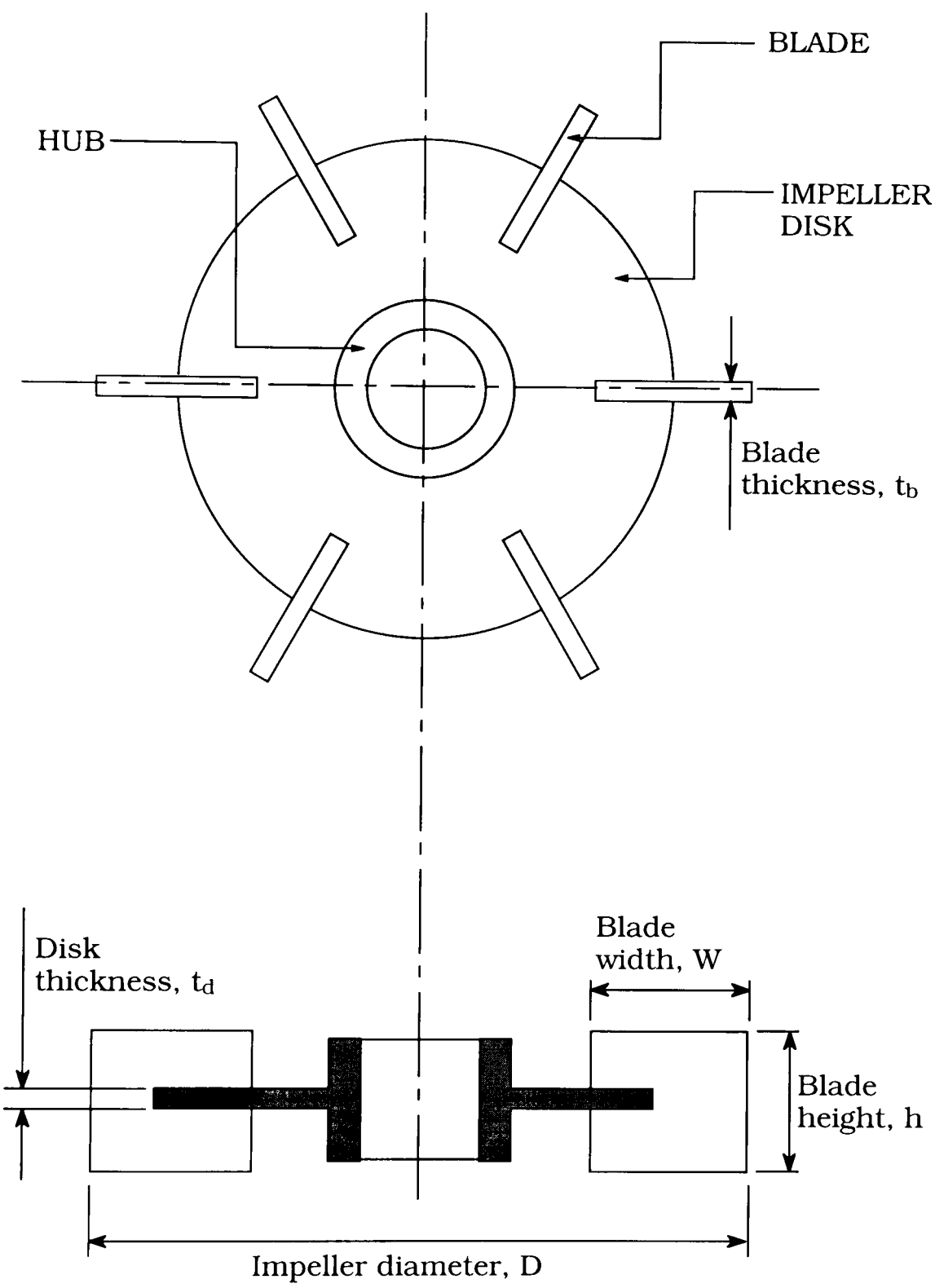


**Figure 1.2** Plan view and cross-section of a Rushton impeller.

(a)

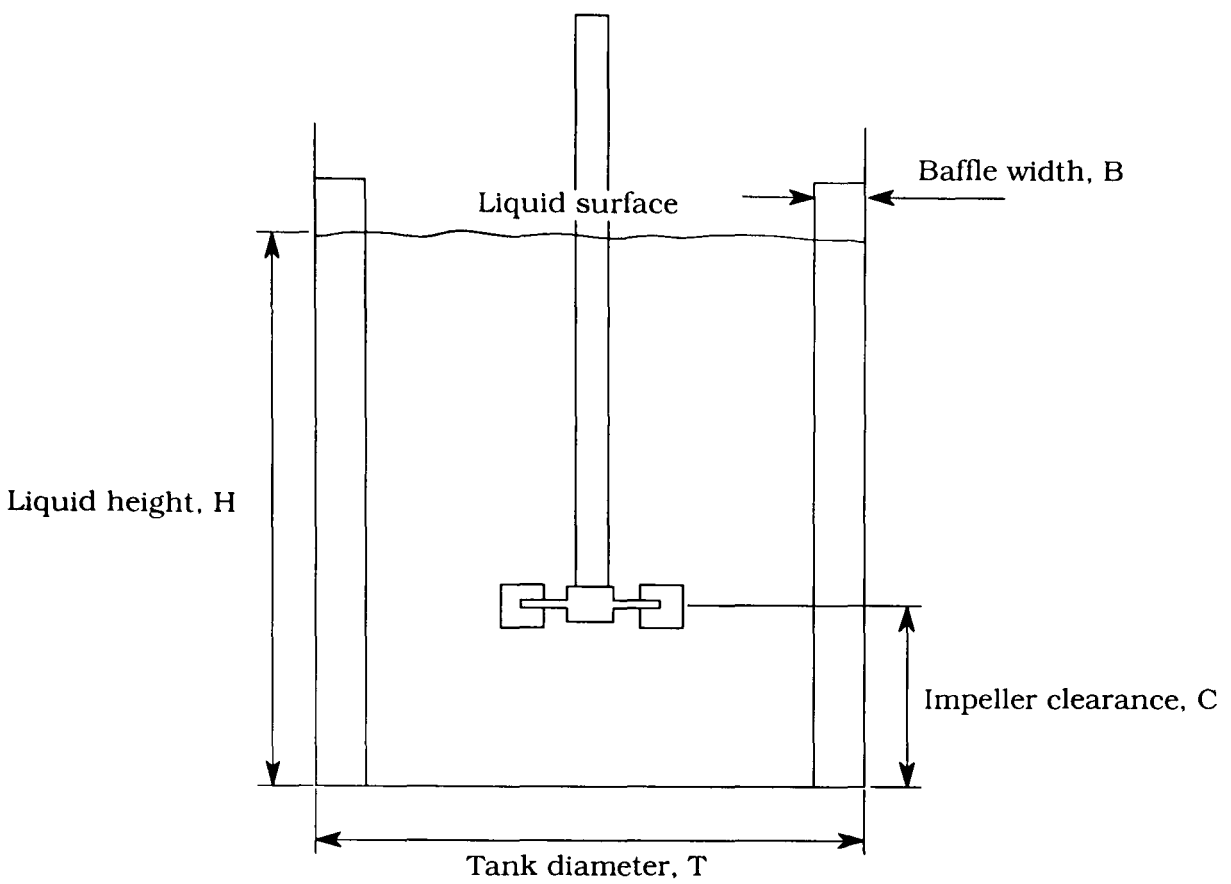


(b)

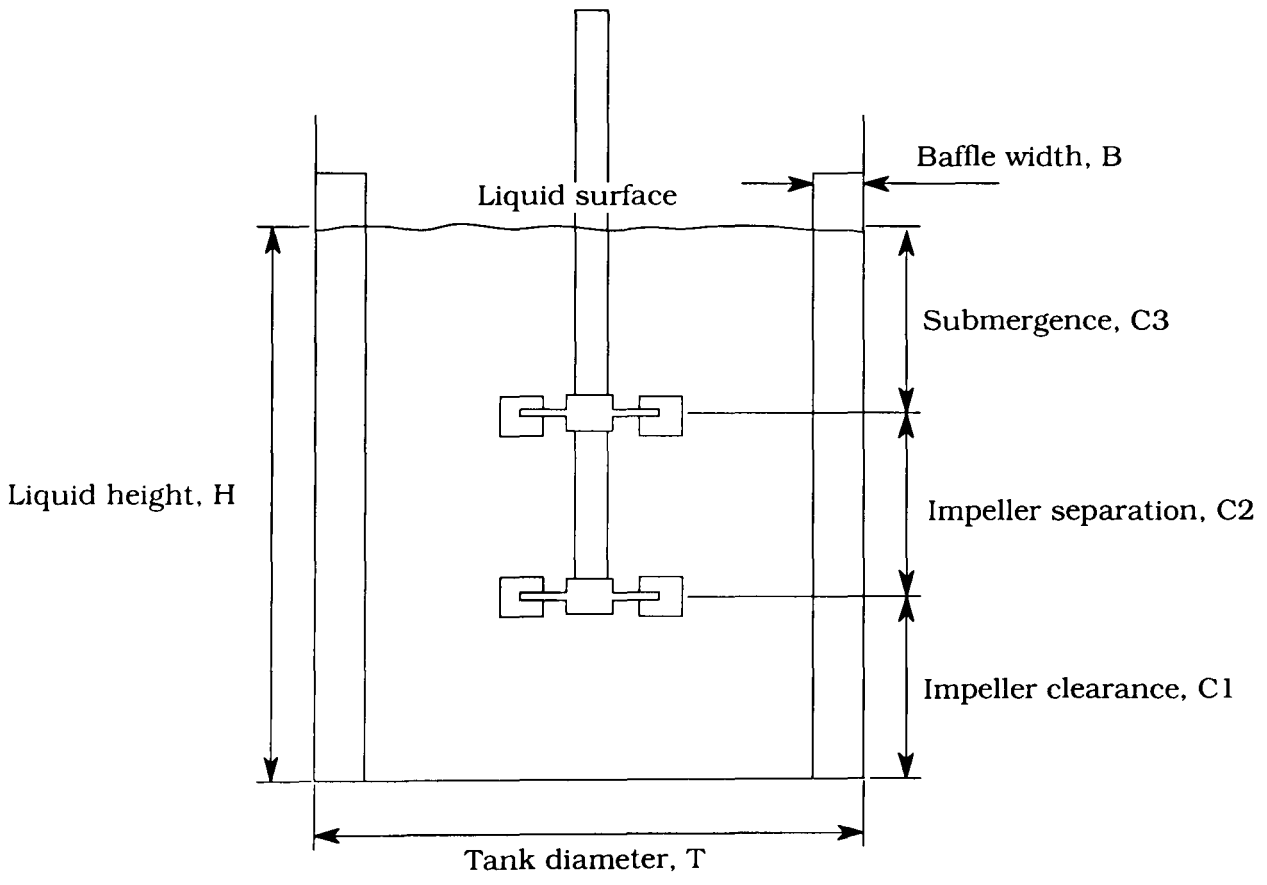


**Figure 1.3** Schematic diagrams of the (a) single-Rushton impeller; (b) double-Rushton impeller systems.

# CHAPTER 2

# MIXING VESSEL CONFIGURATIONS AND FLOW MEASUREMENT TECHNIQUES

## 2.1 INTRODUCTION

The suitability of laser-Doppler anemometry (LDA) for measuring flows in mixing vessels was mentioned in Chapter 1; the technique was employed to obtain detailed mean and rms velocity measurements in a mixing vessel of diameter T = 100 mm, stirred by either one or two Rushton impellers of diameter D = T/3. Velocity measurements were also obtained in a mixing vessel of larger diameter (T = 294 mm) to study scaling effects on the flows.

In the following sections, the mixing vessels and the measurement techniques used will be described in detail. Errors and uncertainties involved will also be discussed and, where appropriate, quantified.

## 2.2 FLOW CONFIGURATION

Figure 2.1 shows the geometry of the mixing vessels used in this investigation. The vessels were identical to the 'standard' configuration used in mixing research (Uhl and Gray, 1966). Most of the measurements were obtained in a cylindrical vessel of diameter T = 100

mm, height of 250 mm and wall thickness of 1 mm. Four equally spaced vertical baffles of width B = T/10 and thickness of 1 mm, were fitted along the internal surface of the vessel. The vessel was made of clear cast acrylic plastic (Perspex); a flat transparent Perspex base was incorporated in the vessel design to maximise optical access.

The vessel was installed in a test section as shown in Figure 2.2. The test section consisted of an aluminium base plate with a circular hole in the centre, and a transparent Perspex trough (170 mm × 170 mm in cross-section and 250 mm high) with a wall thickness of 6 mm. The vessel was secured to the base plate by means of a lip seal. In this way the vessel could be rotated about its axis to enable measurements to be performed at different vertical planes. The gap between the vessel and the Perspex trough was filled with distilled water fed from a constant temperature water bath to remove the heat generated by the impellers and thus to maintain the temperature inside the vessel constant during the experiments, as well as to minimise refraction effects at the cylindrical surface of the vessel.

The impeller shaft was coupled to a shaft sleeving mounted on a detachable top plate with its axis concentric with the vessel axis. The sleeving was supported by a bearing at either end, and was gear-driven by a bi-directional variable speed DC motor. The use of such a sleeving provided a concentric rotation of the impeller shaft in addition to ease of alignment. The clearance between the impeller and the bottom of the vessel was set by sliding the impeller shaft up or down and the shaft was locked to the sleeving by a grub screw.

The sleeving was also coupled to an optical shaft encoder (Hewlett Packard HEDS-6010 036), which provided a marker pulse (TTL low) and a train of 2000 pulses (TTL low) per revolution. The pulses were input to a specially-built gating unit. By counting the number of marker pulses per unit time, the rotational speed of the impeller could be measured; this was displayed on the front panel of the unit.

The midpoint of a blade of the impeller (or the lower impeller when stirred by two impellers) was aligned with the marker pulse, and by counting the number of pulses (1 – 2000) relative to the marker pulse, the blade angle (0° – 360°) could be determined.

The gating unit was also capable of generating a window gate pulse to set the blade angle interval over which measurements were to be obtained. The position of the window gate pulse relative to the marker pulse and its width was determined by two four-digit thumb-wheel switches which set the blade angle interval or gate window opening by the voltage going high and closing by going low.

Figure 2.3 shows the geometry of the Rushton turbines used. They were six-bladed turbines of diameter D = T/3. For the 100 mm diameter vessel both the blade thickness, $t_b$, and the disk thickness, $t_d$, were 1 mm. A clearance C = T/3 was used between the bottom of the mixing vessel and the impeller disk central plane for the single-impeller measurements. Clearances C1 = T/3, between the bottom of the mixing vessel and central plane of the lower impeller disk and C2 = T/3, between the central planes of the lower and upper impeller disks were

used for the dual-impeller measurements. The liquid height in the vessel H, was equal to T (see Figure 2.4).

Measurements were also made in a vessel of larger diameter (T = 294 mm) in order to determine scaling effects. The design of the T = 294 mm vessel was similar to that of the T = 100 mm vessel mentioned above. For the T = 294 mm vessel, a Parvalux 0.25 hp DC motor was used to provide the required torque for the impellers.

The two vessels and their impellers were geometrically scaled to be as similar as permitted by strength of materials considerations and machining restrictions. The dimensions of the two mixing vessels and their impellers are listed in Table 2.1.

**Table 2.1** Dimensions of the two vessels and their impellers

| | | | |
|---|---|---|---|
| **Vessel** | | | |
| Diameter, T | mm | 100 | 294 |
| Height | mm | 250 | 749.2 |
| Wall thickness | mm | 1 | 3 |
| Baffle width, B | mm | 10 | 29.4 |
| Baffle thickness | mm | 1 | 3 |
| | | | |
| **Impeller** | | | |
| Diameter, D | mm | 33.3 | 98 |
| Blade thickness, $t_b$ | mm | 1 | 3 |
| Disk thickness, $t_d$ | mm | 1 | 3 |

The working fluid was distilled water and all measurements were conducted at a Reynolds number of 40000, which corresponded to a constant impeller rotational speed of N = 2165 ± 10 rpm ($V_{tip}$ = 3.77

m/s) for the T = 100 mm vessel, and N = 250 ± 0.5 rpm ($V_{tip}$ = 1.2 m/s) for the T = 294 mm vessel.

The origin of the co-ordinate system used was the centre of the bottom of the vessel(s). All positions in this thesis are described in terms of axial (z), radial (r) and tangential (θ) co-ordinate directions. The locations of the measurement volume for the angle-resolved measurements are expressed in terms of polar co-ordinates r, ϕ, z with respect to the blades calculated from the r, θ, z co-ordinates: ϕ = 0° is the vertical plane through the middle of the blade. The impeller(s) rotated in a clockwise direction as viewed from above the vessel(s). Measurements of all velocity components (i.e. axial, radial and tangential) were performed in the same plane (i.e. θ = 0°, located half-way between two baffles).

For the measurements in the T = 100 mm vessel, a transparent lid was located above the liquid surface at a height H = T so that no air bubbles were entrained into the liquid from the free surface. The lack of a free surface enabled measurements to be made in forward scatter when the beam entered through the bottom of the vessel. This was achieved by attaching a mirror above the lid and filling the space above the lid with water so that the mirror was always submerged. The scattered light was re-directed by 90° by the mirror. The effect of a lid on the flow in a stirred vessel has been previously investigated by Nouri and Whitelaw (1990), who concluded that the use of a lid only affects the flow in the immediate vicinity of the lid/free surface and that the velocities elsewhere in a 144 mm vesel were almost identical to those in a 294 mm vessel.

## 2.3 THE LASER-DOPPLER ANEMOMETER

### 2.3.1 LASER-DOPPLER ANEMOMETRY

This Section describes the main principles of a dual beam, fringe mode LDA system for measuring single components of velocity. When two laser beams cross each other in the measurement volume, they produce an interference fringe pattern as shown in Figure 2.5. The spacing between the light and dark bands, $\lambda^*$, is termed the fringe spacing and is related to the angle of the intersecting beams, $\kappa$ and the wavelength of the laser light, $\lambda$, by the following expression:

$$\lambda^* = \frac{\lambda}{2\ \sin(\kappa / 2)} \tag{2.1}$$

Small particles suspended in the fluid scatter light when passing through the measurement volume. If the particles are small and follow the flow faithfully, then accurate measurements of fluid velocity can be obtained. The intensity modulation of the scattered light as the particle moves through the light and dark fringes results in the generation of "Doppler bursts". A typical Doppler signal produced when a particle crosses the measurement volume is shown in Figure 2.6. Such a signal can be detected by a light sensitive detector. With a suitable signal processor, velocity measurements can be obtained from the photo detector signal.

The velocity U of a particle crossing the measurement volume in the direction perpendicular to the fringes is related to the Doppler frequency $f_D$ by (Drain 1980):

$$f_D = \frac{2U \sin\left(\frac{\kappa}{2}\right)}{\lambda} \qquad (2.2)$$

However the frequency of the Doppler burst does not provide information on the direction of the particle velocity. In order to resolve the direction of the flow, the interference fringes can be made to move within the measurement volume, in a direction perpendicular to the optical axis, by causing the two incoming laser beams to have slightly different optical frequencies, a technique known as frequency shifting. Particles moving in the opposite direction of the movement of the fringes will appear to be moving faster and the light detector will sense a higher modulating frequency. From Equation (2.2) and taking into account an applied frequency shift, $f_s$, velocity measurements can be obtained from the following expression:

$$U = (f_D \pm f_s)\frac{\lambda}{2\ \sin(\kappa / 2)} \qquad (2.3)$$

Two optical arrangements and two types of signal processing systems were used in this work. They are described in the following sections.

### 2.3.2 BEAM SPLITTING AND FREQUENCY SHIFTING

A radial diffraction grating was used for splitting and frequency shifting of the laser beam. The radial grating (Technische Physische Dienst, model H) had 16384 lines chemically etched at a mean diameter of 31.75 mm. The track width of the grating was 0.75 mm. The grating

split the incident beam into different order beams with approximately 70% of the laser power concentrated in the two first order beams.

The grating was mounted onto the shaft of a purpose-built rotating unit, which was belt-driven by a small bi-directional variable speed DC motor (Electro-Craft E350). The unit was designed and built in such a way that the motor-grating assembly could be rotated through 135° in steps of 22.5° about the optical axis thus allowing the plane of the beams to be altered for the measurements of different velocity components. The details of the rotating unit are given in Nadarajah (1991). The frequency shift, $f_s$, of a diffracted beam pair is given by:

$$f_s = \frac{2\ m\ n\ N_g}{60} \qquad (2.4)$$

where m is the order of the diffracted beam pair, n is the number of lines on the grating and $N_g$ is the rotational speed of the grating in rpm.

The grating was rotated at a speed, $N_g$, of 6000 rpm providing a frequency shift of 3.27 MHz between the first order beams for measurements in the T = 100 mm vessel. For the measurements made in the T = 294 mm vessel, the frequency shift used between the first order beams was 3.5 MHz ($N_g$ = 6409 rpm). Considering the maximum velocity to be measured, (i.e. the velocity near the impeller tip, approximately equal to $V_{tip}$), which was 3.77 m/s and 1.2 m/s for the T = 100 mm and the T = 294 mm vessel respectively, and turbulence levels of 50%, the frequency shifts were adequate to resolve the ambiguity in the direction of the flow throughout the two vessels.

### 2.3.3 OPTICAL ARRANGEMENTS

Figure 2.7 shows the arrangement of the optical elements of the anemometer used for the measurements made in the T = 100 mm vessel. A 10 mW Helium-Neon laser (Spectra Physics model 106) was used.

Since steep velocity gradients are expected in the vicinity of the impeller stream, a small measurement volume was considered necessary in order to minimise errors. The diameter of a measurement volume, $b_x$, is given by:

$$b_x = \frac{b}{\cos\left(\frac{\kappa}{2}\right)} \tag{2.5}$$

and the length of the measurement, $b_y$, is given by:

$$b_y = \frac{b}{\sin\left(\frac{\kappa}{2}\right)} \tag{2.6}$$

where $\kappa$ is the beam intersection angle, $b_0$ is the diameter of the beam leaving the laser, and

$$b = \frac{4\ \lambda\ f_1\ f_3}{\pi\ b_0\ f_2} \tag{2.7}$$

Equations (2.5) to (2.7) indicate that a smaller measurement volume can be obtained by using a different combination of the focal lengths $f_1$,

$f_2$ and $f_3$. However due to various limitations such as the physical size of the grating rotating mechanism, the focal lengths of the lenses available and the diameters of lenses supplied by manufacturers, the beam diameter was expanded to obtain a smaller measurement volume.

The beam from the laser was expanded to a diameter $b_0' = 1.82$ mm. The beam was firstly expanded by a bi-concave lens of focal length $f_4 = -40$ mm and then collimated by a plano-convex lens of focal length $f_5 = 100$ mm. The collimation of the expanded beam was checked by measuring the vertical and horizontal diameters of the expanded beam at two positions approximately 1 m apart by means of traversing across the beam a photodiode with a micrometer.

The expanded beam was passed through a spatial filter and focused onto the grating by means of a plano-convex lens of focal length $f_1 = 125$ mm. The first order beam pair diffracted from the grating was selected by masking the remaining beams and collimated by a plano-convex lens of focal length $f_2 = 300$ mm. The collimated beams were focused by a similar imaging lens of focal length $f_3 = 250$ mm to form the measurement volume.

Figure 2.8 shows the optical arrangement of the anemometer used for the measurements in the T = 294 mm vessel. In this case, since the impeller tip speed was lower ($V_{tip} = 1.2$ m/s), the velocity gradients within the measurement volume would not be as steep as those found in the T = 100 mm vessel and the original beam from the laser was used without expansion.

The laser beam was focused onto the grating by a plano-convex lens of focal length $f_1$ = 150 mm. As above, the first order beam pair was selected and then collimated by a plano-convex lens of focal length $f_2$ = 300 mm. A measurement volume was then formed by focusing these two beams by another plano-convex lens of focal length $f_3$ = 300 mm. The characteristics of the two anemometers are summarised in Table 2.2.

**Table 2.2** The principal characteristics of the two laser anemometers.

| | | Anemometer used in vessel of diameter | |
|---|---|---|---|
| | | 100 mm | 294 mm |
| Laser beam diameter, $b_0$ | (mm) | 1.82 | 0.83 |
| Laser beam wavelength, $\lambda$ | (nm) | 632.8 | 632.8 |
| Intersection angle, $\kappa$ (in air) | (°) | 13.12 | 13.64 |
| Focal length $f_1$ of lens $L_1$ | (mm) | 125 | 150 |
| Focal length $f_2$ of lens $L_2$ | (mm) | 300 | 300 |
| Focal length $f_3$ of lens $L_3$ | (mm) | 250 | 300 |
| Focal length $f_4$ of lens $L_4$ | (mm) | -40 | not used |
| Focal length $f_5$ of lens $L_5$ | (mm) | -100 | not used |
| Number of stationary fringes, $N_{fr}$ | | 18 | 48 |
| Measurement volume diameter, $b_x$ | (μm) | ·46.5 | 146 |
| Measurement volume length, $b_y$ | (μm) | 370 | 1400 |
| Fringe spacing, $\lambda^*$ | (μm) | 2.77 | 3.05 |
| Frequency shift, $f_s$ | (MHz) | 3.27 | 3.50 |

Laser beam diameter and measurement volume diameter and length are calculated at $1/e^2$ intensity.

### 2.3.4 BEAM ORIENTATION AND SIGNAL COLLECTION

The optical elements of the anemometer used for the measurements in the T = 100 mm vessel were positioned on an optical bench 1.5 m long mounted on a laboratory jack attached to a compound traversing table. This enabled the optical bench to be traversed in three orthogonal directions (x, y and z). The accuracy in traversing the optical bench in the x and y directions was 0.05 mm and in the z direction 0.1 mm.

The optical bench was aligned to the test section such that the optical axis of the anemometer was contained within a diametrical plane of the vessel (i.e. either the $\theta = 0°$ or the $\theta = 180°$ planes), and was perpendicular to a trough wall.

The radial and tangential velocity components were measured with the beams entering from the bottom of the vessel with the aid of a mirror situated below the test section at an angle of 45° to the vessel axis; and the axial velocity component was measured with the beams entering from the side of the vessel.

Figure 2.9(a) shows schematically the orientation of the beams for measuring the radial velocity component. The two beams lay in a vertical plane coinciding with the $\theta = 0°$ plane and were steered by the mirror underneath the test section. The beams entered the vessel through the bottom, forming a measurement volume in the $\theta = 0°$ plane. By traversing the optical bench in the x direction (i.e. towards or away from the vessel), the measurement volume could be moved in the z direction inside the vessel, and by traversing the optical bench in the

z direction (i.e. upward or downward), the measurement volume could be moved in the r direction inside the vessel.

For the tangential velocity component measurements, the arrangement shown in Figure 2.9 (a) was used, but with the two beams rotated through 90° to lie in a horizontal plane perpendicular to the $\theta = 0°$ plane. The beams were then steered by the mirror entering the vessel through the bottom in planes perpendicular to the $\theta = 0°$ plane. The measurement volume was positioned within the vessel in a similar fashion as for the radial velocity component measurements.

Figure 2.9(b) shows schematically the orientation of beams for measuring the axial velocity component. The two beams entered the vessel through the trough wall forming a measurement volume in the $\theta = 180°$ plane inside the vessel. The measurement volume could be moved to any r and z positions by traversing the optical bench in the x and the z directions respectively.

In all cases, the beams entered the vessel with their optical axes normal to either the vessel wall or the vessel bottom. By taking into account the refractive index of distilled water (the fluid used as the working fluid and to fill the gap between the vessel and the trough), the position of the measurement volume could be determined.

The beams were refracted as they entered the vessel due to the different refractive indices of air, Perspex and water and the intersection angle of the beams, $\kappa$, changed. Though the dimensions of the measurement volume changed due to a change in $\kappa$, the frequency to velocity

conversion factor (and the fringe spacing, $\lambda^*$) did not change. This is due to the fact that when light enters a denser medium, its velocity decreases resulting in a shorter wavelength. By considering Snell's law of refraction, the fringe spacing in water is the same as that found in air (see, for example, Nadarajah, 1992).

Similarly, the anemometer used for measurements in the T = 294 mm could be traversed in three orthogonal directions. The optical elements were positioned on a 2 m long optical bench which was mounted on a compound traversing table attached to a vertical traversing column. The traversing accuracy in the x, y and z directions were 0.05 mm, 0.05 mm and 0.25 mm respectively. All three velocity components were measured with the beams entering from the side of the vessel. The position of the measurement volume within the vessel was determined by an interactive computer programme considering the principles of Snell's Law for the refraction of the laser beams passing from one medium to another. The program calculated the traverse of the compound table in two directions (x and y) required to move the measurement volume from a reference point to the point of measurement. The calculation allowed for the presence of the trough, the cylindrical vessel and the baffles in all possible beam orientations. The program also calculated the frequency-to-velocity conversion factor at each location. This computer program was not required for measurements made in the T = 100 mm vessel, since both beams entered the vessel either through a flat surface (i.e. through the vessel base for the radial and tangential velocity component measurements) or through a diametrical plane (i.e. for the axial velocity component).

The working fluid (distilled water) in both vessels was seeded with neutrally buoyant particles (specific gravity = 1.0 ± 0.2) of 3 μm mean diameter. The forward scattered light produced when these particles crossed through the measurement volume was focused by a 80 – 200 mm zoom lens onto a pinhole of 0.3 mm diameter at the front of the housing of a photo multiplier (EMI 9658B) which was powered by a Brandenburg 10 – 2000 Volts DC power supply.

### 2.3.5 SIGNAL PROCESSING SYSTEMS

Two types of signal processing system were used. A frequency counter was used for angle-resolved measurements, and a burst spectrum analyser was used for time-resolved measurements.

#### FREQUENCY COUNTER

The counter was a TSI model 1990B signal processor (TSI) and consisted of an input conditioner unit and a timer unit; the input conditioner unit essentially provided amplification and filtering of the incoming Doppler signal while the timer unit determined the frequency of the conditioned Doppler signal. The counter had a fixed threshold level of 50 mV to trigger the counting circuit of its timer unit. The counter was operating in 'single measurement per burst' mode (i.e. only one measurement was made for every Doppler burst detected), and eight Doppler cycles were counted.

Figure 2.10 illustrates schematically the signal processing procedure. The signal from the photomultiplier was amplified by a TSI 10099 5×

pre-amplifier and then input to the conditioner unit. The amplified signal was then passed through the band-pass filter within the conditioner to remove low frequency pedestal and high frequency noise. A typical band-pass filtered signal is shown in Figure 2.11.

The filtered signal was then amplified by a variable gain and the quality of the conditioned signal was continuously monitored with an oscilloscope (Philips PM 3267).

The timer then measured the time taken for eight cycles in a Doppler burst using a high resolution clock (± 1 ns). The time measurement was compared with that measured simultaneously for five cycles of the same Doppler burst. A measurement was only accepted when the difference between the two measured times was within 3%, thus eliminating or minimising noise contributions. Whenever a valid measurement was made, the measurement was made available as a digital output in a form of 8-bit time mantissa and 12-bit time exponent together with a 'Data Ready' signal at the output buffer of the counter.

The counter was interfaced with a 80286-processor based PC using a Dostek 1400A Laser Velocimetry Interface. The interface was controlled by a computer program to acquire data from the counter and the arrival time/angle of the data.

For the purpose of this investigation, the reference counter of the interface was clocked by the shaft encoder pulses to obtain the arrival angle of the acquired data. Shaft encoder pulses incremented the

reference counter which was reset every time a marker pulse was received.

Acquisition of data could be enabled by a TTL high signal or disabled by a TTL low signal sent to the auxiliary input of the interface. In this work, the gate window width of the gating unit mentioned in Section 2.2 was set to open to enable acquisition of data between a specified 60° interval (i.e. between two neighbouring blades); the position of the window gate relative to the marker pulse was set according to the desired position of the measurement volume,

For the duration of the window gate open, if a "Data Ready" signal was sent by the counter, the interface acquired the data from the output buffer and stored it onto its on-board memory together with the number of counts registered on the reference counter ('angle' stamping). The procedure of data validation and the gating of the acquisition of data described above is depicted in Figure 2.12.

At the onset of the experiments, the number of samples that required to achieve statistically independent results was carried out, and it was found that at least 500 samples were required for each 1° blade angle. Therefore, for each measurement, over 60000 velocity data were collected between the two impeller blades (i.e. 60° blade angle) so as to ascertain that there were a minimum of 500 data per blade angle. The velocity data and their corresponding arrival angles were then saved on a disk file for off-line processing. For angle-resolved measurements, the mean velocity for each 1° blade angle interval was obtained from:

$$\overline{U}_{\phi} = \frac{\sum_{i=1}^{M} U_{\phi,i}}{M} \tag{2.8}$$

where $U_{\phi,i}$ is the instantaneous velocity at blade angle $\phi$, $\overline{U}_{\phi}$ is the mean velocity at blade angle $\phi$ and M is the number of samples. The rms velocity of each blade angle $\phi$, $u'_{\phi}$,was obtained from:

$$u'_{\phi} = \sqrt{\frac{\sum_{i=1}^{M}\left(U_{\phi,i} - \overline{U}_{\phi}\right)^2}{M}} \tag{2.9}$$

**BURST SPECTRUM ANALYSER**

A Dantec BSA Enhanced Burst Spectrum Analyser (BSA) was used for the time-resolved measurements. The BSA is built around a hard-wired Fast Fourier Transform (FFT) processor and can measure at signal-to-noise (SNR) levels as low as -6 dB (noise relative to the filter bandwidth), providing a higher data rate comparing with a counter-type signal processor and enabling time-resolved measurements to be performed with high data rates.

The BSA was interfaced with a 80286-processor based PC via an IEEE-488 interface. The BSA could be set up and controlled both from its front panel and via software (BURSTware 2.00) installed in the PC. The software was also used to acquire data from the BSA, calculate various statistical quantities, and export the acquired data to disk files for off-line processing.

The signal processing procedure of the BSA is depicted in Figure 2.13. Signals from the photomultiplier were amplified and filtered and fed to the FFT processor via a mixer, an A/D converter and an input buffer. Only signals that were detected by the separate burst detector unit were stored in the input buffer. The output of the FFT processor was then fed to a post processor to determine and validate the Doppler frequency measured. Validated measurements were then stored in the output buffer.

If a measured Doppler frequency was within the current setting of the bandwidth, Bw, it would be indicated on an instantaneous spectrum slidebar on the front panel of the BSA. The setting of either the bandwidth or the centre frequency ($F_c$) of the instrument could then be adjusted, where necessary, so that all measured Doppler frequencies were contained within the set bandwidth.

In order to optimise the data rate, the measured Doppler frequencies were monitored with an oscilloscope (Philips PM 3267). The gain of the input signals was adjusted to maximise the data rate, which was displayed on the front panel of the BSA, while ensuring that the instrument was not saturated.

The data rate was then further optimised by selecting the optimum record length (number of samples used by the BSA to digitise a Doppler burst). The record length was set to maximise the data rate while maintaining a high validation rate (number of validated bursts divided by total number of burst detected, in %), which was displayed on the front panel.

The BSA was operated in 'Burst' mode, i.e. only one measurement was performed per detected burst, and the measured frequencies were either time stamped or 'angle' stamped. When time stamping, the arrival times of the measured data were clocked by the internal clock of the BSA. When the pre-set number of data had been obtained, the measured data together with their arrival times were acquired by the PC from the output buffer of the BSA. Frequency data was then transformed to velocity data by the software and stored on disk files for off-line processing.

For angle stamping, measurements were synchronised with the shaft encoder pulses. Measured data was stamped with the pulse count registered. Since the counter required a TTL high signal to reset, the marker pulse of the shaft encoder was fed to the BSA via a voltage converter to give a TTL high signal per revolution. Similarly, when the pre-set number of data had been obtained, the 'angle' stamped data was acquired by the PC and stored on disk files for further processing.

### 2.3.6 SOURCES OF ERROR AND UNCERTAINTY IN THE LDA SYSTEMS

In this section a brief analysis of the errors involved in the LDA measurements is made and where appropriate the uncertainties in the measurements are quantified.

## FREQUENCY SHIFTING

The frequency shift between the two first order beams was provided by a radial diffraction grating as mentioned in Section 2.2, rotated by a bi-directional DC motor with feedback control.

In this project, the same motor was used for the anemometers used in both the T = 100 mm and T =294 mm vessels. Variations of rotational speed were minimised by the use of a voltage stabiliser which reduced the effects of surges in the main supply. As a result the maximum rms variation in speed was about 0.5% and the maximum speed fluctuation within ±1%. The influence of such variations in frequency shift on the measured rms values has been shown by Melling (1977) to be small; the errors introduced did not exceed 2% even in regions of low turbulence intensity.

## SEEDING

LDA measures the instantaneous velocities of the seeding particles. Thus it is important that the particles follow the flow faithfully to obtain accurate results. In both vessels, the working fluid was seeded with Optimage seeding particles, which had a specific gravity of 1.0 ± 0.2. 90% of the seeding particles had diameters less than 3 μm, thus the particles are neutrally buoyant in water. The terminal velocity of the particles due to drag and gravity forces, $U_T$, is given by:

$$U_T = \left( \frac{4\ d_p(\rho_p - \rho)\ g}{3\ \rho\ C_D} \right)^{0.5} \qquad (2.10)$$

where $d_p$ is the mean diameter of the particles in m, $\rho_p$ is the density of the particles in kg/m$^3$, $\rho$ is the density of the fluid in kg/m$^3$, g is the acceleration due to gravity in m/s$^2$ and $C_D$ is the drag coefficient. Using values of $C_D$ = 10 and 0.44 for laminar and turbulent flows around the particles respectively (Nouri et al, 1987b), the estimated $U_T$'s are 0.8 mm/s and 4.2 mm/s respectively: they can be considered negligible and the velocity fidelity of the particles can be considered excellent.

The seeding particles were mixed with a small amount of distilled water to form a suspension. This suspension was introduced to the working fluid gradually, so that an adequate number of Doppler bursts was observed on the oscilloscope, to minimise signal drop-outs. Care was taken to ensure that the fluid was not over-seeded.

### POSITIONING ERRORS

The uncertainty in locating the measurement volume depends on the traversing mechanism of the anemometers. As mentioned earlier, the accuracy of traversing the anemometer used for the T = 100 mm vessel was 0.05 mm in the x and y directions, and 0.1 mm in the z direction. Taking into account of the refractive index of water, the maximum uncertainties in locating the measurement volume inside the vessel in the x, y and z directions were 0.07 mm, 0.07 mm and 0.13 mm respectively.

For measurements in the T = 294 mm vessel, the anemometer was traversed by the compound tables with accuracies of 0.05 mm in the x and y directions and 0.25 mm in the z direction. As the laser beams entered the vessel from the side, the location of the measurement volume was determined by a well-tested computer programme. The displacement of the measurement volume due to refraction, albeit small, varied according to the position of the measurement volume itself and was accounted for at all locations. The maximum uncertainties estimated, taking into account the refractive index of water, were 0.08 mm in the x and y directions and 0.33 mm in the z direction.

To align the marker pulse with the midpoint of an impeller blade, a laser beam positioned in the y = 0 mm plane, which contained the $\theta$ = 0° and the $\theta$ = 180° planes, was shone at the mid-section of the impeller disk, and the impeller shaft was rotated slowly until the midpoint of a chosen blade coincided with the laser beam. The marker pulse was then aligned to the blade by rotating the shaft sleeving slowly until the marker pulse (TTL low) was displayed on the oscilloscope. The estimated uncertainties in aligning the marker pulse with the impeller blade were 0.17° and 0.06° for the T = 100 and 294 mm vessels respectively.

Since the reference counters in the TSI and BSA for blade angle measurements could miss one pulse from the shaft encoder pulse train, and there were 2000 pulses per revolution, the corresponding uncertainty in blade angle measurement was 0.18°.

## IMPELLER ROTATIONAL SPEED

The impeller rotational speed was continuously monitored, and experiments commenced only when the speed had stabilised. For measurements made in the T = 100 mm vessel, the impeller speed was 2165 rpm and the variation of impeller speed was kept within ±10 rpm (0.46%). For the T = 294 mm vessel, the impeller speed was 250 rpm, and the variation in speed was kept within ±0.5 rpm (0.2%). During any set of measurements, if the variation of speed exceeded these values, the measurements were rejected.

## BROADENING EFFECTS

A number of errors may broaden the measured Doppler frequency spectrum. Such broadening can result from a number of causes; gradients in mean velocity ($\sigma_G$), small velocity fluctuations within a measurement volume of finite dimensions ($\sigma_F$), the finite time taken by particles to cross the measurement volume ($\sigma_T$), and finite instrument bandwidth ($\sigma_I$). Brownian motion and the laser linewidth also contribute to the broadening effect (Durst et al, 1981). Since the last two contributions have been shown by Durst et al (1981) to have a negligible effect, the total mean square contribution of the broadening errors, $(\sigma_b)^2$, is given by:

$$(\sigma_b)^2 = (\sigma_G)^2 + (\sigma_F)^2 + (\sigma_T)^2 + (\sigma_I)^2 \qquad (2.13)$$

and the measured mean square of fluctuation $(\sigma_D)^2$ is the sum of the actual flow $(\sigma_V)^2$ and the broadening contributions $(\sigma_b)$:

$$(\sigma_D)^2 = (\sigma_V)^2 + (\sigma_b)^2 \tag{2.14}$$

When measurements are made across a velocity gradient, particles crossing different parts of the measurement volume will have different velocities. This may result in both broadening and skewing of the Doppler frequency spectrum, causing errors in both the mean and rms velocities. The magnitude of the error is a function of the particular velocity distribution and the dimension of the measurement volume parallel to the gradient. The errors can be estimated by the following equations:

$$\overline{U}_m = \overline{U}_a + \left(\frac{{\sigma_{mv}}^2}{2}\right)\left(\frac{\partial^2 \overline{U}}{\partial r^2}\right)_a \tag{2.15}$$

and

$$\left(\frac{u'}{\overline{U}}\right)_m = \left|\left(\frac{{\sigma_{mv}}^2}{\overline{U}}\right)_a \left(\frac{\partial \overline{U}}{\partial r}\right)_a\right| \tag{2.16}$$

where $\overline{U}_m$ is the measured mean velocity, $\left(\frac{u'}{\overline{U}}\right)_m$ is the measured turbulent intensity, $\overline{U}_a$ is the true velocity corresponding to a point measurement, and $\sigma_{mv}^2$ is the standard deviation of the measurement volume dimension along its long axis.

Equations (2.15) and (2.16) indicate that if the velocity gradient is nearly linear along the measurement volume, the error in the mean velocities will be small, whereas if the mean velocity gradient is steep and non-linear, it will cause a large error in turbulent intensity, particularly if the mean velocity is small or there is a reversed flow.

For measurements in the T = 100 mm vessel, a small measurement volume was formed by expanding the laser beam diameter as mentioned earlier; broadening effects due to velocity gradients were therefore minimised. In the 294 mm vessel the volume was larger but the gradients were less steep and therefore related errors may be expected to be small.

Broadening due to small scale velocity fluctuations within the measurement volume, $\sigma_F$, has been approximated by George and Lumley (1973):

$$\sigma_F{}^2 = \frac{2}{15}\left(\sigma_{mv}{}^3\right)\left(\frac{\varepsilon}{\upsilon}\right)\left(\frac{4\pi\ \sin\kappa}{\lambda}\right)^2 \qquad (2.17)$$

where $\sigma_{mv}$ is the standard deviation of the length of the measurement volume near the Kolmogorov microscale, $\varepsilon$ is the turbulent energy dissipation rate, $\upsilon$ is the Kolmogorov microscale and other symbols have their usual meanings. This requires prior knowledge of the rate of turbulent energy dissipation, $\varepsilon$, and the Kolmogorov microscale, and the actual calculation is difficult. Melling (1975) estimated this error to be of the same order as the velocity gradient broadening.

Finite transit time broadening, $\sigma_T$, and instrument bandwidth broadening, $\sigma_I$, are important in frequency tracking or spectrum analysis but not in frequency counting systems. The errors associated with the BSA processor cannot be directly determined without an extensive knowledge of all parts of the instrument. Only comparative error estimates are therefore possible. Comparison of measurements

obtained with the burst spectrum analyser and with the frequency counter was made in selected locations; the two values were similar (within 2%) in all cases.

## STATISTICAL ERRORS

The number of samples for measurements of the ensemble-averaged mean and rms velocities can also result in an experimental error. Tests with different numbers of samples were made in various locations in the T = 100 mm vessel.

Statistical error may be estimated from the equations suggested by Yanta (1973) for mean velocity:

$$M = \left(\frac{Z_c}{E^2}\right)\left(\frac{rms}{mean}\right)^2 \qquad (2.16)$$

and for rms velocity:

$$M = \left(\frac{Z_c}{E^2}\right) \qquad (2.17)$$

where M is the number of samples, E is the percentage error and $Z_c$ is a function of confidence level which is equal to 1.645, 1.96 and 2.58 for 90, 95, and 99 percent confidence levels respectively.

Assuming a turbulence level of 50%, according to Equations (2.16) and (2.17), a minimum sample size of 500 data points allows the mean velocity to be estimated with a maximum error of 3% and a confidence

level of 95%. For the same confidence level, this sample size enables the rms value to be determined with a maximum error of 6.3%.

## BIAS EFFECTS

When ensemble-averaged measurements are made with a constant seeding density in a turbulent flow, the measured probability distribution function (pdf) is biased towards higher velocities (McLaughlin and Tiederman, 1973). This is due to the fact that more fast moving than slow moving particles are observed crossing the measurement volume over the measuring period. Many researchers have tried to introduce correction methods. The reliability of such methods is often questionable.

Hoesel and Rodi (1977) suggested weighting of the velocity data from individual particles with their residence time. Random sampling of the measured velocities obtained by individual particles after sorting the data obtained by all particles was proposed by Durao and Whitelaw (1975). Drain (1980) proposed randomising the time intervals between measurements.

However, a suitable method to eradicate this type of error has not been devised as yet, particularly for three-dimensional flows. In the present work as the turbulence intensities of the flow are high, velocity bias errors are expected to be low and thus bias correction methods are not expected to improve significantly the accuracy of the results (see also Yianneskis, 1982).

## 2.4 EPILOGUE

Though there are a number of possible errors involved in an LDA system as mentioned in the preceding section, measurement uncertainties vary with location and are difficult to calculate precisely. Suen (1992) checked the accuracy of a LDA system similar to that employed in the present work by measuring the known velocity of a pin rotated by a DC motor. He found that the mean and rms velocities were determined within 1% and 2% respectively. The accumulated errors in the mean and rms velocity measurements presented here were estimated to be, on average, 1 – 5% and 5 – 10%, respectively, of the values quoted. In addition, a comparison of the normalised radial mean and rms velocity profiles with those reported by Mahmoudi (1994) shows that they are in very close agreement. Thus the uncertainties introduced by the aforementioned error sources are small enough so as not to have any significant effect on the measurements of mean velocity and turbulence presented in the present work.

Detailed mean velocity, turbulence level and turbulence kinetic energy results obtained with the single- and double-impeller configurations are presented in Chapters 4 and 5 respectively. In order to minimise interpolation and velocity gradient related errors which are expected to be the most significant sources of uncertainty in the present work, small measuring volumes were employed and the density of the grid of the measurement locations was non-uniform. More data were obtained near the impeller where the velocity gradients are steeper and fewer data further away where the velocity gradients are smaller.

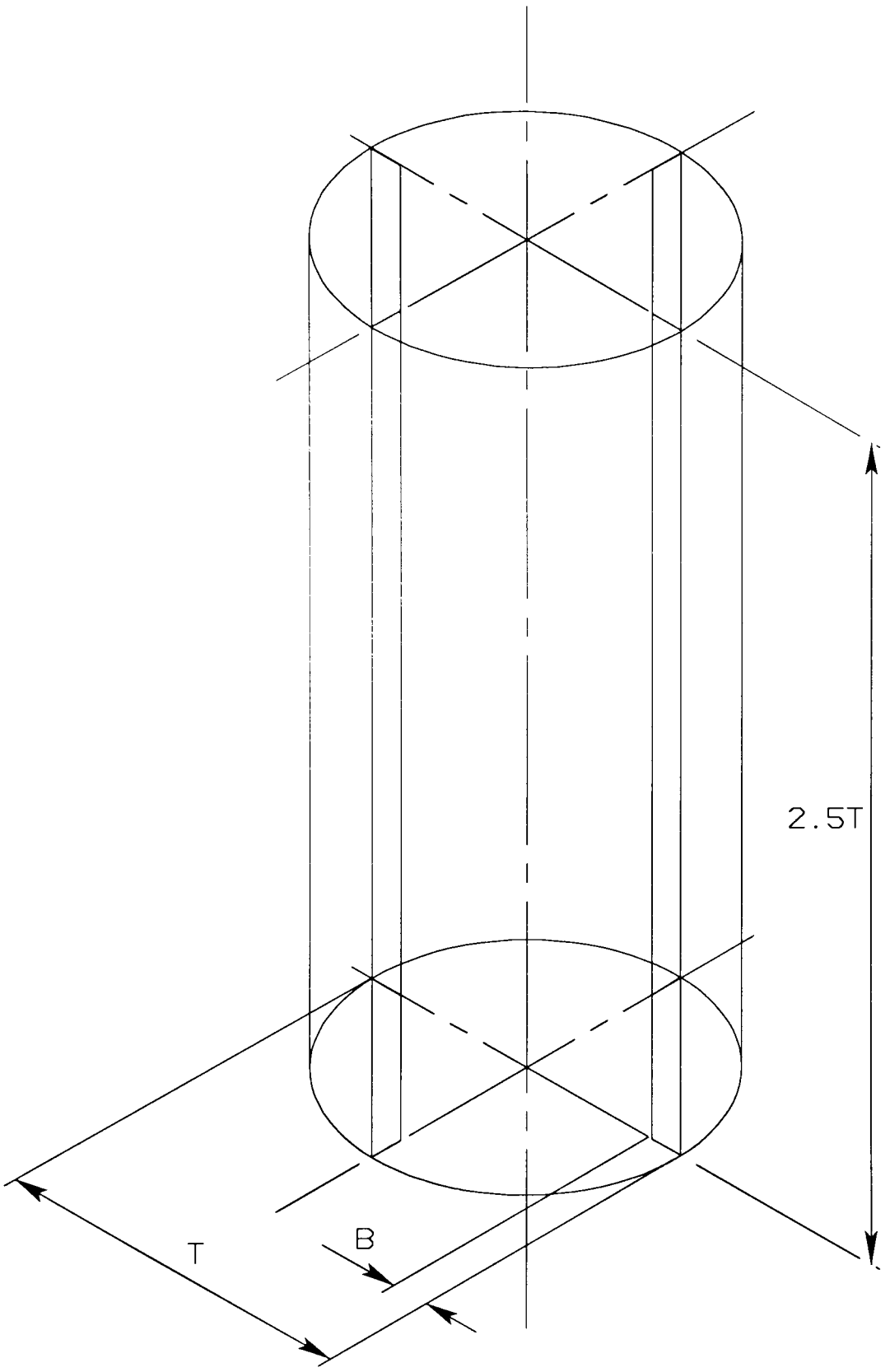


**Figure 2.1** The geometry of the mixing vessels.

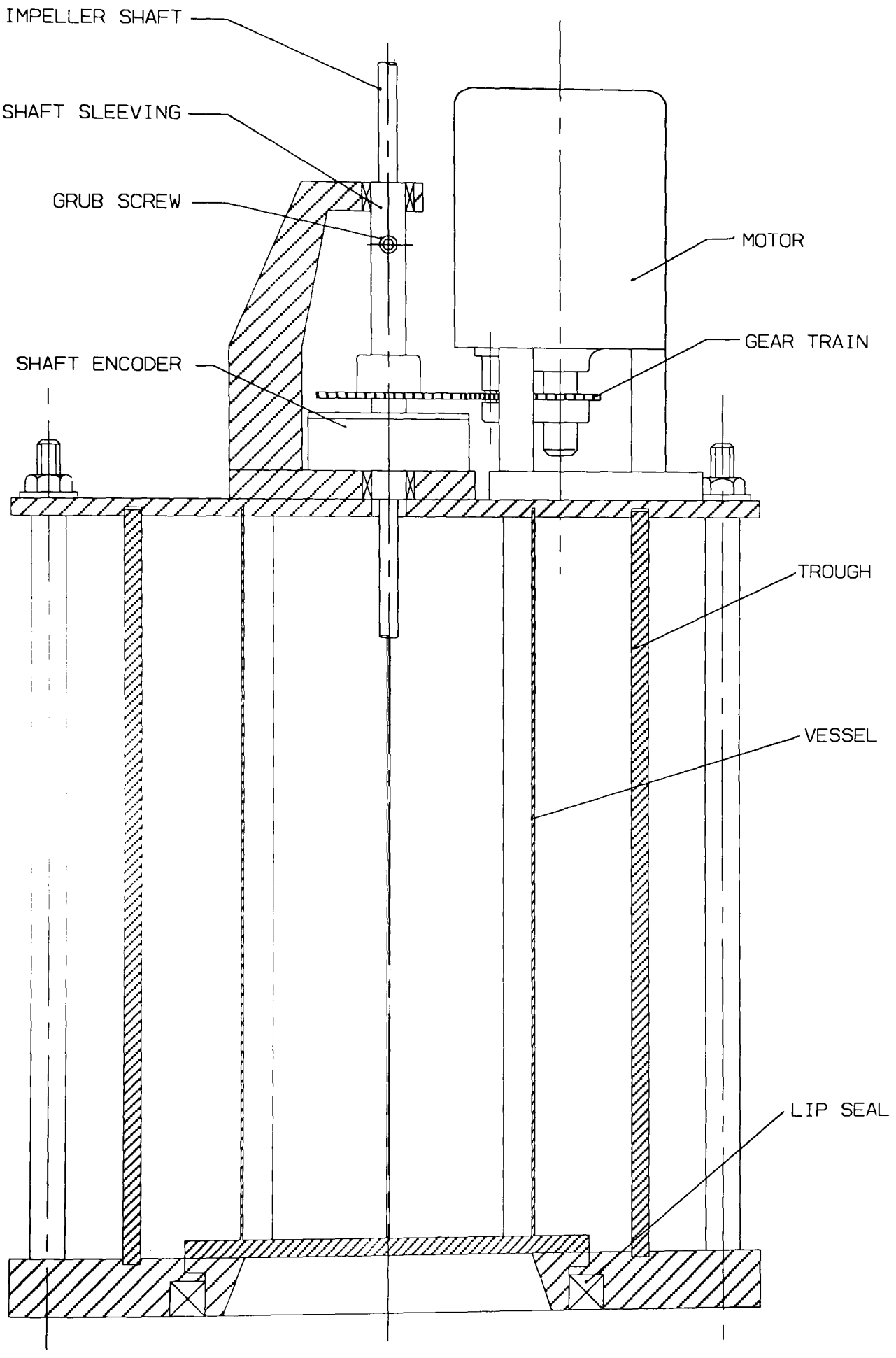


**Figure 2.2** The T = 100 mm vessel test section.

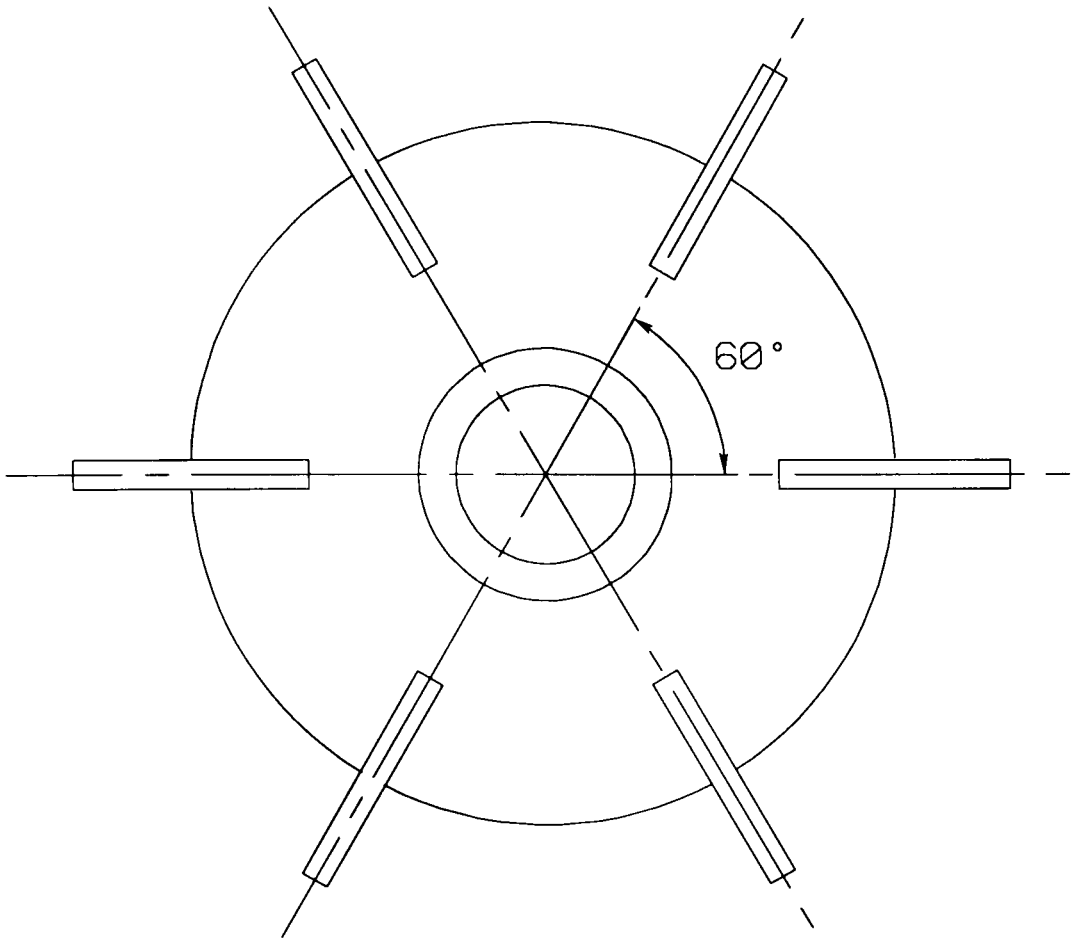


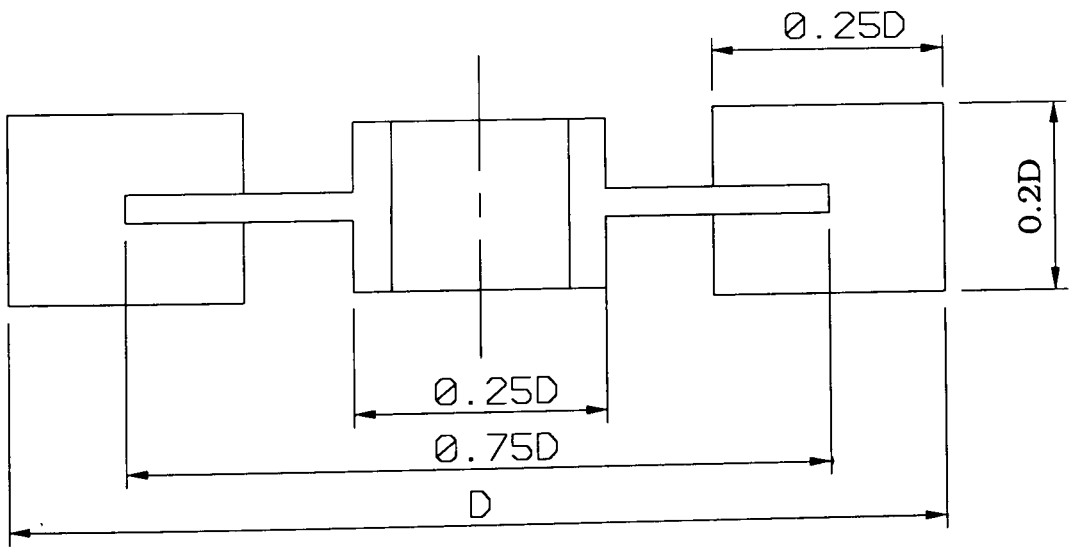


**Figure 2.3** The geometry of the Rushton impellers.

(a)

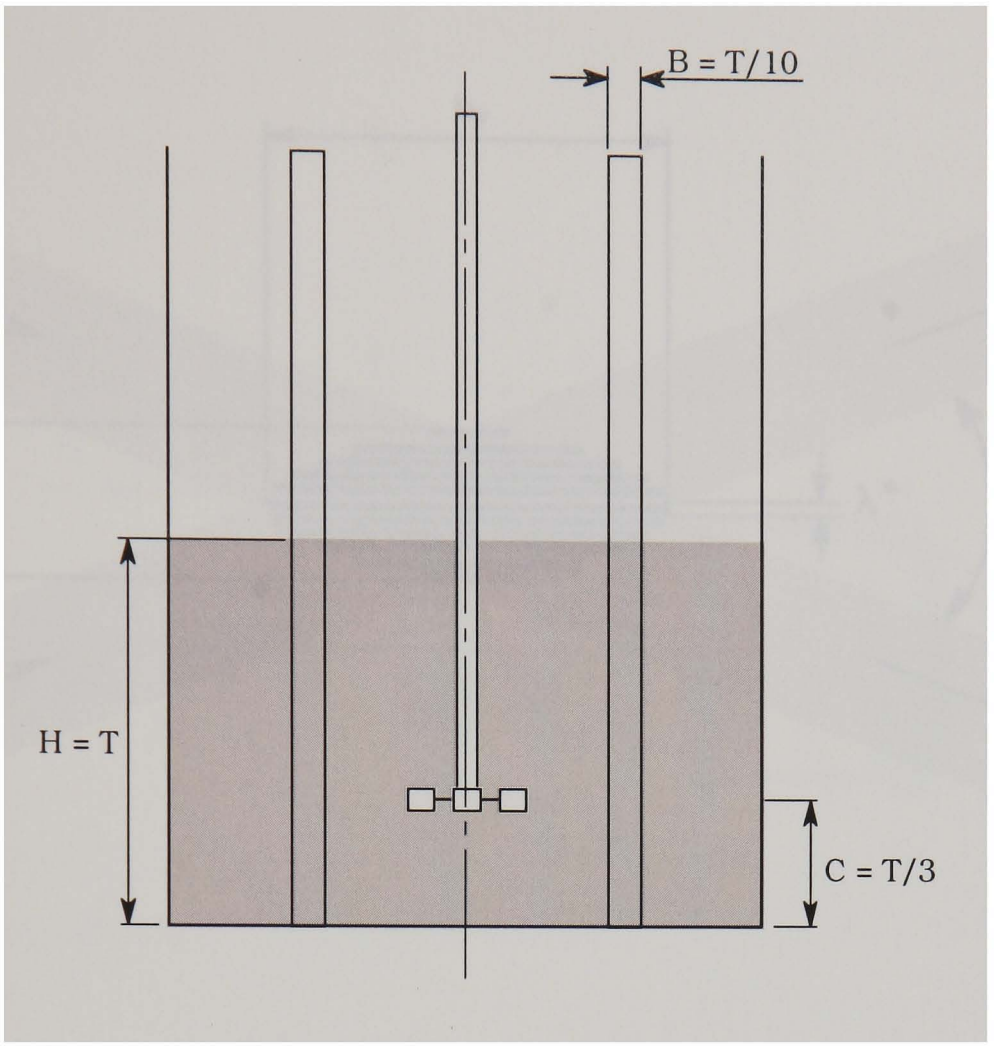


(b)

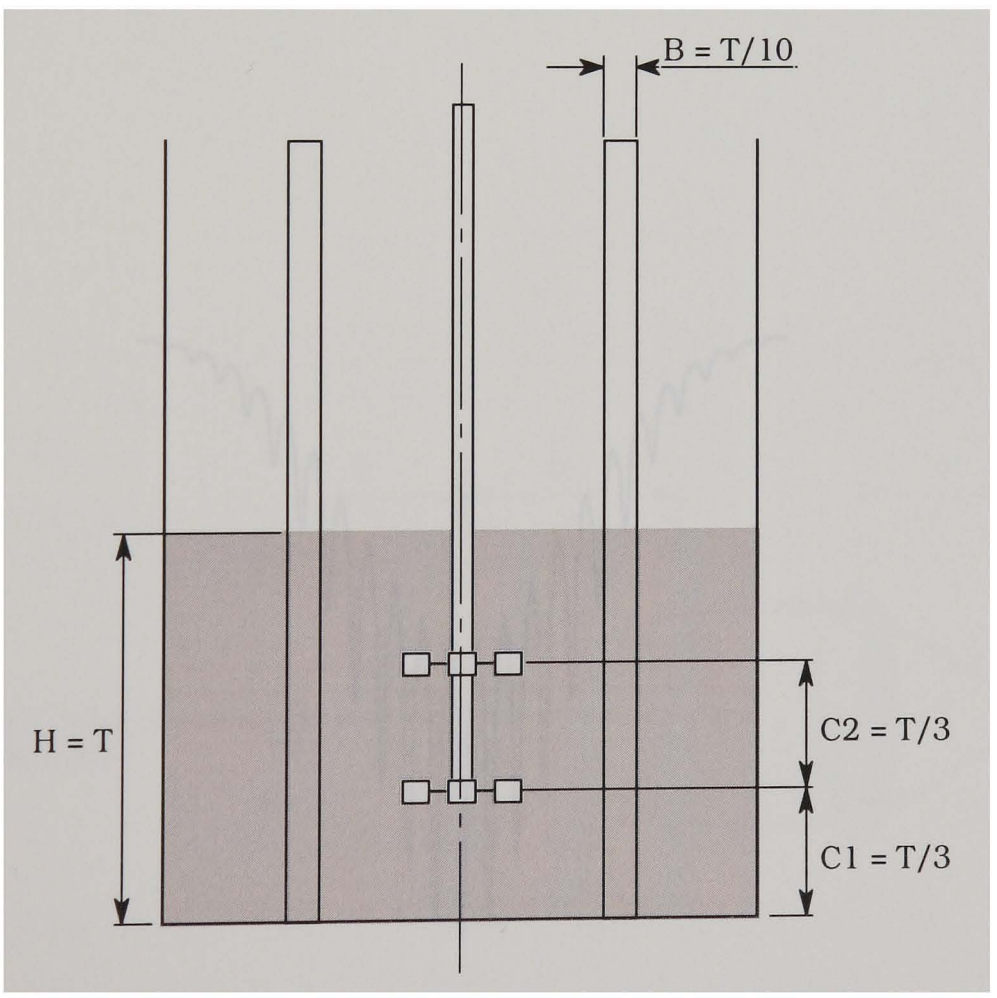


**Figure 2.4** The flow configuration for (a) one impeller; and (b) two impellers.

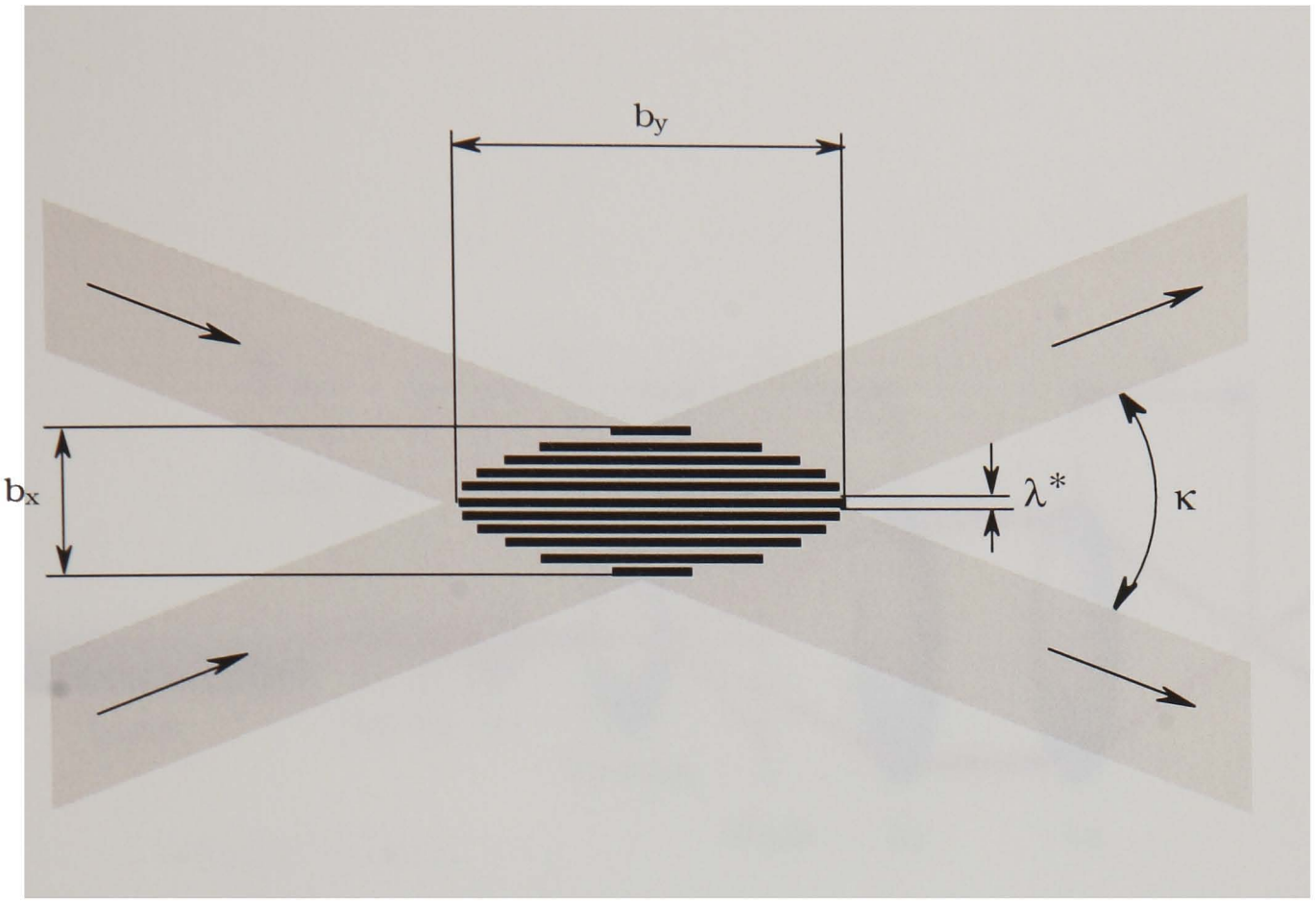


**Figure 2.5** A typical interference fringe pattern produced by two crossing beams.

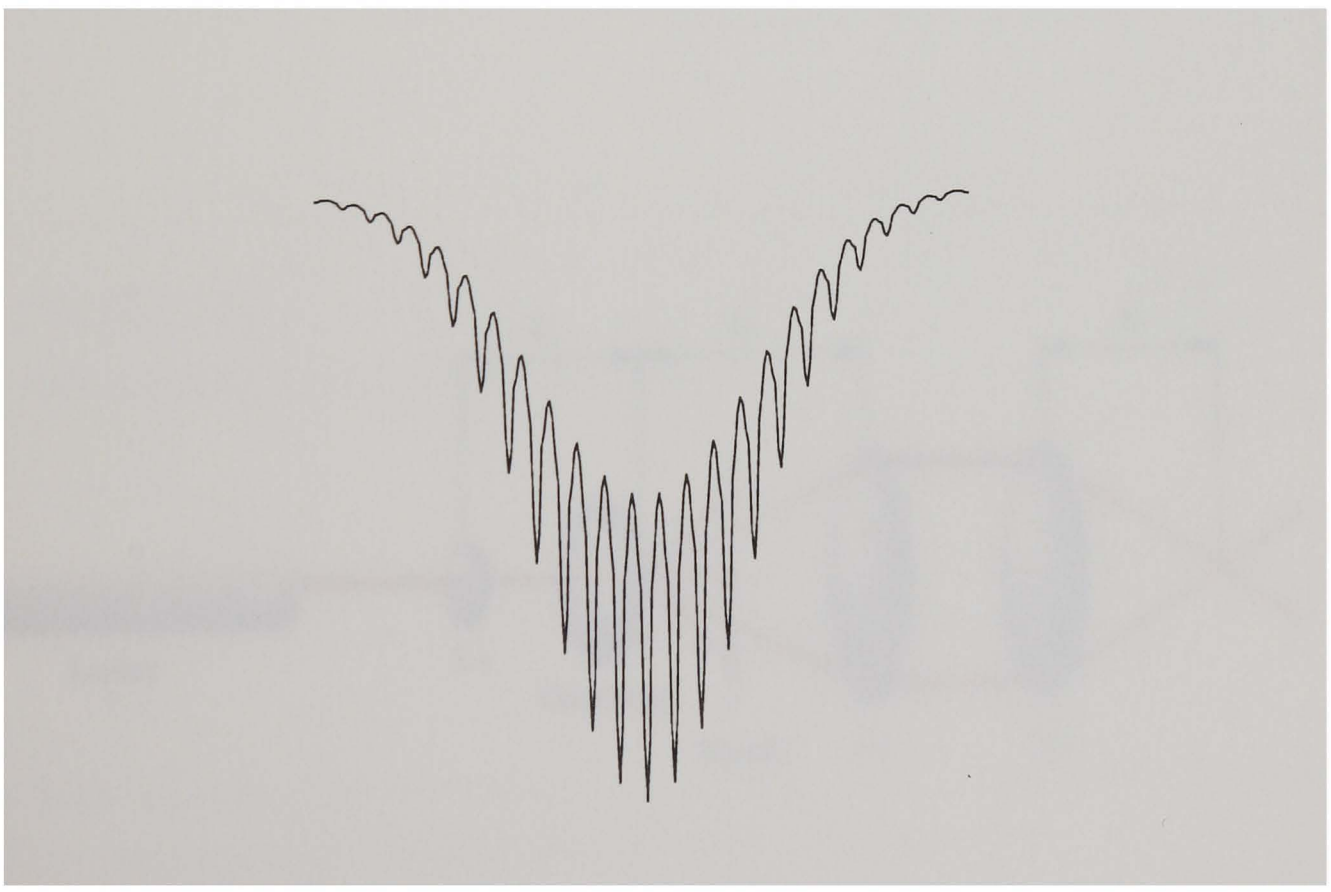

**Figure 2.6** A typical Doppler signal produced when a particle crosses a measurement volume.

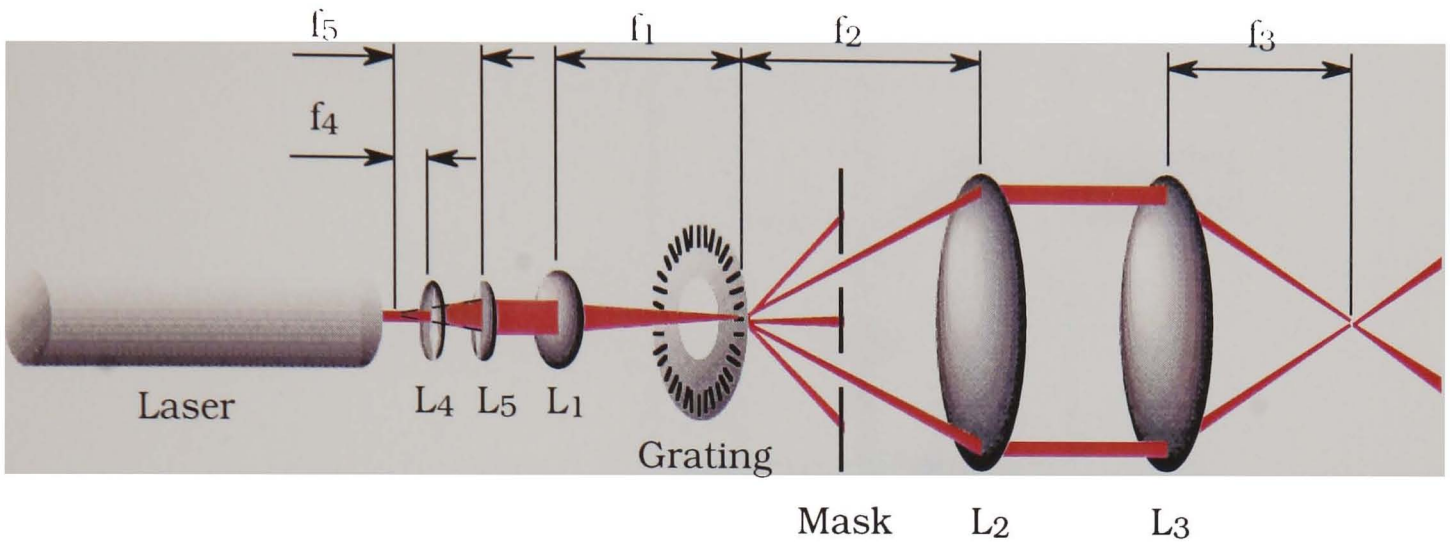


**Figure 2.7** The optical arrangement of the anemometer used for the T = 100 mm vessel.

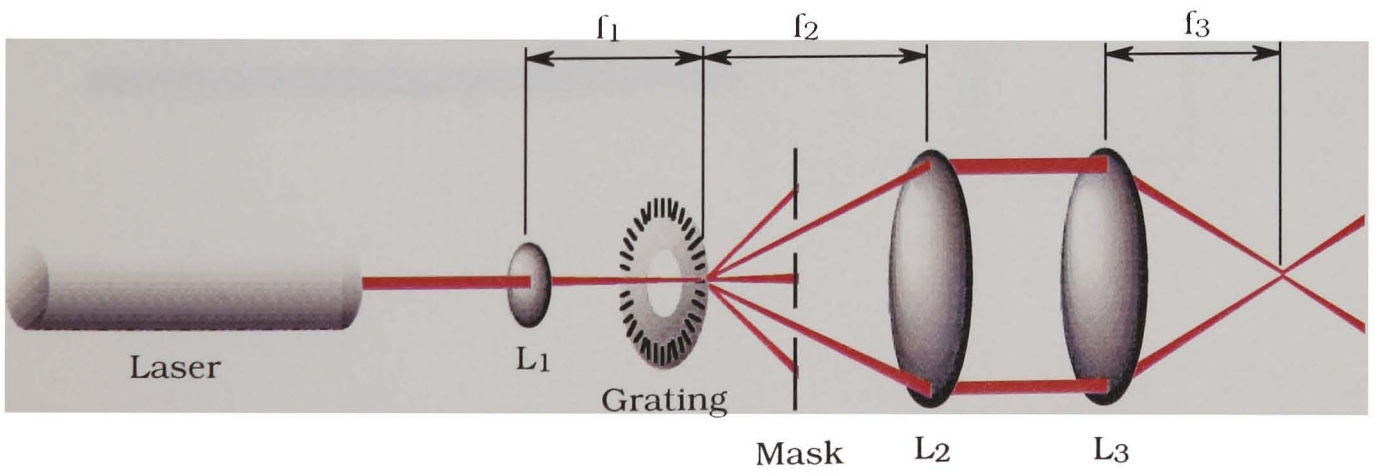


**Figure 2.8** The optical arrangement of the anemometer used for the T = 294 mm vessel.

(a)

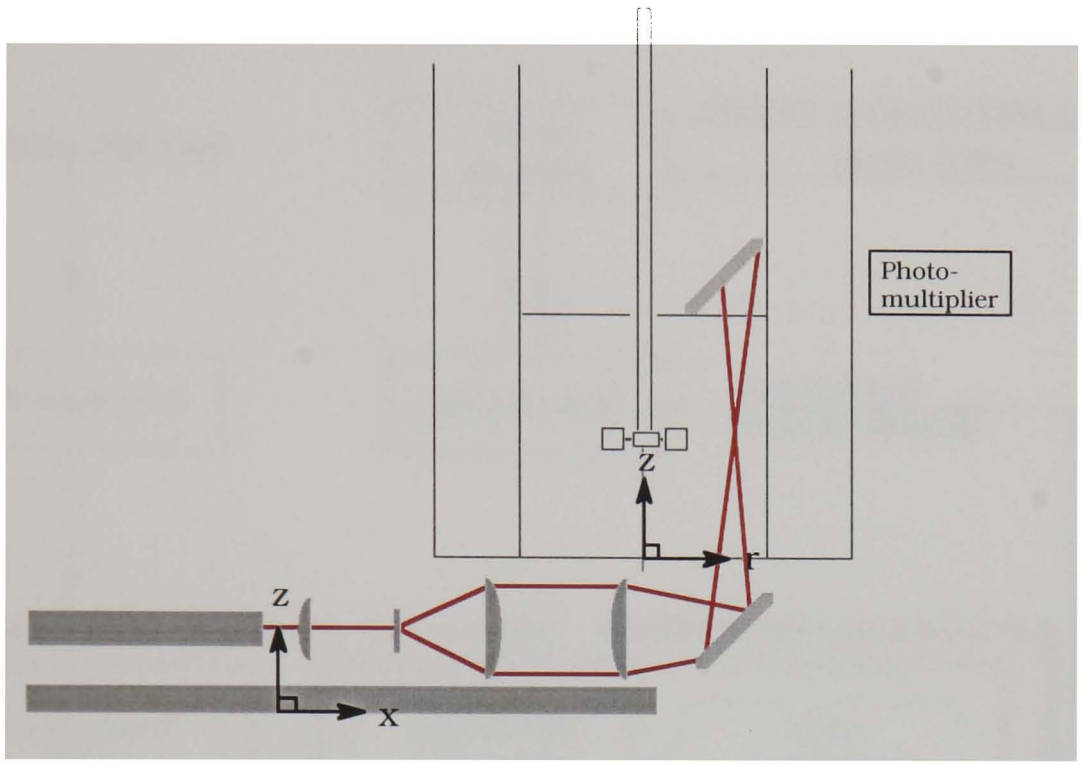


(b)

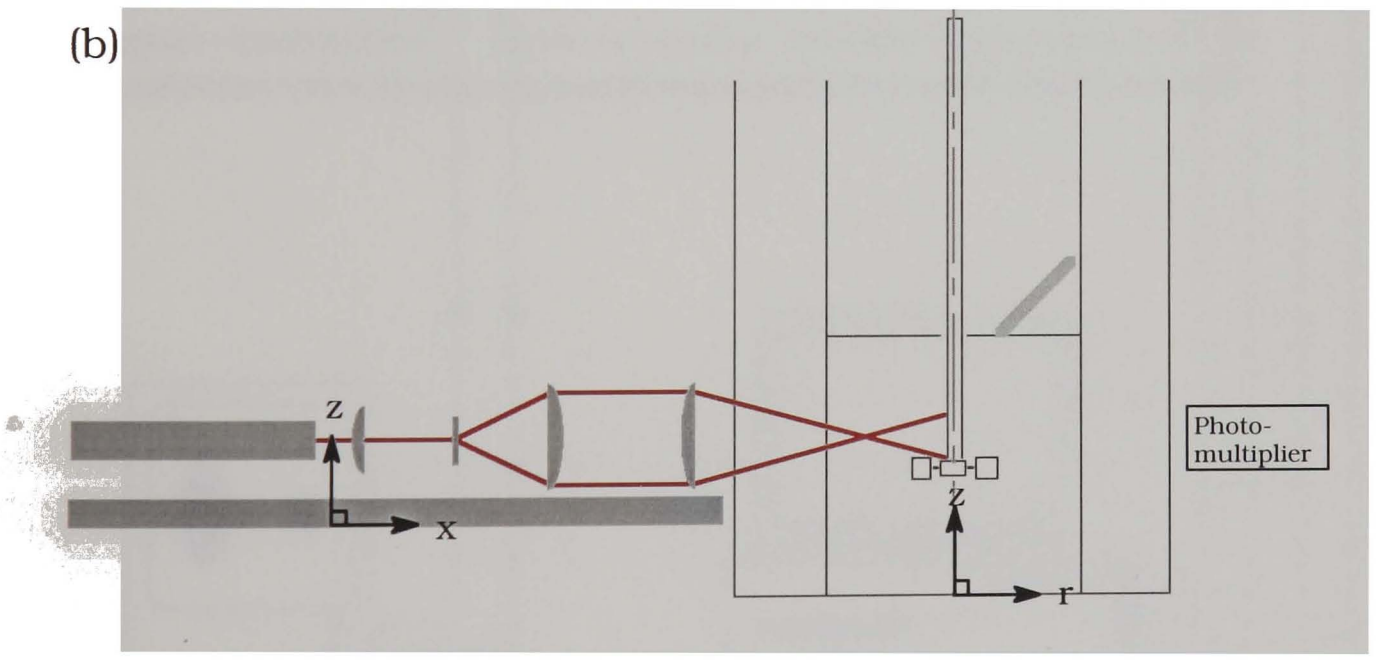


**Figure 2.9** Beams orientation for measuring (a) the radial component; and (b) the axial component in the T = 100 mm vessel.

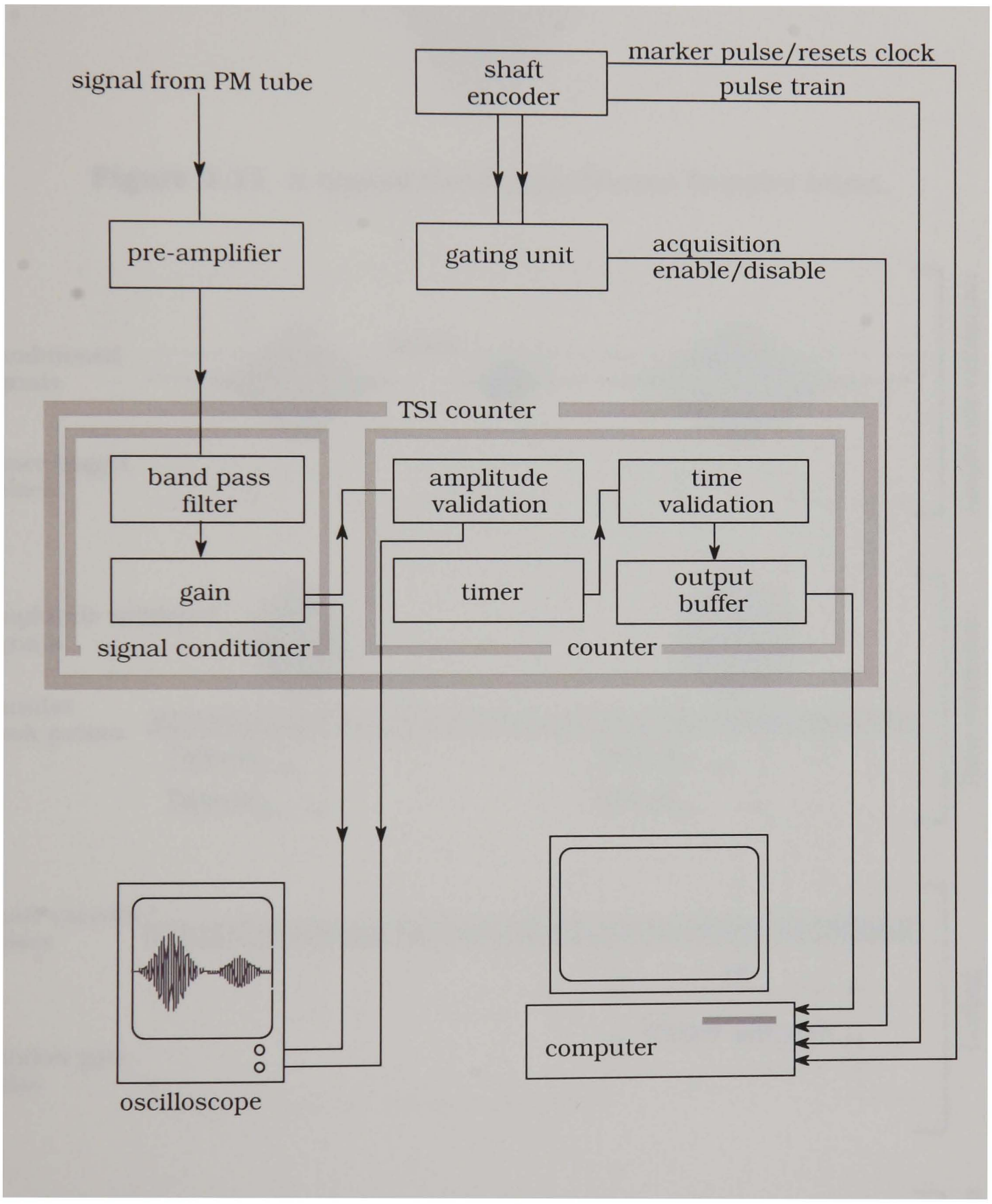


**Figure 2.10** The frequency counter signal processing procedure.

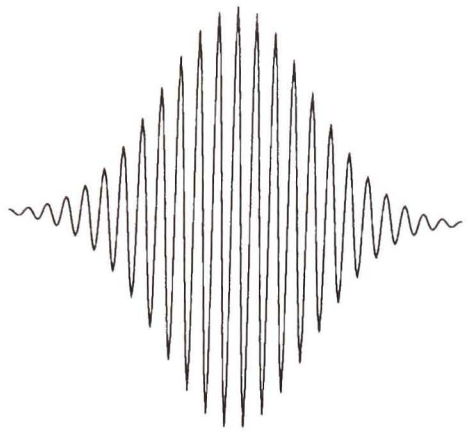

**Figure 2.11** A typical band-pass filtered Doppler burst.

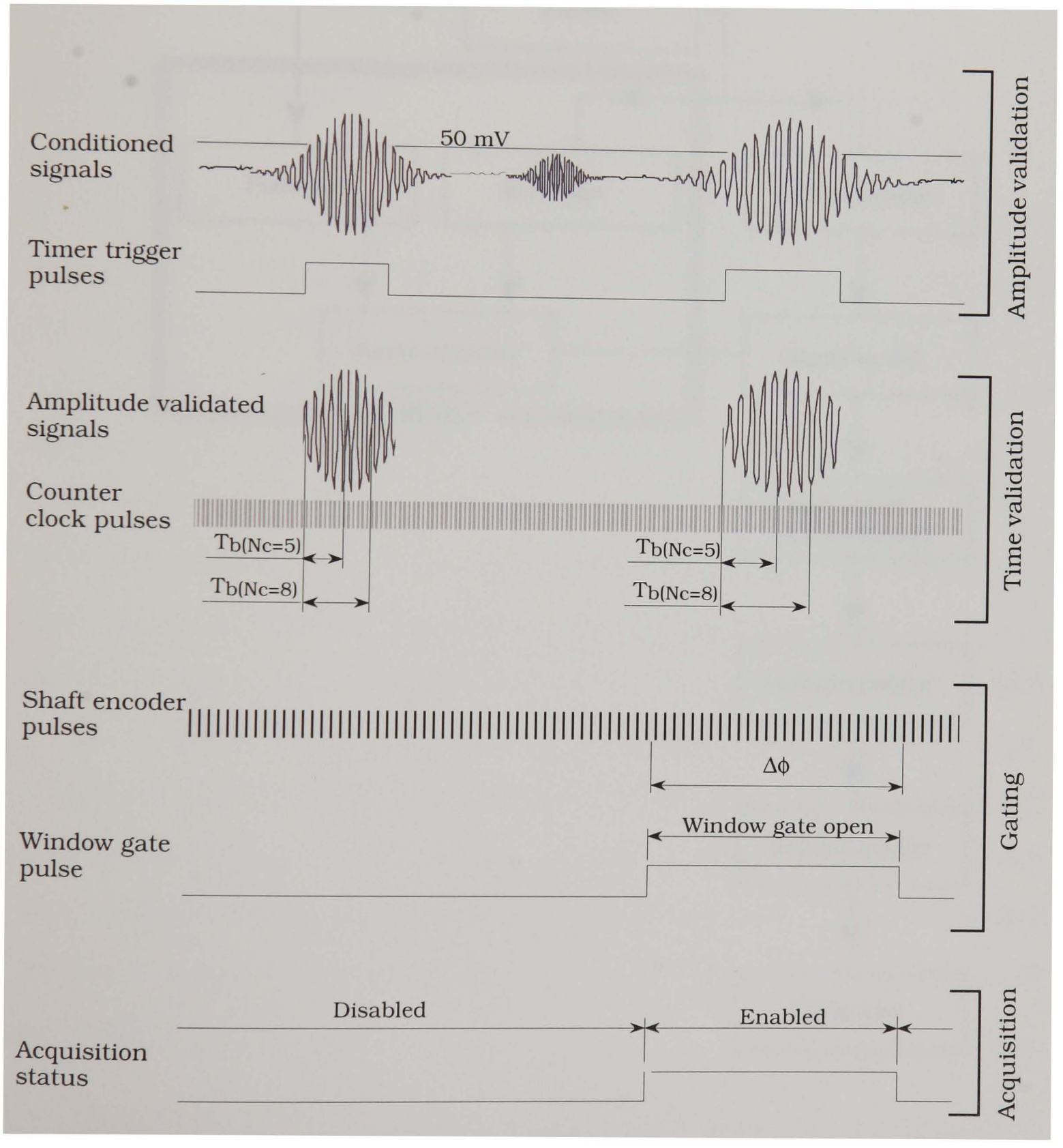


**Figure 2.12** The amplitude validation, time validation, gating and acquisition status of measurements obtained with the frequency counter.

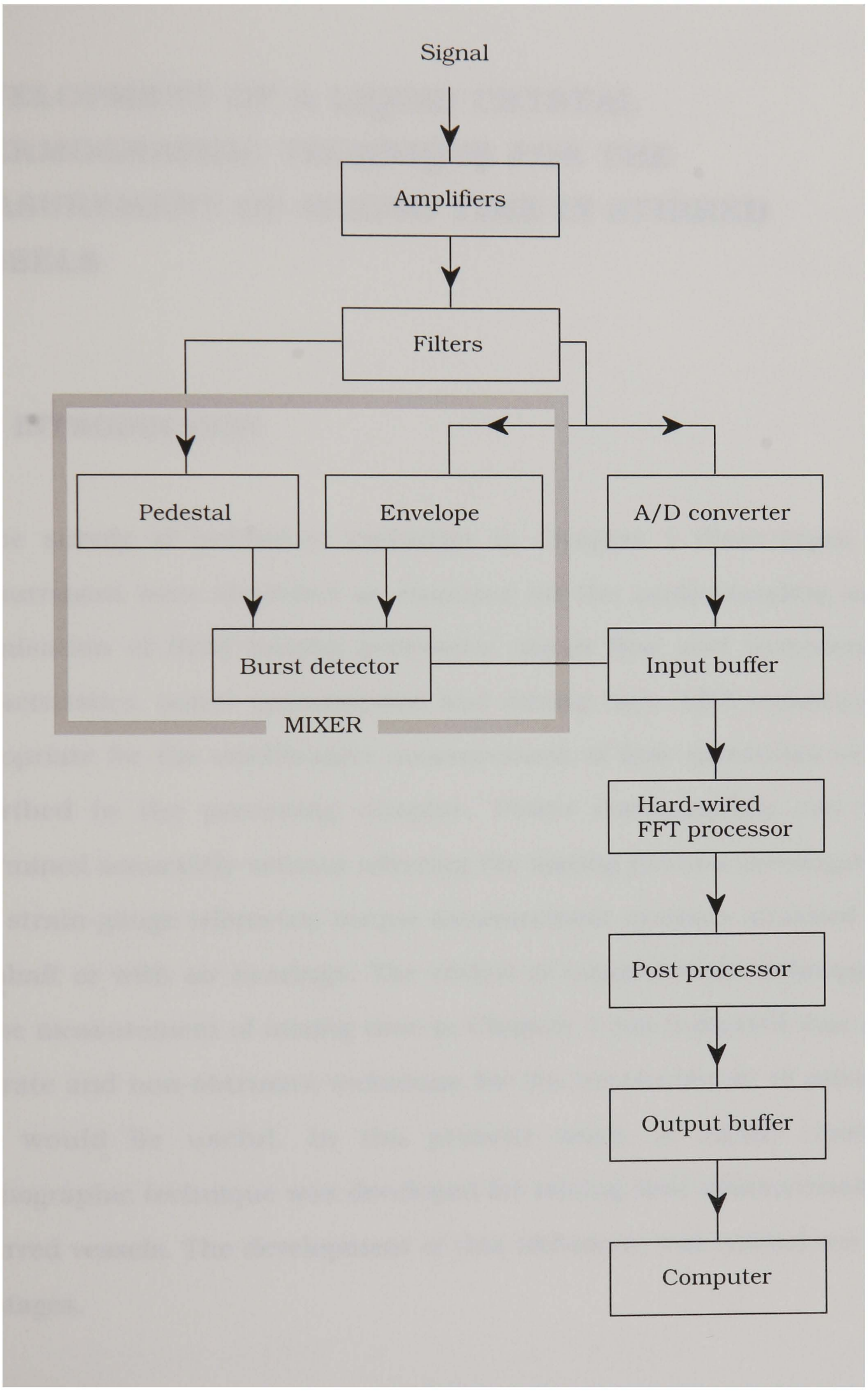


**Figure 2.13** The signal processing procedure of the BSA.

# CHAPTER 3

# DEVELOPMENT OF A LIQUID CRYSTAL THERMOGRAPHIC TECHNIQUE FOR THE MEASUREMENT OF MIXING TIME IN STIRRED VESSELS

## 3.1 INTRODUCTION

In the survey of published literature in Chapter 1 three types of measurement were identified as essential for the understanding and optimisation of fluid mixing processes: mean flow and turbulence characteristics, power consumption and mixing time. LDA techniques appropriate for the unobtrusive measurement of flow quantities were described in the preceding chapter. Power consumption can be determined accurately without affecting the mixing process investigated with strain-gauge telemetric torque measurement systems attached to the shaft or with air bearings. The review of experimental techniques for the measurement of mixing time in Chapter 1 has indicated that an accurate and non-obtrusive technique for the measurement of mixing time would be useful. In the present work, a liquid crystal thermographic technique was developed for mixing time measurements in stirred vessels. The development of this technique was carried out in two stages.

Initially, in order to study the feasibility of applying liquid crystal thermography in mixing vessels, a specially-designed vessel was

constructed and liquid crystal thermography was applied to measure the transient temperature distributions in the vessel produced both under free convection conditions and by a propeller agitator.

Subsequently, a thermographic technique using insertion of liquid crystal tracers was developed and applied in the 100 mm diameter mixing vessel described in the previous chapter. In the following sections, the principles and methodology of liquid crystal thermography and the digital image processing system and the experimental procedure used in all three stages of technique development are described.

## 3.2 LIQUID CRYSTAL THERMOGRAPHY (LCT)

Liquid crystals are organic materials which exhibit a phase between the boundaries of the solid phase and the conventional, isotropic liquid phase. This is termed a mesomorphic phase, often abbreviated to mesophase. An essential requirement for mesomorphism to occur is that the molecule must be highly geometrically anisotropic, like a rod or a disk. A substance in this state is strongly anisotropic in some of its properties typical of the crystalline state, such as optical anisotropy and birefringence; on the other hand, it also exhibits mechanical properties typical of the liquid state, such as fluidity and surface tension.

Liquid crystals are divided into two broad categories: lytropic and thermotropic. Lytropic liquid crystals are compounds that show optical anisotropy when dissolved in a particular solvent; one example is soapy

water. On the other hand, thermotropic liquid crystals are compounds that display an anisotropic liquid character at a temperature between those of their pure crystalline and isotropic liquid states.

Thermochromic liquid crystals are a type of thermotropic liquid crystals with rod-like molecules, which reflect light at a specific wavelength for a given temperature. Liquid crystal thermography utilises the temperature dependency of thermochromic liquid crystals. By evaluating the colour display, accurate temperature measurements can be obtained.

Details of the chemical and physical properties of liquid crystals are given, for example, by Chandrasekhar (1977). In the following section a general description of thermochromic liquid crystals is given, and the methodology for the interpretation of the colour display is described in Section 3.2.2.

### 3.2.1 THERMOCHROMIC LIQUID CRYSTALS

Following the nomenclature proposed originally by Friedel (Chandrasekhar, 1977), thermotropic liquid crystals with rod-like molecules are classified broadly into three main groupings according to their optical properties or their molecular arrangements: smectic, nematic and chiral nematic (cholesteric).

Smectic liquid crystals are distinguished not only by their stratified structures, but also by the parallelism of the long axes of their molecules. Over a dozen distinct smectic phases have been identified

and the structure of the simplest form is depicted in Figure 3.1. As shown in the figure, the molecules are upright with their centres irregularly spaced. The interlayer attractions are weak compared to the lateral forces between molecules so that the layers are able to slide over one another relatively easily. Hence this mesophase has fluid properties, though it is considerably more viscous than the other phases.

In the nematic phase the molecules are spontaneously oriented with their axes approximately parallel, but the positions of their centres are more disorganised than in the smectic phase. Hence no discrete layers can be identified, as shown in Figure 3.2. The preferred molecular direction usually varies from point to point in the medium.

Chiral nematic liquid crystals are composed of optically active molecules. They are usually referred to as cholesteric liquid crystals as the first compounds found to exhibit this phase were derivatives of cholesterol. Thermochromic crystals used in liquid crystal thermography are mixtures of chiral nematic crystals.

In the chiral nematic phase, the molecules are arranged in thin layers. Within each plane layer the molecules are aligned with their long axes parallel like in the nematic phase, and have an average direction defined by a unit vector $\hat{r}$. Each layer is slightly twisted with respect to the next. The effect is cumulative and an overall helical structure is formed as shown in Figure 3.3. The average molecular direction of each layer, $\hat{r}$, traces out a helix in space. The pitch length, P, defined as the

longitudinal distance in which the direction vector, $\hat{r}$, undergoes a complete 360° revolution, is used to quantify the degree of twist.

This spiral arrangement of molecules in this mesomorphic phase is responsible for the unique optical properties, namely, selective reflection of incident white light to show bright iridescent colours and a rotatory power about a thousand times greater than that of most optically active substances. Changes in temperature affect the rotation angle between adjacent layers and hence the pitch of the helix. Light is reflected from the crystals due to Bragg diffraction from molecular layers whose axes are aligned and the colour of the reflected light changes with molecular orientation. According to Chandrasekhar (1977), an elementary picture of the temperature dependence of the pitch can be given in analogy with the theory of thermal expansion in crystals. Assuming anharmonic oscillations of the molecules about the helical axis, the mean angle between successive layers, $\bar{\theta}$, is given by:

$$\bar{\theta} = \frac{A\ K\ T}{2\ I\ \omega_0^{\,4}} \qquad (3.1)$$

where A is the coefficient of the cubic anharmonicity term, K is a constant, T is the temperature, I is the moment of inertia of the molecules and $\omega_0$ is the angular frequency. Thus the pitch, $P \propto 1/\bar{\theta}$, decreases slightly with temperature. Chiral nematic liquid crystals usually turn from colourless to red (long wavelength) at low temperatures, passing through the colours of the visible spectrum to blue/violet (short wavelength) and finally to colourless again at higher

temperatures. The characteristic wavelength at which a particular chiral nematic crystal scatters light, $\lambda_0$, is given by:

$$\lambda_0 = \bar{\mu}\, P \qquad (3.2)$$

where $\bar{\mu}$ is the mean refractive index, and P is the pitch of the helix.

$\lambda_0$ generally depends on the liquid crystal composition, the imposed electric and magnetic fields, pressure, shear stress, vapour present in the fluid and the angles of incidence and reflection of the light, as well as temperature. Moreover, as liquid crystals do not change colour abruptly at a single precise temperature, but sweep through the spectral range from red to blue over a range of temperatures, the interpretation of liquid crystal images is complicated and may be made more complex by the often imperfect colour response of the crystals.

In order to extract the temperature information from the liquid crystal colour displays, it is necessary to calibrate the liquid crystals at the outset of an experiment so as to ascribe particular colours to temperatures over the response range of the liquid crystals. Furthermore, since liquid crystals are subject to contamination and deterioration, calibration may also be necessary in regular intervals to ensure that no change of the response characteristics has occurred. The methodology of measuring colour as so to ascribe particular colours to temperatures is described in the following section.

### 3.2.2 COLOUR MEASUREMENT

Light might be conceived as consisting of an agglomeration of light rays and is generally considered as electro-magnetic radiation, like X-ray and radio waves. The monochromatic radiations of light rays are distinguished by their frequencies. Frequency (f) and wavelength ($\lambda$) are related by:

$$c = \lambda f \tag{3.3}$$

where c is the velocity of light (= $2.998 \times 10^8$ m/s). Though light has different velocities in different media, changes in c are small. Therefore, monochromatic radiations can be characterised either by their frequencies, or by their wavelengths and wavelength is the most frequently used characteristic.

Monochromatic radiations with wavelengths smaller than 380 nm or larger than 780 nm are in general invisible to the eye. Within the visible spectrum, it is estimated that ten million different colours can be distinguished by humans (Judd and Wyszecki, 1975). Though wavelength is a physical quantity, which can be objectively measured with great accuracy, colours perceived by individuals depend on all kinds of properties of the human visual system. The determination of colours by humans is therefore very complex as it involves a subjective physiological process (Bloomer, 1990).

In order to evaluate colours quantitatively, various schemes of specifying colour have been proposed and adopted. Amongst those

schemes three-colour (or trichromatic) matching has formed the basis of the system of colour specification which has been adopted internationally.

Trichromatic matching involves experiments on the response of the human eye, which uses a set of three monochromatic lights as additive primaries; namely red, green and blue lights to cover the long, medium and short wavelengths, respectively, of the visible spectrum. The intensities of the three primaries are adjusted until a perfect match with a test colour is perceived by an observer.

The data obtained from two separate trichromatic matching experiments carried out by Guild and Wright (Hunt, 1991) were combined by transforming each set of data mathematically to obtain the same results as if the following monochromatic matching stimuli, called the RGB tristimuli, had been used:

| | |
|---|---|
| Red | 700 nm |
| Green | 546.1 nm |
| Blue | 435.8 nm |

However, to match all colours in the visible spectrum using the RGB tristimuli, it is necessary to use negative intensities. In order to ameliorate this, the Commission Internationale de l' Eclairage (CIE) drew up in 1931 an internationally adopted system of colour specification. This system uses the tristimulus values, X, Y and Z to denote the amount of red, green and blue lights needed to form any

given colour. The relationships between the RGB and the XYZ tristimuli are as follows:

$$X = 0.49R + 0.31G + 0.20B \quad (3.4a)$$

$$Y = 0.17697R + 0.81240G + 0.01063B \quad (3.4b)$$

$$Z = 0.00R + 0.01G + 0.99B \quad (3.4c)$$

Important colour attributes are related to the relative magnitudes of the tristimulus values. Relative tristimulus values $x$, $y$ and $z$, called chromaticity co-ordinates, are given by:

$$x = X / (X + Y + Z) \quad (3.5a)$$

$$y = Y / (X + Y + Z) \quad (3.5b)$$

$$z = Z / (X + Y + Z) \quad (3.5c)$$

It is clear from the above equation that $x$, $y$ and $z$ are related by:

$$x + y + z = 1 \quad (3.6)$$

therefore if $x$ and $y$ are known, $z$ can be calculated from Equation (3.6). Hence, all possible colours can be mapped by plotting $y$ as the ordinate against $x$ as the abscissa, which is usually referred to as the $x$, $y$ chromaticity diagram. Figure 3.4 shows an $x$, $y$ chromaticity diagram indicating the spectral locus with its two ends joined by a straight line (known as the purple boundary). The co-ordinates of the tristimuli R, G and B are also marked on the diagram.

The triangle formed by the co-ordinates of the three stimuli R, G and B encloses all colours reproducible by positive RGB tristimulus values. The area enclosed by the spectral locus and the purple boundary defines the domain of all possible colours and any point within this area can be described by its chromaticity co-ordinates ($x$, $y$).

However, the distribution of colours in the $x$, $y$ chromaticity diagram is non-uniform, so that distances between pairs of points representing two colours having the same perceptual differences vary widely over the diagram. To account for this, CIE introduced in 1976 another type of chromaticity diagram. This is known as the CIE 1976 uniform chromaticity scale diagram (commonly referred to as the $u'$, $v'$ diagram), shown in Figure 3.5. The relationships between $u'$, $v'$ and $x$, $y$ are given by:

$$u' = 4x/(-2x + 12y + 3) \tag{3.7a}$$

$$v' = 9y/(-2x + 12y + 3) \tag{3.7b}$$

Thus any colour can be described by its $u'$ and $v'$ co-ordinates as well as by its $x$, $y$ co-ordinates. In addition, the $u'$, $v'$ system also provides two measures to describe colours: the CIE 1976 $u'$, $v'$ hue angle, $h$ and the CIE1976 $u'$, $v'$ saturation, $s$. They are given by:

$$h = \arctan\left((v' - v'_n) / (u' - u'_n)\right) \tag{3.8a}$$

and

$$s = 13\left((v' - v'_n)^2 + (u' - u'_n)^2\right)^{1/2} \tag{3.8b}$$

where $u'_n$ and $v'_n$ are the values of $u'$ and $v'$ of a selected reference white. h lies between 0° and 90° if $(v' - v'_n)$ and $(u' - u')$ are both positive; between 90° and 180° if $(v' - v'_n)$ is positive, and $(u' - u'_n)$ is negative; between 180° and 270° if $(v' - v'_n)$ and $(u' - u'_n)$ are both negative; and between 270° and 360° if $(v' - v'_n)$ is negative and $(u' - u'_n)$ is positive.

Figure 3.6 illustrates the geometrical definition of *h* and *s* for a colour. In the diagram, C and N are the points representing the colour considered and the reference white respectively. h is the angle between the line NC and the horizontal line drawn from N to the right, measured anti-clockwise from the horizontal line; and s is 13 times the distance between N and C.

In colour television/video transmission, the colours are also produced by addition of mixtures of red, green and blue. However, the matching stimuli used in television/video transmission are different from those mentioned earlier, and the chromaticity co-ordinates of the three primaries, *R*, *G* and *B*, chosen as standard for European television, are (Hunt 1991):

| | | | | |
|---|---|---|---|---|
| Red | $x = 0.64$ | $y = 0.33$ | $u' = 0.451$ | $v' = 0.523$ |
| Green | $x = 0.29$ | $y = 0.60$ | $u' = 0.121$ | $v' = 0.561$ |
| Blue | $x = 0.15$ | $y = 0.06$ | $u' = 0.175$ | $v' = 0.158$ |

The co-ordinates of these three primaries are shown on a $x$, $y$ chromaticity diagram and on a $u'$, $v'$ diagram in Figures 3.7 and 3.8 respectively. The areas enclosed by the triangles formed by the three co-

ordinates on both diagrams define the domain of all colours that are reproducible using the three stimuli *R*, *G* and *B*, which is a subset of all possible colours. In the present work the hue angle and saturation of any RGB colour were obtained using Equations (3.8a) and (3.8b) and the above table of $x$, $y$ , $u'$ and $v'$ values.

## 3.3 THE DIGITAL IMAGE PROCESSING SYSTEM

The digital image processing system used in this work to record and interpret the video images of the liquid crystal colour displays is shown schematically in Figure 3.9. It comprised the following equipment:

1. a CCD colour video camera with PAL colour standard composite video signal output (Sony EV1-1011P);
2. a S-VHS PAL video cassette recorder with still frame facility (Panasonic NV-FS200 HQ);
3. a multi-system/RGB monitor (JVC TM-150 PSN-K);
4. a computer (Macintosh II fx);
5. a video frame grabber/digitiser card (Screen Machine) and associated software (SM Camera) installed in (4).

Liquid crystal colour displays are captured by the camera and the composite video signal output of the camera is input to the video cassette recorder. The signals received by the video recorder are observed on the monitor to assess the quality of the images. When satisfactory conditions are attained, the events are recorded onto video tapes at a

rate of 25 frames per second. The frame rate is determined by the PAL colour standard used by the video system.

The recorded events are then played back in a 'frame-by-frame' mode, so that the timing of the frame to be analysed relative to a reference frame/start of the event investigated can be ascertained. The composite video signal of a frame is input to the computer via the frame grabber/digitiser card. The frame grabber decodes the composite video signal and grabs the frame as a *RGB* true colour image.

The grabbed image is digitised into a 24-bit digital image composing of three planes of pixels where each pixel has a red, green and blue intensity, each coded on a 8-bit format (i.e. 256 levels). The digitised image is then stored on disk for off-line colour measurement to obtain the hue, saturation and lightness of each pixel.

Digitisation of an image can be set to 100%, 50% or 25% of the number of pixels recorded according to the resolution required and/or to minimise computational time. Highest resolution is obtained by 100% digitisation with which every pixel of the image is analysed, resulting an image of 756 × 512 pixels. With 50% digitisation, one in every two pixels horizontally and vertically is digitised, resulting in an image size of 378 × 256 pixels. In the case of 25% digitisation, one in every four pixels is digitised and the image size is 189 × 128 pixels. During the first two stages of the technique development, 50% digitisation was used. In order to obtain the highest possible resolution, 100% digitisation was used when the technique was applied for the measurements of mixing time.

The aforementioned descriptions of liquid crystals and colour analysis have indicated the complexity of the tasks involved in the development and application of LCT techniques. The complexity of the flow processes in stirred vessels necessitated the development of the temperature /mixing time measurement technique in three stages, as outlined in Section 3.1. In the following section the natural convection and forced convection stages of development, with liquid crystals already suspended in the flow in a cylindrical vessel, are described. In Section 3.5 the third stage, the extension of the technique for the measurement of mixing time, is described.

## 3.4 DEVELOPMENT AND APPLICATION OF LCT IN TWO CONVECTION EXPERIMENTS

### 3.4.1 FLOW CONFIGURATION

The test section assembly is shown in Figure 3.10. It comprised a cylindrical unbaffled vessel, 100 mm in diameter and 120 mm in height. The vessel was installed inside a trough of square cross-section and the gap between the vessel and the trough was filled with water. This was necessary to minimise refraction effects at the outer curved surface of the cylinder as well as to ensure that the heat generated by the illuminating light source did not affect to any significant extent the colour displayed by the liquid crystals. Both the vessel and the trough walls were made of transparent acrylic material (Perspex) to maximise optical access. The working fluid inside the cylindrical vessel was distilled water and the height of the liquid column was 100 mm.

Thermochromic liquid crystals encapsulated as gelatine-shell micro-spheres of 20 μm mean diameter were suspended in the working fluid. For the forced convection experiments, a three-blade propeller of 30 mm diameter located centrally in the vessel and 10 mm above the bottom was used to agitate the fluid. The propeller rotational speed was kept constant at 60 rpm.

A temperature gradient was generated along the vessel axis by means of two metal plates which formed the lid and the bottom of the cylindrical vessel. Three Peltier-effect heat pumps were attached to the bottom plate to provide a source of heat. Similar pumps were attached to the lid in reverse fashion to remove heat. The reverse sides of the pumps on the lid and the bottom of the vessel were attached to extensive finned surfaces (heat sinks) in order to maximise the heat removal/addition effect of the pumps. The temperatures of the two metal plates were controlled independently by adjusting the voltages and/or currents supplied to the heat pumps. The lid also provided a means of eliminating the formation a vortex and consequent air entrainment from the free surface. This entrainment occurred when the agitator was rotating in the absence of the lid. It was found that air entrainment resulted in large bubbles being suspended in the flow which interfered with the light scattered by the liquid crystal tracers.

In both the free and the forced convection experiments, the temperatures of the outside surfaces of the top and the bottom plates, i.e. the surfaces where the heat pumps were attached, were maintained at 16.1°C and 29.3°C respectively.

### 3.4.2 EXPERIMENTAL PROCEDURE

The liquid crystals used displayed colours which could be visually distinguished for temperatures between 24°C and 29°C. Within this range, small changes in temperature can be registered with a unique value of hue. Outside this range the accuracy is poor and cannot be readily ascertained.

The illumination of the liquid crystal colour display was provided by a collimated 2 mm thick sheet of white light produced by a 1 kW mercury lamp. The heat generated by the light source was dissipated by the water placed in the gap between the vessel and the trough, hence the effect on the colour displayed was negligible.

The liquid crystal colour displays were recorded by the colour video camera mentioned in Section 3.3. The aperture of the video camera lens was kept fully open, the shutter speed used was 1/50 s and the image collecting angle was 90°±2° to the plane of illumination. The physical dimensions of the entire view captured by the video camera was 140 mm × 100 mm, and 50% digitisation was used. This represents a resolution of about 3 pixels/mm in both directions. These conditions as well as the lighting condition used were identical for both the calibration tests and the actual experiments.

In order to calibrate the variation of hue with temperature to obtain an accurate quantitative description of the thermal distribution in the vessel, a diametrical plane was illuminated and the top and the bottom heating plates were set at the same temperature. When steady state

conditions were reached, the temperature of the fluid was measured using a fine-wire thermocouple and the image of the thermal field was recorded. This was repeated for 10 different temperatures. The image was then analysed using the system described in Section 3.3. Although the illuminating sheet of light was collimated, uniform illumination of the entire thermal field viewed and analysed is invariably difficult. Hue angles of the image at various locations were obtained by averaging small parts of the image to account for local variations in the observed colour, therefore, differences in illumination intensity and viewing angle were compensated for (Dabiri and Gharib, 1991).

This process was then repeated with the top and bottom plates set at various temperatures to cover the whole response range of the liquid crystals. The relationship between temperature and hue angle at various locations within the thermal field is obtained by using a third order polynomial curve fitting of the calibration data over the temperature range 24°C to 29°C in the form of:

$$t = a_i + b_i h + c_i h^2 + d_i h^3 \qquad (3.9)$$

where t is the temperature in °C, h is the hue angle (varying from 0 – 255) and $a_i$, $b_i$, $c_i$ and $d_i$ are constants for the area i within the thermal field. A typical calibration curve obtained is shown in Figure 3.11, which has a shape similar to those obtained with other types of thermochromic liquid crystals, for example, Moffat (1990) and Lee and Yianneskis (1993).

The liquid crystal colour display in the actual experiments was recorded onto video tape. The recorded display is then played back in a 'frame-by-frame' mode. Each frame was captured by the frame grabber and digitised into a 24-bit digital image composing of three planes of pixels where each pixel has a red, green and blue intensity, each coded on an 8-bit format (i.e. 256 levels). These intensity values were then transferred to a VAX mainframe computer and read by a specially-written FORTRAN program as three sets of two-dimensional arrays. From these values the program computed the values of hue of each pixel by using Equation 3.8(a). Subsequently the hue distribution was transformed into temperature distribution using the calibration data and temperature contours were then plotted using various UNIRAS software subroutines.

### 3.4.3 RESULTS

#### NATURAL CONVECTION EXPERIMENT

Figure 3.12 shows a topographic map of the distribution of hue from a recording obtained with free convection taking place in the vessel. The figure shows only part of the image captured corresponding to one-half of the vessel cross-section. A pixel-to-pixel analysis was then carried out to transform this hue distribution into temperature contours using the calibration equations obtained for the different pixel locations, and the temperature contours obtained are shown in Figure 3.13(a). This procedure was then repeated for subsequent video frames. Figure 3.13(b) shows the temperature contours obtained from a second video frame, recorded exactly 3 seconds after that shown in Figure 3.13(a).

The contours in Figure 3.13(a) indicate a thermal current rising near the axis of the vessel. As this region of hotter fluid reaches the top of the vessel it is directed towards the cylinder wall. An extensive region of cooler fluid is located near the lower right side of the vessel. A second hot region can be observed near the middle of the vessel wall. The presence of this region indicates that, even though the vessel is axisymmetric, the free convective flow produced is three-dimensional. However, this may be due, to some extent, to an uneveness of the temperature of the lateral walls, as the temperature of the water in the trough, although monitored, it was not controlled.

Figure 3.13(b) shows more evidence of three-dimensionality in the flow: the hot region near the top appears to have broken into two and the second hot region along the wall has increased in size. The temperature distribution along the axis of the vessel is similar to that in Figure 3.13(a) and cooler fluid is present near the wall around z = 25 mm and r = 40 – 50 mm.

**FORCED CONVECTION EXPERIMENT**

Similarly, the recording obtained with the flow in the vessel stirred by the propeller was analysed. Figures 3.14(a) shows one of the temperature contour maps obtained. The temperature gradients, both axial and radial, are significantly smaller in this experiment, as might be expected due to the mixing effect of the propeller. The flow produced by the propeller is predominantly in the axial direction, with a swirling component superimposed. The temperatures near the axis of the vessel, around r = 0 mm to 20 mm, are lower, as the propeller draws

downwards the fluid which is located near the top and hence cooled by the heat pumps. The down-flowing fluid is heated by coming into contact with the bottom (hot) plate and the upward flow along the cylinder wall generated by the propeller is marked by the region of hotter fluid around r = 25 mm to 50 mm. Near the top of the wall (z = 60 mm to 100 mm and r = 40 mm to 50 mm) a region of cooler fluid can be observed. This may be due to the presence there of a small vortex which inhibits the entrainment of hotter fluid from the rising propeller stream, resulting in lower temperatures locally.

The temperature distribution 3 seconds later shown in Figure 3.14(b) is essentially similar. The differences between the recordings at the two instances indicate that there is some unsteadiness in the flow which may be partly due to turbulence.

## DISCUSSION

The results show conclusively that qualitative as well as quantitative results can be obtained using liquid crystal thermography. However, before extending the technique for the measurement of mixing time, certain modifications/improvements are required. First, the temperature of the water in the trough has to be controlled in order to minimise the unevenness of the temperature of the lateral walls.

Second, although the differences in illumination intensity and viewing angle were compensated by averaging small parts of the image across the flow field to account for local variations, in order to obtain accurate results, averaging had to be carried out over a large number of

such parts, which greatly increased the computational time during analysis. Therefore, the lighting of the flow field has to be improved.

## 3.5 APPLICATION OF LIQUID CRYSTALS AS INSERTED TRACERS IN MIXING EXPERIMENTS

### 3.5.1 FLOW CONFIGURATION, CALIBRATION AND EXPERIMENTAL PROCEDURE

The colours displayed by the liquid crystals depend on the lighting conditions as well as on the image collection angle. As mentioned earlier, differences in illumination intensity and viewing angle can be compensated by using different calibration curves for different areas of the flow field. However, such a method greatly increases the computational time, especially in the case of mixing time measurements where a great number of frames have to analysed to determine the mixing time. Therefore, when extending the technique to mixing time measurement, the lighting condition and image collection angle were optimised† so that during the calibration experiments the values of hue of all pixels were within ±5 of the mean value of hue at any particular temperature.

The test section used was the 100 mm diameter stirred vessel described in Chapter 2. The geometry and dimensions of the test section were described in Section 2.2 and shown in Figures 2.1 and 2.2. The working fluid inside the cylindrical vessel was distilled water and the liquid column height was 100 mm. As before, thermochromic liquid crystals

† The lighting condition was improved by passing the sheet of light through a pair of 2 mm slits before it entered the vessel

encapsulated as gelatine-shell micro-spheres of 20 μm mean diameter were suspended in the working fluid. The fluid was agitated by either one or two Rushton impellers (details of the impellers are given in Section 2.2 and Figure 2.3). The clearances used were those described in Chapter 2 (see Figure 2.4). A lid was used to eliminate the formation of a vortex in the free surface as for the LDA measurements.

The liquid crystals used displayed colours in the same temperature range as those mentioned earlier, i.e. between 24°C and 29°C. The illumination of the liquid crystal colour display was provided by a collimated 2 mm thick sheet of white light produced by a 1 kW mercury lamp. The heat generated by the light source was dissipated by the water placed in the gap between the vessel and the trough, hence the effect on the colour displayed was negligible.

The aperture of the video camera lens was kept fully open, the shutter speed used was 1/50 s and the image collecting angle was 90°±2° to the plane of illumination. The physical dimensions of the entire view captured by the video camera was 150 mm × 100 mm, and 100% digitisation was used. This represents a resolution of about 5 pixels/mm in both directions. These conditions as well as the lighting conditions used were identical for both the calibration tests and the actual experiment.

The recordings were subjected to a 'frame-by-frame' analysis to obtained the intensity values of the *R*, *G* and *B* planes. The values were then transferred to the VAX mainframe computer and processed to obtained the hue distributions of the images. Since imperfections in the liquid

crystals used were inevitable, a process was considered to be fully-mixed when 95% of the pixels in each image had the same value of hue.

To calibrate the variation of hue with temperature, the $\theta = 0°$ plane was illuminated. The constant temperature water bath which feeds water into the trough of the test section was set at the desired temperature. When steady state was reached in the vessel, the temperature inside the vessel was measured by a fine-wire thermocouple, and the thermal field was recorded. This process was repeated to cover the response range of the liquid crystals. The recording was then analysed using the image processing system described previously to obtain the calibration curve which is shown in Figure 3.15.

It can be observed from Figure 3.15 that, within the temperature range of 25°C to 27.5°C, small changes in temperature can be registered with a unique value of hue and inside this range the value of hue varies approximately linearly with temperature. Experiments were therefore only conducted within this temperature range. It should be noted that differences in calibration and crystal response with the earlier experiments stem from differences in lighting conditions and vessel constructions.

For the mixing time measurements, the temperature of the working fluid inside the vessel was kept constant at 25.2°C. A 5 ml tracer of liquid crystals suspended in distilled water, having the same crystal concentration as the fluid in the vessel, was heated in a constant temperature water bath to 27°C and inserted into the vessel at $r = 25$ mm in the $\theta = 0°$ plane through the lid[†]. The transient process of the

[†] The tracer was inserted into the vessel at the liquid surface by applying a dead weight to a

mixing of the inserted tracer in the vessel was recorded onto video tape. The tracer insertion was performed after the video recording had commenced so that the beginning of the insertion could be accurately determined.

Experiments were conducted at four impeller rotational speeds for both the single- and double-impellers configurations. The rotational speeds were 540, 1083, 1625 and 2165 rpm, corresponding to Reynolds numbers of 10000, 20000, 30000 and 40000 respectively.

### 3.5.2 SAMPLE RESULTS

Figure 3.16(a) shows an unprocessed (colour) image obtained from a recording made with the flow stirred by a single impeller at a speed of 540 rpm. This image was obtained 160 ms after the start of the insertion of the tracer and only half of the vessel cross-section at the $\theta = 0°$ plane is shown. The tracer jet, which was at a higher temperature than the fluid in the vessel, is indicated by the blue region of the figure. It can be observed that the jet has penetrated as far as the impeller region. The tracer jet path is affected by the impeller stream, curving slightly towards the vessel wall.

Figure 3.16(b) shows the corresponding hue contour map of the image obtained 160 ms after the start of the insertion of the tracer. The region with hue values between 120 and 135 observed near the bottom the vessel, indicates that the tracer jet has already reached the bottom of the vessel.

## 3.6 EPILOGUE

In this chapter, the principles of liquid crystal thermography, digital colour analysis and the various stages of the development of the liquid crystal thermographic technique for the measurement of mixing time have been described. The results obtained during the development of the technique show that the LCT method can be used to determine qualitatively and quantitatively temperature/mixing time in stirred vessels.

The mixing time measurements obtained in the vessel stirred by single and double impellers at various speeds using the liquid crystal technique developed are presented in Chapter 6.

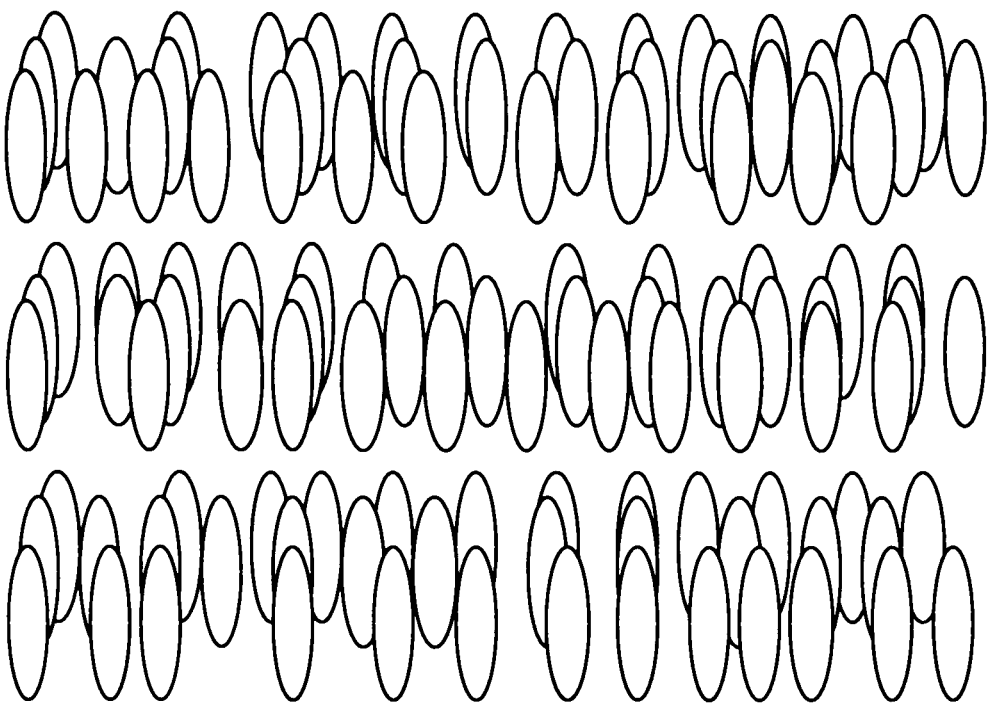

**Figure 3.1** The smectic liquid crystal structure.

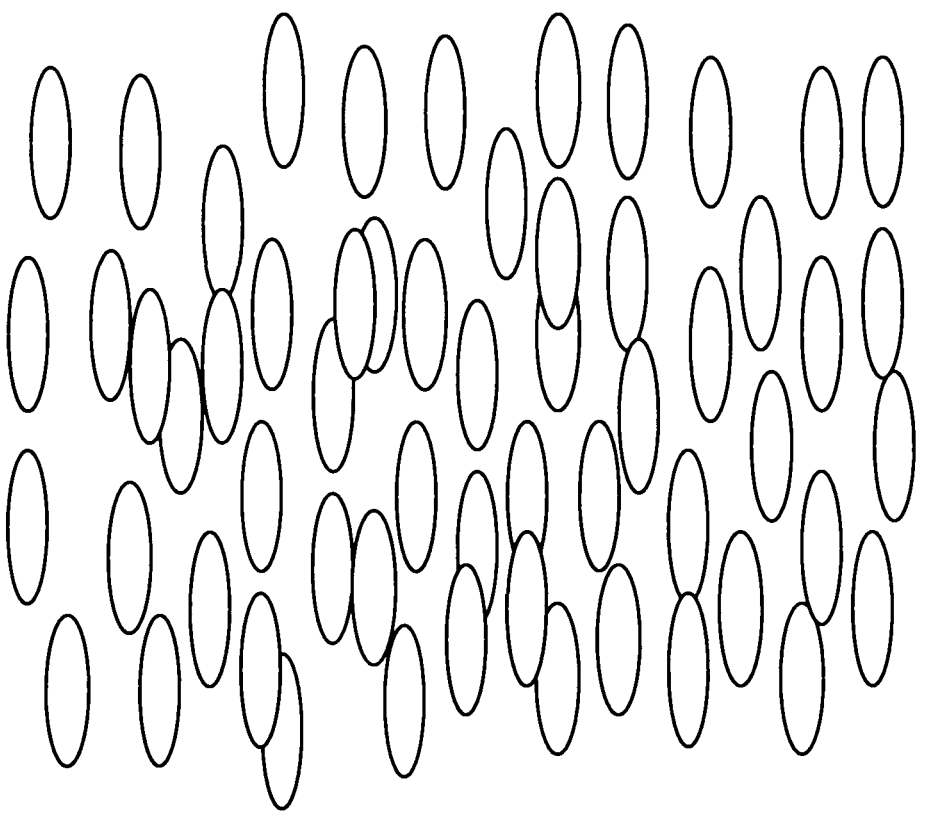

**Figure 3.2** The nematic liquid crystal structure.

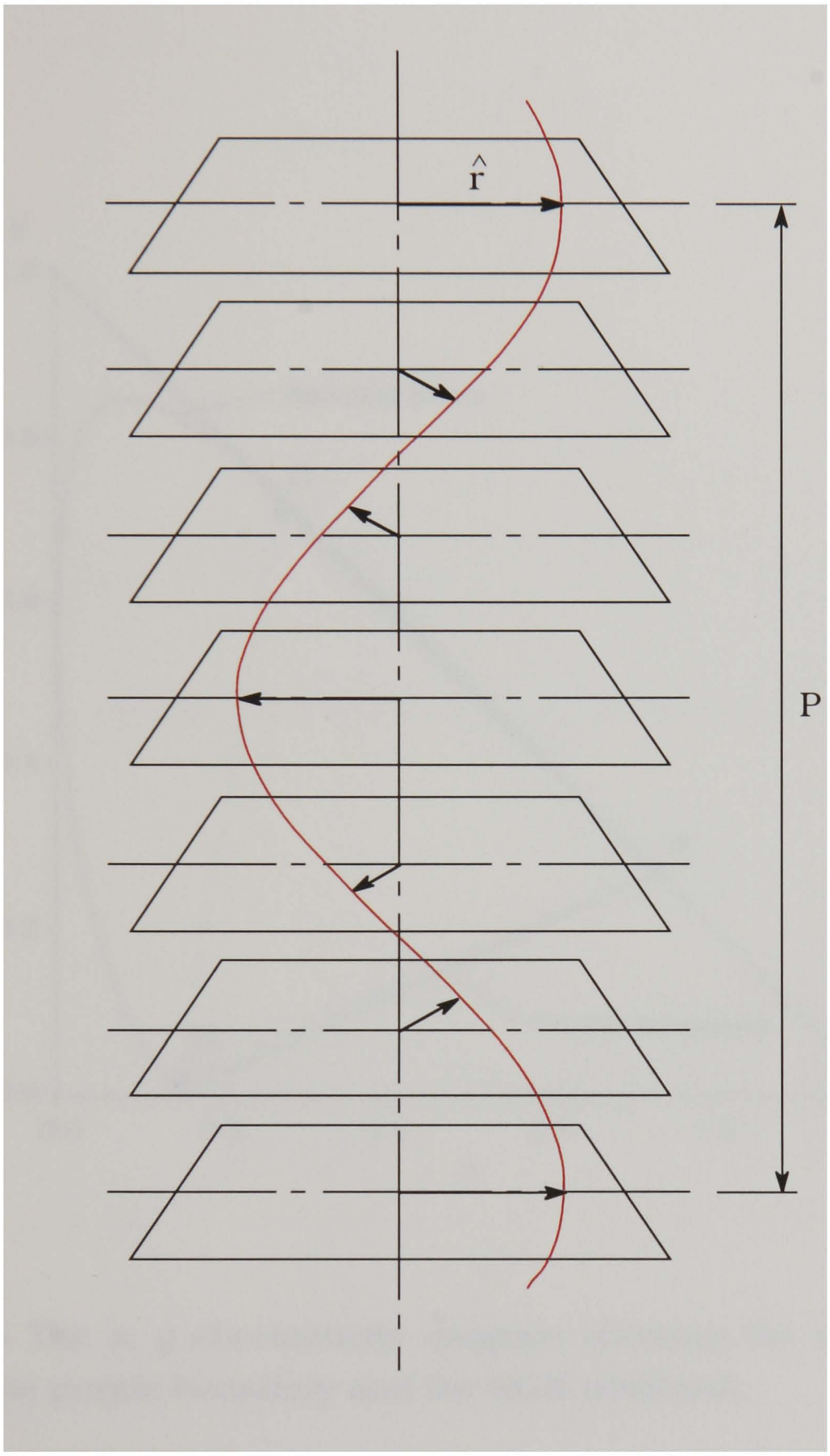


**Figure 3.3** The chiral nematic liquid crystal structure.

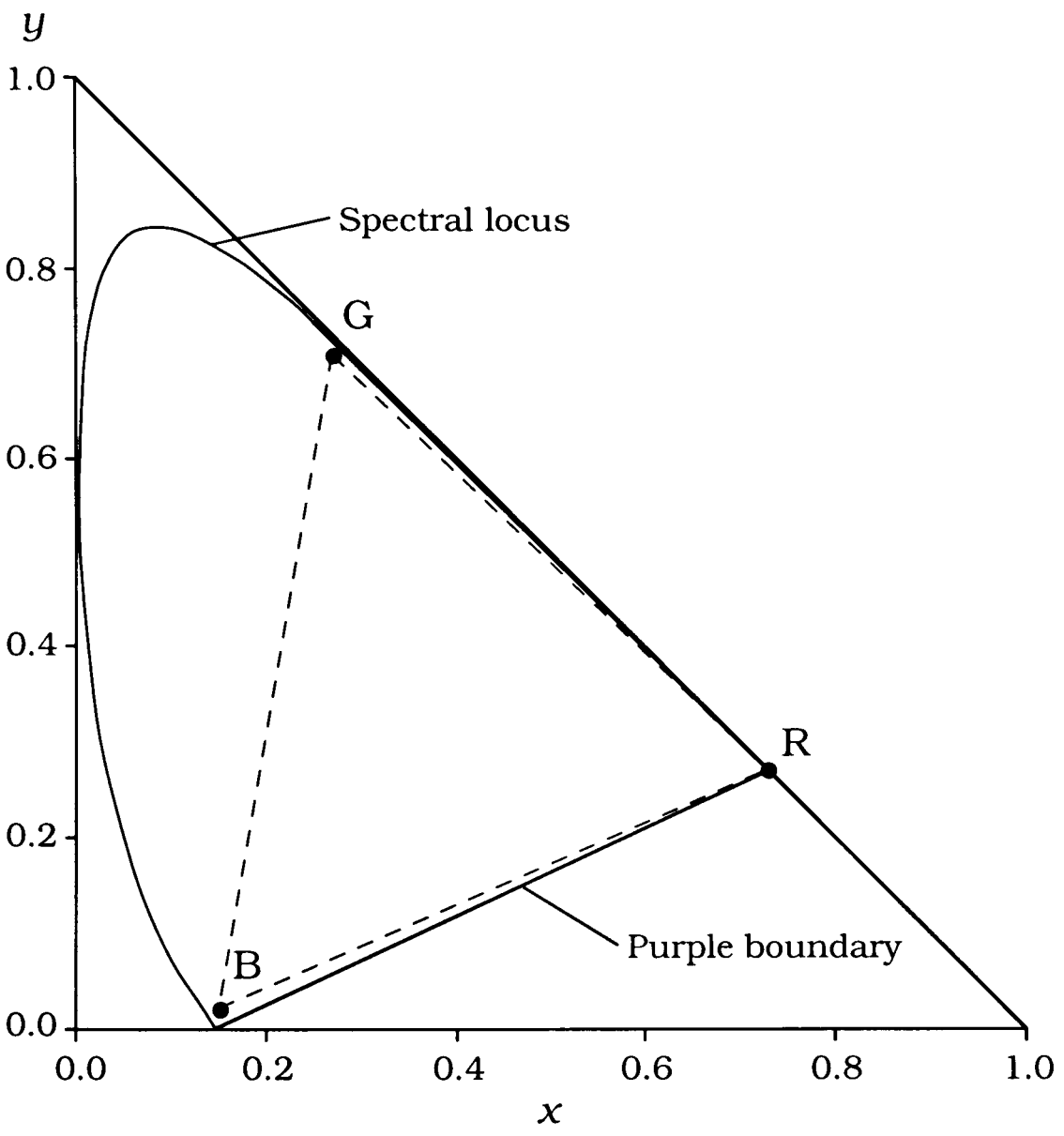


**Figure 3.4** The $x$, $y$ chromaticity diagram showing the spectral locus joined by the purple boundary and the RGB tristimuli.

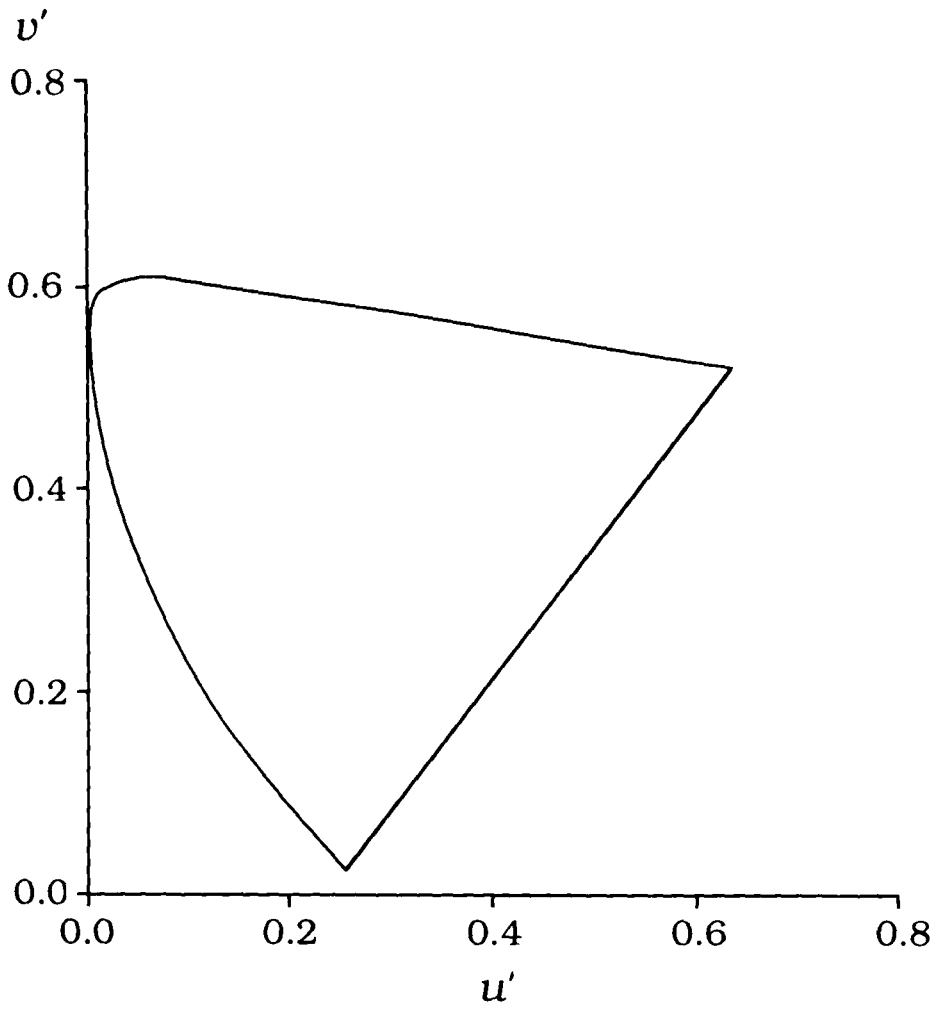


**Figure 3.5** The CIE 1976 $u'$, $v'$ diagram.

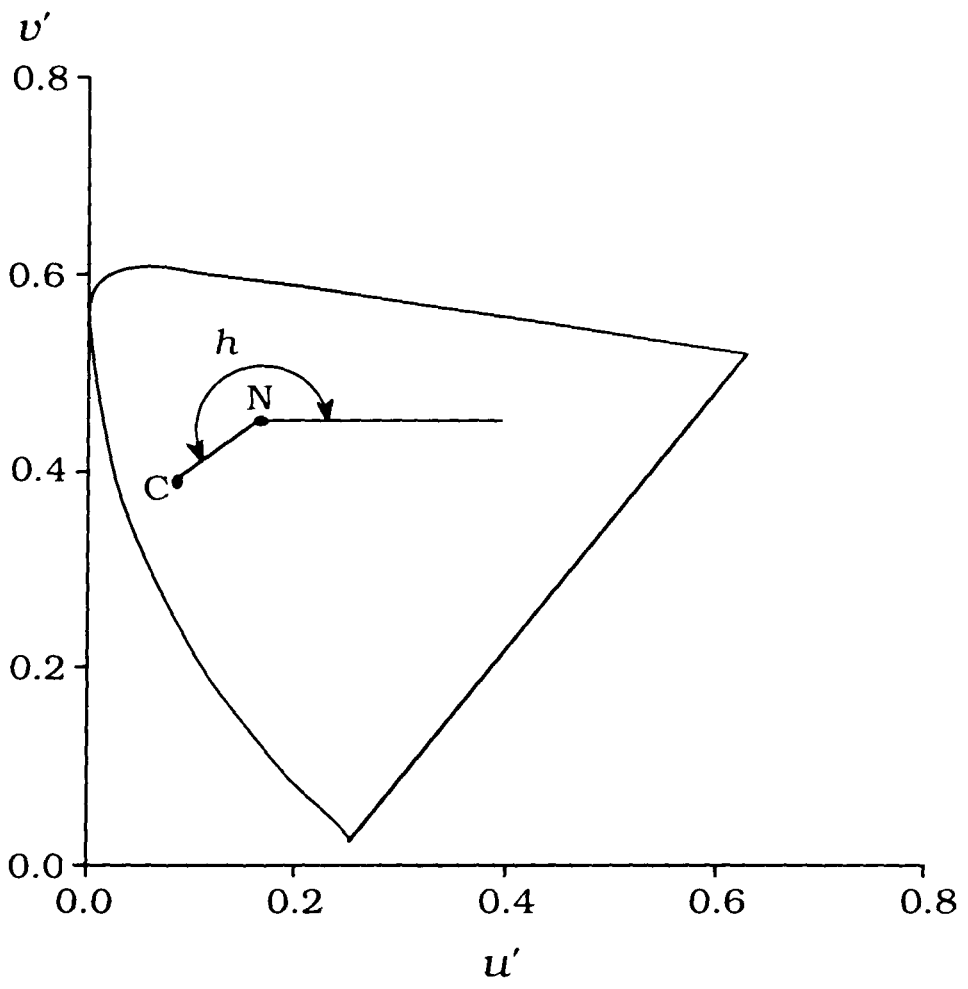


**Figure 3.6** A graphical representation of the hue and saturation of a colour C.

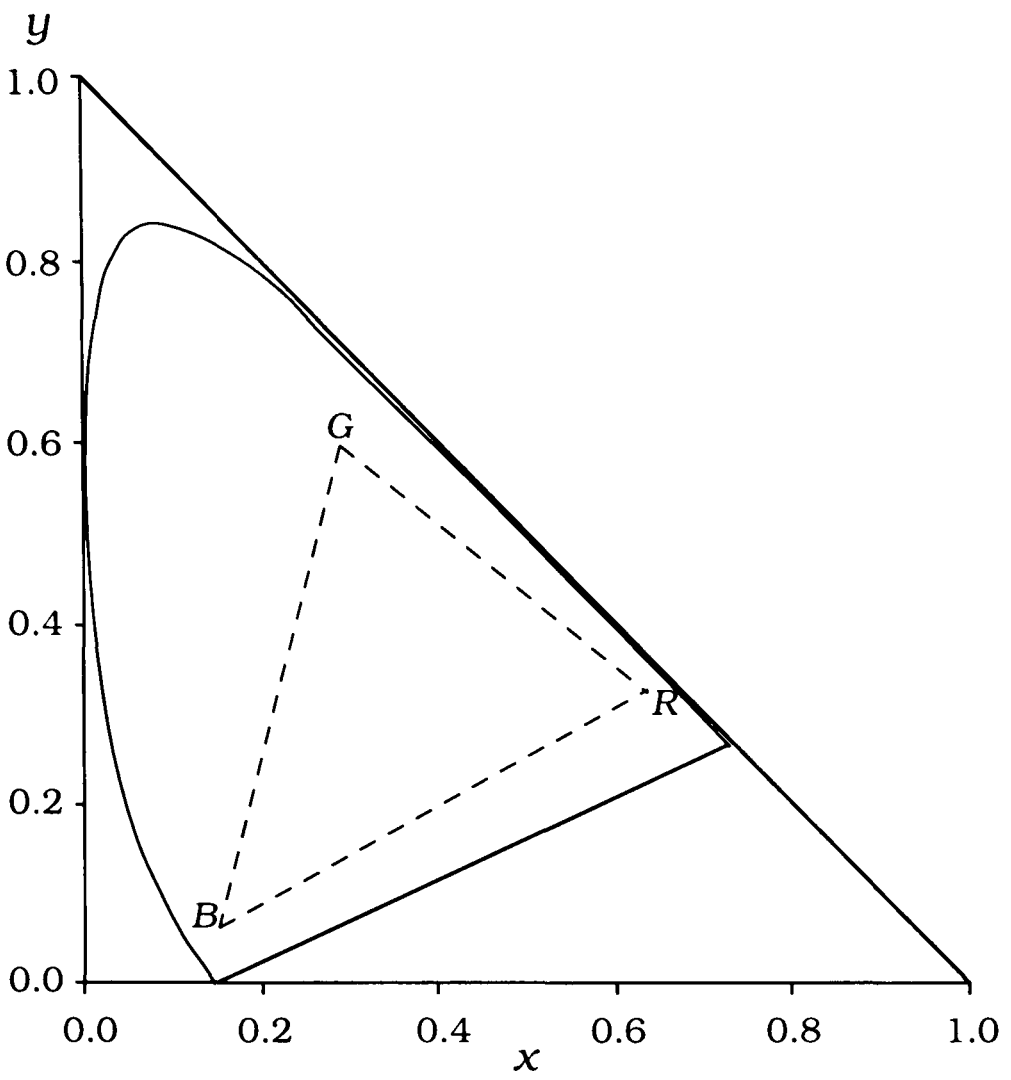


**Figure 3.7** The television/video *RGB* tristimuli on a *x*, *y* chromaticity diagram.

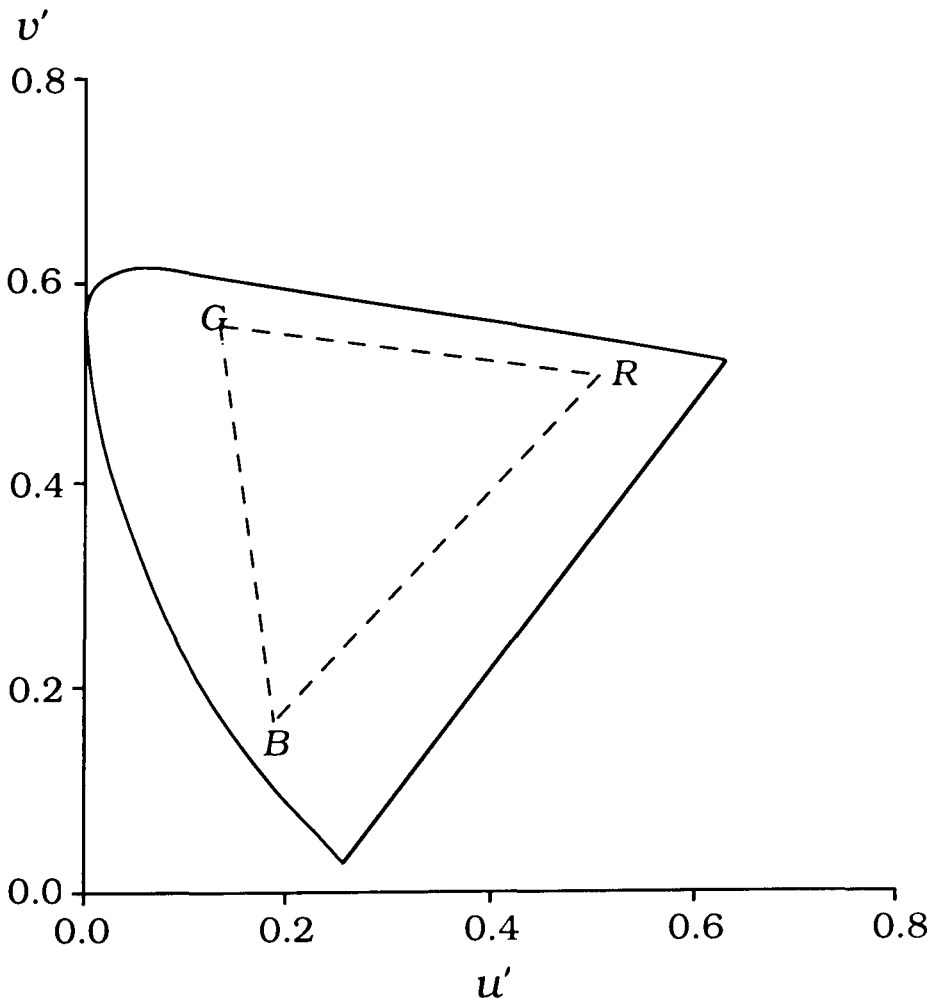


**Figure 3.8** The television/video *RGB* tristimuli on a *u′*, *v′* diagram.

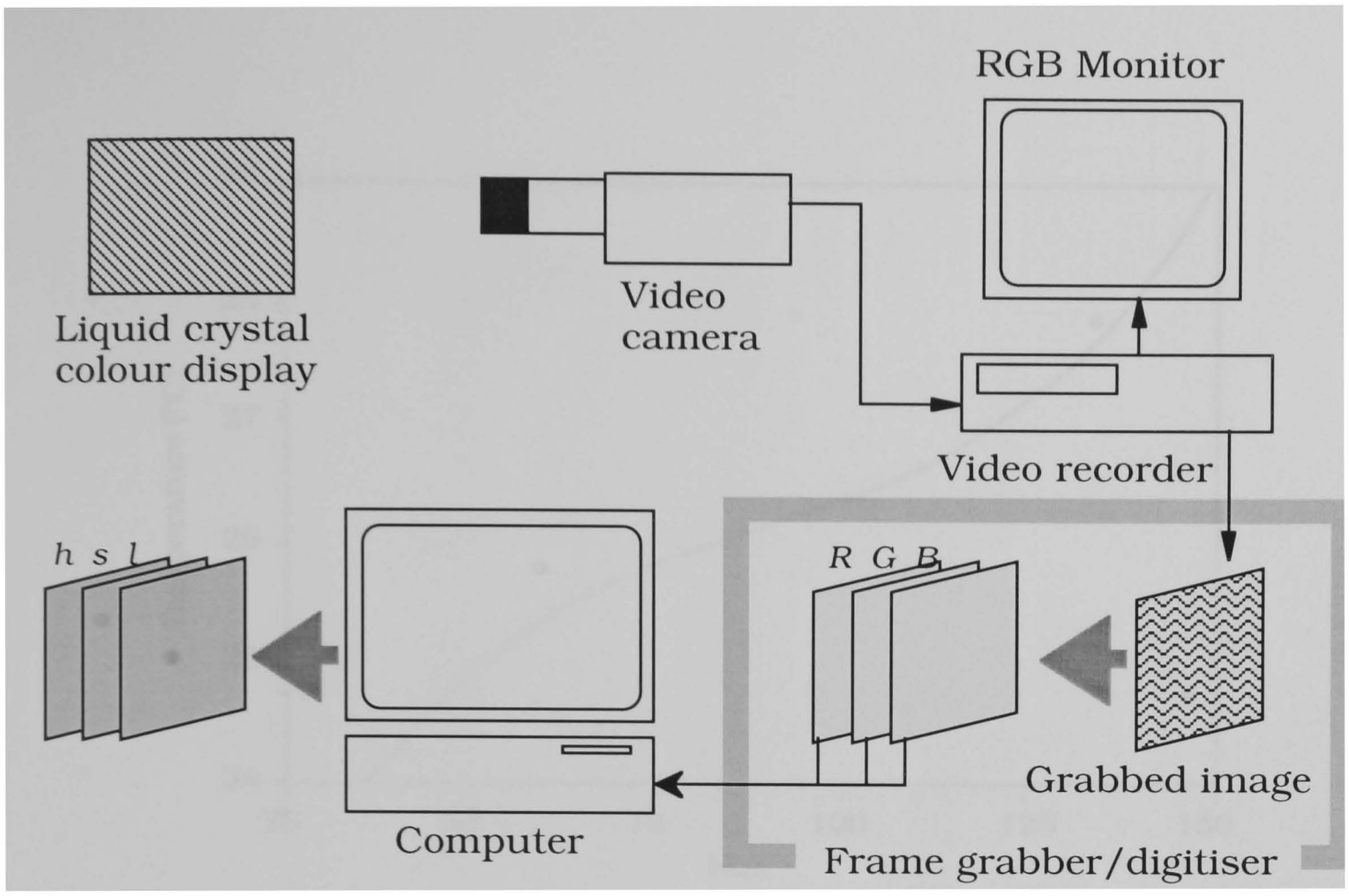


**Figure 3.9** Schematic diagram of the digital video image processing system.

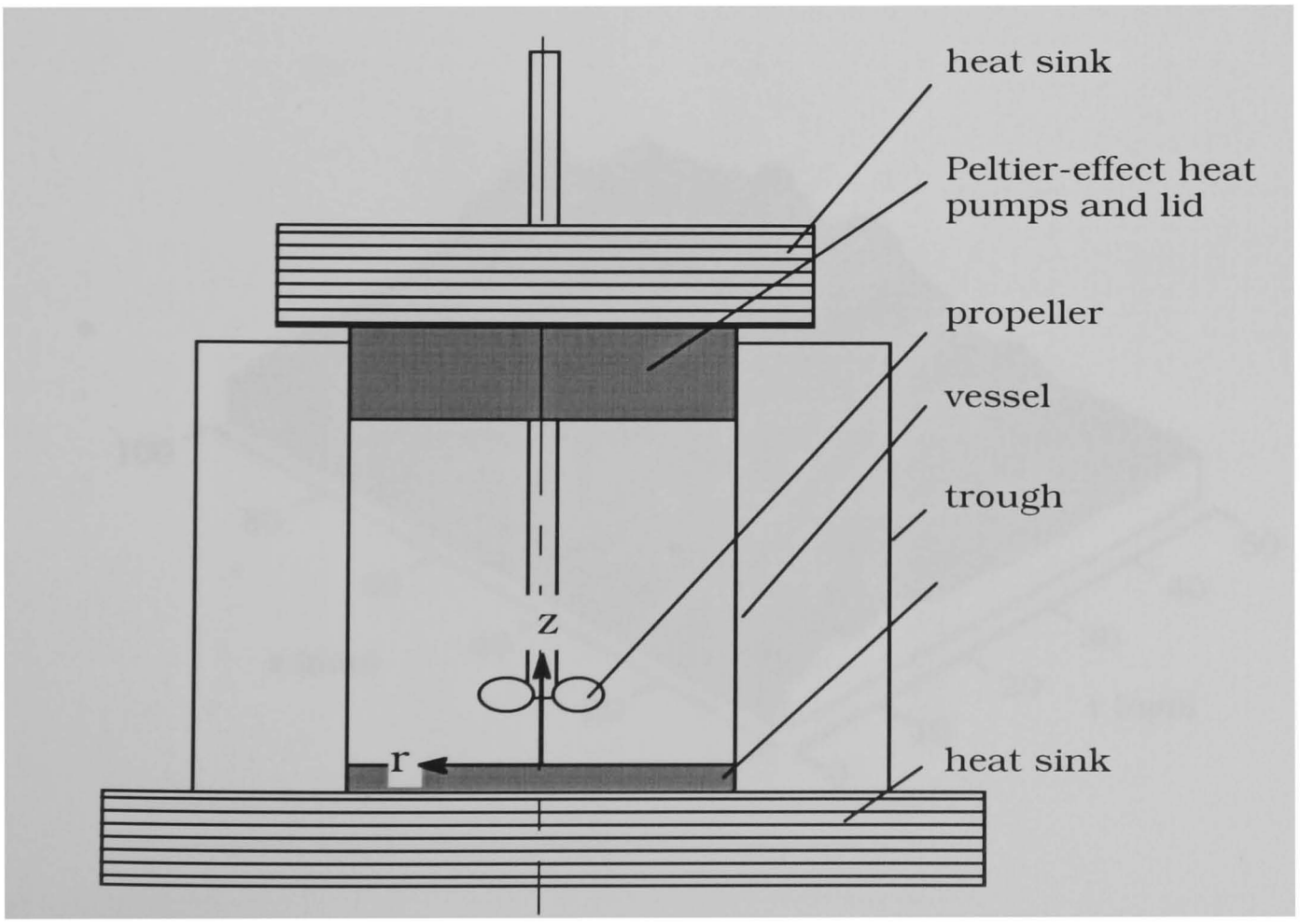


**Figure 3.10** Schematic drawing of the stirred vessel used in the development stage.

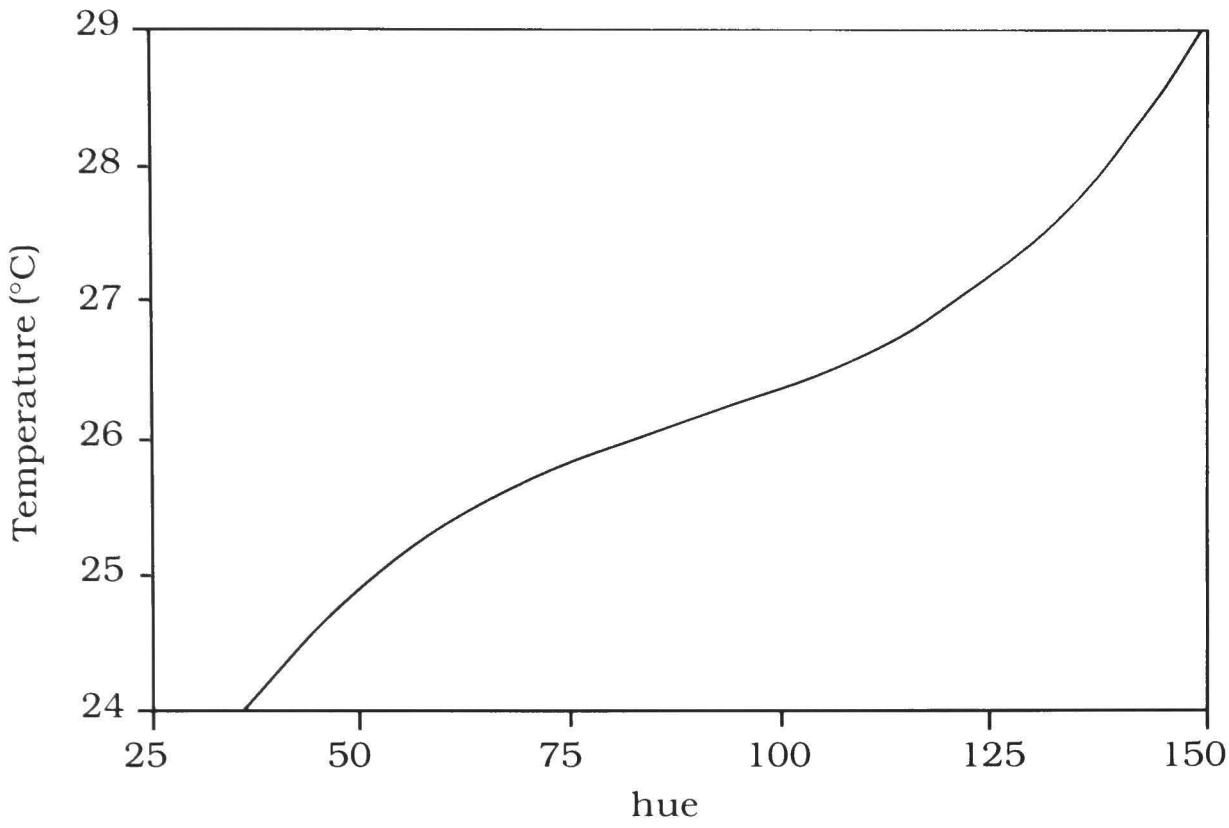


**Figure 3.11** A typical calibration curve.

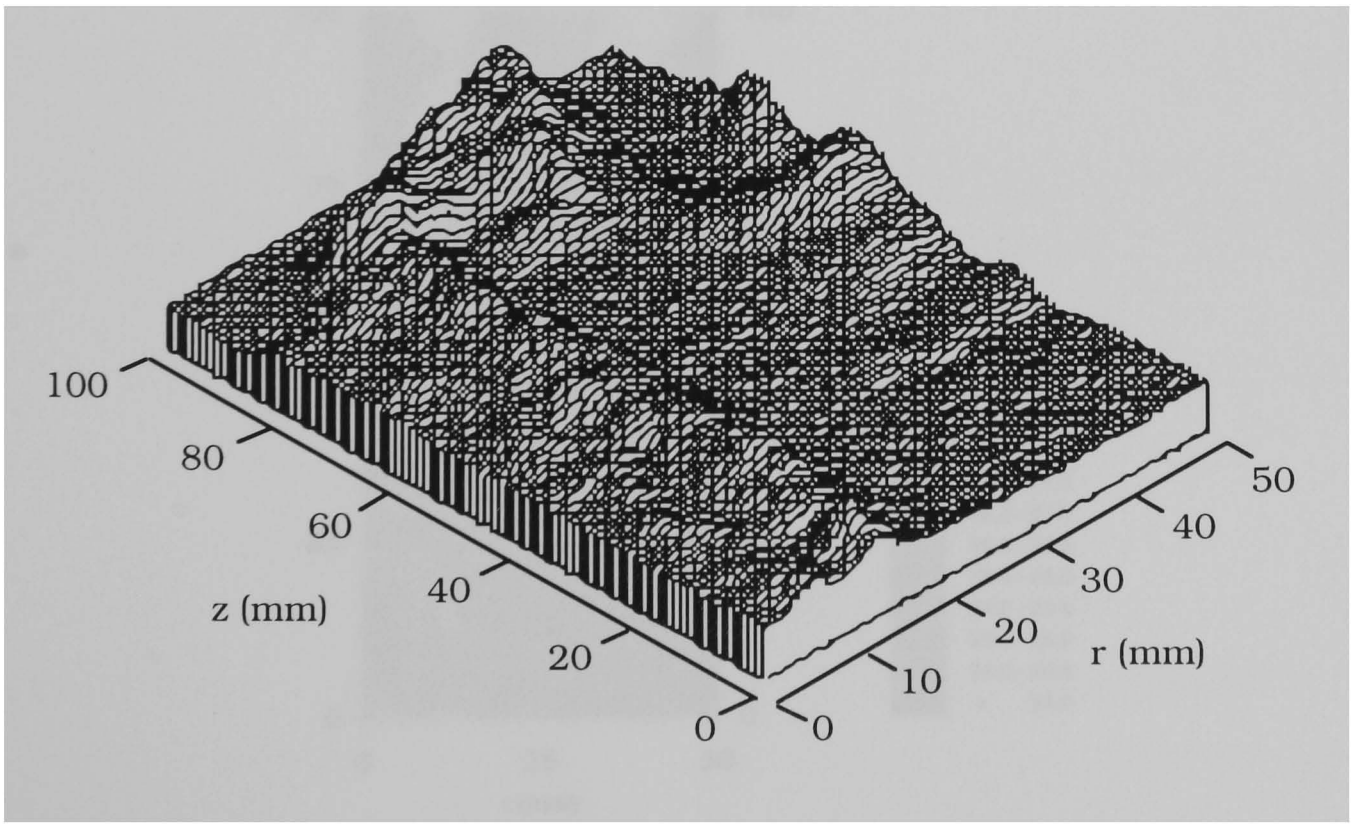


**Figure 3.12** A topographic map of the distribution of hue of a recording obtained with free convection taking place in the vessel.

(a)

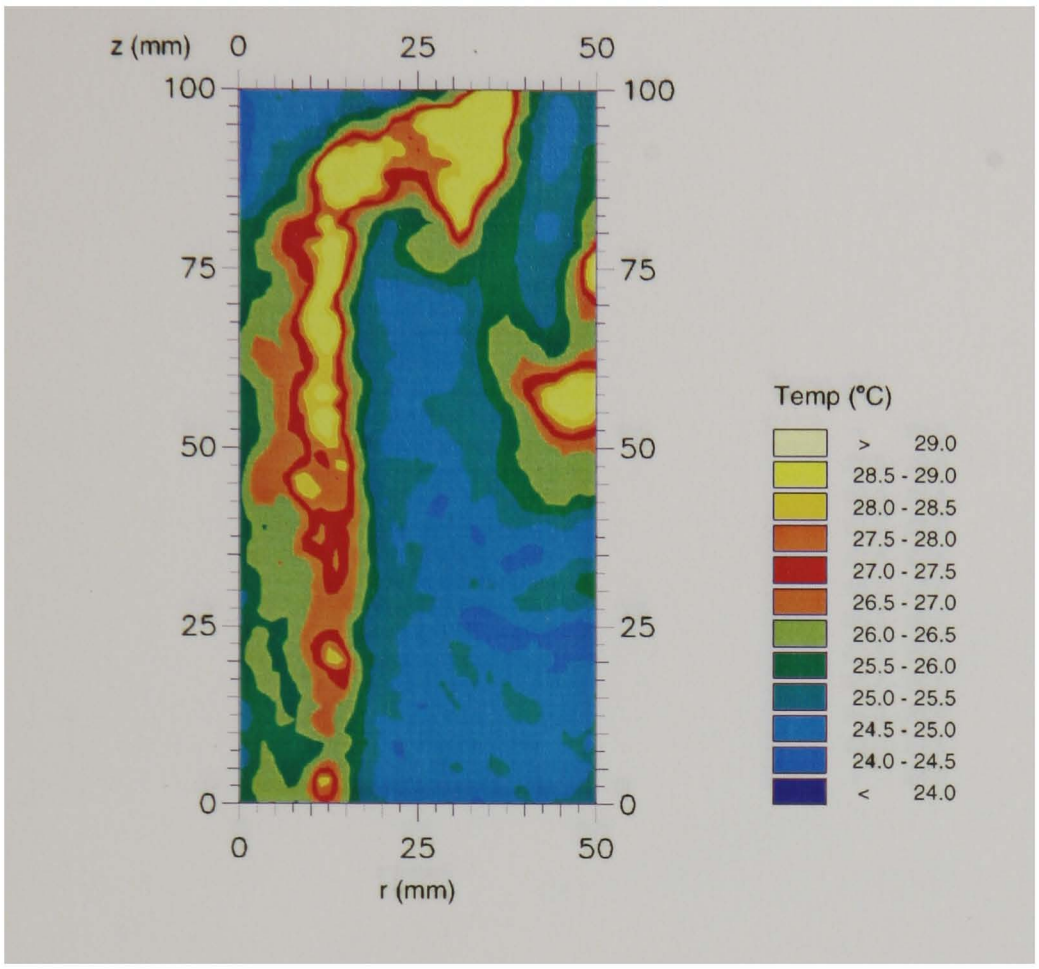


(b)

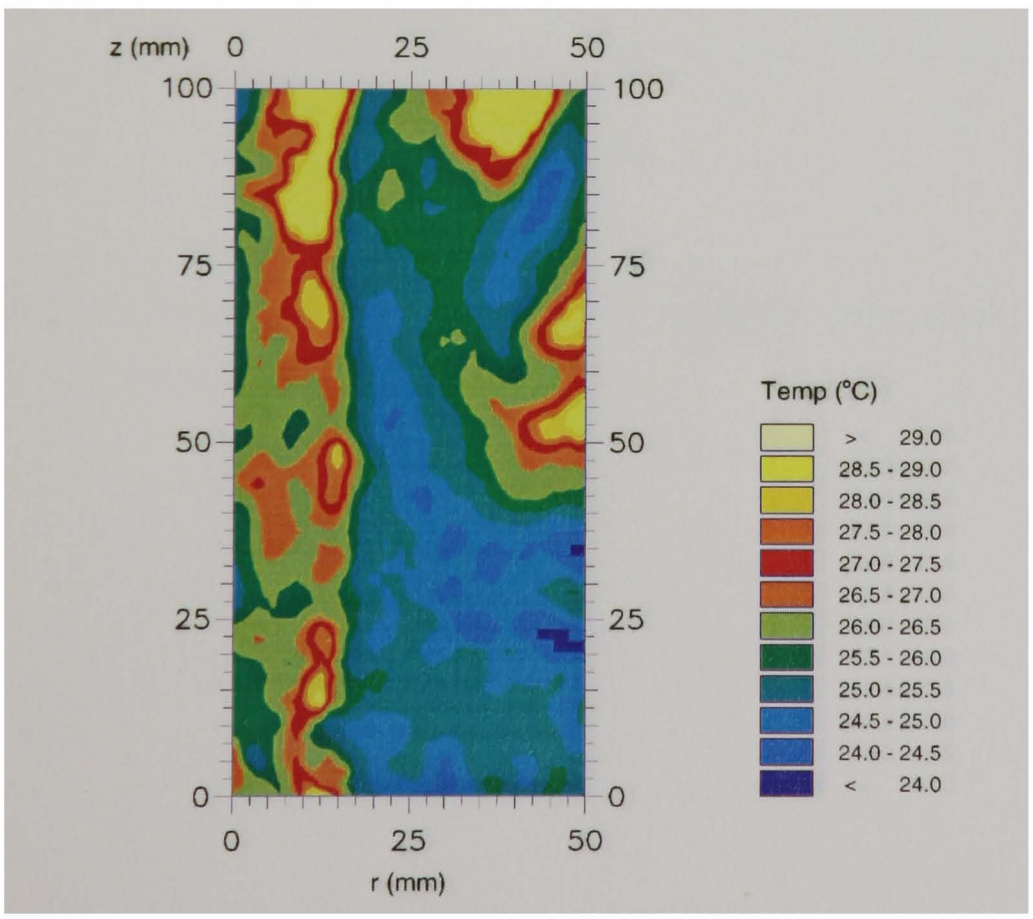


**Figure 3.13** Temperature contours of the free convection flow field: (a) start of observation; (b) three seconds later.

(a)

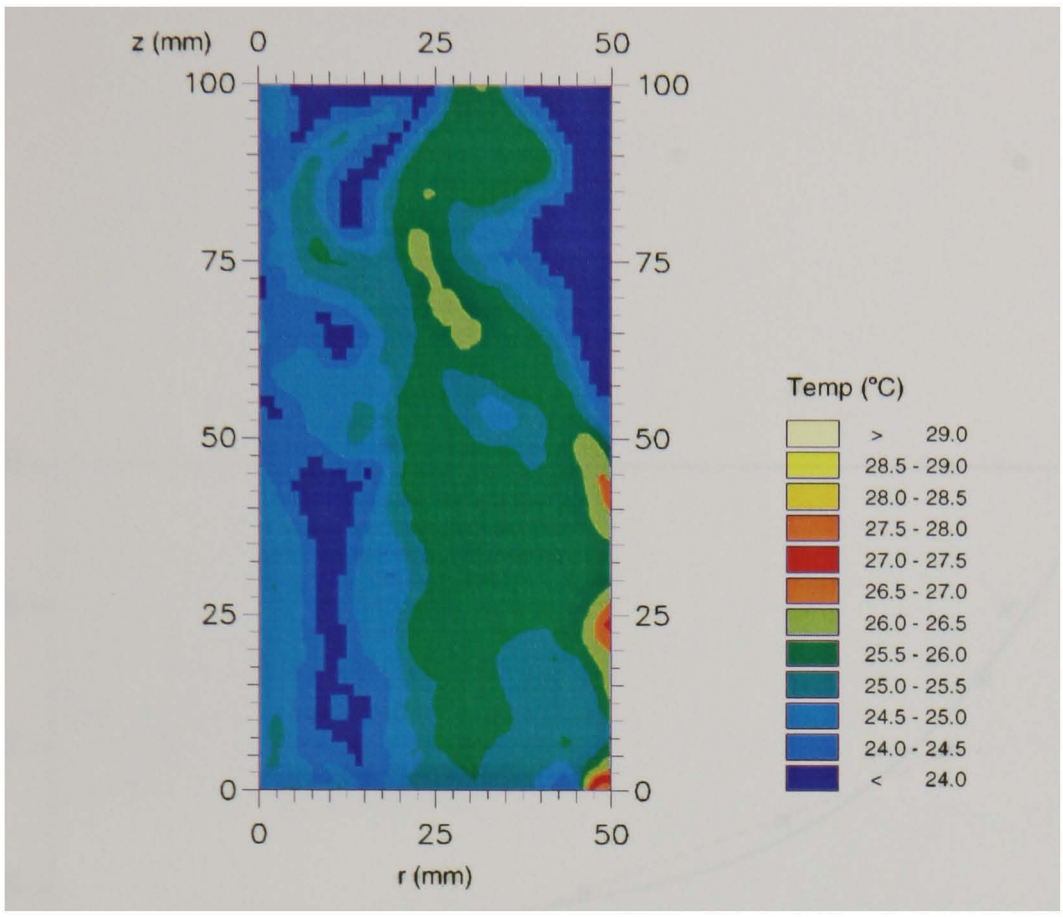


(b)

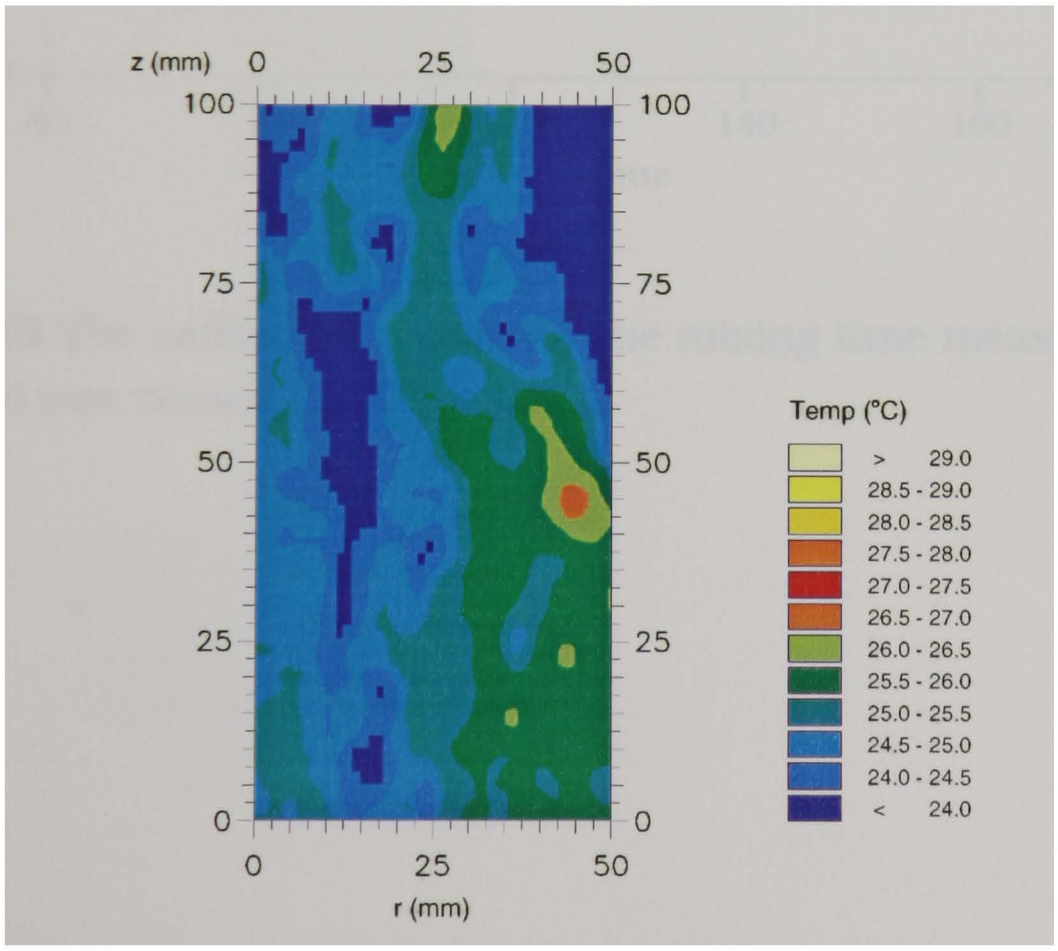


**Figure 3.14** Temperature contours of the flow field in the stirred vessel: (a) start of observation; (b) three seconds later.

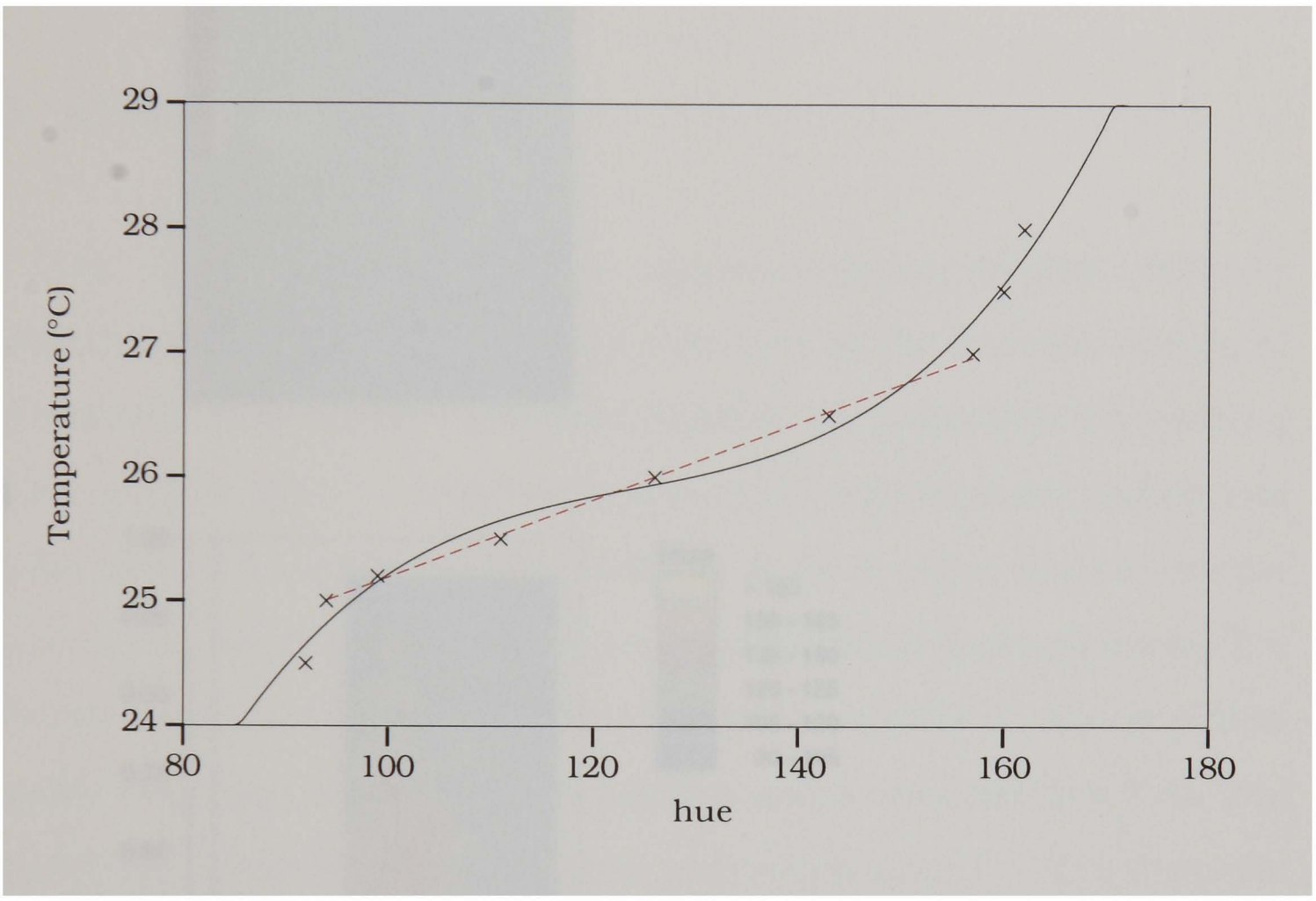


**Figure 3.15** The calibration curve for the mixing time measurements in the T = 100 mm vessel.

(a)

(b)

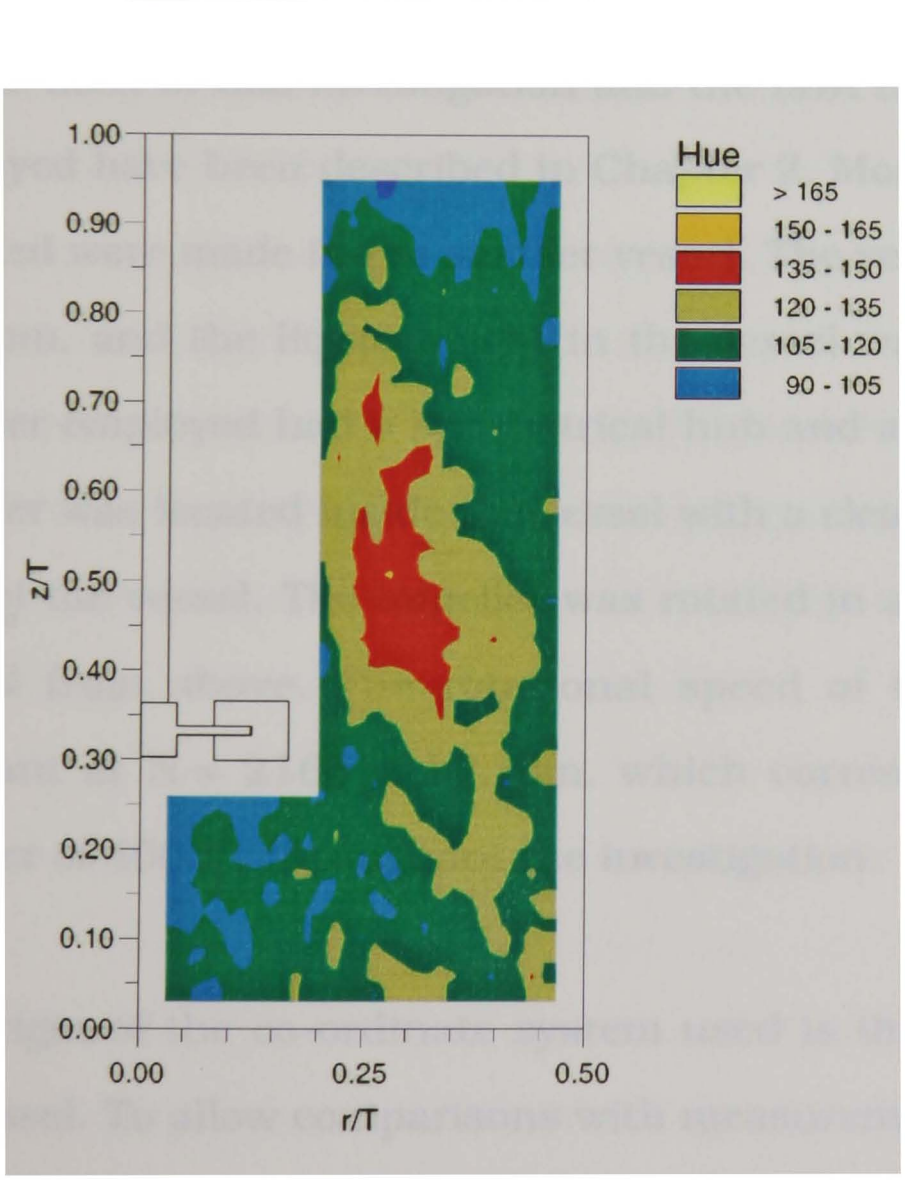


**Figure 3.16** Sample results: (a) image of half of the flow field stirred by a single Rushton impeller at 540 rpm, 160 ms after the start of the insertion of the tracer; and (b) the corresponding hue distribution.

# CHAPTER 4

# VELOCITY CHARACTERISTICS OF A STIRRED VESSEL WITH A SINGLE RUSHTON IMPELLER

## 4.1 INTRODUCTION

In this chapter detailed LDA measurements of the velocity characteristics of the trailing vortex structure in the impeller stream of a vessel stirred by a single Rushton impeller are presented. The mixing vessels used in this investigation and the LDA experimental techniques employed have been described in Chapter 2. Most of the measurements reported were made in the smaller vessel. The vessel had a diameter T = 100 mm, and the liquid height in the vessel was H = T. The Rushton impeller employed had a symmetrical hub and a diameter D = T/3. The impeller was located inside the vessel with a clearance C = T/3 from the base of the vessel. The impeller was rotated in a clockwise direction as viewed from above. The rotational speed of the impeller was kept constant at N = 2165 ± 10 rpm, which corresponded to a Reynolds number of 40000, throughout the investigation.

The origin of the co-ordinate system used is the centre of the base of the vessel. To allow comparisons with measurements made in vessels of different sizes, all distances are normalised with the vessel diameter T, and all locations are described in terms of normalised axial (z/T), normalised radial (r/T) and tangential (θ) co-ordinates. All

measurements were conducted in the $\theta = 0°$ plane, located azimuthally halfway between two adjacent baffles (i.e. 45° away from each baffle).

At the start of the experiments, various methods of processing the velocity data were considered to establish the most appropriate ones. Even though the flow in the impeller vicinity of stirred reactor vessels is periodic, ensemble-averaged LDA measurements obtained over 360° of impeller revolution are widely employed for the description of the velocity and turbulence fields. These measurements do not account for the pseudo-turbulence due to the passage of the impeller blades (van't Riet and Smith (1976)). Through the use of an optical shaft encoder Yianneskis et al (1987), Calabrese and Stoots (1989) and Yianneskis and Whitelaw (1993) performed angle-resolved LDA measurements over 60° of impeller revolution where the data were arranged in 1° averages. Such angle-resolved measurements do show the variation of the mean flow velocities and the turbulence fluctuations with blade angle $\phi$. It has been shown that in comparison with 1° angle-resolved measurements, 360° ensemble-averaged measurements can lead to an overestimation of turbulence quantities in the impeller stream by up to 400% (Yianneskis and Whitelaw, 1993).

At the onset of the present investigation, the differences between various methods of measurement were assessed (namely, angle-resolved, 360° ensemble-averaged and time-resolved). The results obtained are presented in Section 4.2, and they indicate that angle-resolved data over 1° intervals would provide more appropriate estimates of the levels of turbulence in the flow than 360° ensemble-averaged data. In addition, time-resolved data can be used to obtain

information about the frequency content of the velocity fluctuations and to calculate turbulence quantities of interest.

Therefore, in this investigation measurements were primarily obtained as angle-resolved (i.e. ensemble-averages over intervals of 1° of revolution) mean velocities and turbulence levels; and as time-resolved velocity recordings. The LDA systems used to obtain angle-resolved and time-resolved results have been described in Chapter 2 .

Angle-resolved measurements were made of the axial, radial and tangential mean velocity components ($\overline{U}$, $\overline{V}$ and $\overline{W}$ respectively); and of the corresponding turbulence levels (u', v' and w' respectively), at 8160 locations in the vicinity of the impeller stream. The measuring grid was selected in order to reveal in detail the structure of the trailing vortices while minimising the measurement time. The azimuthal location of the measuring volume for the angle-resolved measurements is expressed in terms of angle ($\phi$) with respect to the blade, which is calculated from the corresponding $\theta$ co-ordinate. The $\phi = 0°$ plane is located at the centre of the leading blade.

In order to determine the flow motion relative to the rotating blade, the rotational velocity $V_r$ was subtracted from the angle-resolved mean tangential velocities. $V_r$ was defined as

$$V_r = \frac{2\ \pi\ N\ r}{60}\ (m/s) \qquad (4.1)$$

where N is the impeller rotational speed in revolutions per minute and r is the radial distance from the axis of the vessel to the point of measurement.

For the purpose of comparison with data obtained in vessels of different sizes which is made later on in this thesis, all angle-resolved mean velocities have been normalised with the blade tip velocity $V_{tip} = \pi ND/60$ and are denoted by $\overline{U} / V_{tip}$, $\overline{V} / V_{tip}$ and $\overline{W} / V_{tip}$ respectively for the axial, radial and tangential components. The turbulence level results were also normalised with $V_{tip}$ and are denoted by $u'/V_{tip}$, $v'/V_{tip}$ and $w'/V_{tip}$ for the axial, radial and tangential components respectively.

Angle-resolved turbulence kinetic energy results were also obtained from the u', v' and w' data by using the following relationship:

$$k = \frac{1}{2}\left(u'^2 + v'^2 + w'^2\right) \tag{4.2}$$

The turbulence kinetic energy results were normalised with $V_{tip}^2$ and the normalised values are denoted by $k/V_{tip}^2$.

To facilitate interpretation of the results, the outline of a quarter of the impeller disk is drawn to scale in all figures depicting the results obtained in horizontal (z) planes; while in the figures depicting the results obtained in vertical ($\phi$) planes, the outline of one-half of the cross-section of the impeller and of the impeller shaft are drawn to scale. In those figures depicting results in z planes, the impeller should be considered to be rotating clockwise, while in those figures depicting

results in $\phi$ planes, the impeller should be considered to be moving out of the plane of the paper towards the viewer.

In order to aid the interpretation of the results, a reference scale having the magnitude of $V_{tip}$ is drawn in each figure depicting angle-resolved mean velocity vectors. Turbulence level and turbulence kinetic energy results are plotted in contour form. Two contour scales were used: one for all rms velocity components (turbulence levels); and one for turbulence kinetic energy results. For comparison purposes, the same contour levels were used throughout this thesis for the turbulence levels and similarly for the k results.

In order to investigate the extent of the periodicity of the flow in the vessel, instantaneous velocity recordings of the radial component, V, were also made at a number of radii in the $z/T = 0.33$ plane, and their corresponding energy spectra were computed. The instantaneous velocity recordings presented in this chapter were also normalised with the blade tip velocity $V_{tip}$ and are denoted by $V/V_{tip}$.

## 4.2 COMPARISON OF ENSEMBLE-AVERAGED AND ANGLE-RESOLVED MEASUREMENTS

In order to compare different data acquisition techniques, characteristic results were obtained using time-resolved, 1° angle-resolved and 360° ensemble-averaged LDA techniques in the T = 100 mm vessel and they are shown in Figure 4.1. In Figure 4.1(a) the time-resolved (instantaneous) velocity data are compared with 1° angle-

resolved data. The time-resolved data show large velocity fluctuations, while the periodicity of the flow is indicated by the six cycles per revolution in the 1° angle-resolved mean velocity variation, each cycle corresponding to the passage of an impeller blade. The shortcomings of the use of 360° ensemble-averaged techniques in the periodic flow (van't Riet et al, 1976) are obvious from Figure 4.1(b) where the 360° ensemble-averaged velocity is represented by a straight line, in contrast to the 1° angle-resolved data which clearly shows the periodic variation in the mean velocity due to the blade passages.

It was observed during the experiments that the data rate varied with angle $\phi$ and therefore the number of data per 1° average in the angle-resolved measurements also varies. Tests were made to determine the minimum number of data required to provide statistically independent values of mean velocity and turbulence level in each 1° window. This value is, of course, dependent on the local turbulence intensity (Yanta, 1973). The measurements showed that the minimum number of data required was 500 for most locations. Provided the minimum number was exceeded, the data rate variation with $\phi$ did not affect the results.

A comparison of the 1° angle-resolved mean velocity variation with an uneven number of data per degree and the corresponding variation with an equal number of data per degree (as in Figures 4.1(a) and (b)) is shown in Figure 4.1(c). There is no discernible difference between the two curves, hence it can be concluded that the effect of the number of data on the angle-resolved values is negligible, provided that a statistically appropriate number of data contributes to each 1° average. It should be noted that this data rate effect is very important for the

accurate characterisation of the flows; nevertheless it has not been identified in earlier investigations.

Figure 4.2 shows the variation of the percentage of the total number of data obtained with blade angle $\phi$ at r/T = 0.17 and 0.19 at z/T = 0.33. It can be seen from the figure that at both locations the data is not evenly distributed over the 60° interval. At r/T = 0.17, over 50% of the velocity realisations occur within the first 20° of the impeller revolution, approximately 35% lie between 20° and 40° and the remainder occur in the final 20° interval. Though the variation in the percentage of total data obtained at r/T = 0.19 is not as large as at r/T = 0.17, it can be seen from the figure that the number of velocity realisations occurring in the first 30° is higher.

The results presented above indicate that 1° angle-resolved measurements should provide more appropriate estimates of the turbulence levels in the flow than 360° ensemble-averaged values. Furthermore, the results have important implications for Computational Fluids Dynamics (CFD) prediction methods, the majority of which at present essentially treat the impeller as a rotating disk. Such methods have in general employed 360° ensemble-averaged LDA data for boundary conditions and validation; the shortcomings of the use of 360° data are discussed further below.

Therefore, in this investigation data were primarily obtained as angle-resolved or time-resolved measurements. In order to compare results obtained in this investigation with already published results, 360°

ensemble-averaged values were also calculated from the data. The results obtained are presented and discussed in the following sections.

## 4.3 RESULTS

### 4.3.1 MEAN VELOCITY DISTRIBUTIONS

The mean velocity vectors relative to the blade (i.e. with the rotational velocities subtracted from the tangential components) obtained in the z/T = 0.33 plane, where the middle of the impeller disk is located, are shown in Figure 4.3.

The vectors show that near the impeller blade, at r/T = 0.17, and r/T = 0.19, there are large radial velocities between $\phi = 0°$ and $\phi \approx 45°$. As the flow moves further away from the impeller blade towards the vessel wall, the radial velocities decrease in magnitude and the flow direction after r/T = 0.25 becomes predominantly tangential.

In Figure 4.4 the mean velocity vectors in the z/T = 0.35 plane are depicted. It can be seen that there is a recirculation region behind the leading blade at r/T = 0.17 and between $\phi = 0°$ and $\phi \approx 45°$. The region is associated with the trailing vortex generated behind the blade and is discussed further below in Section 4.4. Similar to the results obtained in the z/T = 0.33 plane, the flow after r/T = 0.25 becomes predominantly tangential.

Figure 4.5 shows the velocity vectors obtained in the z/T = 0.37 plane. Radial velocity magnitudes are very small in this plane and the flow is moving primarily in the tangential direction.

Figures 4.6(a)–(b) show the velocity vectors in four $\phi$ planes (0°, 15°, 30° and 45°). In these figures, a dashed horizontal line is drawn at z/T = 0.33 in all $\phi$ planes in order to aid the assessment of the inclination of the impeller stream. It can be seen that at all $\phi$ angles, the flows discharged by the impeller are directed towards the vessel wall with a slight upward inclination, on average around 3° – 4° to the horizontal. This is in agreement with the previously reported observation of Yianneskis and Whitelaw (1993). The vectors shown in Figures 4.6 (a) and (b) indicate that near the blade (at r/T = 0.17 up to 0.30) the impeller stream is inclined upwards. The angle of inclination generally decreases with radial distance from the blade tip. By r/T = 0.35 the stream is either horizontal ($\phi$ = 0°) or inclined downwards.

The velocity vectors in Figures 4.6(a) and (b) show also the merging of the ring vortices (one of which is formed above and one below the impeller) in the vicinity of the impeller. The formation of these vortices has been previously documented (see, e.g. Yianneskis et al, 1987). It can also be seen from Figure 4.6 that the velocities near the blade tip vary considerably with $\phi$. This is indicative of the complex variation of the mean flow behind the blade. In the $\phi$ = 15° plane small circulatory motions can be observed near the upper and lower edges of the blade tip, which indicate the presence of the trailing vortices generated above and below the impeller disk respectively. It will be shown later (Section 4.4) that at this blade angle the vortex axis is located at approximately

r/T = 0.17. The z- and $\phi$-plane results provide evidence that each trailing vortex is contained within a relatively small region; for example the vortex formed above the disk at $\phi$ = 15° is located between z/T = 0.34 and 0.36 approximately.

### 4.3.2 TURBULENCE LEVEL DISTRIBUTIONS

The normalised turbulence levels, $u'/V_{tip}$, $v'/V_{tip}$ and $w'/V_{tip}$, at the z/T = 0.33 plane are shown in Figures 4.7, 4.8 and 4.9 respectively. High levels of $u'/V_{tip}$ can be observed behind the leading blade in Figure 4.7. These are associated with the trailing vortex structure. High levels of turbulence might be expected to be generated in the immediate vicinity of the trailing vortices where steep mean velocity gradients are present and therefore contours of turbulence levels and k can provide a good indication of the extent of the trailing vortex structure.

At $\phi$ = 0°, the $u'/V_{tip}$ = 0.24 – 0.28 region is associated with the trailing vortex produced by the preceding blade. Therefore, it can be concluded that the high $u'/V_{tip}$ turbulence levels produced by each blade crossing can be distinguished up to 15° after the following blade.

The $u'/V_{tip}$ gradients diminish with increasing radial distance from the blade at all $\phi$ angles, reaching values of 0.16 – 0.20 at r/T ≈ 0.29 and 0.12 – 0.16 at r/T ≈ 0.33.

In Figure 4.8, the region of high $v'/V_{tip}$ values behind the leading blade extends further than that for the $u'/V_{tip}$ results shown in Figure 4.7. This might be expected, as the velocity gradients and flow activity are

far more pronounced in the radial direction than in the axial. Locally higher $v'/V_{tip}$ levels at around r/T = 0.20 to 0.30 next to the leading blade (i.e. at $\phi = 0°$) are also evident, indicating again the presence of the trailing vortex produced by the previous blade. The $v'/V_{tip}$ levels drop to around 0.16–0.20 at $r/T \approx 0.32$.

Figure 4.9 shows the $w'/V_{tip}$ levels obtained in the z/T = 0.33 plane. The two well defined regions of locally high $w'/V_{tip}$ levels indicate again the presence of two trailing vortices; one produced by the leading blade and one by the blade preceding it.

The high $w'/V_{tip}$ levels behind the blade indicate the presence of the trailing vortex produced by the leading blade centred at $r/T \approx 0.19$ and the locally high $w'/V_{tip}$ levels at $r/T \approx 0.24$ next to the leading blade indicate the presence of the tail end of the trailing vortex produced by the previous blade as before. $w'/V_{tip}$ levels, although higher than the $u'/V_{tip}$ ones at $r/T \approx 0.17 - 0.20$ are reduced to 0.12 – 0.16 by $r/T \approx 0.30$, i.e. nearer the blade than in the $u'/V_{tip}$ and $v'/V_{tip}$ distributions.

Figures 4.10, 4.11 and 4.12 show the contours of $u'/V_{tip}$, $v'/V_{tip}$ and $w'/V_{tip}$ turbulence levels respectively in the z/T = 0.35 plane (i.e. 2 mm above the middle of the impeller disk). In these figures, the presence of the trailing vortex produced by the leading blade and the trailing vortex generated by the previous blade can be clearly observed by the two well-defined regions of locally high turbulence levels. The locally high $u'/V_{tip}$ levels (above 0.28) observed in Figure 4.10 indicate the presence of the trailing vortex produced by the leading blade. The centre of this region is at $r/T \approx 0.18$, similar to that found in the z/T = 0.33 plane. However,

the area of high $u'/V_{tip}$ levels is greater than that in the $z/T = 0.33$ plane.

Figures 4.13, 4.14 and 4.15 show the $u'/V_{tip}$, $v'/V_{tip}$ and $w'/V_{tip}$ turbulence levels respectively in four $\phi$ planes (0°, 15°, 30° and 45°). The high $u'/V_{tip}$ levels (0.24 – 0.28) between $r/T = 0.22$ and 0.27 and between $z/T = 0.31$ and 0.36 at $\phi = 0°$ in Figure 4.13 indicate the presence of the trailing vortices from the previous blade. Conversely, the high levels of $u'/V_{tip}$ near the blade tip (for $r/T < 0.18$) are associated with the trailing vortices being generated by the blade located in this plane. At the $\phi = 15°$ plane the two pronounced semi-circular regions of high $u'/V_{tip}$ levels near the blade tip show clearly the presence of the two trailing vortices produced by the leading blade. The second high $u'/V_{tip}$ region (which is associated with the vortices from the preceding blade) is now located further away into the stream (centred at about $r/T = 0.26$, $z/T = 0.34$). As the vortex moves away from the blade and into the impeller stream, the $u'/V_{tip}$ maxima move accordingly, from $r/T = 0.17$ at $\phi = 15°$ to $r/T = 0.19$ at $\phi = 30°$ and $r/T = 0.21$ at $\phi = 45°$. The contours also show the inclination of the impeller stream to the horizontal by around 3°: this was also indicated by the velocity vectors shown in Figure 4.6.

The $v'/V_{tip}$ and $w'/V_{tip}$ levels contours in the same four $\phi$ planes are shown in Figures 4.14 and 4.15 respectively. In these two figures, the presence of the two pairs of trailing vortices is indicated, as in the $u'/V_{tip}$ plots of Figure 4.13: one pair produced by the preceding blade and one produced by the leading blade. In general, the inclination of

the impeller stream shown by the $w'/V_{tip}$ contours is similar to those shown by the $u'/V_{tip}$ and $v'/V_{tip}$ results at corresponding $\phi$ planes.

It has been observed (van't Riet et al (1973), Yianneskis et al (1987)), that the trailing vortex axis is nearly horizontal, while Stoots and Calabrese (1994) found that with C = T/2, the vortex axis is inclined 8° – 10° to the horizontal. Therefore the influence of the periodicity of the flow might not be expected to extend far above or below the impeller blades.

Comparisons of the $u'/V_{tip}$, $v'/V_{tip}$ and $w'/V_{tip}$ results obtained in z/T and $\phi$ planes clearly indicate that the turbulence is in general not isotropic in the impeller stream (i.e. $u' \neq v' \neq w'$). For example, at $\phi = 0°$, r/T = 0.18 and z/T = 0.33, $u'/V_{tip} = 0.20 - 0.24$, $v'/V_{tip} = 0.12 - 0.16$ and $w'/V_{tip} = 0.28 - 0.32$. This has implications for CFD predictions of the flow which employ turbulence models for which an implicit assumption of isotropic turbulence is made, and will be discussed later.

### 4.3.3 TURBULENCE KINETIC ENERGY DISTRIBUTIONS

Figure 4.16 shows the turbulence kinetic energy contours in four $\phi$ planes (0°, 15°, 30° and 45°). At $\phi = 0°$, the locally high $k/V_{tip}^2$ levels indicate the presence of the trailing vortices produced by the preceding blade. This region is centred slightly above the impeller disk at $r/T \approx 0.23$ and $z/T \approx 0.34$.

The presence of the trailing vortices produced by the previous blade is still evident at $\phi = 15°$, indicated by a region of $k/V_{tip}^2$ levels between

0.08 – 0.10 centred at z/T ≈ 0.34, and r/T ≈ 0.25. However, $k/V_{tip}^2$ levels associated with this pair of vortices cannot be distinguished at $\phi$ = 30° and 45°. It is however expected that the elongated shape of the 0.06 – 0.08 contour is indeed associated with this pair.

At $\phi$ = 15° the $k/V_{tip}^2$ levels above 0.10 near the blade, and the similar $k/V_{tip}^2$ levels at $\phi$ = 30°, and 45°, are associated with the vortex pair generated by the leading blade. The centre of this region of high $k/V_{tip}^2$ is found further out in the impeller stream as $\phi$ increases, moving from r/T = 0.17 at $\phi$ = 0°, to r/T = 0.19 at $\phi$ = 30° and to r/T = 0.21 at $\phi$ = 45°.

At all $\phi$ angles in Figure 4.16, $k/V_{tip}^2$ levels above 0.02 are confined to a region which in general is between z/T = 0.29 and z/T = 0.40. The $k/V_{tip}^2$ levels become low (< 0.02) and nearly uniform at around 1.5 blade heights above and below the impeller disk.

Figure 4.17 shows the $k/V_{tip}^2$ contours obtained in the z/T = 0.31 plane (2 mm below the disk). The trailing vortex produced by the leading blade is clearly indicated in this figure. In Figure 4.18, the presence of the trailing vortex generated by the previous blade is evident in the z/T = 0.33 plane.

Figure 4.19 shows the $k/V_{tip}^2$ levels in the z/T = 0.35 plane. The trailing vortex produced by the previous blade extends further compared to that observed in the previous z/T plane. In the z/T = 0.37 plane (Figure 4.20), the $k/V_{tip}^2$ levels do not exceed 0.06 – 0.08. Figure 4.21 shows the $k/V_{tip}^2$ levels in the z/T = 0.41 plane; here the $k/V_{tip}^2$ levels are entirely uniform and below 0.02.

### 4.3.4 TIME-RESOLVED VELOCITY MEASUREMENTS

#### INSTANTANEOUS VELOCITIES AND NORMALISED ENERGY SPECTRA

In order to quantify the decay of the trailing vortex structure away from the blades, time-resolved velocity measurements of the radial component, V, were made. Some characteristic recordings made at a number of locations in the disk midsection elevation are presented below.

Both Calabrese and Stoots (1989) and Yianneskis and Whitelaw (1993), showed that for single impeller systems a cyclic variation of the velocity is obtained with each blade passage in the vicinity of the trailing vortices. The expected six cycles (blade crossings) per revolution are clearly defined in the instantaneous radial velocity recording, obtained at r/T = 0.17, z/T = 0.33, shown in Figure 4.22(a). A similar recording of V obtained at r/T = 0.18, z/T = 0.33 is shown in Figure 4.22(b). The six cycles of the instantaneous velocity per revolution, as in Figure 4.22(a), are also clearly shown. Figure 4.22(c) shows a recording obtained at a location further away from the impeller, at r/T = 0.22, z/T = 0.33. In this velocity recording, although cyclic fluctuations are still discernible, their magnitude has decreased.

Figure 4.22(d) shows a recording of V made at r/T = 0.25, z/T = 0.33. Comparing this velocity recording with those shown in Figures 4.22(a)–(c), the decay of the trailing vortex structure expected from the results presented in the previous sections can be clearly seen. Fluctuations of the velocity behind some, but not all, blades are still discernible.

A better way to assess the influence of periodicity to the flow is by quantifying the changes of the strength of the frequency components along the impeller stream, therefore spectral analysis of the velocity recordings shown in Figures 4.22(a)–(d) was performed. Since velocity realisations with LDA are obtained at random intervals, the Lomb method, which is a method of spectral analysis for unevenly sampled data, was employed to obtain the normalised energy spectrum, $P(f) = E'(f)/u'^2$ in the manner described by Press et al (1992). The energy spectrum, E(f) was calculated using 'pseudo-equi-time spaced' data in the manner described in the following section. P(f) spectra are presented here as they aid the identification of discrete frequencies in the flow. E(f) spectra are presented in the following section to quantify the slope of the spectra at high frequencies.

The normalised energy spectrum of the velocity recording obtained at r/T = 0.17, z/T = 0.33 is shown in Figure 4.23(a). A peak at the spectral frequency of 216 Hz can be observed, indicating a well-defined periodic motion, which corresponds to the blade passage frequency. The harmonic of this frequency can also be observed in the figure, which is indicated by the smaller peak at the frequency of 432 Hz. The normalised spectrum of the velocity recording obtained at r/T = 0.18, z/T = 0.33 is shown in Figure 4.23(b). Two peaks can again be observed: one at 216 Hz, and one at 432 Hz. The 216 Hz peak, though smaller in magnitude compared with that found at r/T = 0.17, z/T = 0.33, also indicates that there is a well-defined periodic motion in the flow at this location. The normalised spectrum of the velocity recording made at r/T = 0.22, z/T = 0.33 (Figure 4.23(c)) shows a small peak at 216 Hz with a magnitude of about 10% of that found at r/T = 0.17, z/T = 0.33,

indicating that the periodic motion in the flow at this location is not as pronounced. Finally, Figure 4.23(d) shows the normalised spectrum of the velocity recording made at r/T = 0.25, z/T = 0.33. No distinctive peak can be observed in this figure, indicating that the vortex structure has begun to break down into random turbulence. This trend is in agreement with Mujumdar et al (1970), who observed that 80% to 90% of the turbulence intensities measured close to the impeller blade were due to the periodic component and that this component decayed quickly to a negligible value at about 0.66 of the tank radius (i.e. at 0.33 T).

## ENERGY SPECTRA AND SCALES OF TURBULENCE

It is useful to compute the energy spectrum to describe a turbulent flow. The instantaneous velocity, U, can be expressed as:

$$U = \overline{U} + u \tag{4.3}$$

where U is the instantaneous velocity, $\overline{U}$ is the average value of U and u is the fluctuating velocity component. The one-dimensional energy spectrum E(f) is obtained from the Fourier transform of $u^2$ and represents the energy contained between frequencies f and f + df such that:

$$u'^2 = \int_0^\infty E(f)\, df \tag{4.4}$$

and

$$u' = \sqrt{\overline{u^2}} \tag{4.5}$$

As mentioned earlier, the velocity realisations with LDA are obtained at random intervals and therefore some complications are introduced in the calculation of E(f). However, it is possible to obtain "pseudo-equi-time spaced" data by conditionally resampling the velocity recording (see, for example, Durao et al, 1980). In order to determine a suitable resampling interval, each velocity recording was resampled with various resampling intervals. The resampling interval of each recording was then selected by comparing the normalised energy spectra obtained from the resampled records with those obtained from the raw data such that the resampling process did not distort the raw data.

Figure 4.24 shows two energy spectra plotted in log-log scale. The spectrum shown in red in the figure was computed from the resampled fluctuating velocity component, v obtained at r/T = 0.17 and z/T = 0.33. This spectrum exhibits a sharp peak at the blade passing frequency, in agreement with Mujumdar et al (1970). They observed a sharp peak at the blade passing frequency in the energy spectra obtained near the impeller, and noted that such a peak was due to the periodicity in the flow.

Therefore, in order to obtain the E(f) of the real turbulence, it is necessary to correct the velocity fluctuations to account for the periodic component present in the flow (i.e. the pseudo-turbulence). A number of methods can be employed to obtain the 'real' turbulence velocity component, for example, by subtracting the 1° ensemble-averaged mean velocities from the instantaneous velocities, or by estimating the instantaneous mean velocities using the moving-window averaging method. However, the former method generally does not yield a zero-

mean velocity fluctuation due to cycle-to-cycle variations (see, for example, Yianneskis and Whitelaw, 1993), while the latter acts as a high-pass filter and thus information on low-frequency turbulence will be lost. Therefore, a band-stop frequency filtering technique was employed in the present work. The E(f) computed from the corrected v obtained at r/T = 0.17 and z/T = 0.33 is shown in black in Figure 4.24. In this spectrum, no peak can be discerned at 216 Hz.

A straight line of -5/3 slope is also drawn on Figure 4.24, which represents the energy distribution predicted for isotropic turbulence by Kolmogorov from a dimensional analysis for the inertial subrange (Lancaster (1976), Nishikawa et al (1976), Landahl and Mollo-Christensen (1986)). The slopes of both spectra shown in Figure 4.24 are around -1.3 for frequencies above 1 kHz.

Figures 4.25 – 4.27 show characteristic energy spectra computed from the corrected v at various r/T locations in the z/T = 0.33 plane. These figures are again plotted in log-log scales, and a straight line of -5/3 slope is drawn on each figure.

Figure 4.25 shows the energy spectra of the corrected v obtained at r/T= 0.17, 0.19 and 0.21. No regions with a -5/3 slope can be observed from the energy spectra of v at r/T = 0.17 and 0.19. The deviation of the slopes of the spectra taken at r/T = 0.17 and 0.19 from the value of -5/3 might be considered to indicate the anisotropy of the turbulence at these two locations. The difference between the slope of the spectrum obtained at r/T = 0.21 and the -5/3 line is also large at low frequencies, however, a small region with a -5/3 slope at frequencies above

approximately 2 kHz can be observed which may be considered to indicate that the degree of anisotropy of turbulence is smaller.

In Figure 4.26, the energy spectra obtained at r/T = 0.23, 0.25 and 0.27 are presented. It can be observed that the frequency range with a -5/3 slope increases with increasing r/T. At r/T = 0.23, the region with -5/3 slope is confined to frequencies above approximately 2 kHz, while at r/T = 0.25 and 0.27 regions with -5/3 slope can be observed for frequencies above about 1 kHz. Figure 4.27 shows the energy spectra of v further away from the impeller, at r/T = 0.31, 0.33 and 0.35. Regions with -5/3 slope can be observed for all three energy spectra for frequencies above about 200 Hz.

The results presented in this section indicate that the turbulence in the impeller stream deviates from isotropy. Further away from the impeller the deviation becomes smaller and the turbulence might be regarded as isotropic.

### TEMPORAL SCALES OF TURBULENCE

A characterisation of the eddy size distribution within a turbulent flow can be obtained from the autocorrelation of the velocity fluctuations. The autocorrelation function coefficient is defined by Equation 4.6, and can be obtained by the Fourier transform of $E(f)/u'^2$.

$$R(\tau) = \frac{\overline{u(t)\ u(t+\tau)}}{u'^2} \qquad (4.6)$$

where t is time and $\tau$ is the correlation time. The integral time scale of turbulence, $\Lambda_t$, is defined from the autocorrelation coefficient as:

$$\Lambda_t = \int_0^\infty R(\tau)\, d\tau \tag{4.7}$$

Although the integral time scale is defined as the integral of $R(\tau)$ from zero to infinity, in practice it is computed to the first zero of the autocorrelation function (Yianneskis et al, 1991). The micro time scale $\lambda_t$ is given by:

$$\frac{-2}{\lambda_t^2} = \left[\frac{\partial^2 R(\tau)}{\partial t^2}\right]_{t=0} \tag{4.8}$$

The autocorrelation function coefficients $R(\tau)$ of the corrected v variation at various r/T locations were computed from the energy spectra using an FFT technique. From the $R(\tau)$ obtained, the integral time scale, $\Lambda_t$ and micro time scale $\lambda_t$ were computed using Equations (4.7) and (4.8) respectively. A characteristic plot of $R(\tau)$ is shown in Figure 4.28, computed from the corrected v variation at r/T = 0.17. The variations of the micro and integral time scales with r/T at z/T = 0.33 are shown in Figures 4.29(a) and 4.29(b) respectively.

The distribution of micro time scales in Figure 4.29(a) shows that the $\lambda_t$ is about 0.11 ms at r/T = 0.17, and increases gradually to around 0.20 ms at r/T = 0.35. In Figure 4.29(b), it can be seen that $\Lambda_t$ is small ($\approx$ 0.25 ms) near the impeller blade at r/T = 0.17 and increases gradually to approximately 0.35 ms at r/T = 0.25 and to around 1.24

ms at r/T = 0.35. This distribution might be expected since the velocities near the impeller are higher and the corresponding time scales are therefore shorter. The integral time scales are approximately 3–6 times higher than the corresponding micro time scales.

## SPATIAL SCALES OF TURBULENCE

Spatial scales of turbulence can be obtained by multiplying the temporal scales with an appropriate convective velocity. G I Taylor (see Lancaster, 1976) showed that temporal and spatial scales of turbulence could be related by:

$$\Lambda_x = L_t \overline{U} \qquad (4.9)$$

and

$$\lambda_x = \lambda_t \overline{U} \qquad (4.10)$$

where $\Lambda_x$ and $\lambda_x$ are the integral and micro length scales respectively. However Equations (4.9) and (4.10) are accurate only when $\overline{U}$ is constant and the relative turbulence intensity is much smaller than unity (i.e. $\overline{U} >> u'$), which is true for flows at low Reynolds number when the turbulence of the flow moving past a location is effectively "frozen" (Hinze, 1975). Both conditions are not satisfied in many parts of the flow studied here, since the Reynolds number is large and the mean flow in the vicinity of the impeller stream is periodic.

An alternative convective velocity has been suggested for high Reynolds number flows by Heskestad (1965), to account better for the coupling of micro time and length scales in a non-swirling flow, i.e. where the

tangential mean velocity is zero. However, this is not true in the present work where a strong tangential flow is induced by the impeller and it is inappropriate to apply Heskestad's suggestion. Therefore, $\Lambda_x$ and $\lambda_x$ were estimated using Equations (4.9) and (4.10) respectively with the local ensemble-averaged mean velocities as the convective velocities. The scales computed are shown only as approximate indications of eddy sizes, as the conditions mentioned above are not satisfied in all locations concerned.

The distributions of $\Lambda_x$ and $\lambda_x$ along the impeller stream in the z/T = 0.33 plane are shown in Figure 4.30. It can be observed that $\Lambda_x$ has a minimum value of around 0.6 mm at r/T = 0.17, approximately equal to 0.1 W; and increases with increasing r/T, reaching a maximum value of about 1.7 mm at r/T = 0.35, approximately equal to 0.3 W. The values of $\Lambda_x$ obtained in the present work are generally smaller than those reported previously. Cutter (1966), who conducted experiments in a T = 292 mm vessel, obtained values of $\Lambda_x$ of approximately 0.2 W and 0.4 W at r/T ≈ 0.17 and 0.35 respectively; Mahouast et al (1989) reported a minimum value of approximately 0.48 W and a maximum of around 1.32 W for $\Lambda_x$ in the impeller stream in a T = 200 mm vessel; and a value of 0.4 W for the $\Lambda_x$ near the blade tip was reported by Wu and Patterson (1989). Notwithstanding the different methods employed to calculate $\Lambda_x$ by the various researchers, there is reasonable agreement between the values measured in this work and those reported by Cutter and by Wu and Patterson. Mahouast's $\Lambda_x$ values are higher and do not agree with the frequently employed assumption that $\Lambda_x$ = 0.1W near the blade tip (Kresta(1992), Ruszkowski (1992)).

It can also be seen from the figure that the value of $\lambda_x$ remains almost constant with increasing r/T and the average value of $\lambda_x$ is around 0.25 mm. This value compares well with that reported by Wu and Patterson, who obtained micro length scales of 0.3 to 1.0 mm in the impeller stream. However, $\lambda_x$ might be expected to increase with r/T; the near-constant variation obtained is likely to stem from the approximations and corresponding uncertainties involved in its determination.

**RATE OF DISSIPATION**

The rate of dissipation of turbulence kinetic energy, $\varepsilon$, is a parameter of great interest both for the characterisation of turbulence and the identification of regions where energy is disipated in stirred vessels. Furthermore, as most CFD prediction methods employ the k-$\varepsilon$ turbulence model, knowledge of the local energy dissipation rate is very important. Several methods have been proposed for the determination of $\varepsilon$. Wu and Patterson (1989) proposed that:

$$\varepsilon = \frac{0.85k^{3/2}}{\Lambda_x} \qquad (4.11)$$

The values of $\varepsilon$ were calculated in the present work using Equation (4.11). The values of k were obtained from the 60° ensemble-averaged turbulence levels, while the values of $\Lambda_x$ presented above were used. The variation of $\varepsilon$, normalised with $N^3D^2$, with (r/R) in the disk mid-section elevation (z/T = 0.33) plane is shown in Figure 4.31. For comparison purposes, the results reported by Patterson and Wu (1985) are also shown in the figure.

It can be observed from Figure 4.31 that the value of $\varepsilon/N^3D^2$ decreases from around 40 near the blade tip to values comparable with those of Patterson and Wu further away from the blade. The values obtained in the present work are generally higher than those reported by Patterson and Wu. It should be noted that Patterson and Wu found that near the blade tip $\varepsilon/N^3D^2$ increases with rotational speed, but further away it is not strongly affected. Therefore, the relatively high $\varepsilon/N^3D^2$ values at $r/R < 1.5$ in the present work may be attributed to the higher speed (2165 rpm compared with 200 rpm in Patterson and Wu) employed here. This might have important implications for the scaling of stirred reactor flows and should be investigated further.

Furthermore, it can be seen from Equation (4.11) that $\varepsilon$ is a function of $k$ and $\Lambda_x$, therefore the accuracy of $\varepsilon$ depends on the accuracy of $\Lambda_x$. However, as mentioned earlier the calculation of $\Lambda_x$ using Equations (4.9) is only accurate when $\overline{U}$ is constant and $\overline{U}$ and >> u', which is not true in the flow studied, and this may therefore introduce inaccuracies in the $\varepsilon$ values obtained.

## 4.4 DISCUSSION

### 4.4.1 THE TRAILING VORTEX AXIS

The location of the mean axis of the trailing vortex produced by the Rushton impeller is plotted in Figure 4.32. For comparative purposes the trailing vortex axes determined previously by van't Riet et al (1975),

Yianneskis et al (1987) and Stoots and Calabrese (1994) for single Rushton impeller configurations are also shown.

Van't Riet et al (1975) utilised a photographic technique to find the shape of the axis by determining the locations where the axial velocity component perpendicular to the axis was zero. The investigations of Yianneskis et al (1987) and Stoots and Calabrese (1994) determined the vortex axis from angle-resolved LDA mean velocity data. The discrepancies between the vortex axis presented in these three investigations were attributed by Stoots and Calabrese to differences between various system characteristics such as the impeller geometry, the clearance of the impeller from the base of the vessel and the impeller rotational speed. The vortex axis for the present work was also determined from the locations where the mean axial velocity component was zero.

It can be seen from Figure 4.32 that the axis of the trailing vortex obtained from the present results is very similar to that reported by Yianneskis et al (1987). The close agreement of the two axes can be attributed to the geometrical similarities of the vessels and impellers used by Yianneskis et al and in the present work ($t_b/D = 0.01$ and $C = T/3$). As neither van't Riet et al nor Stoots and Calabrese quote $t_b/D$ values for their impellers and the latter used a clearance $C = T/2$, the observed variation of the present axis from those studies may be due to such geometrical differences.

### 4.4.2 EFFECT OF VESSEL SIZE

In order to assess the influence of vessel size on the mean velocities and turbulence levels, measurements obtained in the 100 mm vessel are compared in this section with those performed in the 294 mm vessel. The vessel and impeller geometries of the T = 100 mm and T = 294 mm vessels have been described in Chapter 2.

Angle-resolved mean velocities and turbulence levels of the radial component over 60° of impeller revolution ( i.e. between a specific blade pair) were made. The measured values were subsequently ensemble-averaged over the 60° interval and normalised with their respective impeller tip speeds to obtain the normalised mean velocities and turbulence levels of the radial component at a number of elevations and at two radii in the impeller stream.

#### MEAN VELOCITIES AND TURBULENCE LEVELS

The normalised radial mean velocity and turbulence level profiles obtained at r/T = 0.17 and r/T = 0.22 in the impeller stream are shown in Figures 4.33 (a)–(b) and 4.34 (a)–(b) respectively.

Comparing the profiles of normalised mean velocity in Figures 4.33(a) and (b), it is evident that there is good scaling of the flows in the two vessels. The maximum velocities are identical at both r/T = 0.17 and r/T = 0.22. In addition, both profiles in each location show very similar velocity gradients. The profiles for the T = 294 mm vessel are skewed slightly upwards compared to those for the T = 100 mm vessel. As

expected, these profiles show the maximum mean velocity to decrease with increasing radial distance from the blade tip, and the development and spread of the profiles with increasing radius due to entrainment of fluid into the radial discharge flow is evident.

Relative good scaling is also observed between the normalised turbulence level profiles shown in Figures 4.34(a) and (b). As with the normalised mean velocity profiles, the turbulence level profiles for the T = 294 mm vessel are located only slightly above those for the T = 100 mm vessel, but the gradients are very similar. In all of the turbulence level profiles presented here is a slight upward inclination, in agreement with the findings of Yianneskis et al (1987) who reported an inclination of the impeller stream of around 4° to the horizontal for a Rushton impeller configuration similar to the present one. There is also a noticeable dip in the centre of the profiles around z/T = 0.33 corresponding to the elevation of the impeller disk, particularly at r/T = 0.17.

The results presented in this section show that, for the 100 and 294 mm tanks where all vessel and impeller features are scaled precisely, both mean velocities and turbulence levels in the flow field around the impellers scale well with vessel size. It may be concluded that differences with vessel size reported in earlier investigations (for example, van der Molen and van Maanen, 1978) were due to imprecisions in the scaling of the impeller geometries. This is evident, for example, in Kusters's (1991) work where mean velocities in a T = 102 mm vessel with $t_b/D = 0.019$ were smaller than in the T = 200 mm ($t_b/D = 0.016$) and T = 388 mm ($t_b/D = 0.023$) vessels investigated.

Such differences cannot be explained by consideration of the effect of blade thickness (see, for example, Rutherford et al,1996b), but the relatively thicker impeller disk employed by Kusters in the smaller vessel is likely to be the reason for the discrepancy.

**FLOW NUMBER**

For 360° ensemble-averaged data, the pumping capacity (Q) and the Flow number (Fl) are given by the following relationships:

$$Q = \int_{-h^*}^{h^*} 2\pi r \overline{V} \; dz \tag{4.9}$$

$$Fl = \frac{Q}{ND^3} \tag{4.10}$$

where $\overline{V}$ is the radial mean velocity component and r and z are the radial and axial co-ordinates of the measurement locations. The integration limits h* and -h* are set for each radial mean velocity profile as the points where the mean velocity above or below the impeller is zero.

Since in the present work data were obtained as 1° angle-resolved measurements in order to eliminate data rate effects present in the 360° ensemble-averaged measurements as mentioned in Section 4.2, the pumping capacities in the T = 100 mm and 294 mm vessels were calculated using the relationship proposed by Stoots and Calabrese (1994) and Rutherford et al (1996b):

$$Q_\phi = 6 \int_{-h^*}^{h^*} \int_{\phi=0^\circ}^{\phi=60^\circ} \left(\frac{2\pi r}{360}\right) \overline{V} \, d\phi \, dz \qquad (4.11)$$

and accordingly, the Flow numbers were calculated by using:

$$Fl = \frac{Q_\phi}{ND^3} \qquad (4.12)$$

With the relationship shown in Equation (4.11), the 1° angle-resolved radial mean velocities are integrated first azimuthally over the range of impeller blade angles over which the data was acquired ($0^\circ \leq \phi \leq 60°$), and the resulting profiles are then integrated axially over the impeller stream. The integration limits h* and -h* are set according to the manner described for Equation (4.9). The factor, $2\pi r/360$, represents the arc subscribed by 1° of azimuthal angle at radius r, and the factor 6 is required to account for the passage of six pairs of impeller blades during one impeller revolution. Equations (4.10) and (4.12) yield identical Fl values with the same set of data.

Figure 4.35 shows the Flow numbers obtained at three radii at z/T = 0.33 using Equations (4.11) and (4.12) for the T = 100 mm and 294 mm vessels. For comparative purposes, the Fl value calculated from 360° ensemble-averaged data obtained by Mahmoudi (1994) in the T = 294 mm vessel is also shown in Figure 4.35.

It can be seen from Figure 4.35 that both the Flow numbers calculated for the T = 100 mm ($Fl_{100}$) and T = 294 mm ($Fl_{294}$) vessels increase significantly with increasing radius. Fl increases from $Fl_{100}$ = 0.645 and

$Fl_{294}$ = 0.636 at r/T = 0.17, to $Fl_{100}$ = 1.048 and $Fl_{294}$ = 0.962 at r/T = 0.22. The increase of Fl values with r/T is to be expected due to the fluid entrainment into the radial discharge stream and the broadening of the radial mean velocity profile which has been shown to occur with increasing radial distance from the impeller tip. Wu and Patterson (1989) also found that Fl increased with increasing radius. They reported a significantly higher value of Fl = 0.82 at the impeller tip location than those found in the present study ($Fl_{100}$ = 0.645, $Fl_{294}$ = 0.636). However, they found that Fl = 2.0 at r/T = 0.33, a value comparable to the Fl calculated at a similar location from the data obtained in the T = 100 mm vessel ($Fl_{100}$ = 1.960 at r = 0.35T). This Fl value shows good agreement with the results of Wu and Patterson (1989), and indicates considerable fluid entrainment into the impeller stream some distance from the impeller. Differences between the data reported by Wu and Patterson (1989) and the present results could be attributed to differences in, for example, the impeller geometry, since the impeller thickness ratio was not quoted in their work.

The Flow numbers presented ($Fl_{100}$ and $Fl_{294}$) were found to be in good agreement with Fl values reported by Stoots and Calabrese (1994). Revill (1982) conducted a literature review of the pumping capacity of Rushton turbines and recommended that Fl should lie within the range Fl = 0.75±0.15 when the impeller diameter is between 0.20T and 0.50T, and the clearance of the impeller from the base of the vessel is greater than 0.30T and less than 0.50 T. The present results at the impeller blade tip for both vessels lie within the range predicted by Revill.

With respect to the influence of vessel scale, the results presented suggest that Fl scales between the vessels to within 8%. $Fl_{100}$ is always higher than $Fl_{294}$, and the differences between the values increase with radial distance from the impeller. This could be attributable to a number of factors such as the difference between the radial arc over which the integration is applied in the two vessels, that is the spatial resolution in absolute terms is not the same in each vessel.

### 4.4.3 VELOCITY VARIATION IN IMPELLER STREAM

Van der Molen and van Maanen (1978) used vessels from 0.12 m to 0.9 m in diameter with Rushton turbines and found that for fully-turbulent flow, the mean radial velocity $\overline{V}$ just off the tip of the blade and on its centre line was a constant ratio (0.85) of the impeller tip speed $V_{tip}$, and decayed as it moved out along the radius, r, such that:

$$\frac{\overline{V}}{V_{tip}} = 0.85 \left(\frac{r}{R}\right)^{-7/6} \qquad (4.13)$$

where r is the radial distance and R is the radius of the impeller.

The normalised 360° ensemble-averaged mean velocities and turbulence levels obtained in the impeller disk plane (i.e. z/T = 0.33) against r/R are shown in Figures 4.36(a) and (b) respectively. In Figure 4.36(a), the 'best fits' of the data obtained in the present work, by van der Molen and van Maanen (1978) and by Dyster et al (1993) are shown. The best fit of the present data is given by:

$$\frac{\overline{V}}{V_{tip}} = 0.74 \left(\frac{r}{R}\right)^{-0.99} \qquad (4.14)$$

The correlation in Equation (4.14) agrees very well with that reported by Dyster et al (1993), but not as well with that obtained by van der Molen and van Maanen.

Dyster et al attributed the discrepancies between the best fit of their data and that obtained by van der Molen and van Maanen to the minor differences in the impeller geometries and to the fact that the latter used closed-top vessels. However, Nouri and Whitelaw (1990) concluded that the use of a lid only affects the flow in the immediate vicinity of the lid/free surface and that the flow velocities elsewhere in a 144 mm vessel were almost identical to those in a 294 mm vessel. Furthermore, the present work was carried out in a vessel with a lid but the data match well those of Dyster et al. Therefore, the discrepancies are likely to be attributed to differences in the impeller geometries employed by van der Molen and van Maanen.

The best fit of the $v'/V_{tip}$ data obtained in the present work is shown in Figure 4.36(b). The best fit of the present data is given by:

$$\frac{v'}{V_{tip}} = 0.48 - 0.16 \left(\frac{r}{R}\right) \qquad (4.15)$$

The correlation proposed by Dyster et al (1993):

$$\frac{v'}{V_{tip}} = 0.45 - 0.13 \left(\frac{r}{R}\right) \qquad (4.16)$$

is also shown in the figure. The results of the present work show agreement with the data of Dyster et al near the impeller blade but the two sets of results diverge with increasing r/R. The reason for this divergence is not clear; however, the local v' values are relatively small (around 0.15 $V_{tip}$) and it should be noted that there is scatter in both the present data as well as in those of Dyster et al.

### 4.4.4 ISOTROPY OF THE IMPELLER DISCHARGE FLOW

In order to ascertain whether the turbulence in the impeller region is isotropic, the three turbulence level distributions throughout the measurement region were compared. This was undertaken as most CFD predictions of the flows employ the k-ε model of turbulence, in the formulation of which there is an implicit assumption of isotropic eddy viscosity.

As the discharge flow out of a Rushton impeller is primarily radial, the turbulence levels of the axial and tangential components were compared with the radial component to quantify the degree of isotropy/anisotropy of the turbulence in the vicinity of the impeller. Figures 4.37 and 4.38 show the contour plots of u'/v' and w'/v' in four $\phi$ planes (0°, 15°, 30° and 45°) respectively.

From Figure 4.37, it can be clearly observed that in all $\phi$ planes shown, the turbulence over most of the measured region is anisotropic (i.e. $u'/v' \neq 1$). The w'/v' contour plots shown in Figure 4.38 also indicate that the turbulence is anisotropic in many parts of the measurement region.

However, it should be noted that although both the u'/v' and w'/v' values vary from 0.30 to 1.7 in the impeller stream, there are large values of u'/v' and especially w'/v' in the boundaries of the measurement region, where the turbulence levels were reported earlier (Section 4.3.2) to be quite similar. This is due to the relative magnitudes of the turbulence levels: for example for w' = 0.02 and v' = 0.01, w'/v' = 2.0, whereas in absolute terms the levels are similar and within experimental error. A better way to assess the degree of isotropy is by considering the absolute difference between the different turbulence levels normalised by $V_{tip}$, i.e. $|u' - v'|/V_{tip}$ and $|w' - v'|/V_{tip}$. When these values tend to zero, u' $\rightarrow$ v' and w' $\rightarrow$ v' and the turbulence may be considered isotropic.

Contours of $|u' - v'|/V_{tip}$ and $|w' - v'|/V_{tip}$ in the $\phi$ = 0°, 15°, 30° and 45° planes are shown in Figures 4.39 and 4.40 respectively. In Figure 4.39, regions of locally high values of $|u' - v'|/V_{tip}$ can be observed near the impeller blade in all $\phi$ planes. Most of the regions near the edges of the measurement area have values of $|u' - v'|/V_{tip}$ between 0.00 and 0.02. In these regions, the turbulence can be considered to be isotropic. Locally high values of $|w' - v'|/V_{tip}$ can be observed near the blade in all $\phi$ planes in Figure 4.40. At $\phi$ = 15° locally high values of $|w' - v'|/V_{tip}$, which are associated with the trailing vortex of the preceding blade, can also be seen between r/T = 0.22 and 0.32, z/T = 0.30 and 0.36. In regions away from the impeller stream in all $\phi$ planes, the values are between 0.00 and 0.04, and the turbulence in these regions can again be considered to be isotropic.

## 4.9 EPILOGUE

In this chapter, detailed LDA results obtained in the T = 100 mm vessel have been presented, and the flow pattern produced in the vicinity of a single Rushton impeller has been described in detail. Micro and integral time scales calculated from time-resolved measurements had values of 0.11 – 0.2 ms and 0.22 – 1.24 ms respectively. The periodicity of the flow was established through spectral analysis and estimates of length scales and ε were provided. The location of the trailing vortex axis was also determined and compared with the results of earlier investigations. In order to investigate the influence of vessel size, measurements were also made in the T = 294 mm vessel. The results obtained from the two vessels were compared. The comparisons show that where all vessel and impeller features were scaled precisely, both mean velocities and turbulence levels in the flow field around the impeller scale well with vessel size. The comparison of Flow numbers obtained in the two vessels show that the Flow numbers scaled between the two vessels within 8%.

In the following chapter, the results obtained in the T = 100 mm vessel stirred by two Rushton impellers will be presented.

(a)

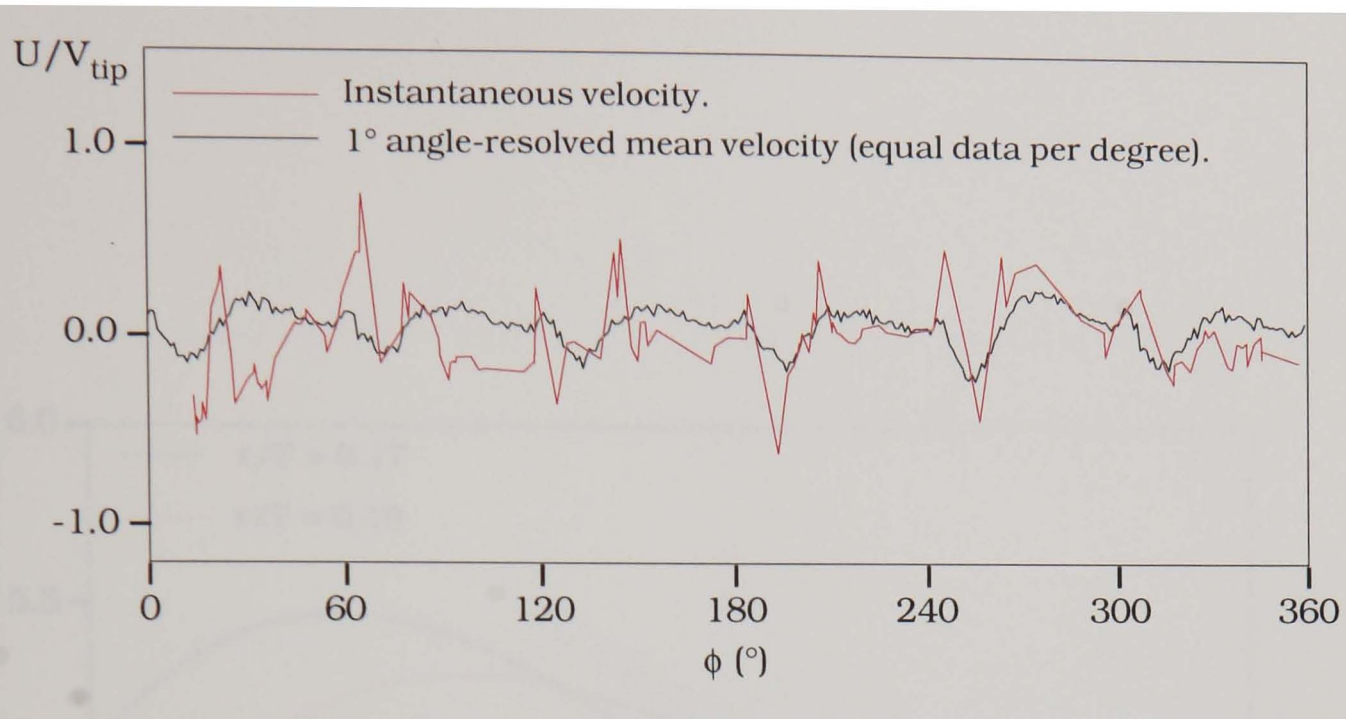


(b)

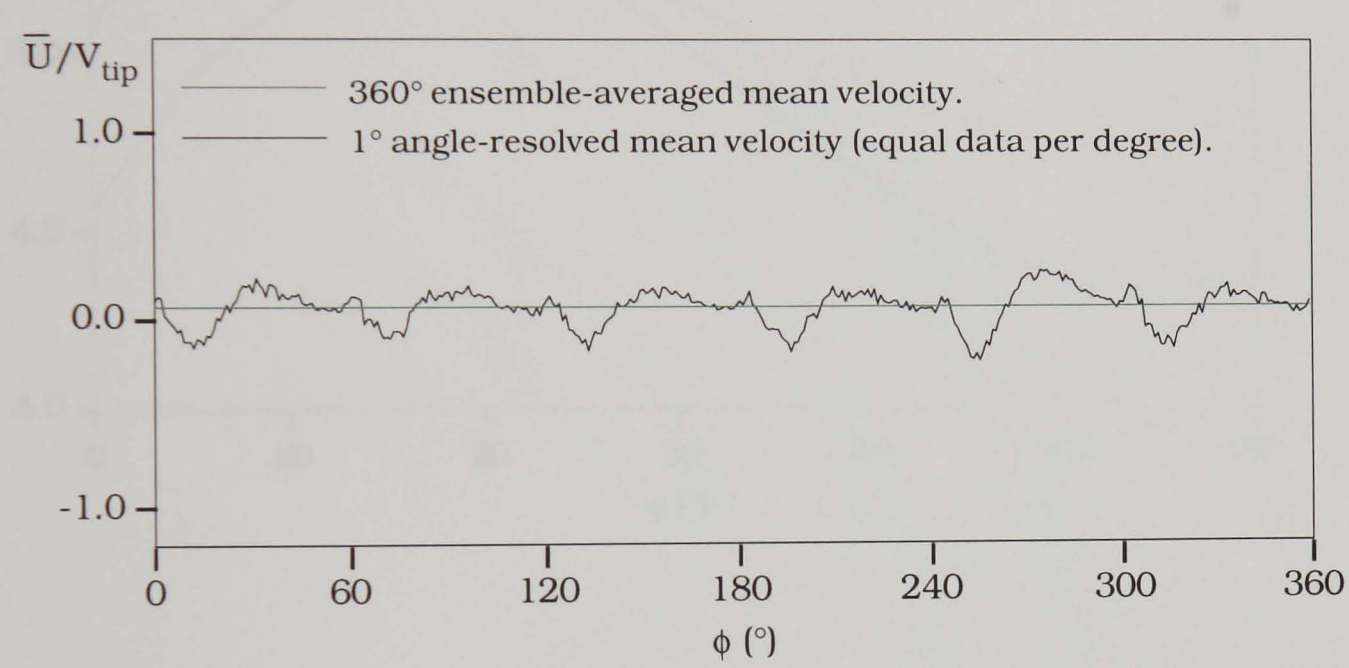


(c)

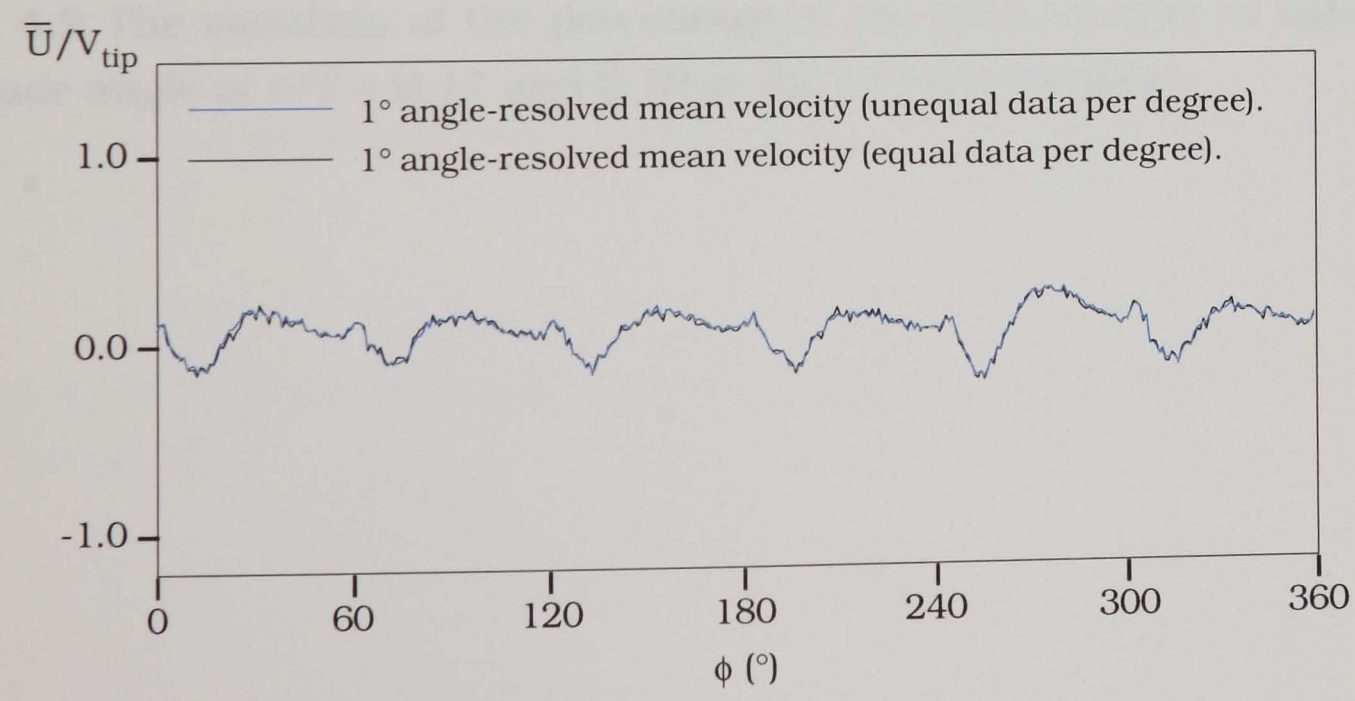


**Figure 4.1** Comparison of time-resolved, 1° angle-resolved and 360° ensemble-averaged data over six blade passages in the T = 100 mm vessel, at r/T = 0.17 and z/T = 0.33.

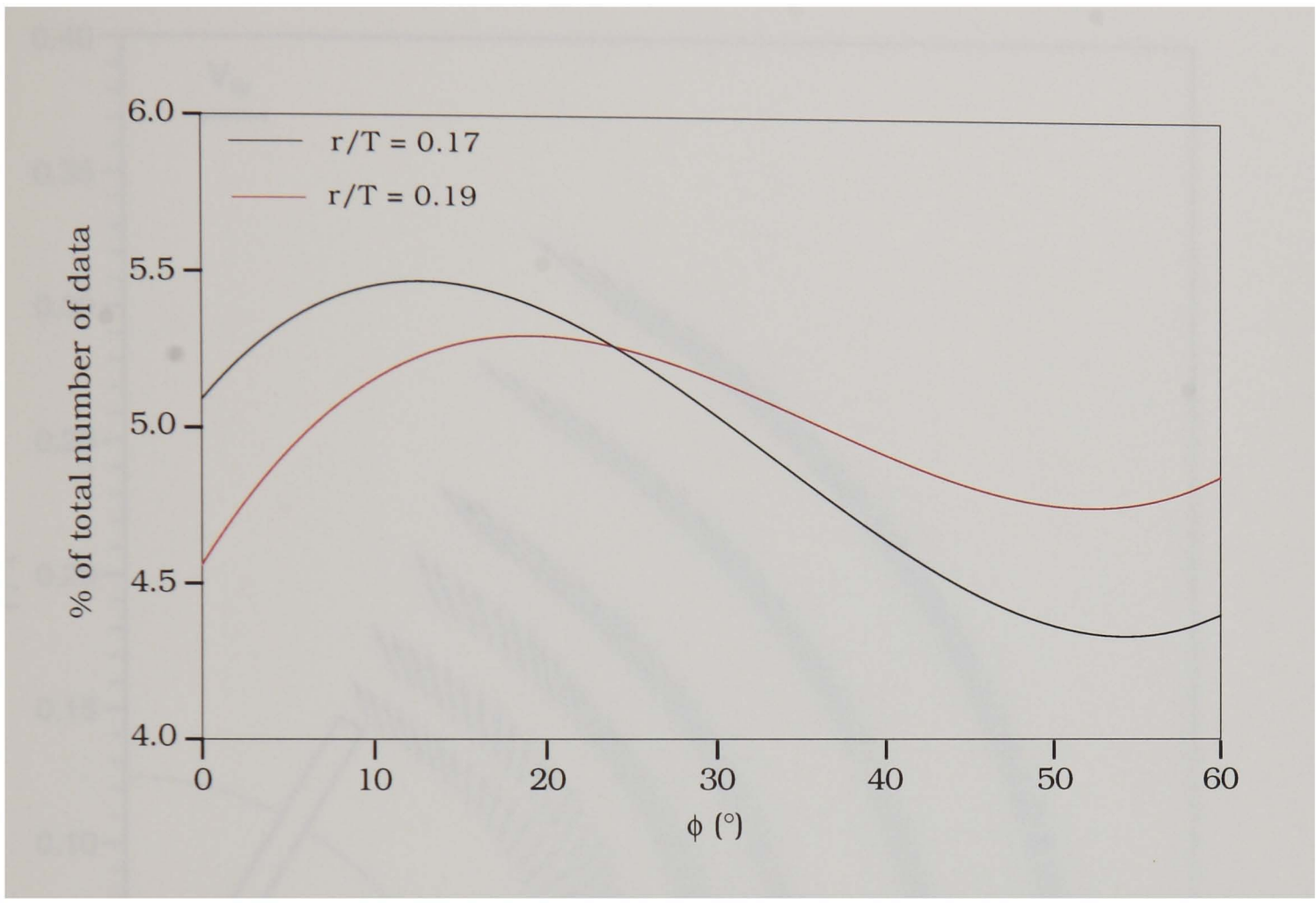


**Figure 4.2** The variation of the percentage of the total number of data with blade angle at r/T = 0.17 and 0.19 in the z/T = 0.33 plane.

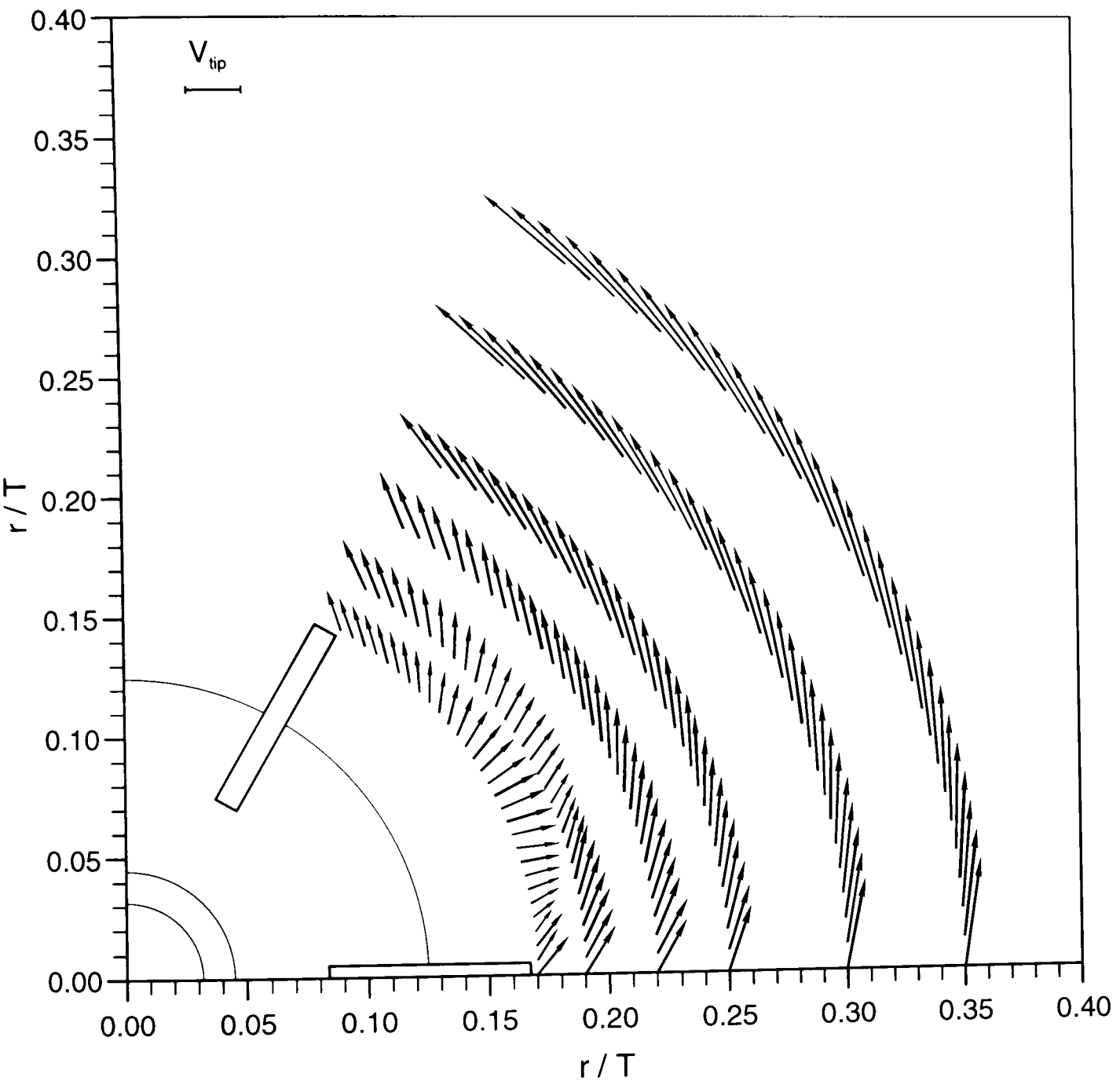


**Figure 4.3** Single Rushton impeller configuration: velocity vectors in the z/T = 0.33 plane.

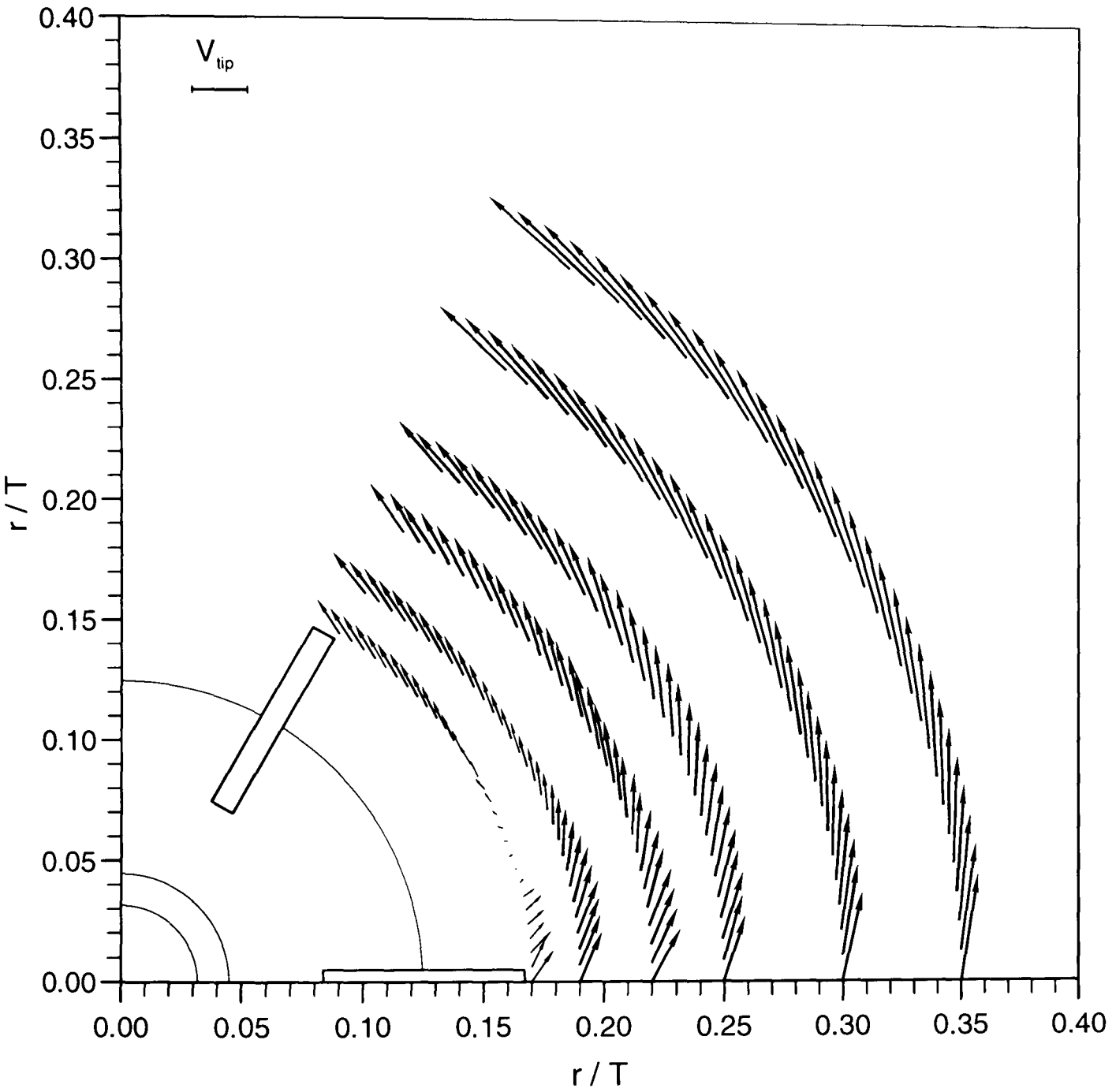


**Figure 4.4** Single Rushton impeller configuration: velocity vectors in the z/T = 0.35 plane.

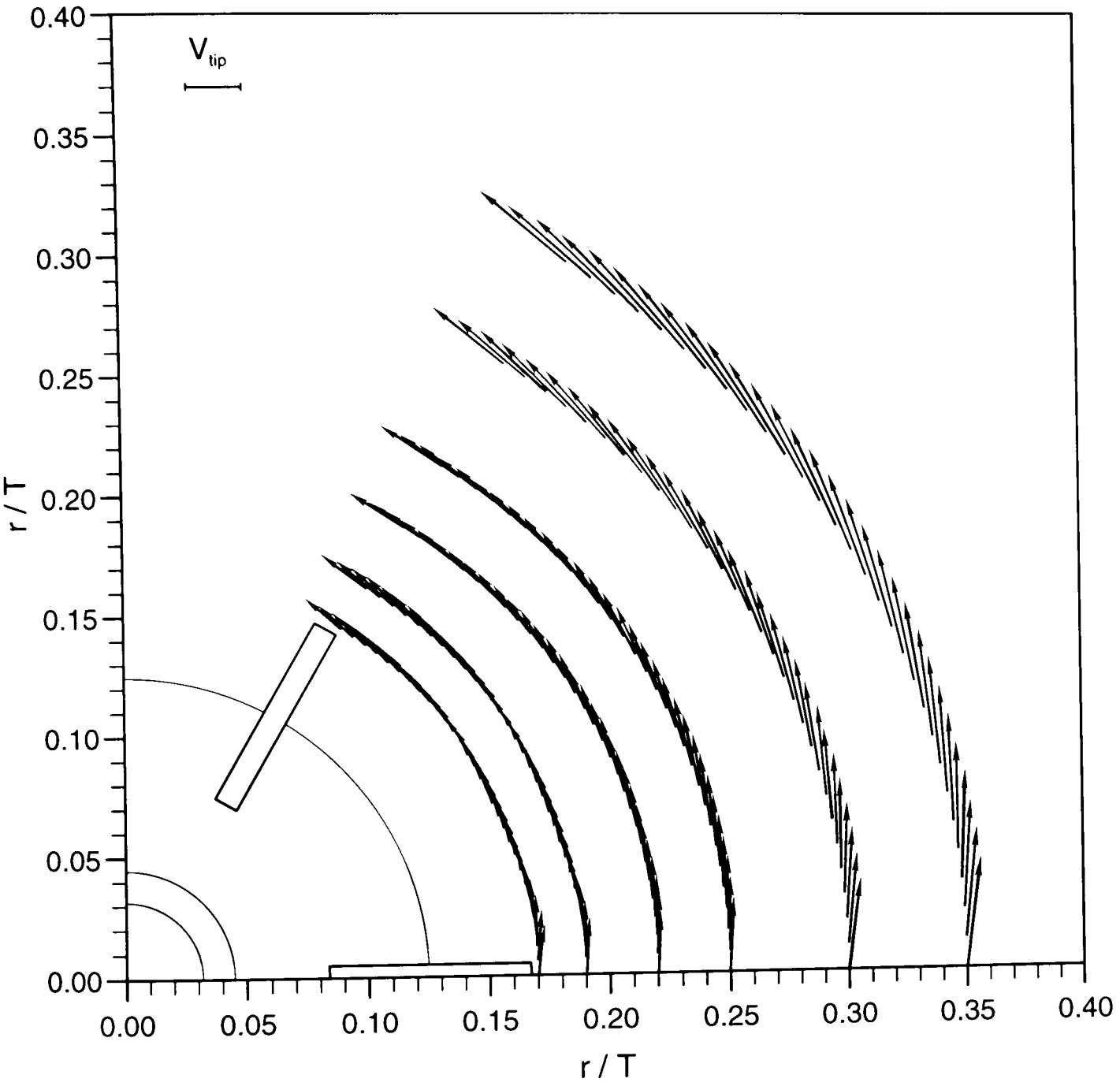


**Figure 4.5** Single Rushton impeller configuration: velocity vectors in the z/T = 0.37 plane.

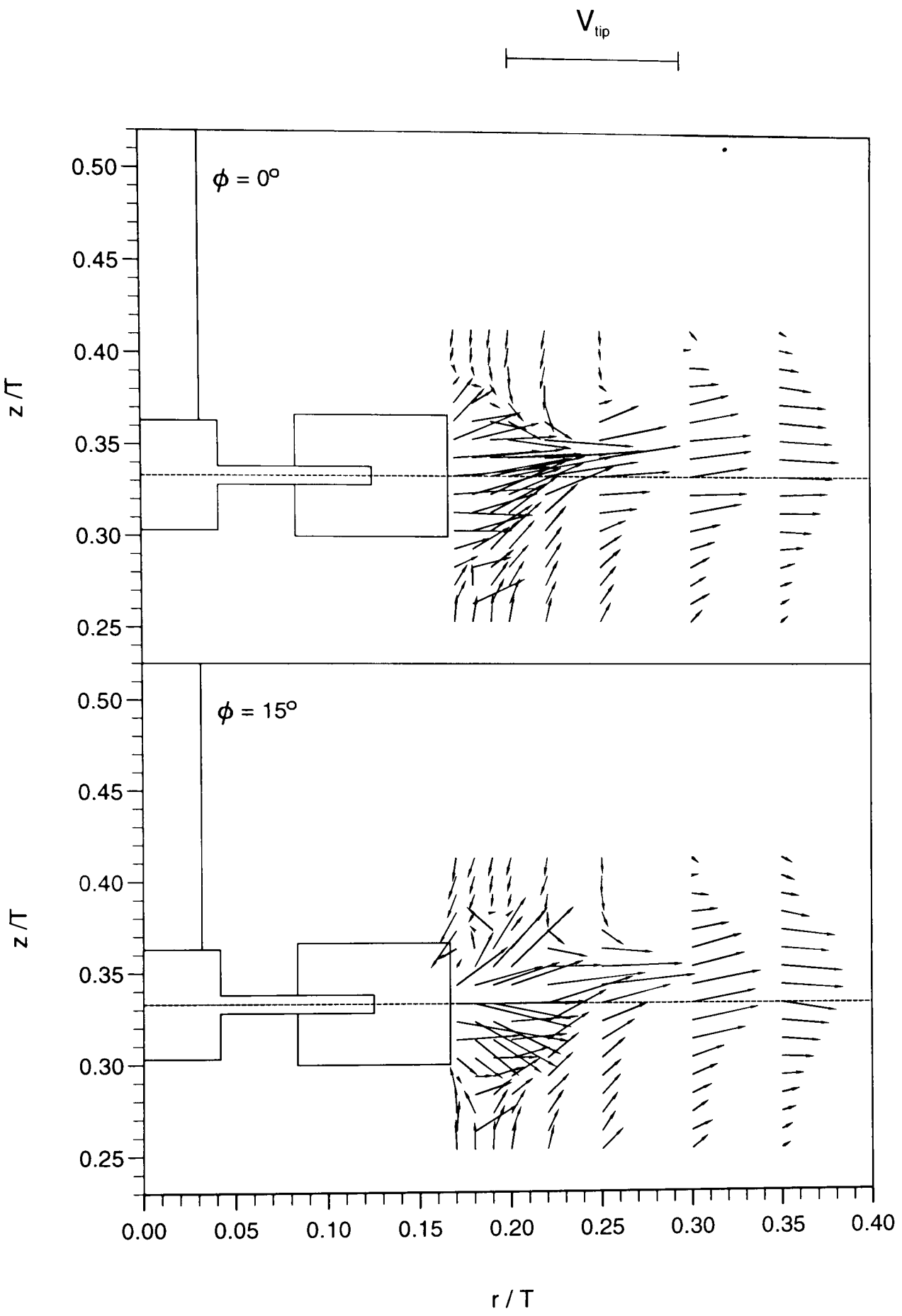


**Figure 4.6(a)** Single Rushton impeller configuration: velocity vectors in the $\phi = 0°$ and $15°$ planes.

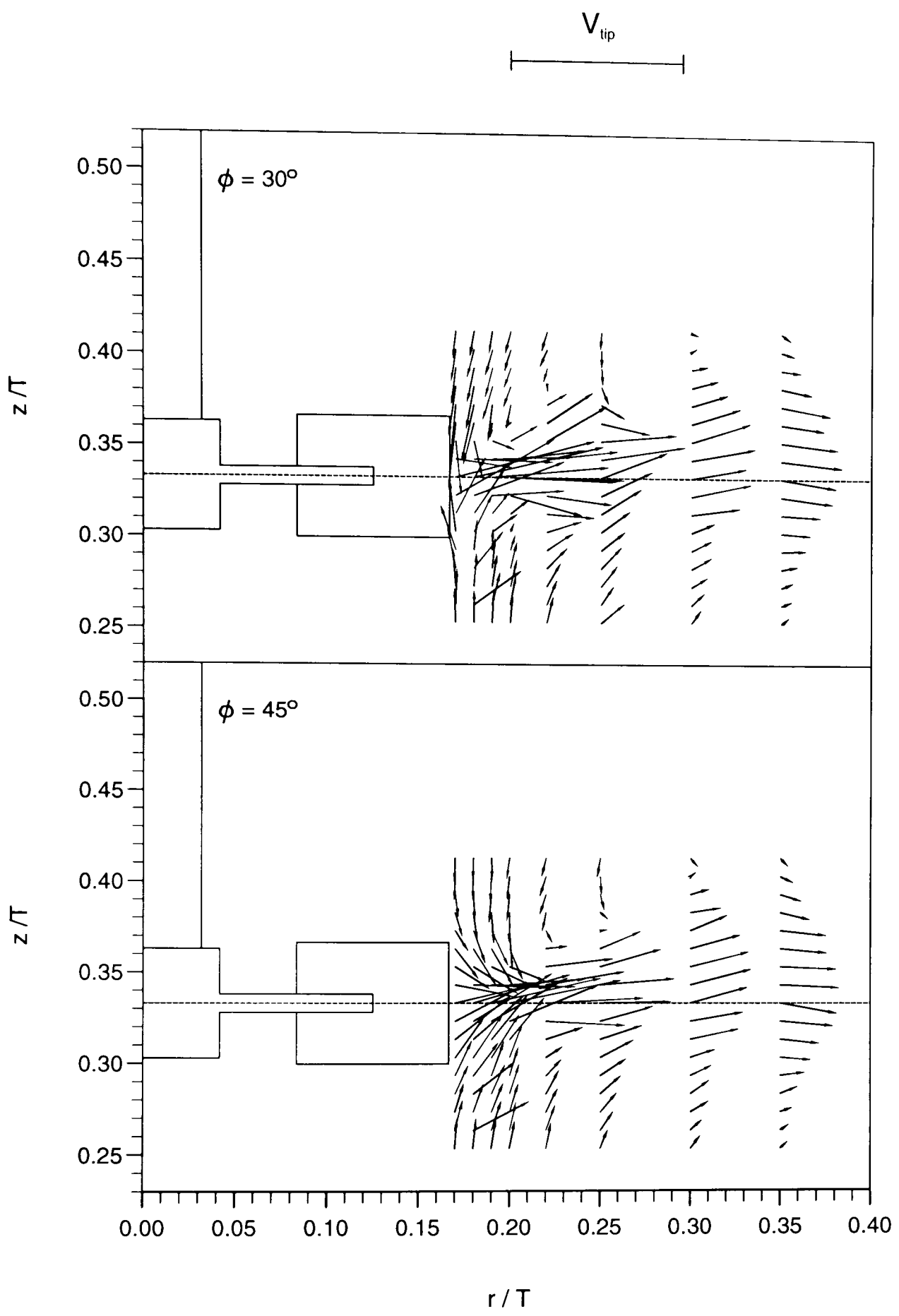


**Figure 4.6(b)** Single Rushton impeller configuration: velocity vectors in the $\phi$ = 30° and 45° planes.

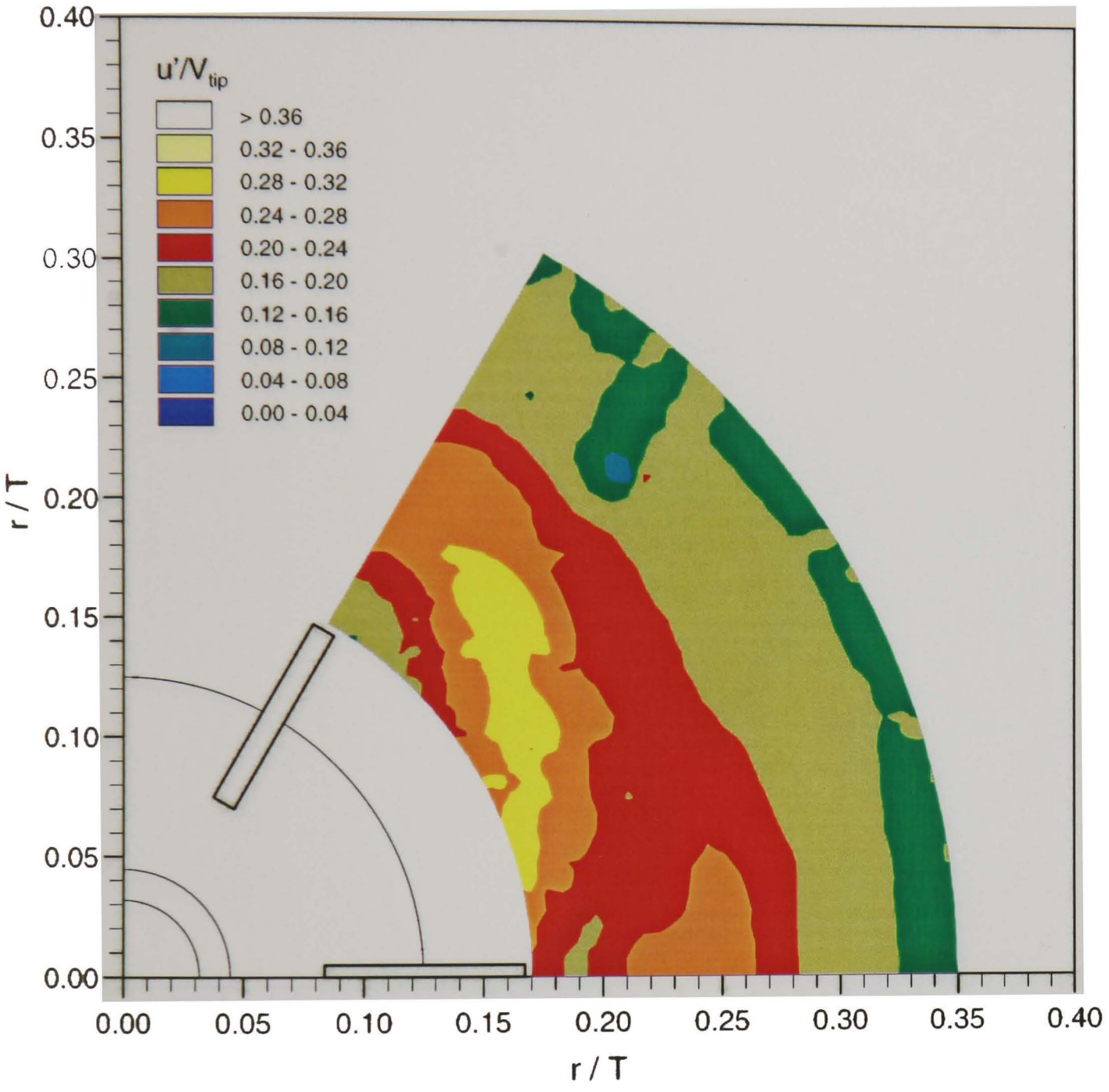


**Figure 4.7** Single Rushton impeller configuration: axial turbulence level contours in the z/T = 0.33 plane.

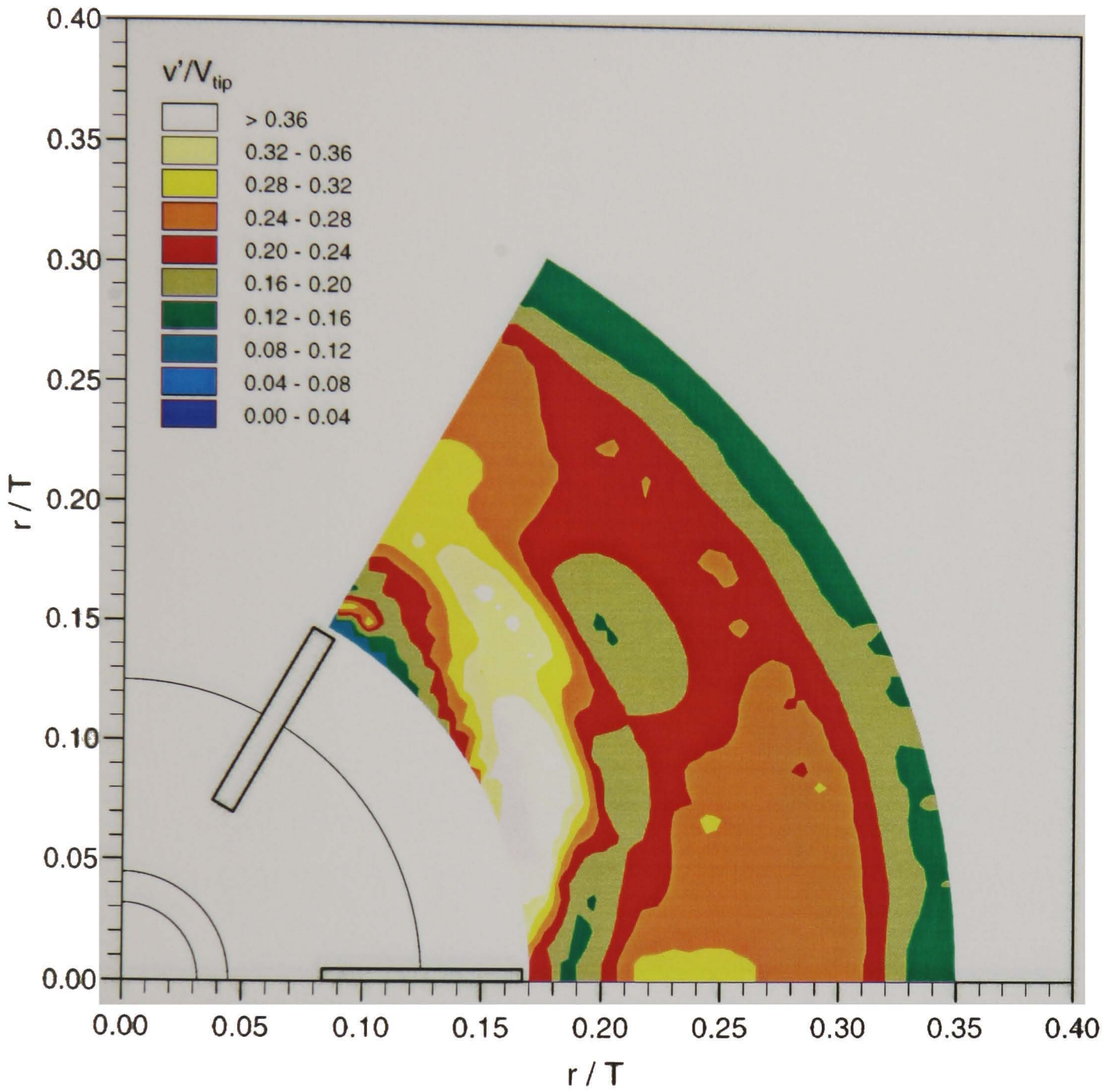


**Figure 4.8** Single Rushton impeller configuration: radial turbulence level contours in the z/T = 0.33 plane.

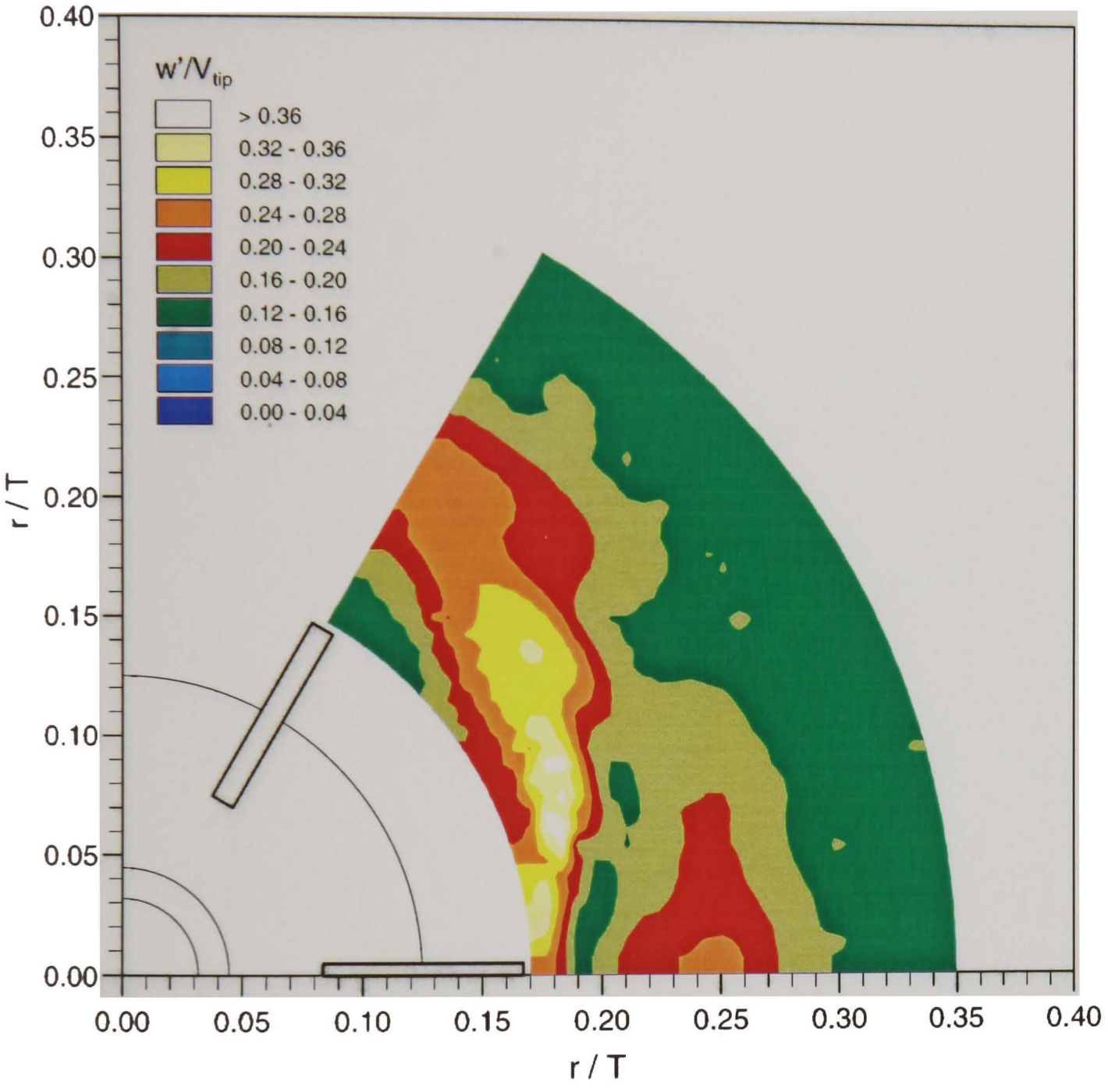


**Figure 4.9** Single Rushton impeller configuration: tangential turbulence level contours in the z/T = 0.33 plane.

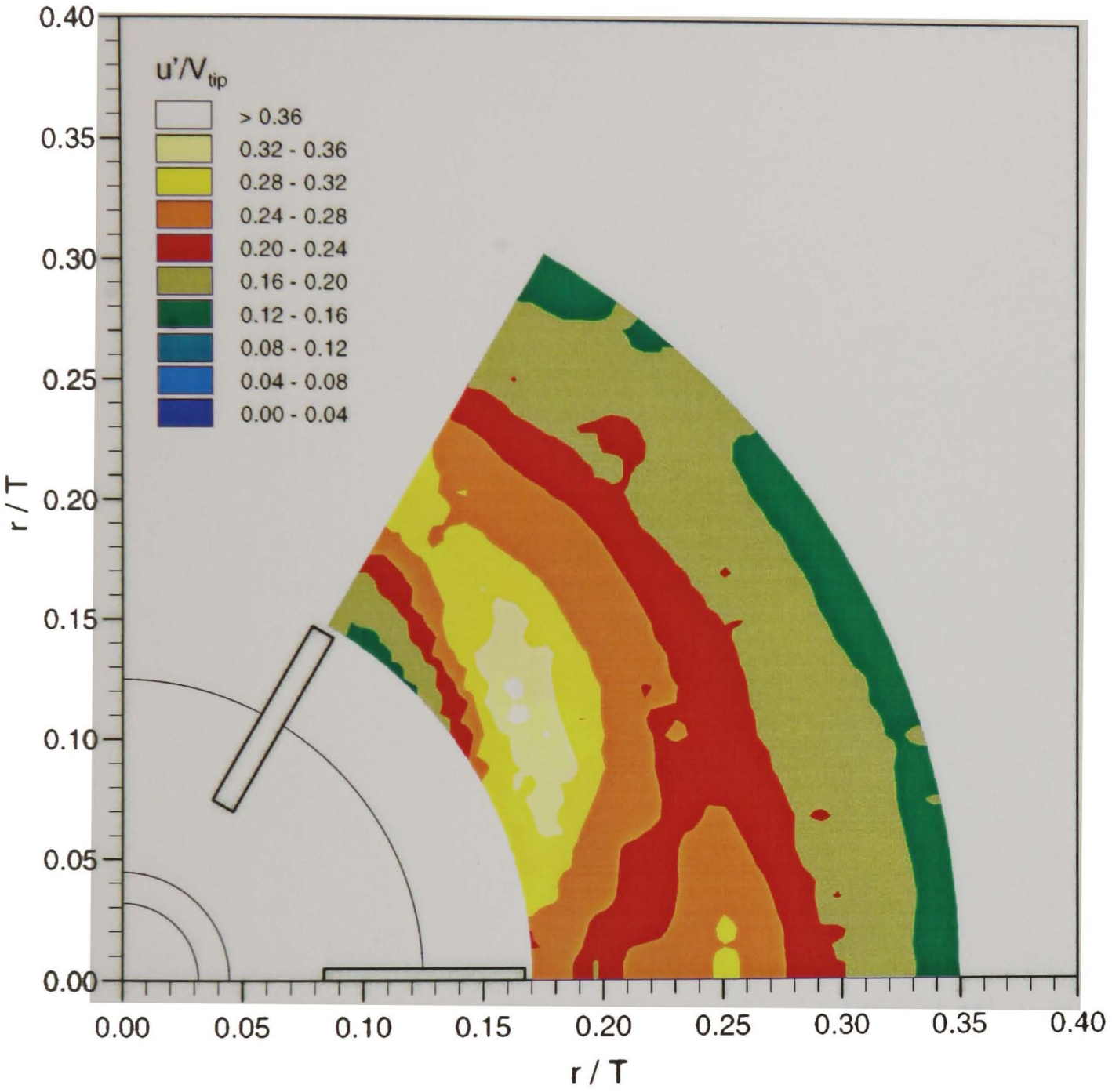


**Figure 4.10** Single Rushton impeller configuration: axial turbulence level contours in the z/T = 0.35 plane.

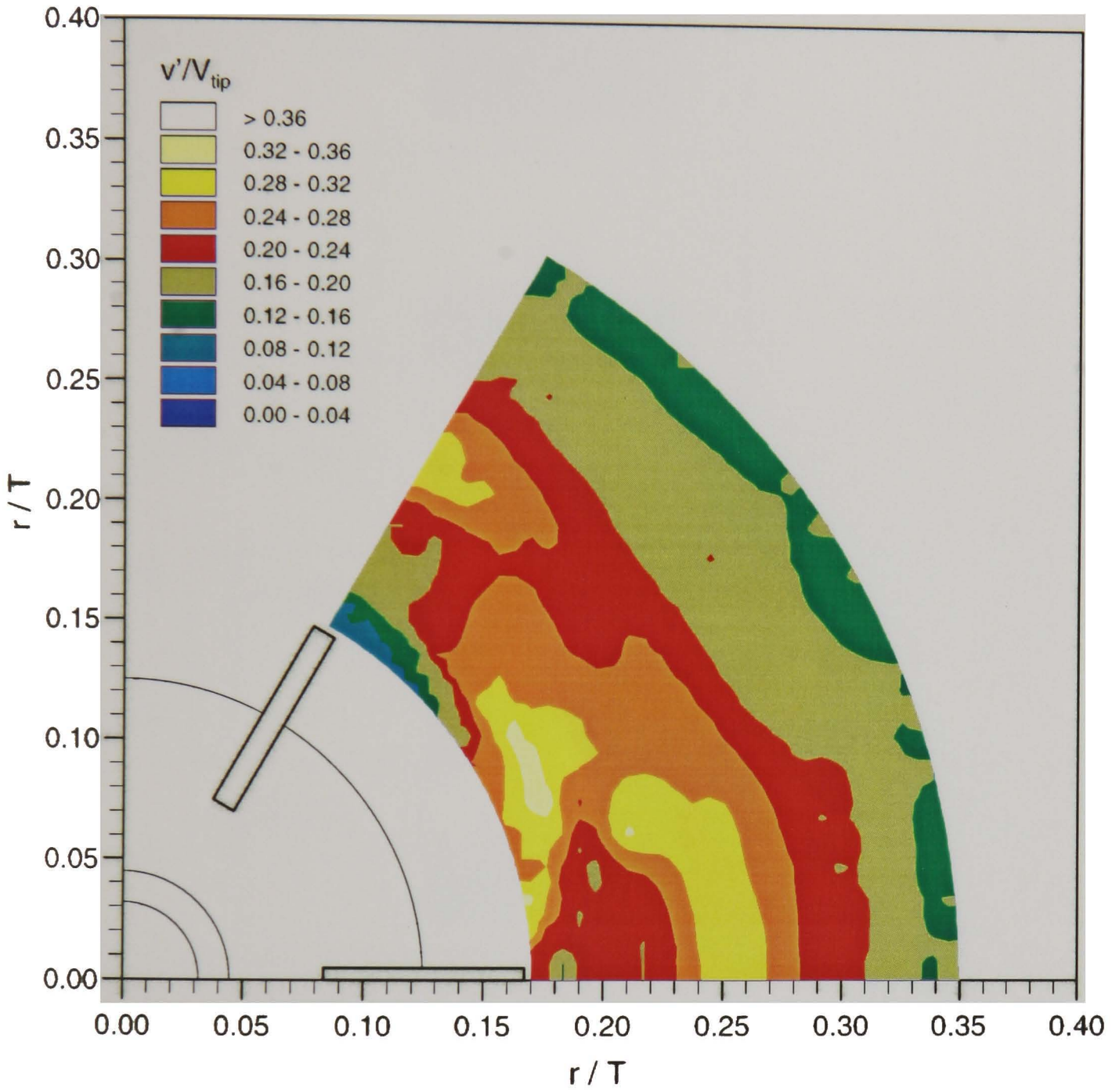


**Figure 4.11** Single Rushton impeller configuration: radial turbulence level contours in the z/T = 0.35 plane.

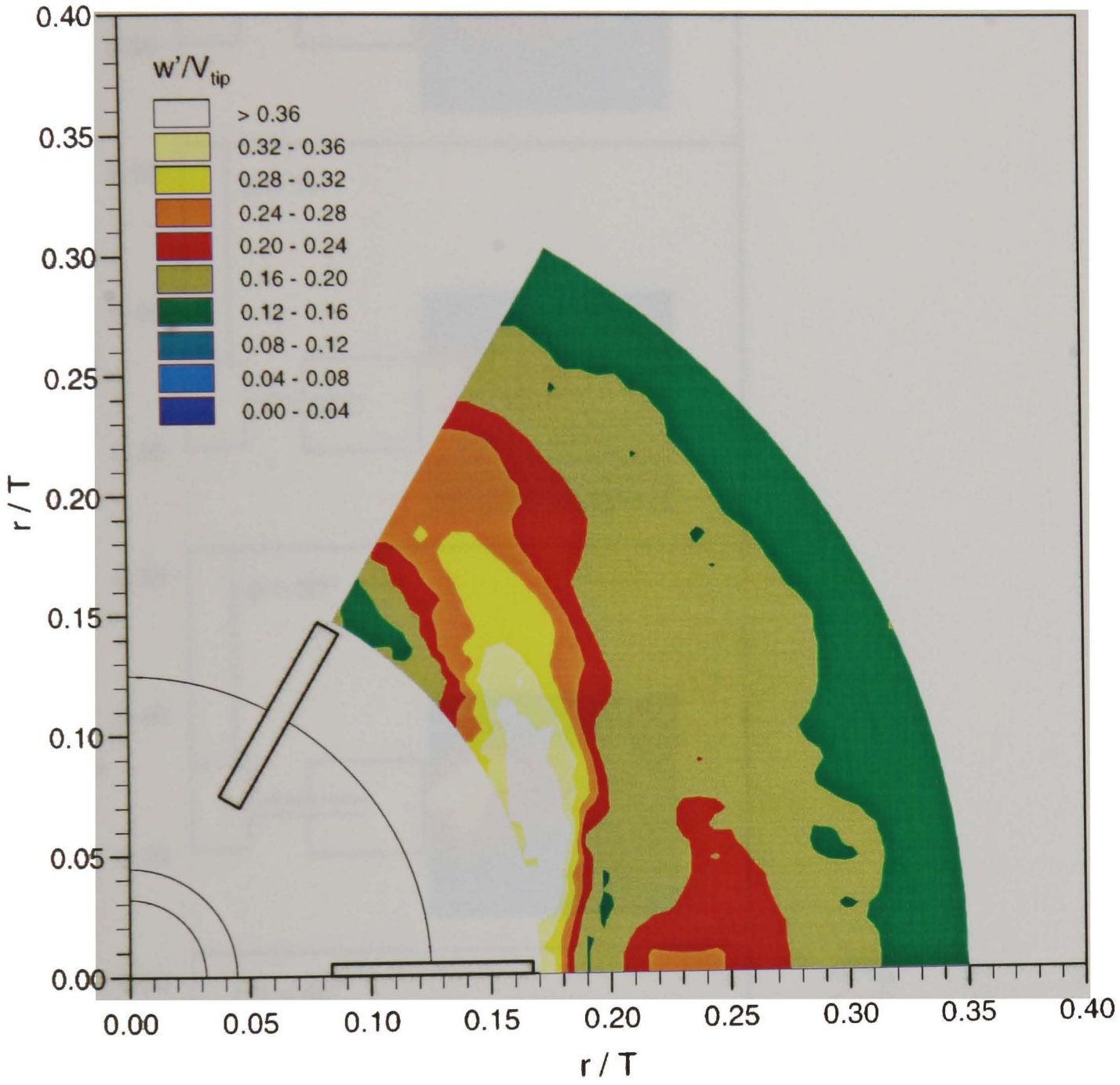


**Figure 4.12** Single Rushton impeller configuration: tangential turbulence level contours in the z/T = 0.35 plane.

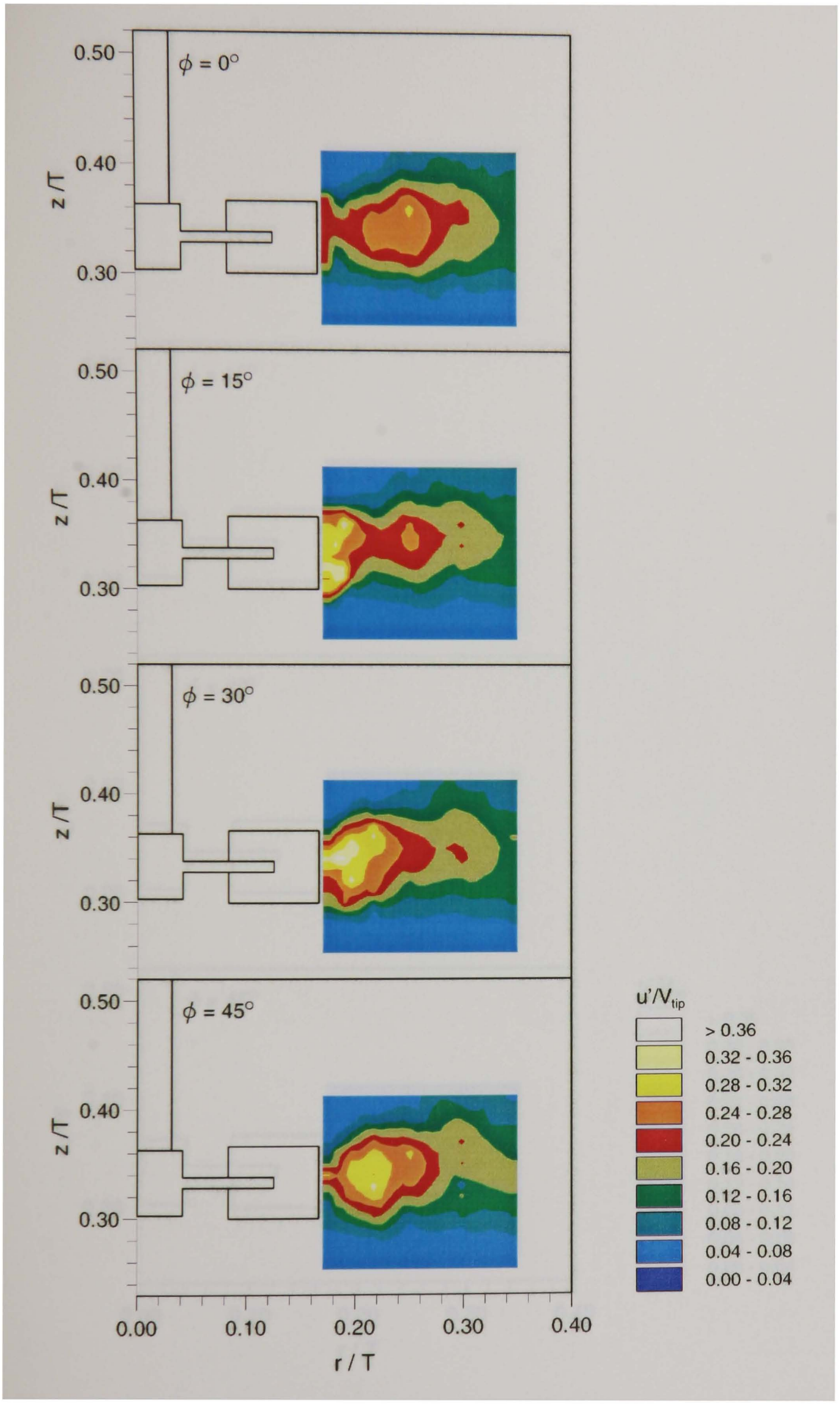


**Figure 4.13** Single Rushton impeller configuration: axial turbulence level contours in the $\phi = 0°$, 15°, 30° and 45° planes.

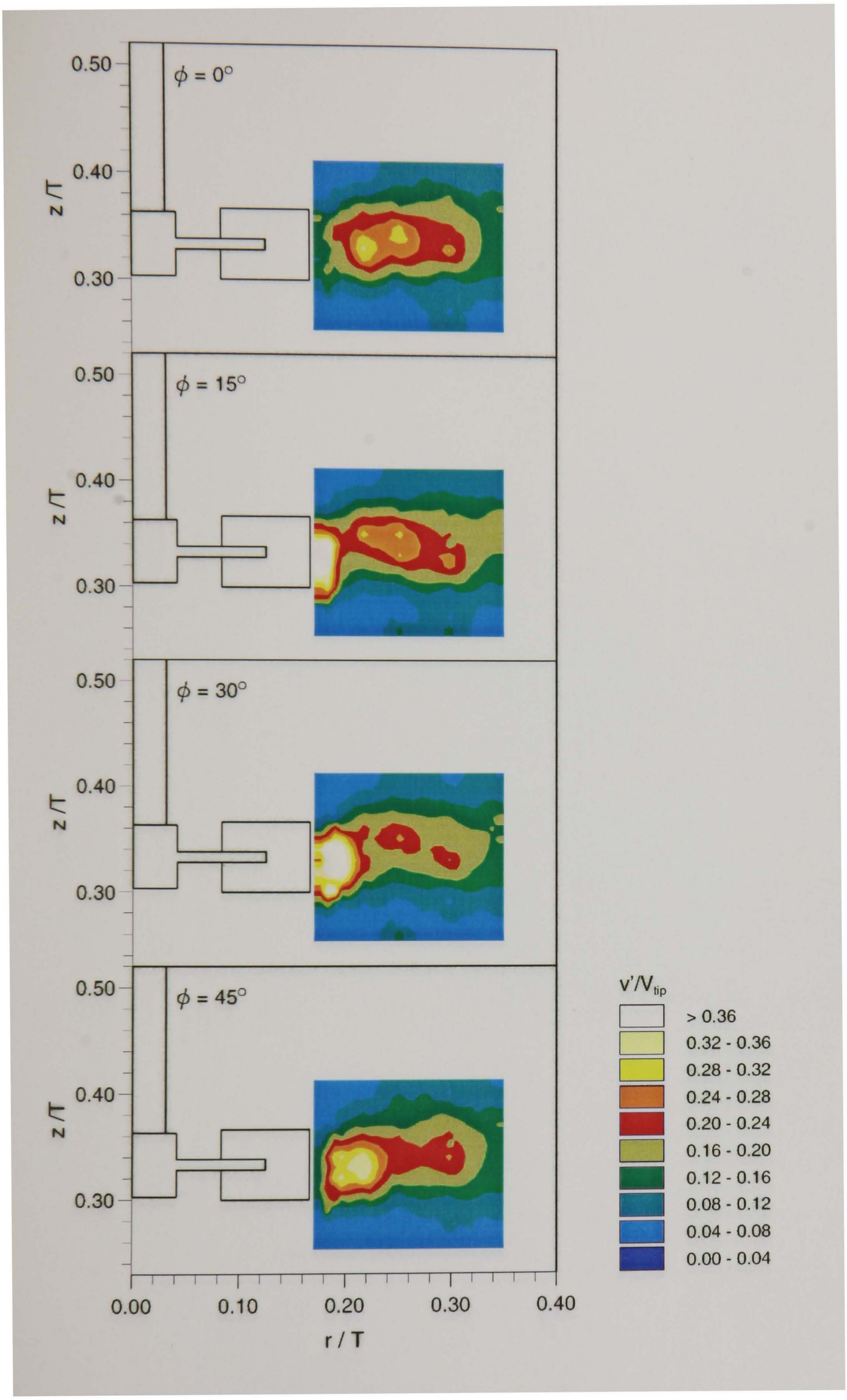


**Figure 4.14** Single Rushton impeller configuration: radial turbulence level contours in the $\phi = 0°$, 15°, 30° and 45° planes.

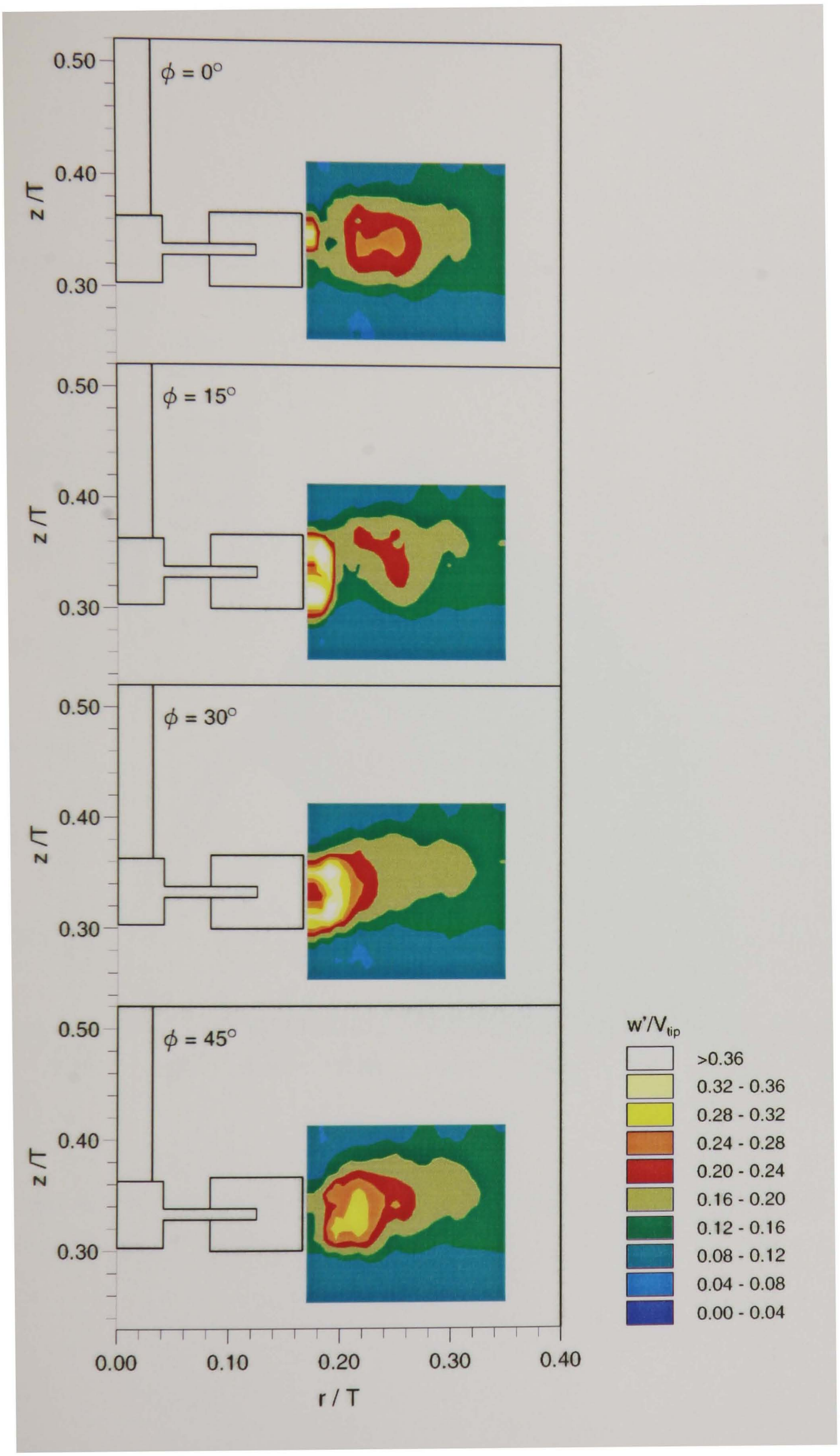


**Figure 4.15** Single Rushton impeller configuration: tangential turbulence level contours in the $\phi = 0°$, 15°, 30° and 45° planes.

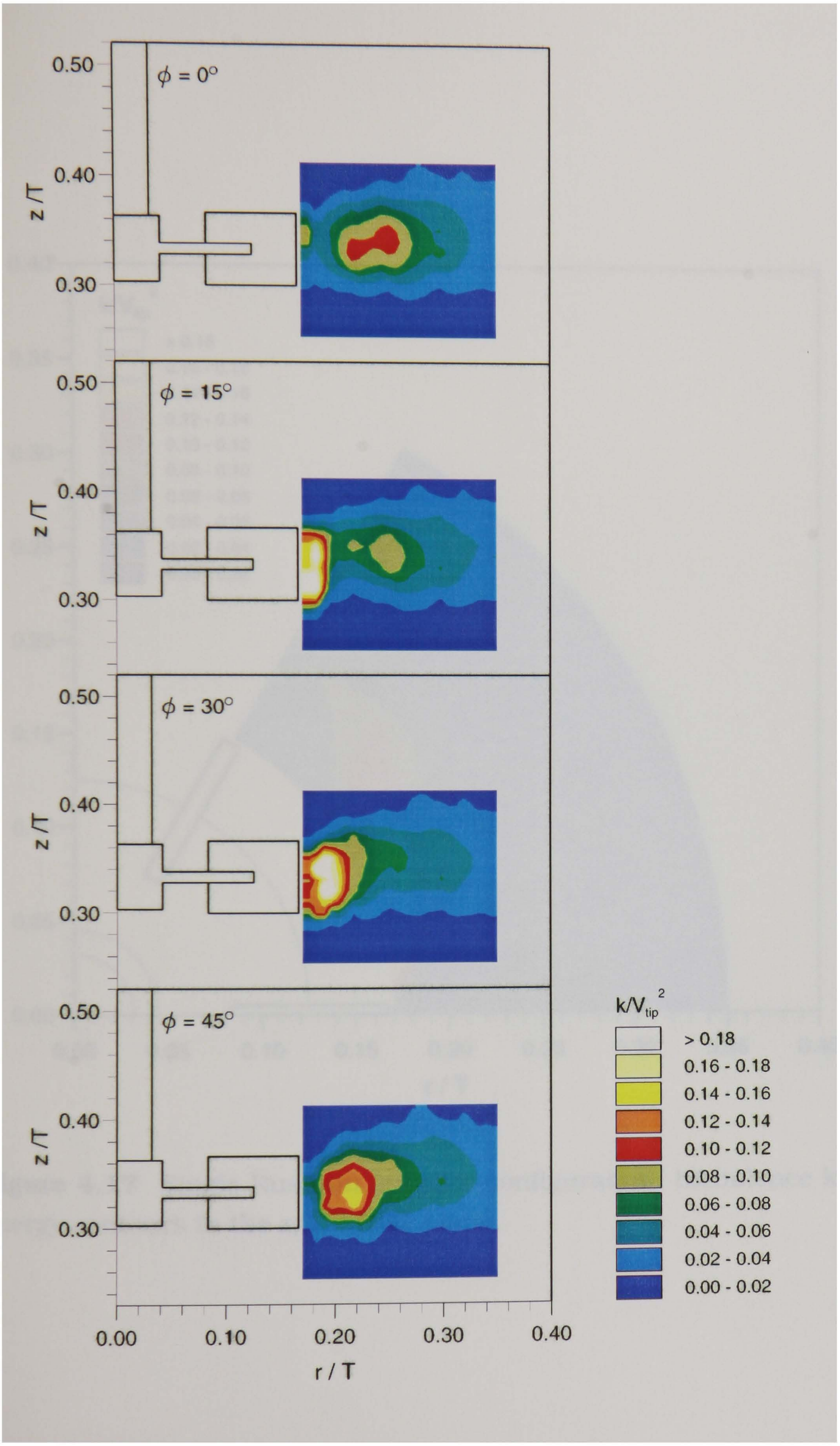


**Figure 4.16** Single Rushton impeller configuration: turbulence kinetic energy contours in the $\phi$= 0°, 15°, 30° and 45° planes.

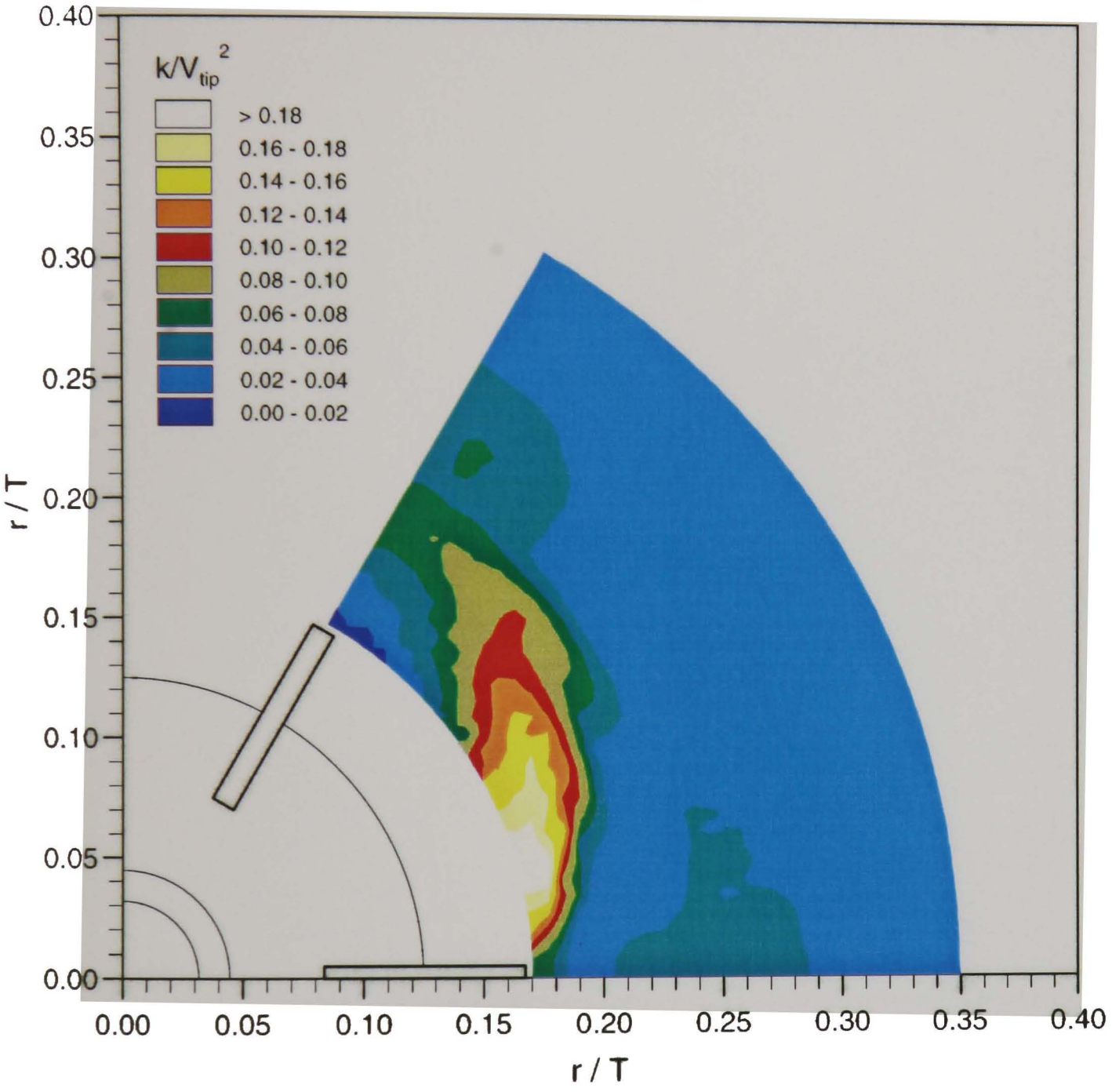


**Figure 4.17** Single Rushton impeller configuration: turbulence kinetic energy contours in the z/T = 0.31 plane.

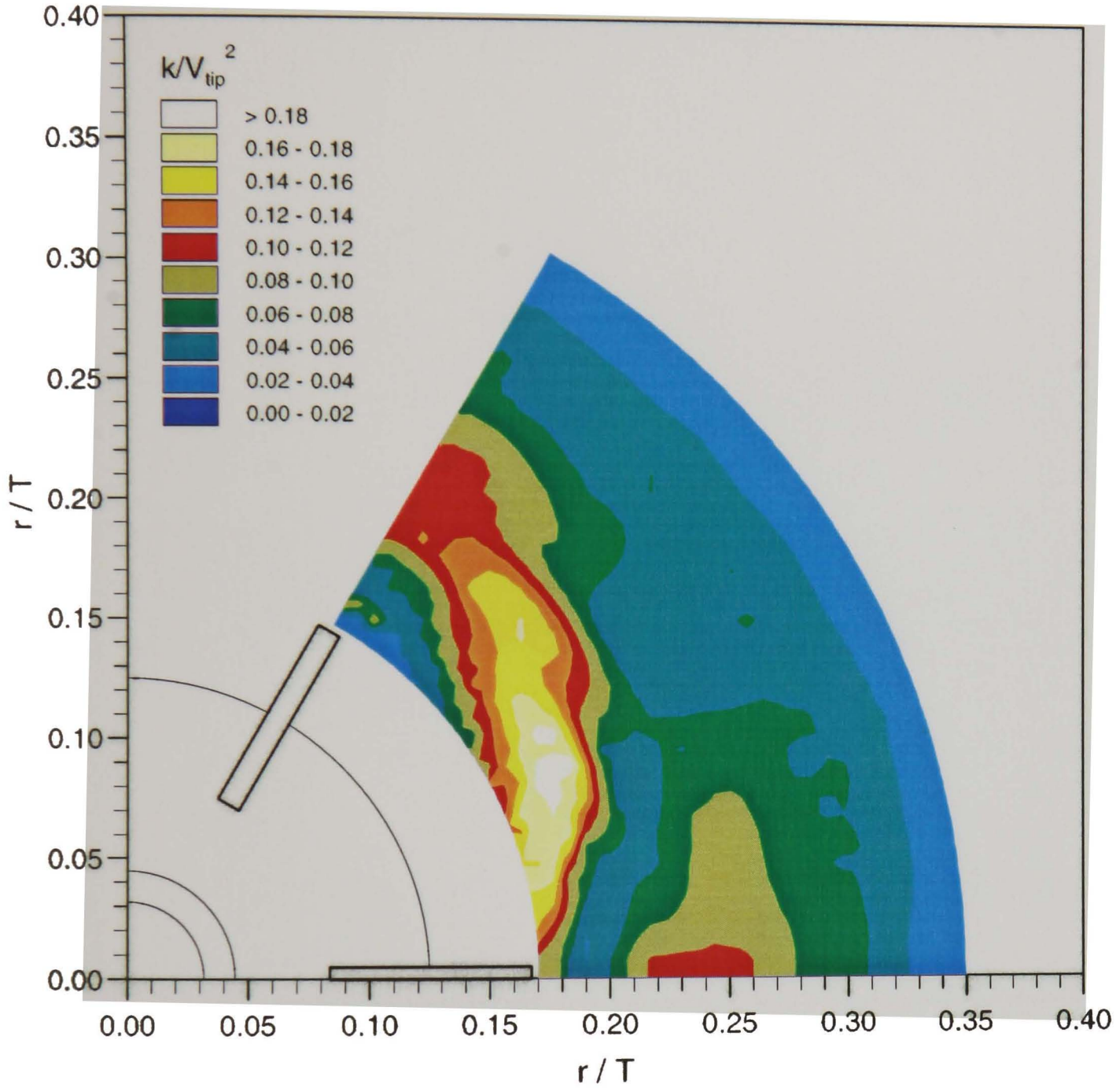


**Figure 4.18** Single Rushton impeller configuration: turbulence kinetic energy contours in the z/T = 0.33 plane.

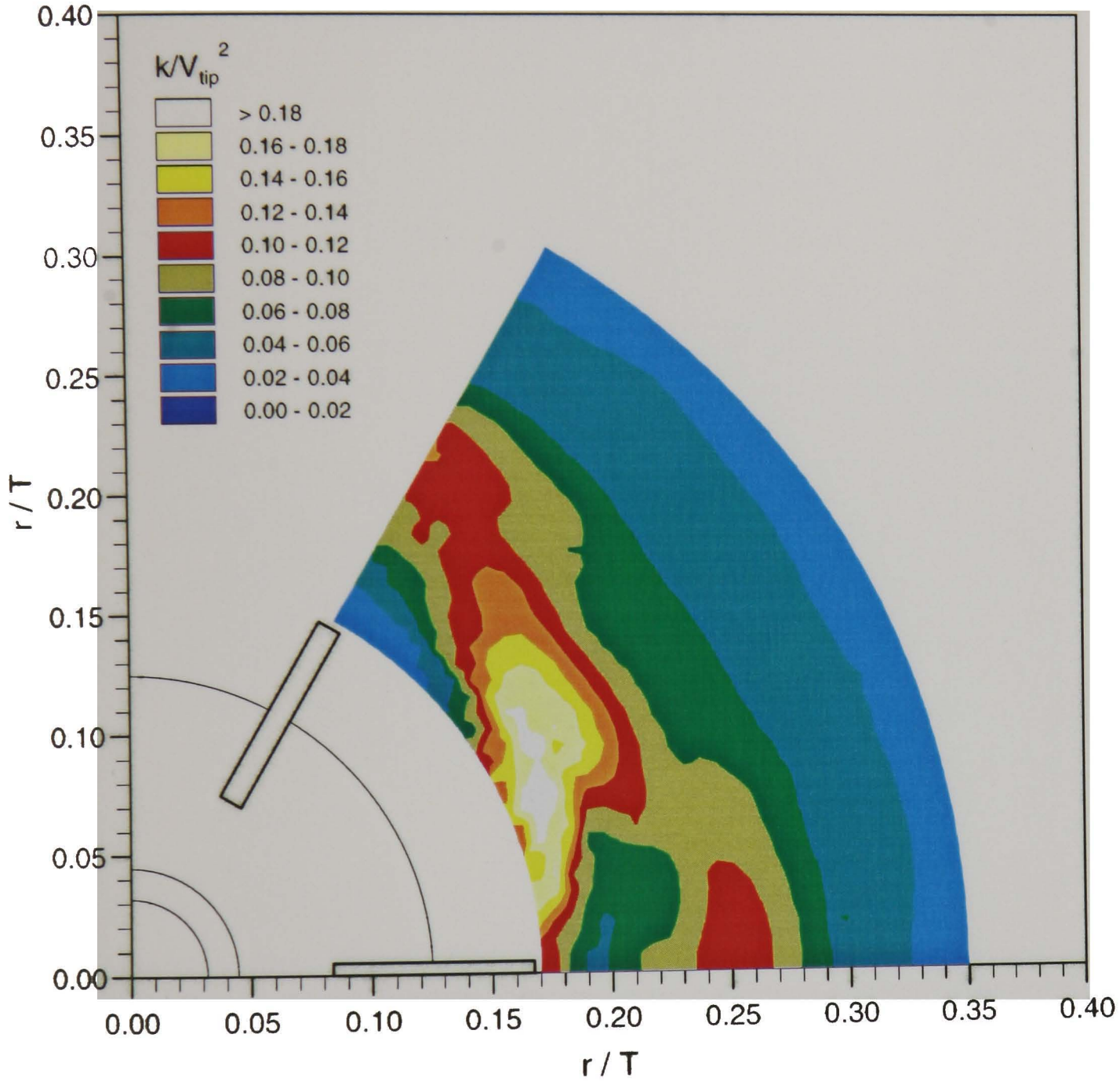


**Figure 4.19** Single Rushton impeller configuration: turbulence kinetic energy contours in the z/T = 0.35 plane.

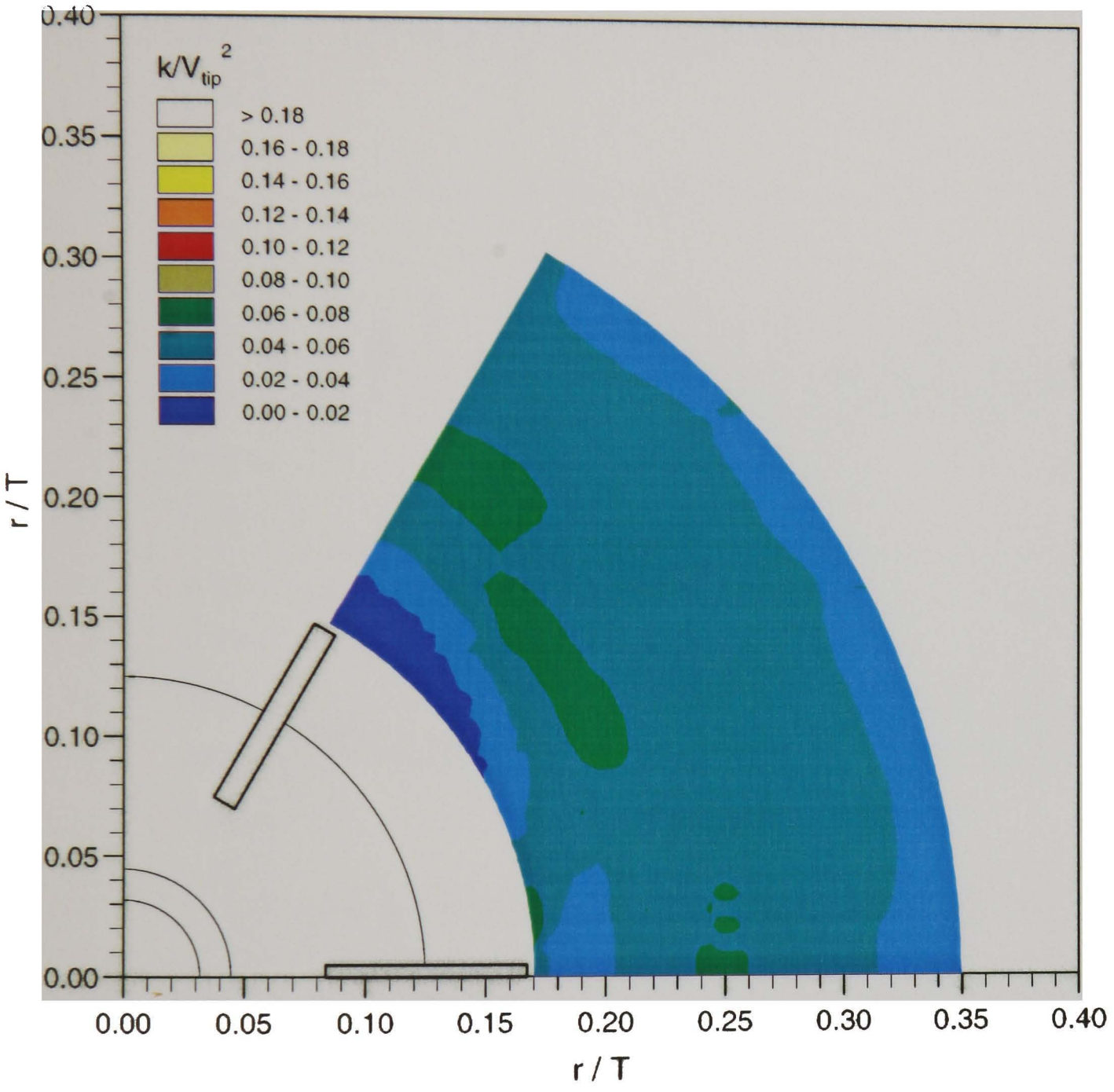


**Figure 4.20** Single Rushton impeller configuration: turbulence kinetic energy contours in the z/T = 0.37 plane.

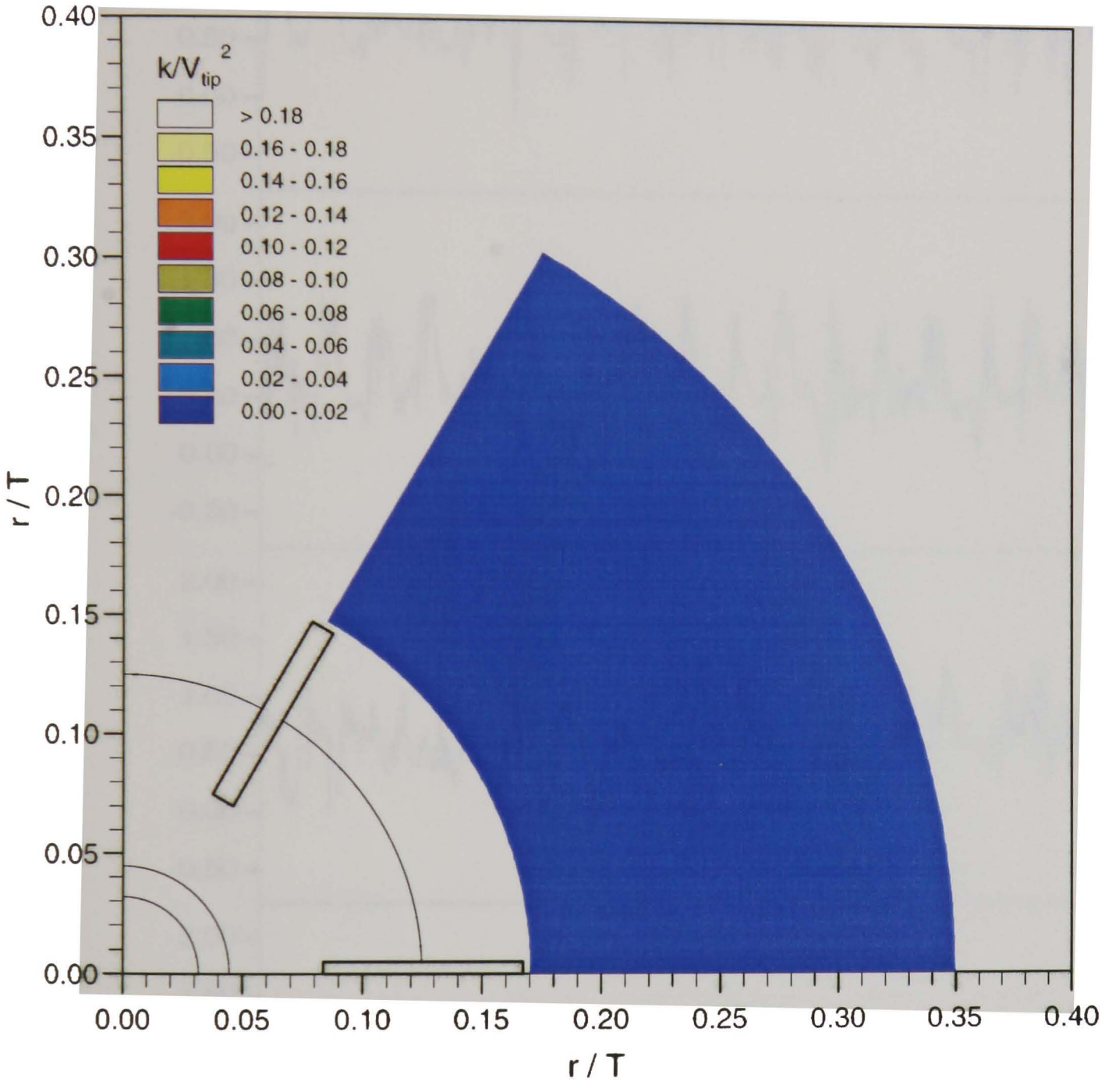


**Figure 4.21** Single Rushton impeller configuration: turbulence kinetic energy contours in the z/T = 0.41 plane.

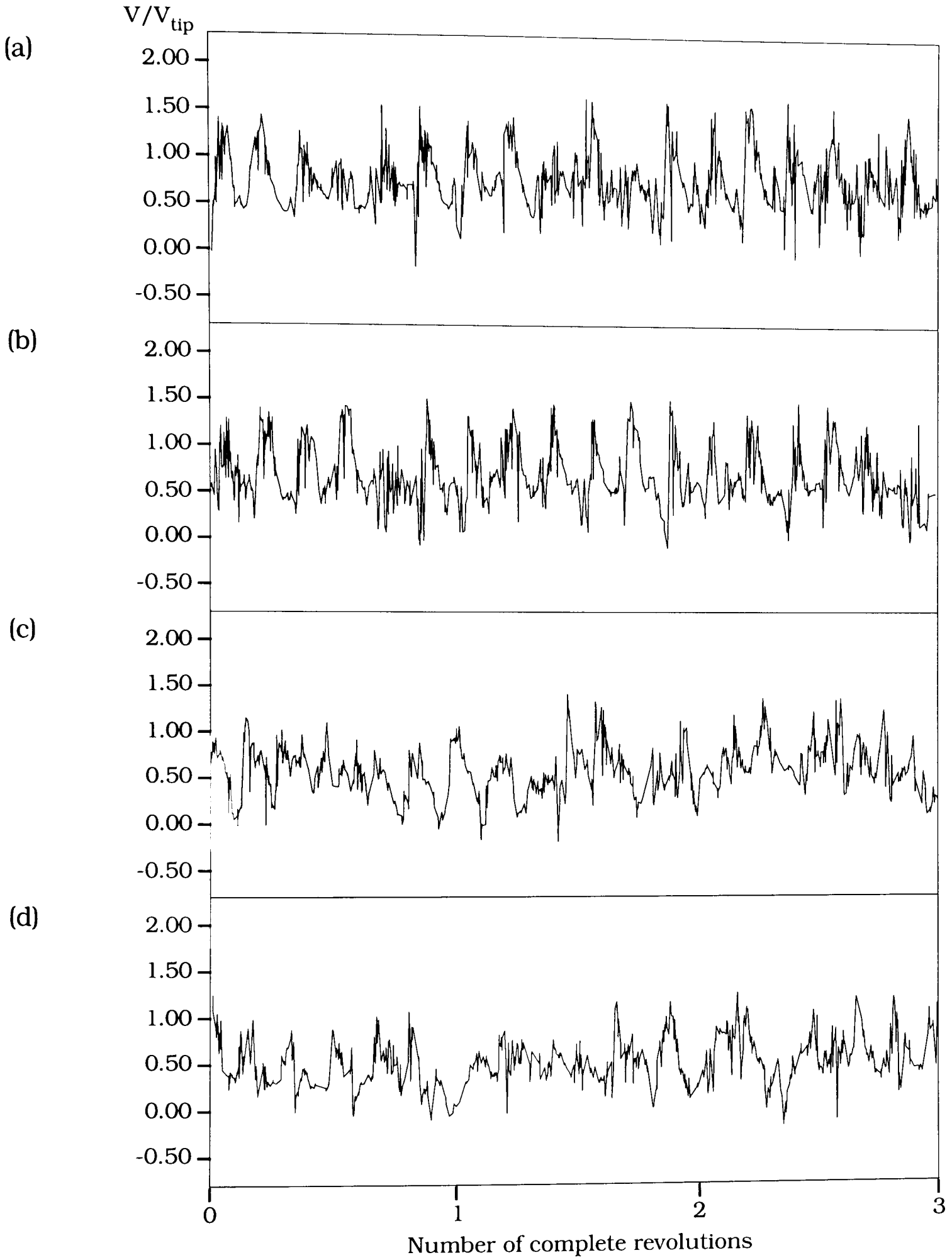


**Figure 4.22** Normalised instantaneous radial velocity recordings made in the z/T = 0.33 plane at (a) r/T = 0.17; (b) r/T = 0.18; (c) r/T = 0.22 and (d) r/T = 0.25.

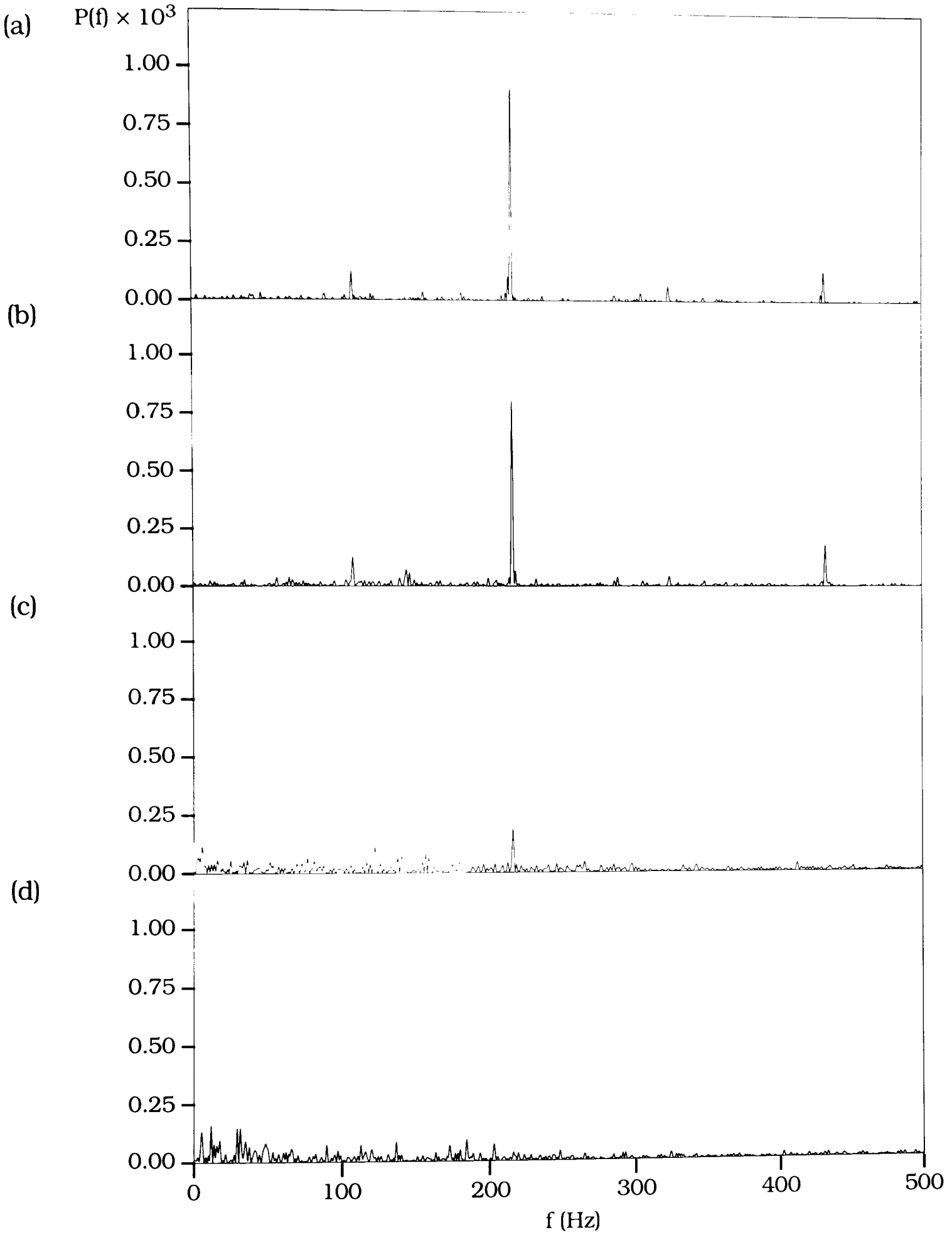


**Figure 4.23** Normalised energy spectra of the instantaneous radial velocity recordings made in the z/T = 0.33 plane at (a) r/T = 0.17; (b) r/T = 0.18; (c) r/T = 0.22 and (d) r/T = 0.25.

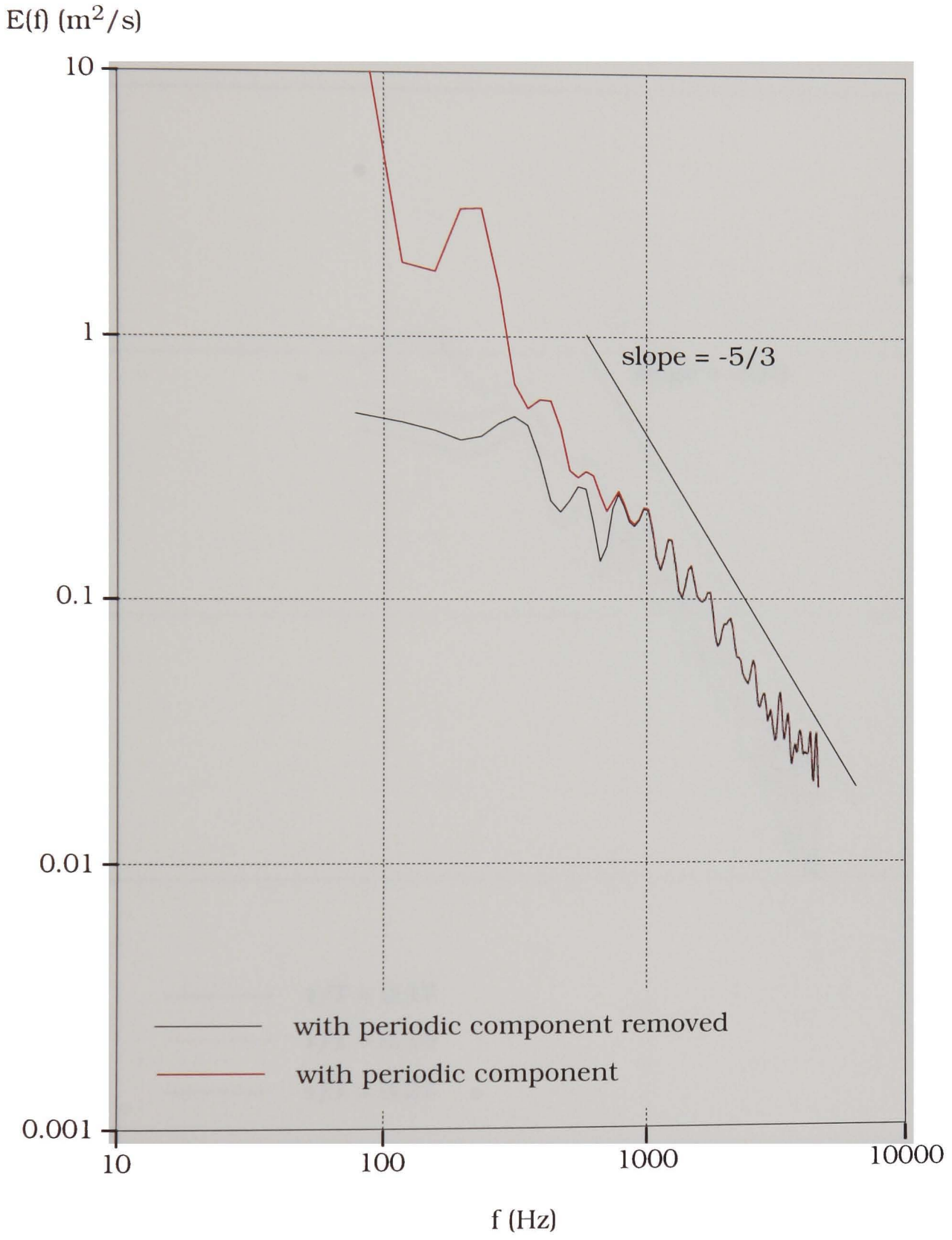


**Figure 4.24** Energy spectrum of the radial velocity fluctuations at r/T = 0.17, z/T = 0.33, with and without the periodic component.

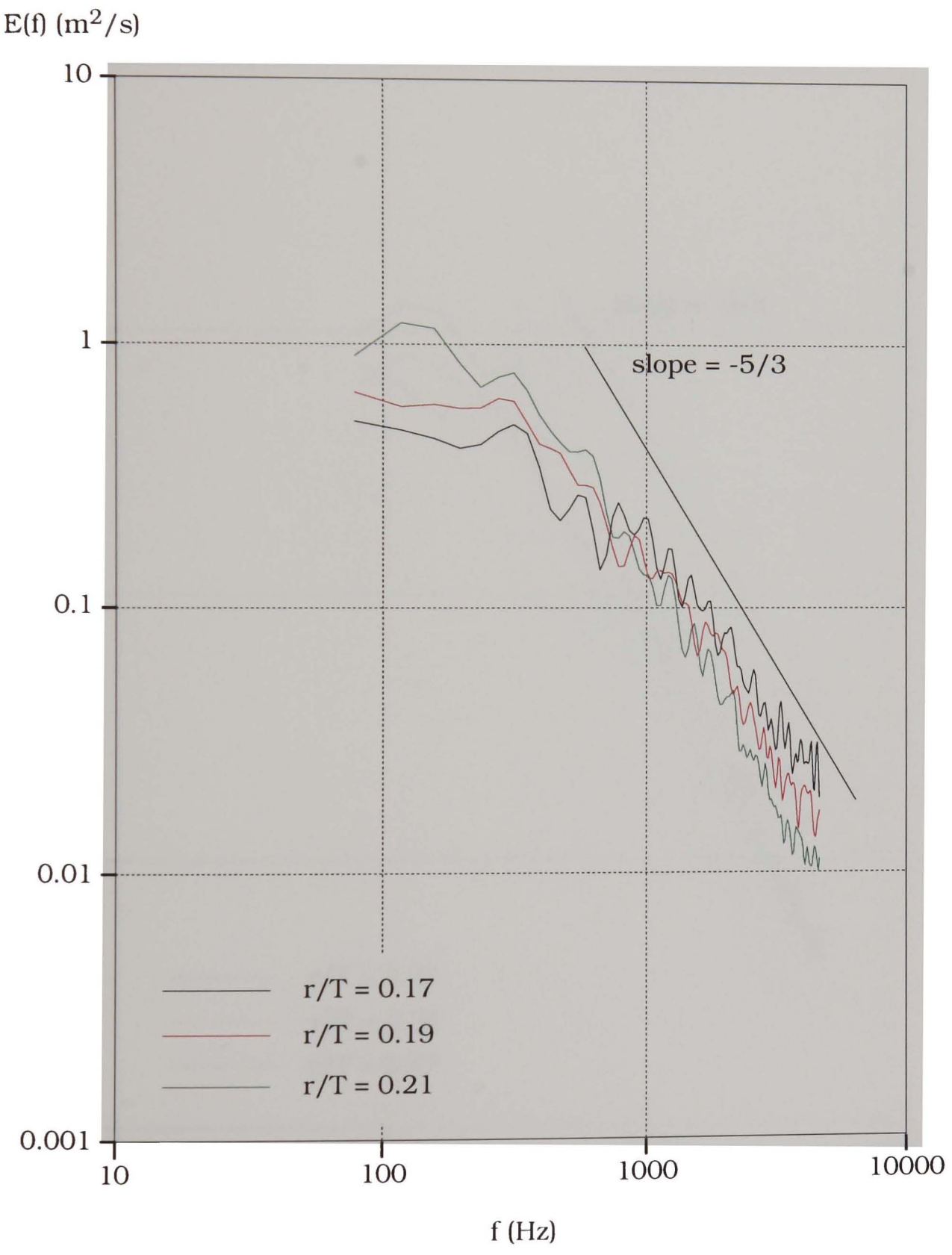


**Figure 4.25** Energy spectrum of the radial velocity (with the periodic component removed) at r/T = 0.17, 0.19 and 0.21, z/T = 0.33.

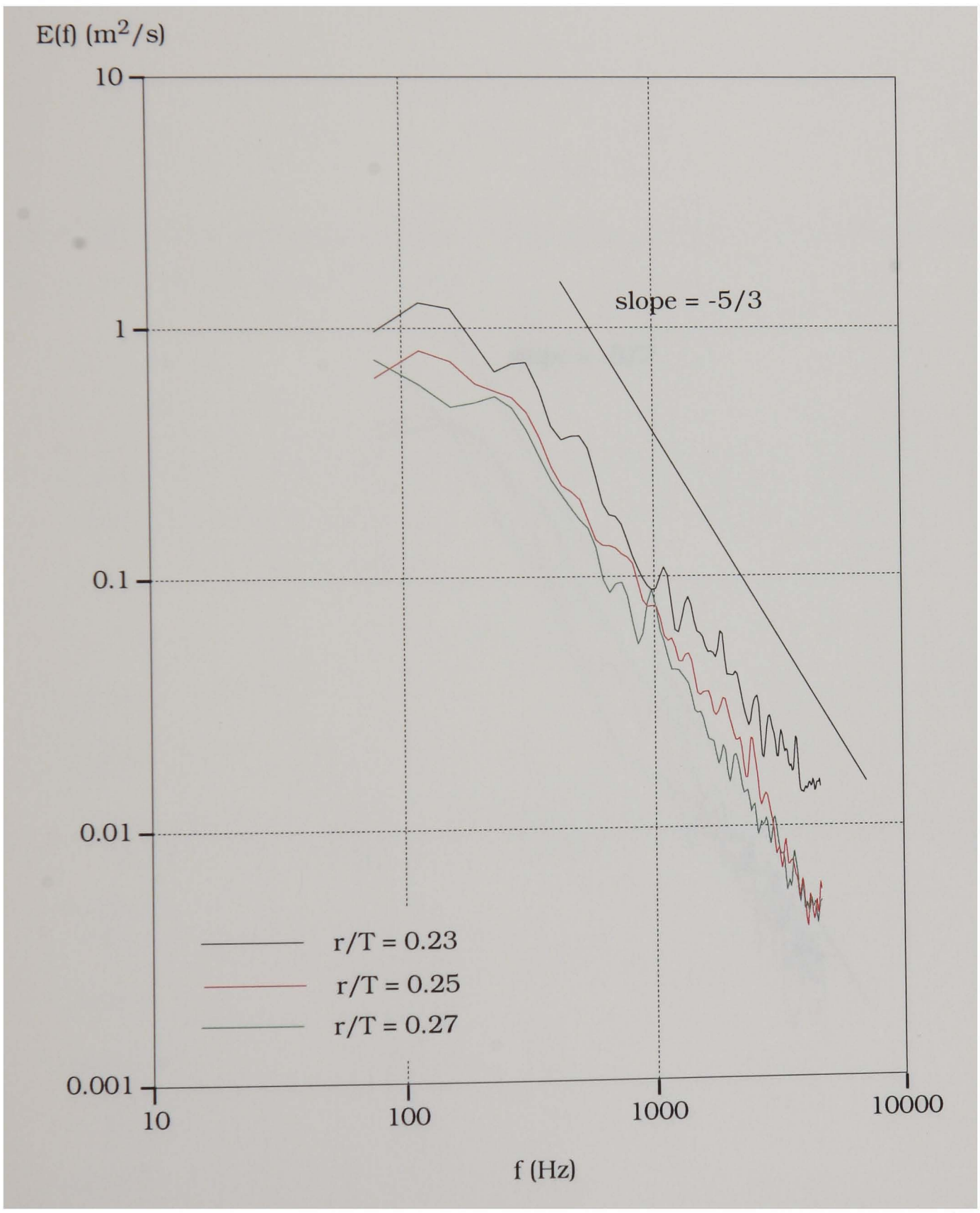


**Figure 4.26** Energy spectrum of the radial velocity (with the periodic component removed) at r/T = 0.23, 0.25 and 0.27, z/T = 0.33.

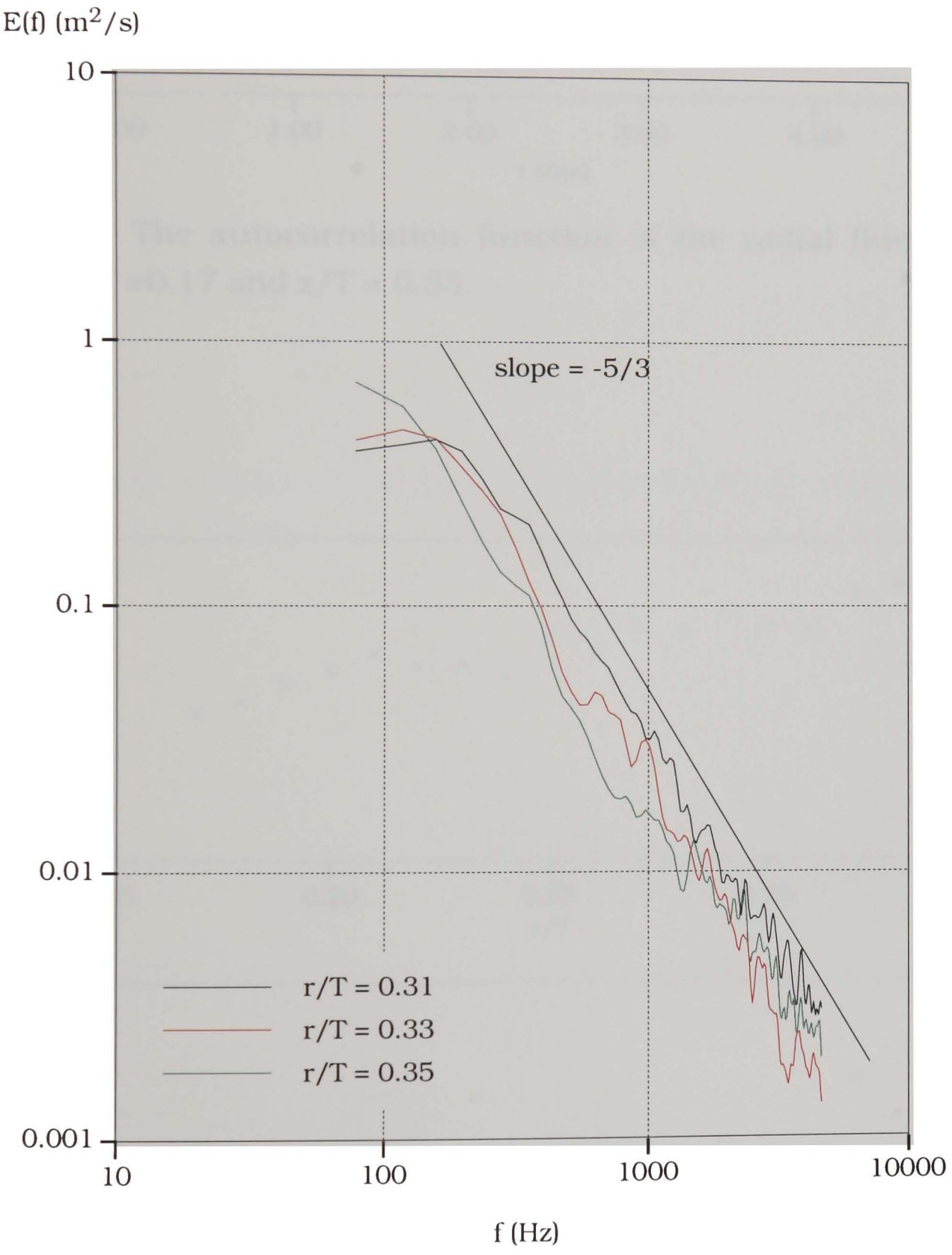


**Figure 4.27** Energy spectrum of the radial velocity (with the periodic component removed) at r/T = 0.31, 0.33 and 0.35, z/T = 0.33.

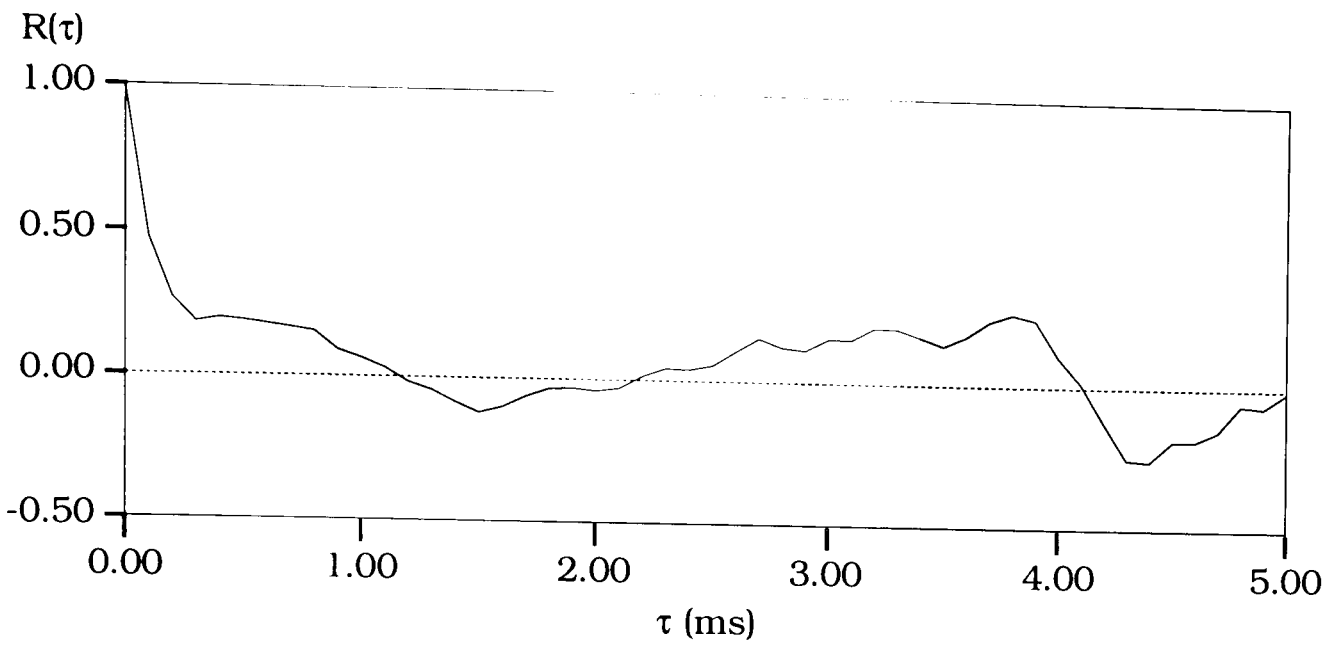


**Figure 4.28** The autocorrelation function of the radial fluctuating velocity at r/T =0.17 and z/T = 0.33.

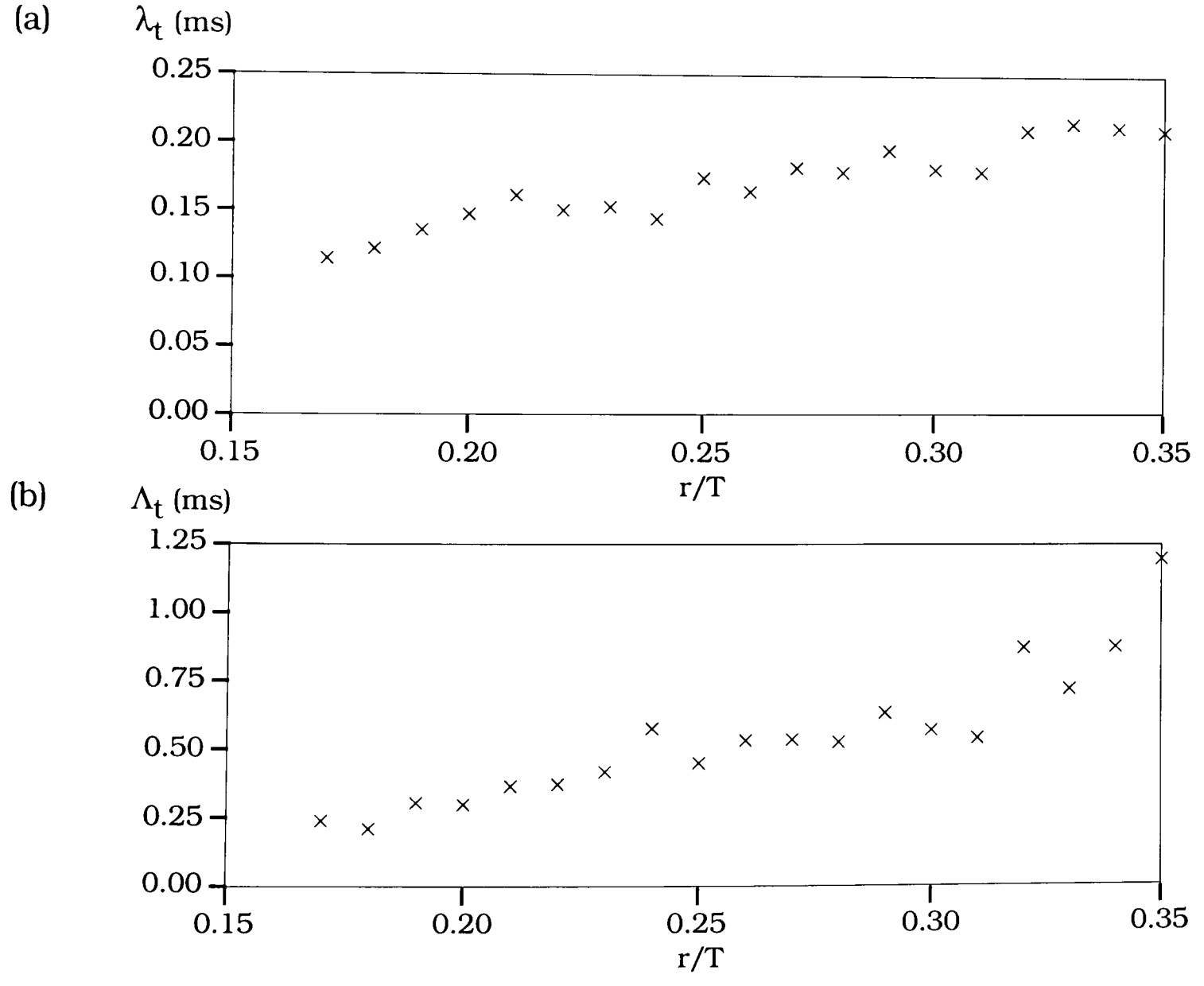


**Figure 4.29** The variation of (a) micro time scales; and (b) integral time scales; with r/T in the z/T = 0.33 plane.

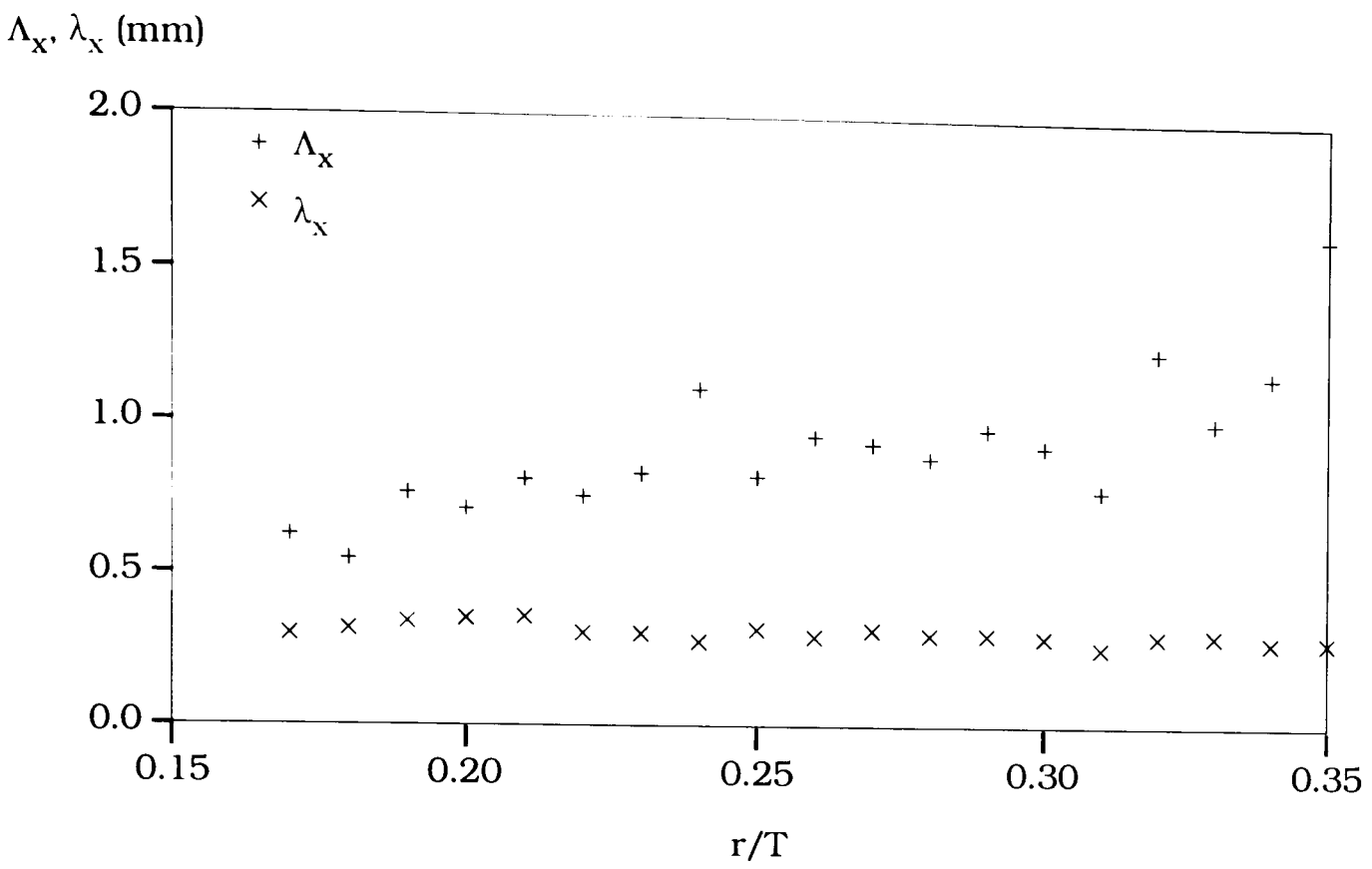


**Figure 4.30** The variation of the micro and integral length scales with r/T in the z/T = 0.33 plane.

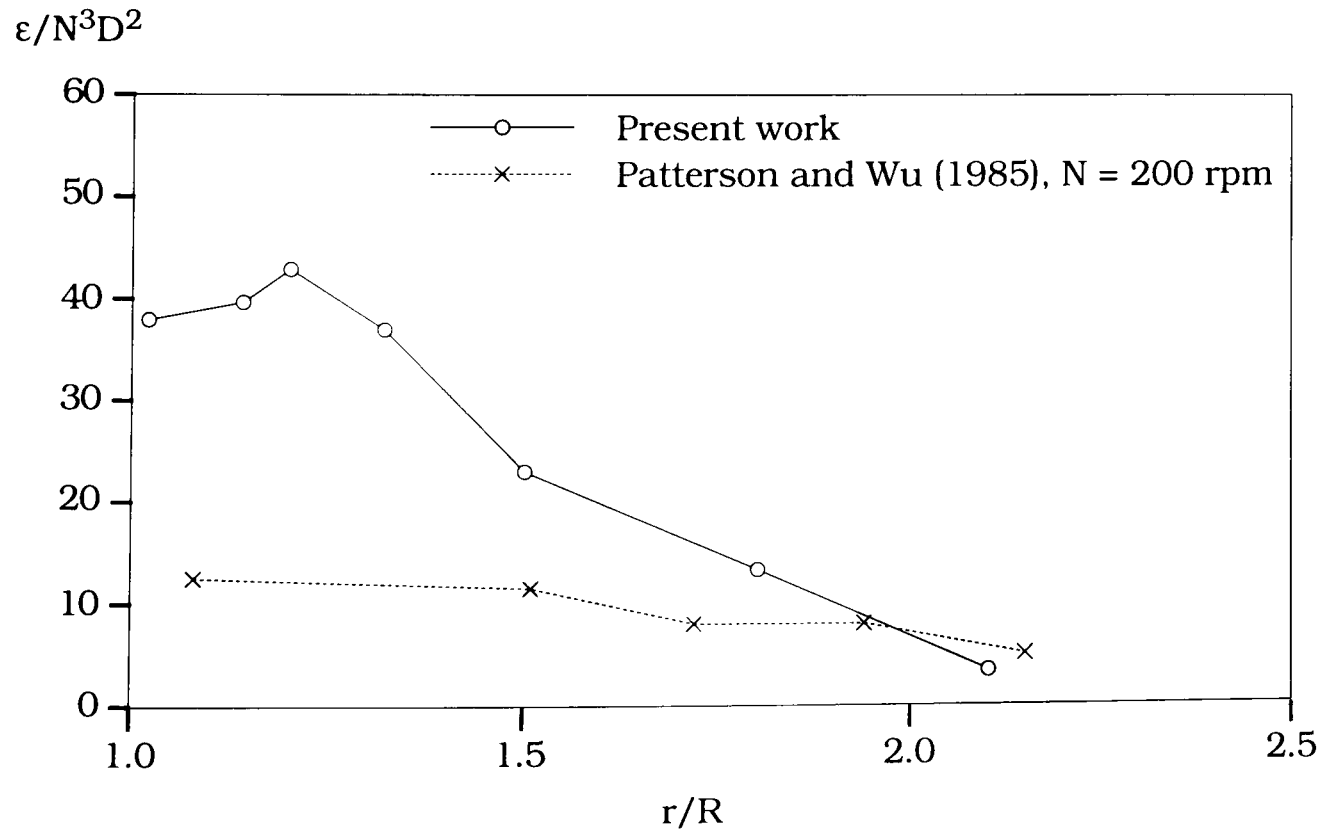


**Figure 4.31** Variation of the normalised rate of dissipation with r/R in the z/T = 0.33 plane.

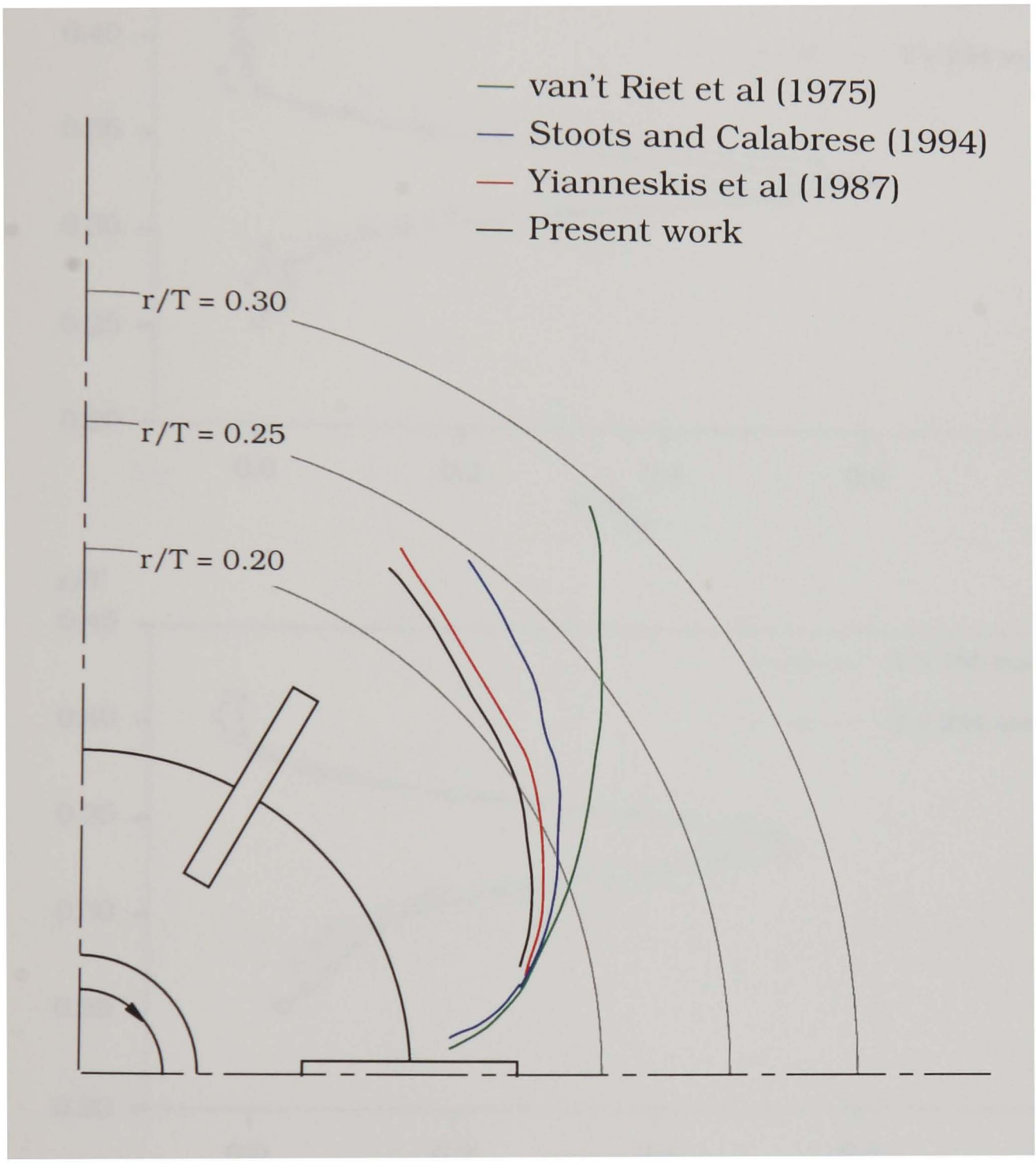


**Figure 4.32** Comparison of the axis of the trailing vortex shed from the Rushton impeller as viewed from above the vessel.

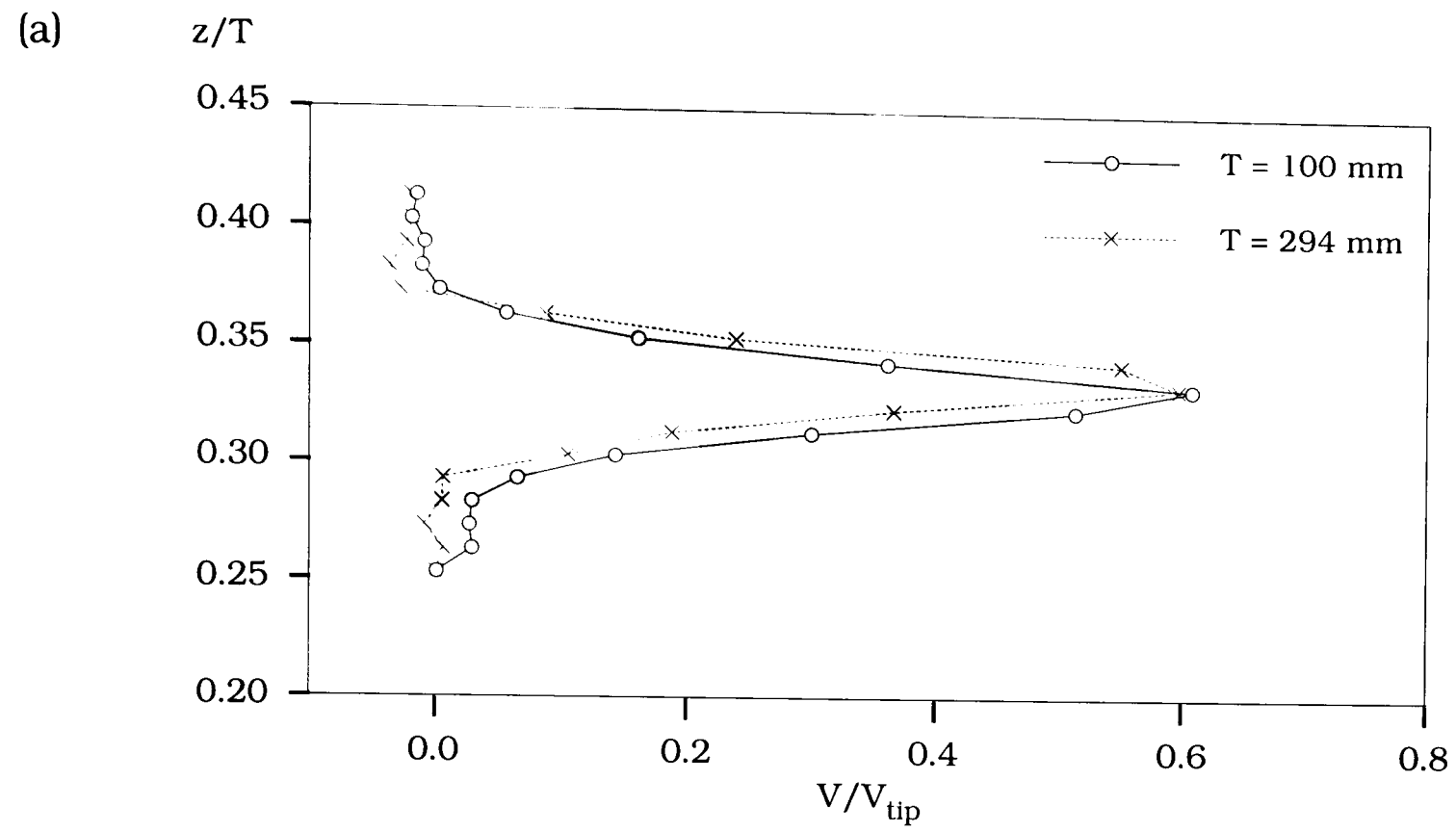


**Figure 4.33** Comparison of normalised radial mean velocity profiles obtained in the T = 100 mm and T = 294 mm vessels at (a) r/T = 0.17 and (b) r/T = 0.22.

(a)

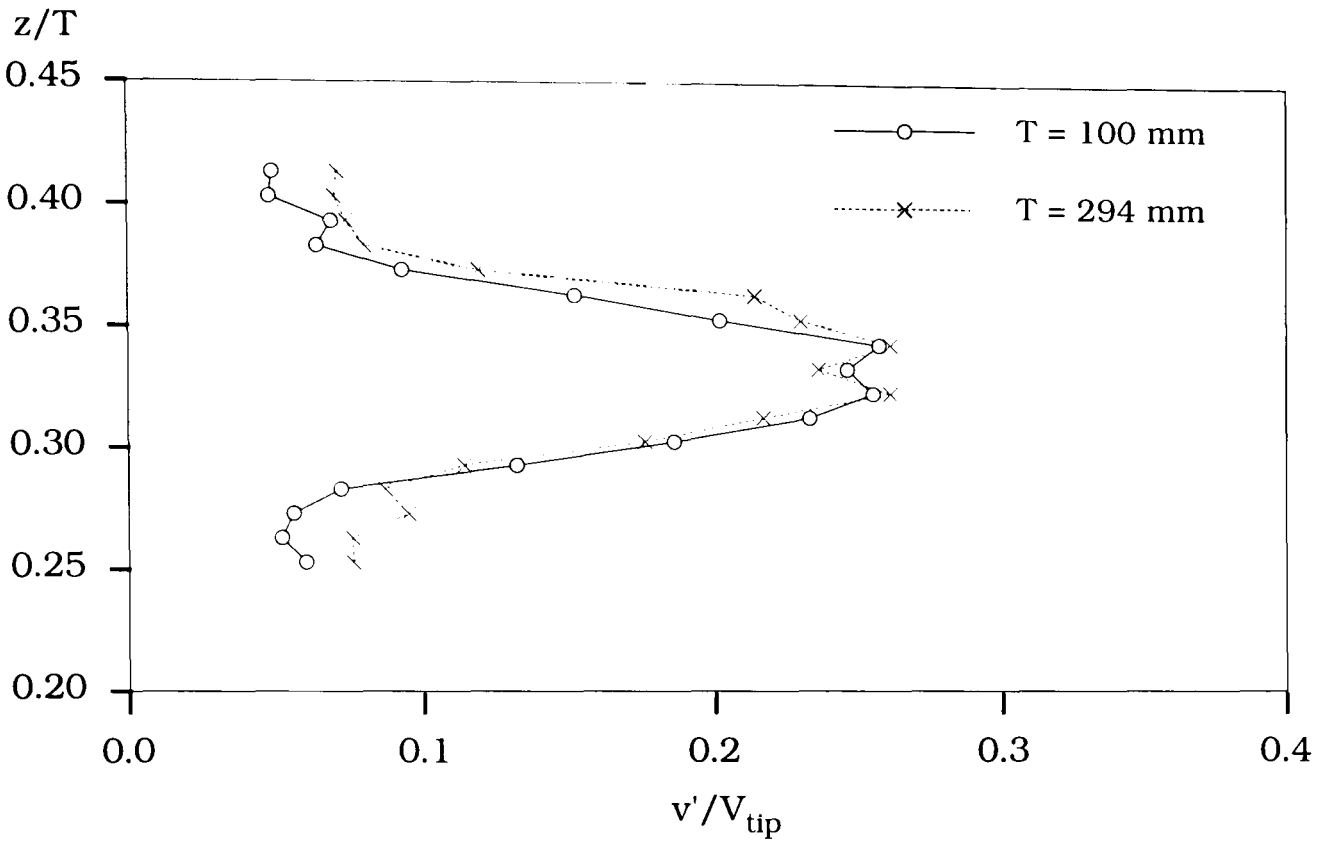


(b)

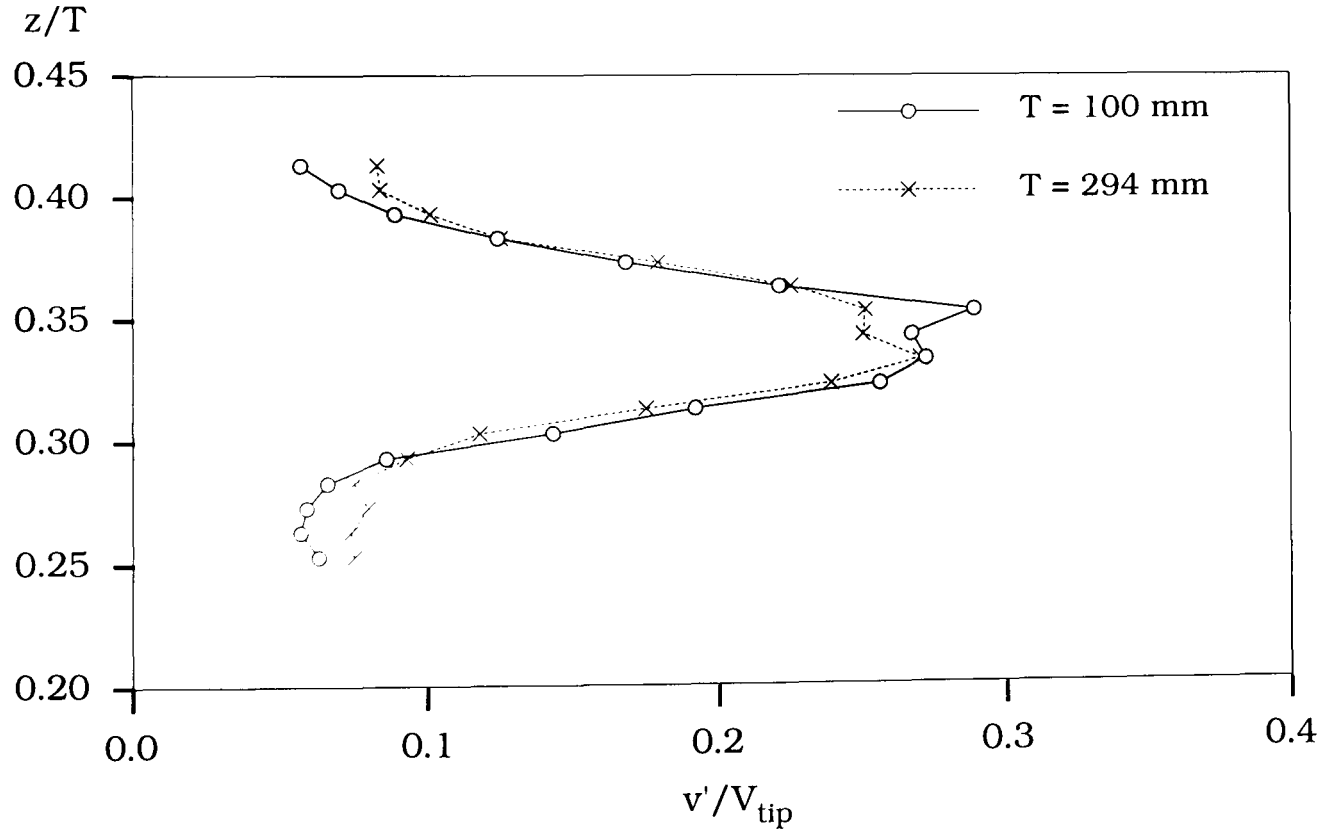


**Figure 4.34** Comparison of normalised radial turbulence level profiles obtained in the T = 100 mm and T = 294 mm vessels at (a) r/T = 0.17 and (b) r/T = 0.22.

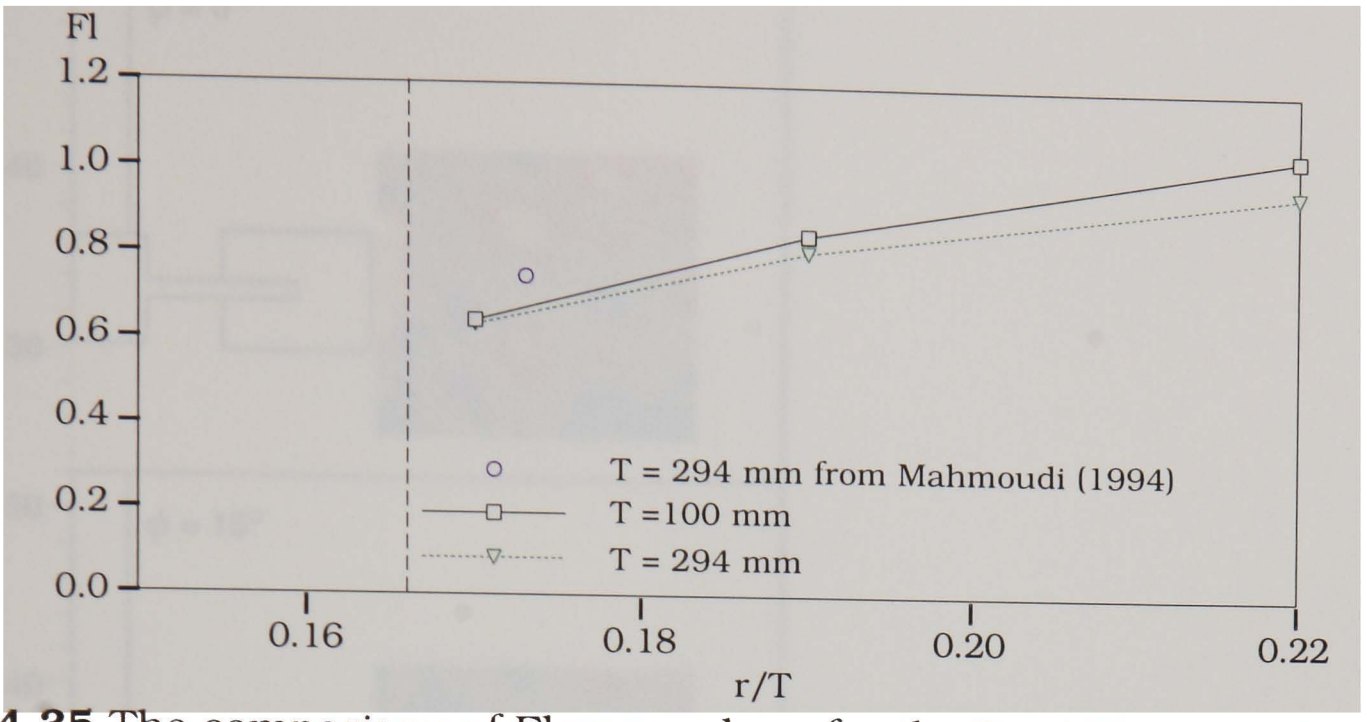


**Figure 4.35** The comparison of Flow numbers for the T = 100 mm and T = 294 mm vessels.

(a)

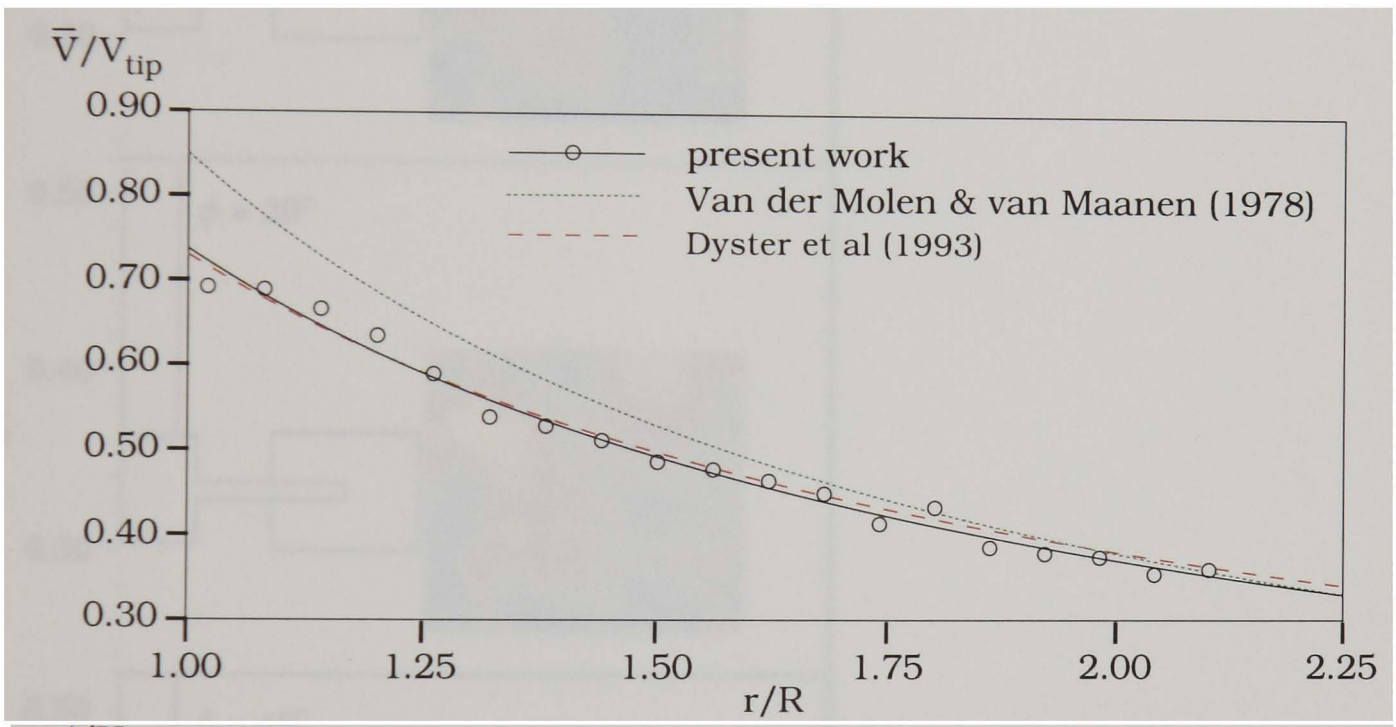


(b)

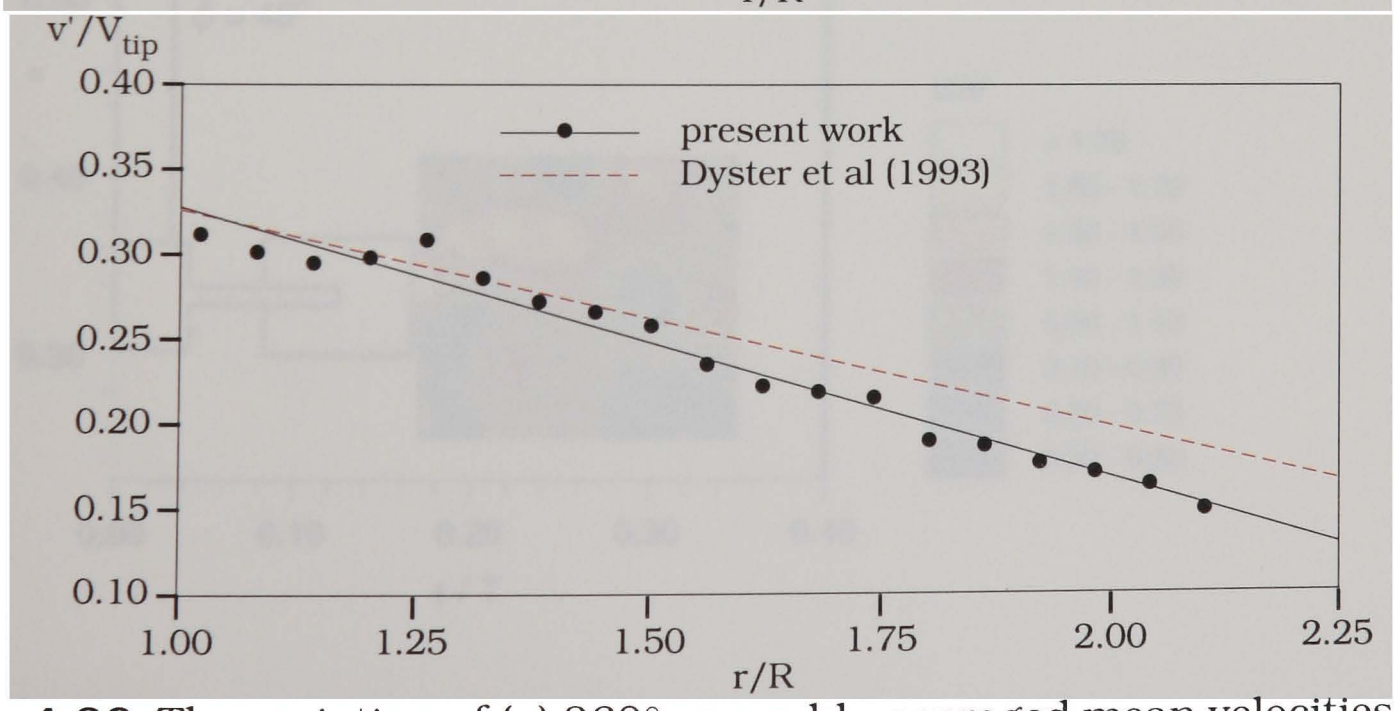


**Figure 4.36** The variation of (a) 360° ensemble-averaged mean velocities profile and (b) 360° ensemble-averaged turbulence velocities with r/R in the z/T = 0.33 plane.

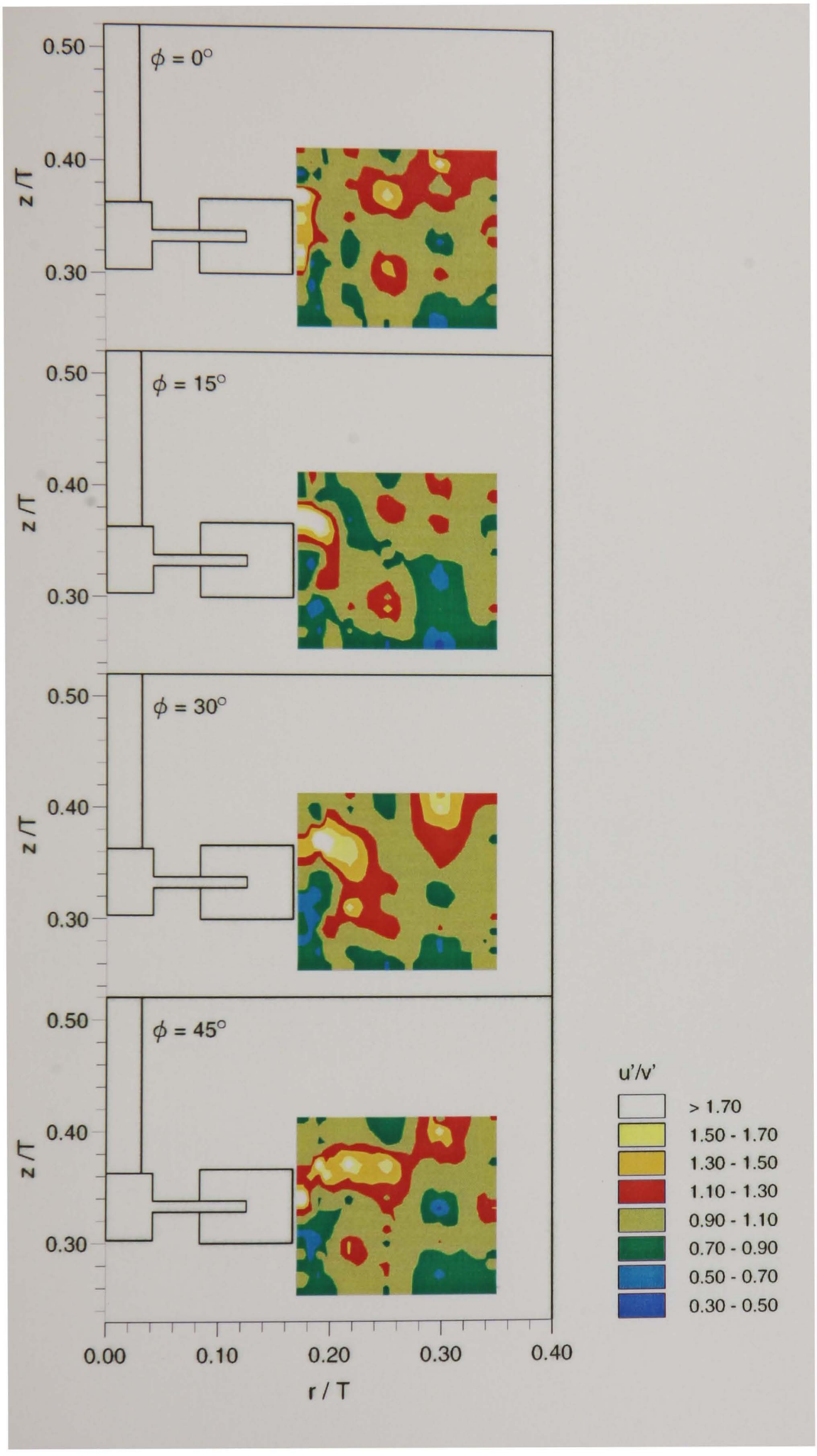


**Figure 4.37** Single Rushton configuration: u'/v' contours in the $\phi = 0°$, 15°, 30° and 45° planes.

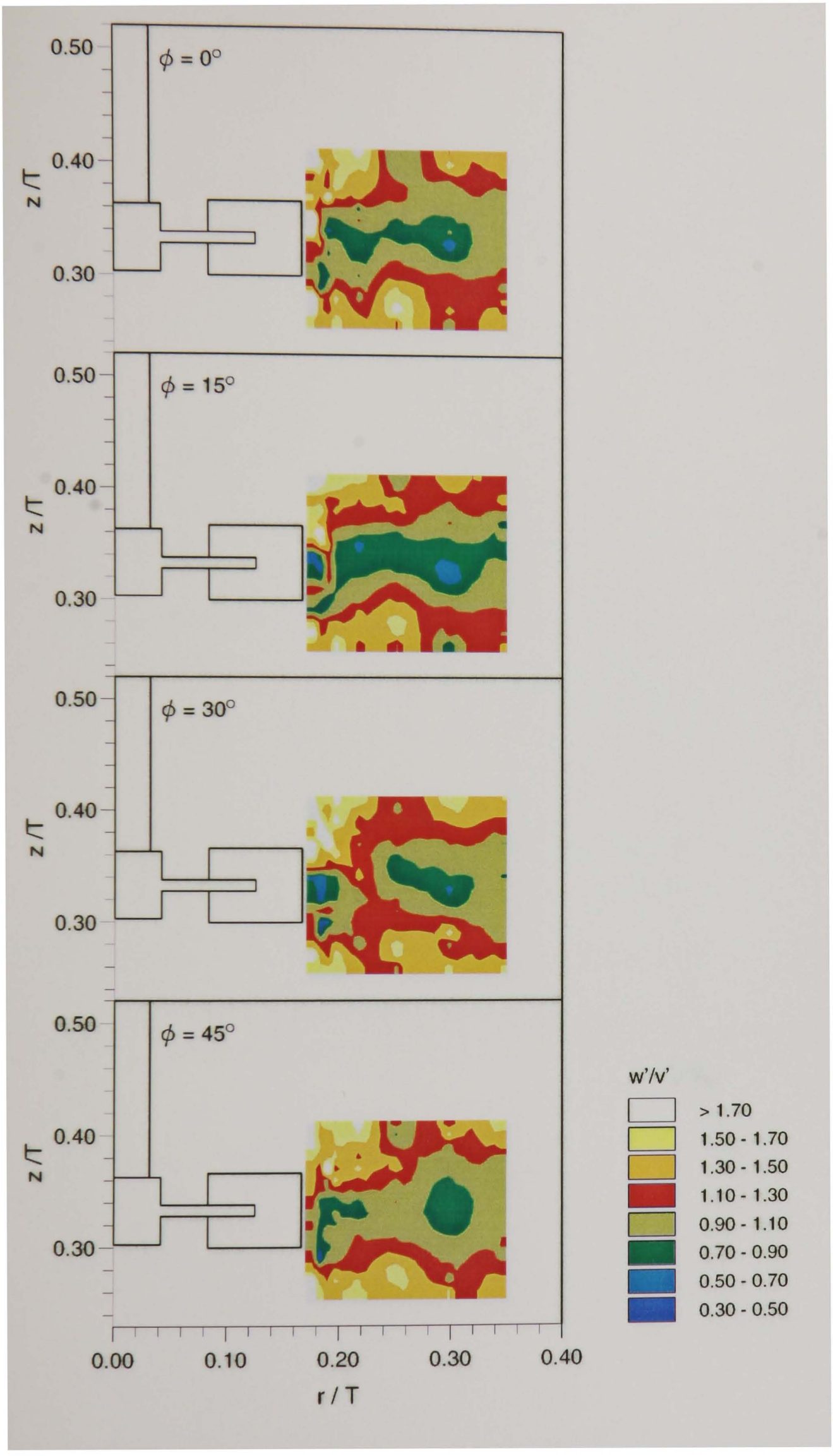


**Figure 4.38** Single Rushton configuration: w'/v' contours in the $\phi = 0°$, 15°, 30° and 45° planes.

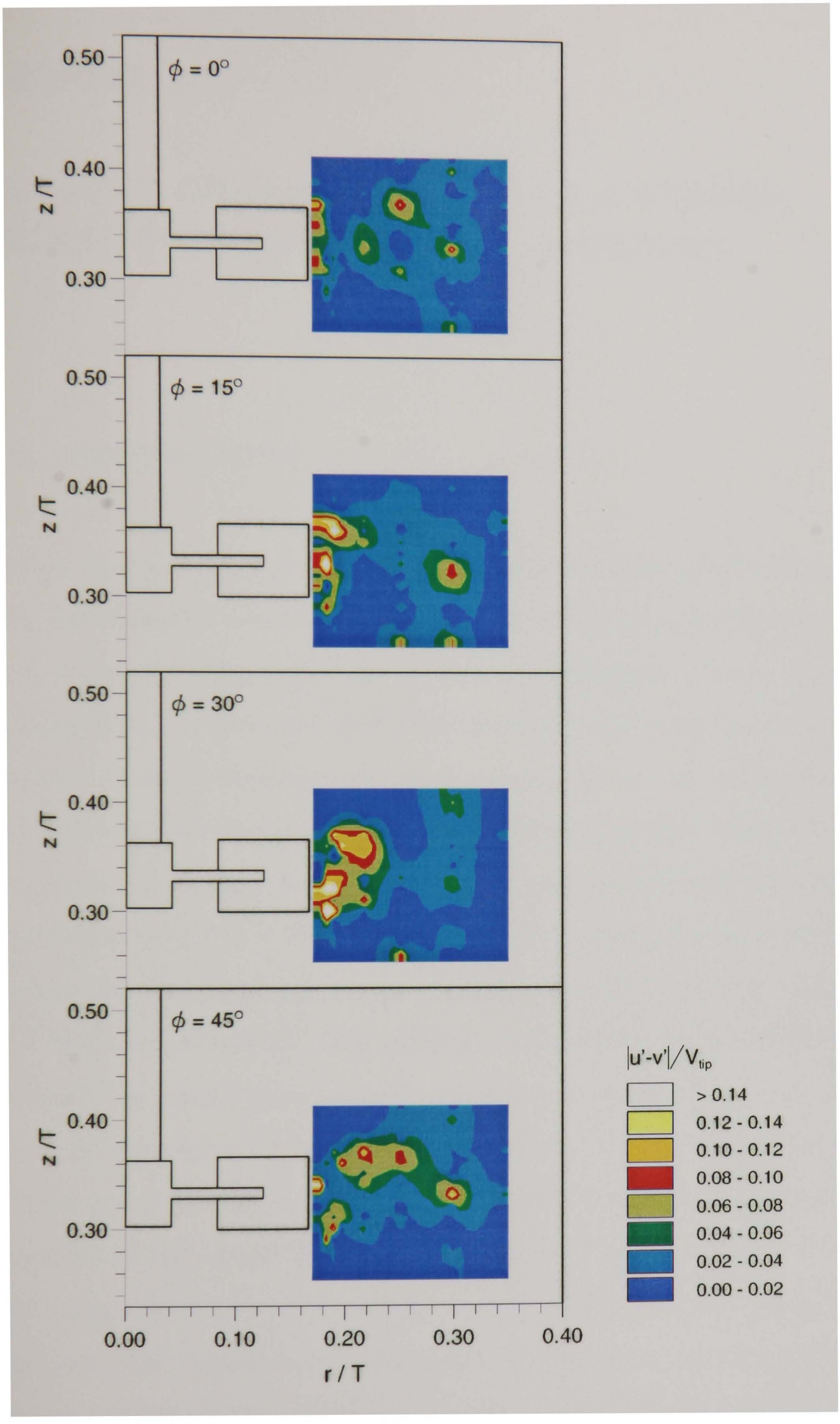


**Figure 4.39** Single Rushton configuration: $|u'-v'|/V_{tip}$ contours in the $\phi$ = 0°, 15°, 30° and 45° planes.

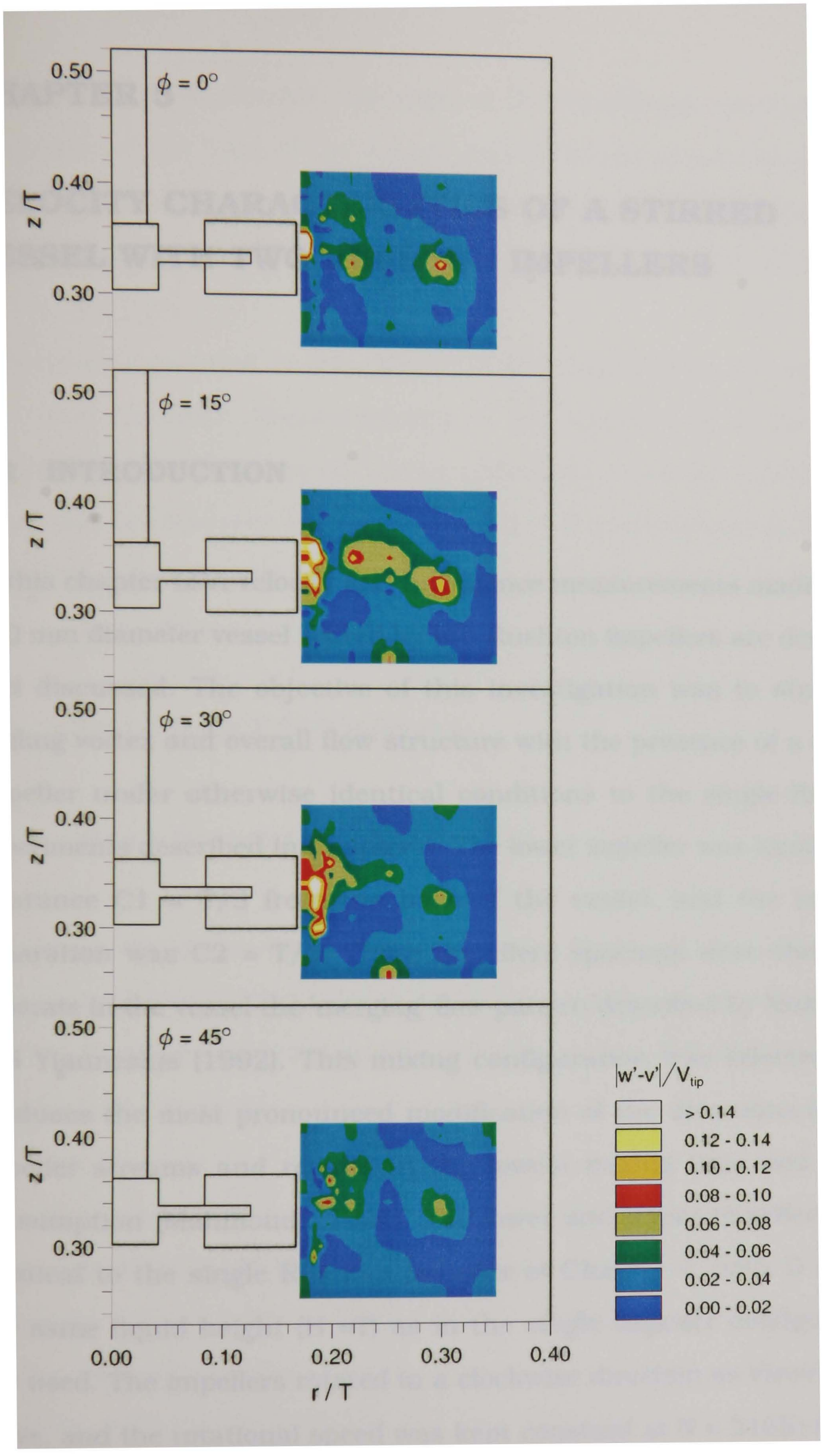


**Figure 4.40** Single Rushton configuration: $|w'-v'|/V_{tip}$ contours in the $\phi$ = 0°, 15°, 30° and 45° planes.

# CHAPTER 5

# VELOCITY CHARACTERISTICS OF A STIRRED VESSEL WITH TWO RUSHTON IMPELLERS

## 5.1 INTRODUCTION

In this chapter LDA velocity and turbulence measurements made in the 100 mm diameter vessel stirred by two Rushton impellers are described and discussed. The objective of this investigation was to study the trailing vortex and overall flow structure with the presence of a second impeller under otherwise identical conditions to the single-Rushton experiments described in Chapter 4. The lower impeller was located at a clearance C1 = T/3 from the base of the vessel, and the impeller separation was C2 = T/3. These impellers spacings were chosen to generate in the vessel the 'merging' flow pattern described by Mahmoudi and Yianneskis (1992). This mixing configuration was selected as it produces the most pronounced modification of the directions of both impeller streams and results in the lowest mixing time and power consumption (Mahmoudi, 1994). The lower and upper impellers were identical to the single Rushton impeller of Chapter 4, with D = T/3. The same liquid height (H =T) as in the single-impeller configuration was used. The impellers rotated in a clockwise direction as viewed from above, and the rotational speed was kept constant at N = 2165±10 rpm (Re = 40000).

As in the previous chapter, the origin of the co-ordinate system used is the centre of the base of the vessel, and all locations are described in terms of normalised axial (z/T), normalised radial (r/T) and tangential ($\theta$) co-ordinates. All measurements were conducted in the $\theta = 0°$ plane.

Results are presented in this chapter only for the flow in the vicinity of the lower impeller. Measurements in the upper half of the vessel showed that the flows are effectively symmetric about the middle of the vessel as the clearance (C1), spacing (C2) and submergence (C3) of the impellers are all identical.

## 5.2 RESULTS AND DISCUSSION

### 5.2.1 MEAN VELOCITY DISTRIBUTION

The mean velocity vectors relative to the blade (i.e. with the rotational velocities subtracted from the tangential components ) obtained in the $z/T = 0.33$ plane where the middle of the lower impeller disk is located, are shown in Figure 5.1.

The vectors show that near the lower impeller blade, at $r/T = 0.17$, there are strong radial velocities between $\phi = 0°$ and $\phi = 45°$. The magnitudes of the radial velocities found in this region are around 25% smaller than those obtained with the single-impeller at this elevation (compare with Figure 4.3). The $\overline{V} / V_{tip}$ velocities decrease to 0.40 at $r/T = 0.19$ and near-zero velocities are observed after this radius and the flow direction is tangential. The tangential velocities at different

radii vary from around 1.0 $V_{tip}$ at r/T = 0.22 to 1.3 $V_{tip}$ at r/T = 0.25, 1.6 $V_{tip}$ at r/T = 0.30 and 1.8 $V_{tip}$ at r/T = 0.35. The flow therefore resembles solid-body rotation at these locations.

In Figure 5.2 the mean velocity vectors in the z/T = 0.35 plane are shown. Strong radial velocities can again be observed near the blade at r/T = 0.17 between $\phi$ = 15° and $\phi$ = 50° and at r/T = 0.19 between $\phi$ = 20° and $\phi$ = 60°. Though the flow direction after r/T = 0.19 is almost tangential as in the z/T = 0.33 plane, the magnitudes of the radial velocities near the trailing blade at r/T = 0.22 are 80% larger than those in the z/T = 0.33 plane. The tangential velocities increase almost linearly with radial distance after r/T = 0.25, again resembling solid-body rotation.

The mean velocity vectors in the z/T = 0.40 plane are depicted in Figure 5.3. In contrast to the two preceding figures, the radial velocities are near zero at r/T = 0.17 and r/T = 0.19. However, after r/T = 0.19, the radial velocities increase in magnitude. Again, the tangential velocities in this plane increase with radial distance.

Figure 5.4 shows the mean velocity vectors in the z/T = 0.50 plane. The flow direction in this plane is almost entirely tangential and again resembles solid-body rotation.

The results of Figures 5.1 to 5.4 show that the magnitudes of the radial velocities decrease with increasing z/T between r/T = 0.17 and r/T = 0.19. The flow generated with the two impellers is primarily in the tangential direction. This is likely to be attributable to the more

intense rotational flow induced in the vessel due to the additional impeller.

Figure 5.5 shows the velocity vectors in four $\phi$ planes (0°, 15°, 30° and 45°). In this figure, a line is drawn at z/T = 0.33 for all planes depicted in order to aid the assessment of the inclination of the impeller stream. At all $\phi$ angles, the discharge flow is oriented at approximately 45° to the horizontal, in contrast with the near-horizontal discharge flow of the single-Rushton impeller in the previous chapter (Figure 4.6).

The mean flow is generally similar in all four $\phi$ planes except for the region near the impeller (for z/T < 0.42 and r/T < 0.25). It is in this region that vortical flows associated with the trailing vortices from the two impellers can be distinguished at $\phi$ = 30° and 45°.

The centre of the trailing vortex is located at a higher elevation than in the single-Rushton system, for example at z/T = 0.36 and 0.39 at $\phi$ = 30° and 45° respectively. The structure and interaction of the trailing vortices from the two impellers is discussed further in Sections 5.2.4 and 5.2.5 below.

The inclination of the impeller stream and the different location of the trailing vortex compared with the single Rushton case are attributable to the influence of the additional impeller. The presence of the upper impeller prevents the formation of a large ring vortex above the lower impeller which would be present in a single-Rushton impeller system. Conversely, with the lower impeller in place the formation of a large ring vortex below the upper impeller is prevented. Instead, two small

ring vortices are formed near the axis between the two impellers. Part of the small vortex formed above the lower impeller is evident in Figure 5.5, located between z/T = 0.4 and 0.5 and r/T = 0.17 and 0.22. With this impeller separation, the discharge streams are inclined at 45° towards one another, and merge midway between impellers to form two very large ring vortices, as also observed by Mahmoudi and Yianneskis (1991) and Mahmoudi (1994). As a result, the strong downward flow near the impeller tip due to the upper ring vortex above the impeller disk which can be clearly identified in Figure 4.6, is not present in the dual-Rushton flow.

### 5.2.2 TURBULENCE LEVEL DISTRIBUTIONS

The normalised turbulence levels, $u'/V_{tip}$, $v'/V_{tip}$ and $w'/V_{tip}$, in the z/T = 0.33 plane are shown in Figures 5.6, 5.7 and 5.8 respectively. They may be compared with the similar results presented for the single impeller in Figures 4.7, 4.8 and 4.9 respectively.

High levels of $u'/V_{tip}$ can be observed behind the leading blade in Figure 5.6. A small region of locally high $u'/V_{tip}$ levels (between 0.20 and 0.24) at around r/T = 0.20 to r/T = 0.22 can also be observed next to the leading blade (i.e. $\phi = 0°$), indicating the presence of the trailing vortex produced by the preceding blade. It can be seen that values of $u'/V_{tip}$ levels above 0.16 are confined to a smaller region than that for the single-impeller case (see Figure 4.7), extending only up to r/T = 0.24.

The $v'/V_{tip}$ levels (Figure 5.7) show similar features to the $u'/V_{tip}$ distribution. The highest values are again found behind the leading

blade but they are distributed over a larger region ($10° < \phi < 50°$) and are higher (> 0.36 compared with 0.28 – 0.32) than the $u'/V_{tip}$ levels. This might be expected as the V velocity gradients are steeper and mean flow variations are more pronounced in the radial direction. The 0.24 – 0.28 $v'/V_{tip}$ region at $\phi = 0°$ is again associated with the vortex produced by the preceding blade. As for the $u'/V_{tip}$ results, $v'/V_{tip}$ levels above 0.16 are confined to a smaller region than for with the single Rushton impeller. extending only up to r/T = 0.25.

The $w'/V_{tip}$ level distribution (Figure 5.8) is again similar to the $u'/V_{tip}$ and $v'/V_{tip}$ ones. The $w'/V_{tip}$ levels do not exceed 0.36 and the region of $w' > 0.16\ V_{tip}$ extends further, up to r/T = 0.27, than the u' and v' distributions. Although the u', v' and w' levels are similar or identical in many locations in this plane, there are significant differences in many parts of the flow. For example, at $\phi = 45°$ and r/T = 0.21, $v'/V_{tip}$ is greater than 0.36, whereas $w'/V_{tip}$ and $u'/V_{tip}$ are 30% smaller. The three distributions indicate that the turbulence in the vicinity of the impeller blades may be considered anisotropic.

Figure 5.9 shows the $u'/V_{tip}$ levels in the z/T = 0.35 plane. The $u'/V_{tip}$ contours in this figure are similar in magnitude to those in the z/T = 0.33 plane. The high $u'/V_{tip}$ level region associated with the trailing vortices generated by the preceding and the leading blade are also evident, and the region of $u'/V_{tip}$ levels above 0.16 extends slightly further than that in the z/T = 0.33 plane, to around r/T = 0.26.

In Figure 5.10, the $v'/V_{tip}$ contours in the z/T = 0.35 plane are shown. Again the magnitudes of the contours are similar to those in the z/T =

0.33 plane. As for the $u'/V_{tip}$ distribution, the region of $v'/V_{tip}$ levels above 0.16 extends further than at z/T = 0.33, to around r/T = 0.28. The $w'/V_{tip}$ contours in the z/T = 0.35 plane are shown in Figure 5.11 and show similar features to those in Figures 5.6 – 5.10.

From Figures 5.6 to 5.11, it can be concluded that the axes of the trailing vortices are curved inwards more than in single-impeller flows. This can be attributed to the influence of the additional impeller, as the presence of two impellers results in stronger tangential velocities. Furthermore, as a result of the stronger tangential velocities in double-impeller flows, the distributions of the turbulence levels of all three components are confined to smaller radii than in single-impeller flows.

Further away from the impeller disk elevation, at z/T = 0.40 (Figures 5.12 – 5.14) regions of high $u'/V_{tip}$, $v'/V_{tip}$ and $w'/V_{tip}$ levels are found at larger radii than in the two z/T planes considered earlier. Again two regions can be distinguished in all three figures where the levels are high, and these are associated with the preceding and leading blade trailing vortex structures.

Figure 5.15 shows the $u'/V_{tip}$ levels in the z/T = 0.50 plane. In this figure, the presence of high levels associated with the two trailing vortices is no longer evident. The region of $u'/V_{tip}$ levels is now confined between r/T = 0.26 and r/T = 0.32. The $v'/V_{tip}$ contours and $w'/V_{tip}$ contours in the z/T = 0.50 plane are shown in Figures 5.16 and 5.17 respectively. It can be seen that the $v'/V_{tip}$ levels and $w'/V_{tip}$ levels are more uniform, with values of 0.08 – 0.16 across the whole region.

The results presented in Figures 5.12 to 5.17 show that the decay of $u'/V_{tip}$ is not as rapid as that of $v'/V_{tip}$ and $w'/V_{tip}$ even though the highest levels measured at the other z/T planes were the $v'/V_{tip}$ ones. The high $u'/V_{tip}$ values in this plane are likely to be associated with the interaction of the impeller stream with that produced by the upper impeller. This is discussed further below in relation to the turbulence level distributions in vertical ($\phi$) planes. The differences observed in the $u'/V_{tip}$, $v'/V_{tip}$ and $w'/V_{tip}$ distributions in all the z/T planes indicate that, as for the single-impeller case, the turbulence in the impeller stream may be considered to be anisotropic.

A good indication of the direction of the impeller stream in the double-impeller case is given by the $u'/V_{tip}$ contours in four $\phi$ planes (0°, 15°, 30° and 45°) shown in Figure 5.18. At $\phi$ = 0° the high $u'/V_{tip}$ levels around r/T = 0.20 are associated with the flow produced by the preceding blade and they are higher than in the single-impeller case, with their centre located at around r/T = 0.22, z/T = 0.36 (compare with Figure 4.23). The high $u'/V_{tip}$ level region near the tip at $\phi$ = 15° is due to the flow produced by the leading blade, and it is found to extend further into the impeller stream and to merge with the region of high $u'/V_{tip}$ associated with the vortex produced by the preceding blade at subsequent $\phi$ planes. The contours shown in all $\phi$ planes extend outward from the blade at an angle of around 45° to the horizontal and in general the contours of $u'/V_{tip}$ levels above 0.16 extend to z/T = 0.50.

Figures 5.19 and 5.20 show the $v'/V_{tip}$ and $w'/V_{tip}$ distributions respectively at the same four $\phi$ planes. Similar observations as for the $u'/V_{tip}$ distributions can be made: the two high turbulence level regions

associated with the preceding and the leading blade vortex structures can be clearly identified but both $v'/V_{tip}$ and $w'/V_{tip}$ do not exceed 0.16 at the z/T = 0.50 plane. The centres of the high $v'/V_{tip}$ and $w'/V_{tip}$ level regions associated with either the leading or the preceding blade vortices are found to extend only to z/T = 0.39 in all planes. The elongated shape of the region in which $w'/V_{tip} > 0.28$ at $\phi$ = 15° and 30° in Figure 5.20 is expected to stem from the combined effect of the two trailing vortices produced by the lower impeller blade, i.e. one from the top and one from the bottom half of the blade. The high $w'/V_{tip}$ levels associated with the bottom vortex are evident in this case due to the inclination of the impeller stream, in contrast with the single-Rushton configuration. The results indicate that the axes of the vortices are strongly curved and have only a slight upward inclination. A better assessment of the extent of the influence of the trailing vortex structures can be made by reference to the $k/V_{tip}^2$ contour levels presented below.

Comparison of the extent of the high $u'/V_{tip}$ region with that for the single-impeller (Figure 4.13) shows that the two regions are similar in size. However, there are two differences. First, in the two-impeller case, the region extends above the impeller to z/T = 0.50 due to the inclination of the impeller stream, but the shape of the contours indicates that below the impeller this region is unlikely to extend below the lower edge of the blade. Second, due to the combined effect of both impellers the turbulence levels are in general higher and the decay of the vortical structures may be expected to be slower than in the single-impeller case.

### 5.2.3 TURBULENCE KINETIC ENERGY DISTRIBUTIONS

Figure 5.21 shows the $k/V_{tip}^2$ contours in the same four $\phi$ planes (0°, 15°, 30° and 45°). At $\phi$ = 0°, locally high $k/V_{tip}^2$ levels can be observed at around r/T = 0.21, indicating the trailing vortex produced by the preceding blade. The presence of this trailing vortex is still evident at $\phi$ = 15°.

At $\phi$ = 15°, the region of high $k/V_{tip}^2$ levels observed near the tip is associated with the flow from the leading blade. This region spreads progressively outwards at a angle of around 45° to the horizontal in subsequent $\phi$ planes. Due to the inclination of the impeller stream, the regions of $k/V_{tip}^2$ levels above 0.02 in all $\phi$ planes extend above the impeller to z/T = 0.50 but below the disk they might be expected to extend only to the lower edge of the blade.

Figure 5.22 shows the $k/V_{tip}^2$ contours in the z/T = 0.33 plane. Again high $k/V_{tip}^2$ levels can be observed behind the leading blade. This region is curved slightly more inward in comparison with the $k/V_{tip}^2$ results obtained at the same elevation for the single-impeller system (Figure 4.18). After r/T = 0.25 , the $k/V_{tip}^2$ levels decrease to below 0.04, and they decrease further to below 0.02 after r/T = 0.31.

Figure 5.23 shows the $k/V_{tip}^2$ contours in the z/T = 0.35 plane. The distribution of $k/V_{tip}^2$ in this plane is similar to that observed in the z/T = 0.33 plane with one exception: the presence of the trailing vortex produced by the preceding blade is more evident in this plane at r/T = 0.21 and $\phi$ = 0°.

Figure 5.24 shows the $k/V_{tip}^2$ contours obtained in the z/T = 0.40 plane. The two regions of high $k/V_{tip}^2$ may be considered to indicate the trailing vortices produced by the leading and preceding blades. The $k/V_{tip}^2$ levels after r/T = 0.30 are higher than those observed in the previous two planes. This is attributed to the inclination of the impeller streams and the associated movement of the vortex structures away from the impeller.

Figure 5.25 shows the $k/V_{tip}^2$ contours in the z/T = 0.50 plane. The $k/V_{tip}^2$ levels are uniform with values of 0.02 – 0.04 after r/T = 0.19, while between r/T = 0.17 and 0.19 a radial band with $k/V_{tip}^2$ = 0.02 – 0.04 is observed.

## 5.2.4 TIME-RESOLVED VELOCITY MEASUREMENTS

### INSTANTANEOUS VELOCITIES AND NORMALISED ENERGY SPECTRA

It can be observed from the results presented in the previous sections that the impeller stream is inclined at an angle to the horizontal. Therefore, in order to quantify the decay of the trailing vortex structure and compare with the single-impeller case, time-resolved velocity measurements of the radial component, V, were made at the following locations along the inclined impeller stream: r/T = 0.17, z/T = 0.33; r/T = 0.25, z/T = 0.41 and r/T = 0.30, r/T = 0.50.

Figure 5.26(a) shows a recording of $V/V_{tip}$ made at r/T = 0.17, z/T = 0.33. Six cycles per revolution can be observed, as in the single-impeller

case. The maximum $V/V_{tip}$ value is about 20% smaller than that in the single-impeller case. This is expected as the flow is inclined at an angle of about 45° to the horizontal hence the radial velocities would be smaller.

Figure 5.26(b) shows the recording of $V/V_{tip}$ made at r/T = 0.25, z/T = 0.41. No discernible periodicity can be observed in this recording. Similarly, no periodicity can be observed in the $V/V_{tip}$ recording made at r/T = 0.30, z/T = 0.50 (Figure 4.26(c)).

Normalised energy spectra of the velocity recordings presented above were also computed, using the Lomb method as described in the previous chapter. The normalised energy spectra corresponding to the recordings shown in Figures 4.26(a)–(c) are presented in Figures 4.27(a)–(c) respectively.

In Figure 4.27(a), it can be observed that there is a sharp peak at around 216 Hz, which corresponds to the blade passage frequency, indicating that there is a well–defined periodic motion in the flow at this location. The magnitude of this peak is about 50% of that found in the single-impeller case at the same location. However, unlike the normalised energy spectrum obtained for the single-impeller configuration, no distinctive peaks at 432 Hz can be observed (see Figure 4.23(a)). Furthermore, in Figure 5.27(a) it can be seen that there is also a peak at around 5 Hz.

In the normalised energy spectrum of V at r/T = 0.25, z/T = 0.41 (Figure 5.27(b)), a number of peaks of similar magnitudes (between 0.1 and

0.25) at frequencies between 5 Hz and 10 Hz can be observed instead of a distinctive sharp peak at 216 Hz. This indicates that there is no well-defined periodic or quasi-periodic motion in the flow at this location.

In the energy spectrum of V at r/T = 0.30, z/T = 0.50 (Figure 5.27(c)), a broad band of peaks can be found up to around 50 Hz. The origin of the low-frequency peaks in Figures 5.27(a)–(c) is not understood and further work is required to investigate this.

### ENERGY SPECTRA AND SCALES OF TURBULENCE

The V recordings were resampled and filtered, where necessary, and processed further to obtain the corrected fluctuation velocity component, v (i.e. with the periodic component removed). Thence the energy spectra, integral and micro time scales were computed.

The energy spectrum of v at r/T = 0.17, z/T = 0.33 is shown in Figure 5.28 plotted in log-log scale. For comparison purposes, the energy spectrum obtained at the same location with a single impeller is shown, and a straight line with a -5/3 slope is also drawn in this figure. Similar energy distributions can be observed for the two spectra shown in Figure 5.28. Over most of the frequency range, the magnitude of the spectrum for the double impeller case is smaller than the single impeller one, this may be attributed to the inclination of the impeller stream with the double-impeller configuration. As the flow direction is not primarily in the radial direction as in the case of a single impeller less energy might be contained in the v component. The slope of the spectrum obtained with the double-impeller is similar to that with the

single-impeller configuration, around -1.3 for frequencies above 1 kHz. The deviation of the slope from the value of -5/3, again implies anisotropy. Figure 5.29 shows the energy spectra of v at r/T = 0.25, z/T = 0.41 and r/T = 0.30, z/T = 0.50. It can be observed that, the slope of both spectra is about -5/3 over most of the frequency range, therefore, the turbulence at these two locations may be considered to be isotropic.

Temporal and spatial scales of turbulence were calculated from the v velocity variations in the dual-Rushton case in the manner described earlier for the single-impeller flow. The values are listed in the table below:

**Table 5.1** Values of $\lambda_t$, $\lambda_x$, $\Lambda_t$ and $\Lambda_x$ with double-impeller configuration.

| r/T | z/T | $\lambda_t$ (ms) | $\lambda_x$ (mm) | $\Lambda_t$ (ms) | $\Lambda_x$ (mm) |
|---|---|---|---|---|---|
| 0.17 | 0.33 | 0.09 | 0.15 | 0.13 | 0.22 |
| 0.25 | 0.41 | 0.08 | 0.08 | 0.16 | 0.16 |
| 0.30 | 0.50 | 0.08 | 0.06 | 0.12 | 0.09 |

Clearly the variations of all scales with distance from the impeller blade are not as expected and contrast those found for the single-Rushton case. It must be noted, however, that with two impellers, the flow is not primarily in the radial direction and direct comparisons are not appropriate. Clearly, time-resolved measurements of at least two components or of a single component at 45° to the horizontal are required for the dual-Rushton case. In view of this and of the approximations involved in the determination of the rate of dissipation

which were described in the previous chapter, ε was not calculated for this flow.

### 5.2.5 TRAILING VORTEX AXIS

The location of the mean axis of the trailing vortex generated by the lower impeller is plotted in Figure 5.30. This figure shows the axis in the r-θ plane as viewed from above the vessel, with the impeller rotating in a clockwise direction. For comparative purposes the trailing vortex axes for the single-impeller flow presented in the previous chapter and that determined by Rutherford et al (1996a) in a 294 mm vessel are also shown.

Various techniques used by other researchers to determine the locus of the axis were described in the previous chapter. The vortex axis of this investigation was determined from the turbulence kinetic energy distributions in various z/T planes. This was employed as an approximation since it is not possible to determine the velocity component which is zero in a plane perpendicular to the axis of the trailing vortex, due to the inclination of the impeller streams.

It can be seen from Figure 5.30 that the centre of the trailing vortex produced by the lower impeller does not extend as far into the vessel as for the single-impeller flow. The vortex axis with the single-impeller configuration extends to around r/T = 0.22 at $\phi = 60°$, while the vortex axis with the dual-impeller configuration extends only to r/T = 0.19 at $\phi = 60°$. This is attributed to the stronger tangential velocities due to

the presence of an additional impeller and the inclination of the impeller streams.

It can also be observed from Figure 5.30 that the trailing vortex axis in the 100 mm diameter vessel is very similar to that in the 294 mm diameter vessel, indicating good scaling of the flows.

### 5.2.6 VELOCITY VARIATION IN IMPELLER STREAM

Figures 5.31(a) and (b) show the variation with radial distance from the blade of the normalised 360° ensemble-averaged mean velocities and turbulence levels respectively in the z/T = 0.33 plane. The 360° ensemble-averaged radial mean velocities and turbulence levels were computed from the 1° angle-resolved results. The 'best-fit' of the variation shown in Figure 5.31(a) is given by:

$$\frac{\overline{V}}{V_{tip}} = 0.48 \left(\frac{r}{R}\right)^{-4.39} \qquad (5.1)$$

When compared with that obtained for the single impeller case, which is given by:

$$\frac{\overline{V}}{V_{tip}} = 0.74 \left(\frac{r}{R}\right)^{-0.99} \qquad (5.2)$$

it can be seen that $\overline{V} / V_{tip}$ near the blade tip is about 30% higher and that $\overline{V} / V_{tip}$ decays slower with the single Rushton impeller. These

trends might be expected, as the impeller stream with the two Rushton impellers is not horizontal.

The 'best-fit' obtained for the 360° ensemble-averaged turbulence level results shown in Figure 5.31(b) is given by:

$$\frac{v'}{V_{tip}} = -0.28\left(\frac{r}{R}\right) + 0.63 \qquad (5.3)$$

Clearly, the straight line represents a bad fit in comparison with the single Rushton case (Figure 4.36(b)). Therefore, since the angle of inclination of the impeller stream was found to be 45° to the horizontal, 360° ensemble-averaged mean velocities and turbulence levels at locations within the inclined impeller stream should be calculated. Figure 5.32 shows the variation of $\overline{V} / V_{tip}$ with d/R, where d is the distance of the measurement location from the blade tip along the inclined stream. The 'best-fit' of the data presented in the figure is given by:

$$\frac{\overline{V}}{V_{tip}} = 0.50\left(\frac{d}{R}\right)^{-1.55} \qquad (5.4)$$

As expected, Equation (5.4) shows that the decay of $\overline{V} / V_{tip}$ is not as rapid as that in the impeller disk plane. In addition, Equation (5.4) provides a more appropriate characterisation of the radial velocity decay along the (inclined) impeller stream. However, due to the inclination of the stream it is more appropriate to consider the variation of the resultant velocity $V_{res}/V_{tip}$ with d/R, where

$$V_{res} = \sqrt{\overline{U}^2 + \overline{V}^2} \tag{5.5}$$

The variation of $V_{res}/V_{tip}$ with (d/R) is also shown in Figure 5.32, and the 'best-fit' of the data is given by:

$$\frac{V_{res}}{V_{tip}} = 0.60 \left(\frac{d}{R}\right)^{-1.66} \tag{5.6}$$

The higher value of $V_{res}/V_{tip}$ at the blade tip (i.e. 0.60) indicates that $V_{res}/V_{tip}$ would be more appropriate than $\overline{V} / V_{tip}$ to quantify the decay of the mean velocities in the impeller stream for the double impeller case.

Similarly, the resultant turbulence levels, $v'_{res}$, would be more appropriate than v' to quantify the decay of the turbulence velocities in the impeller stream. Attempts were made to obtain values of $v'_{res}$ from the u' and v' data using the method described by Melling and Whitelaw (1976). However, much scatter could be observed in the results obtained with this method and measurements of the turbulence level component at 45° to the horizontal along the inclined impeller stream are required to calculate the decay of $v'_{res}$ in the dual-Rushton configuration.

### 5.2.7 ANISOTROPY OF THE IMPELLER DISCHARGE FLOW

Figures 5.33 and 5.34 show the normalised |u' - v'| and |w' - v'| contours respectively in four $\phi$ planes. These results may be compared with the corresponding Figures 4.39 and 4.40 for the single-Rushton

case. Similar observations to those in Section 4.4.4 can be made for the double-Rushton case as well.

In order to avoid repetition, it is sufficient to note that the high $|u' - v'|/V_{tip}$ and $|w' - v'|/V_{tip}$ values near the blade indicate that the turbulence in the region near the blade is anisotropic. In the region $z/T > 0.40$ and $r/T > 0.25$ the differences between u', v', and w' are smaller (between 0.0 and 0.04), and the turbulence in this region may be considered as isotropic.

## 5.3 EPILOGUE

In this chapter, detailed LDA results obtained in the T = 100 mm vessel stirred by two Rushton impellers have been presented. The flow pattern produced in the vicinity of the lower impeller has been described in detail and compared with the results obtained with the single-impeller configuration.

The results show that the impeller stream of the lower impeller is inclined at around 45° to the horizontal. They also show that the presence of the additional impeller generates stronger tangential velocities and, as a result, the axes of the trailing vortices curve inwards more than in single-impeller flows. As for the single-impeller case, the extent of influence of the periodicity of the vortical flows can be confined within a cylindrical surface, albeit larger for the double-impeller case. The cylindrical surface in this case is centred around the middle of the vessel and its height and radius are around 1.2 D and

1.0 D respectively. The trailing vortex axis obtained in the present work is very similar to that obtained in a 294 mm vessel reported by Rutherford et al (1996a), indicating good scaling of the flows.

The turbulence near the impeller is indicated to be anistropic and it may be considered to be isotropic after r/T = 0.25, as shown by the normalised relative magnitude of the three turbulence level components and the energy spectra results.

In order to study the mixing processes in the 100 mm vessel stirred by either single- or double-Rushton impeller(s), the liquid crystal thermographic technique developed was employed to determine the transient mixing characteristics in the vessel. In the following chapter, the results obtained with this technique are described.

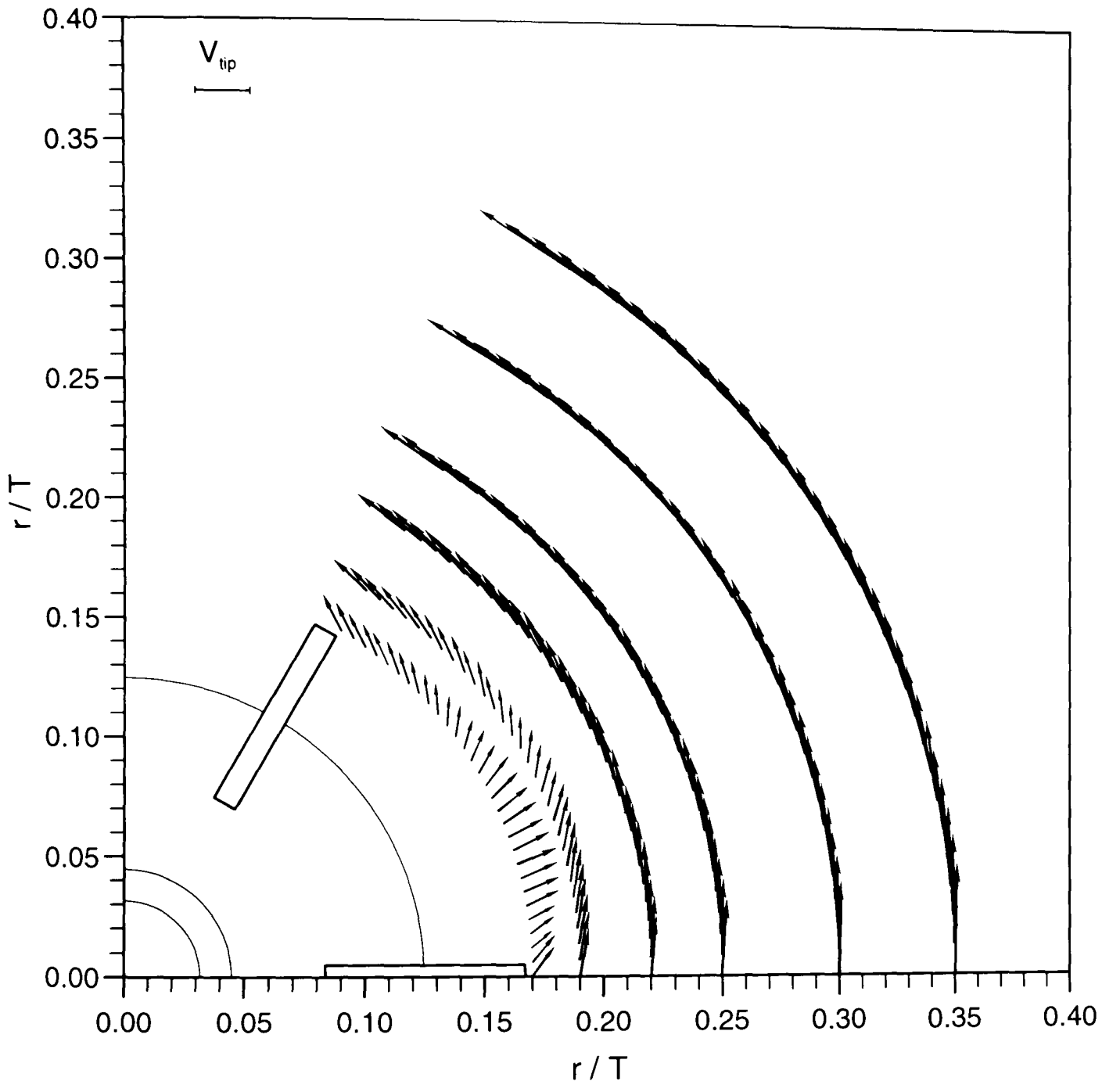


**Figure 5.1** Double Rushton impeller configuration: velocity vectors in the z/T = 0.33 plane.

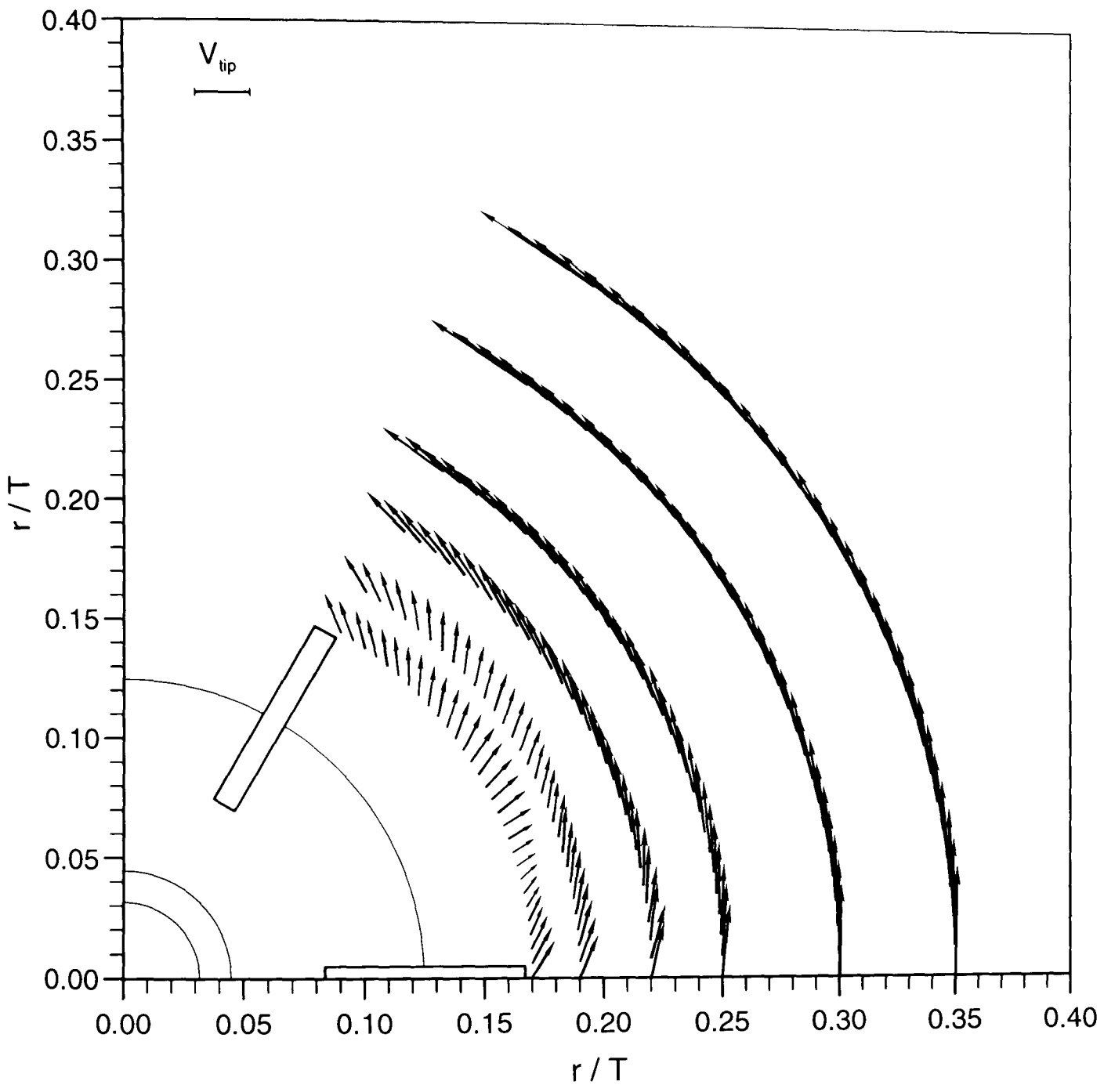


**Figure 5.2** Double Rushton impeller configuration: velocity vectors in the z/T = 0.35 plane.

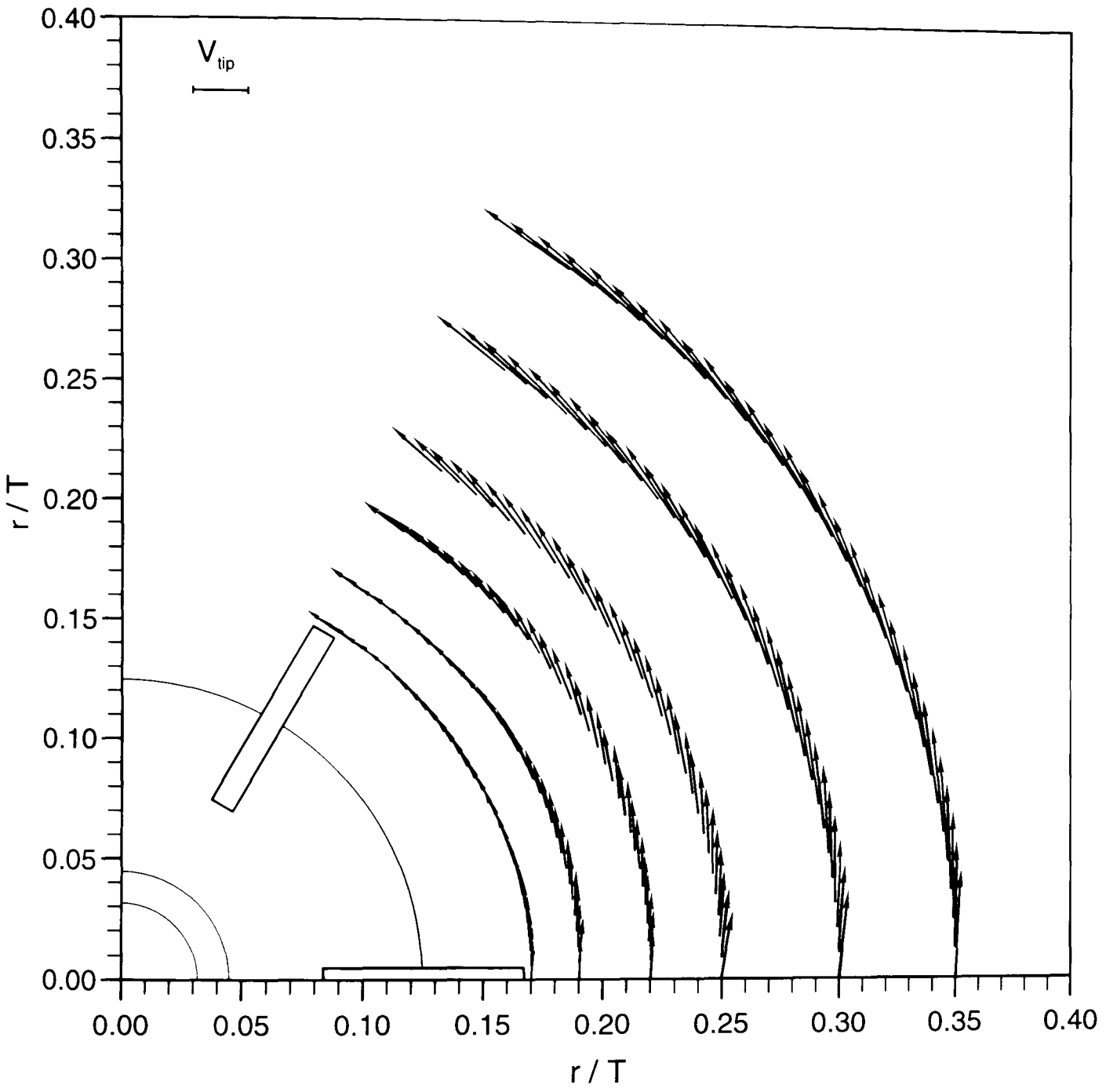


**Figure 5.3** Double Rushton impeller configuration: velocity vectors in the z/T = 0.40 plane.

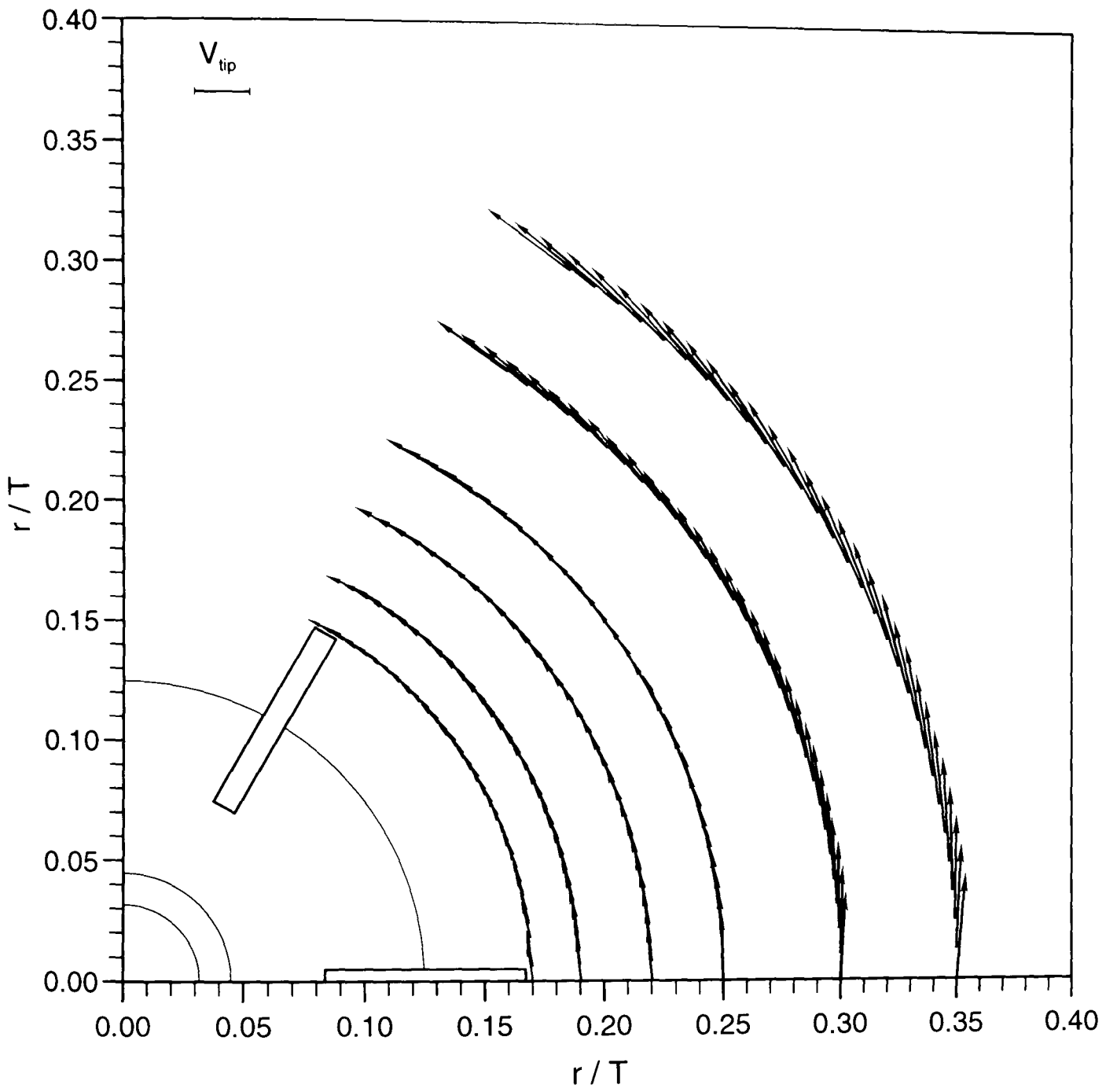


**Figure 5.4** Double Rushton impeller configuration: velocity vectors in the z/T = 0.50 plane.

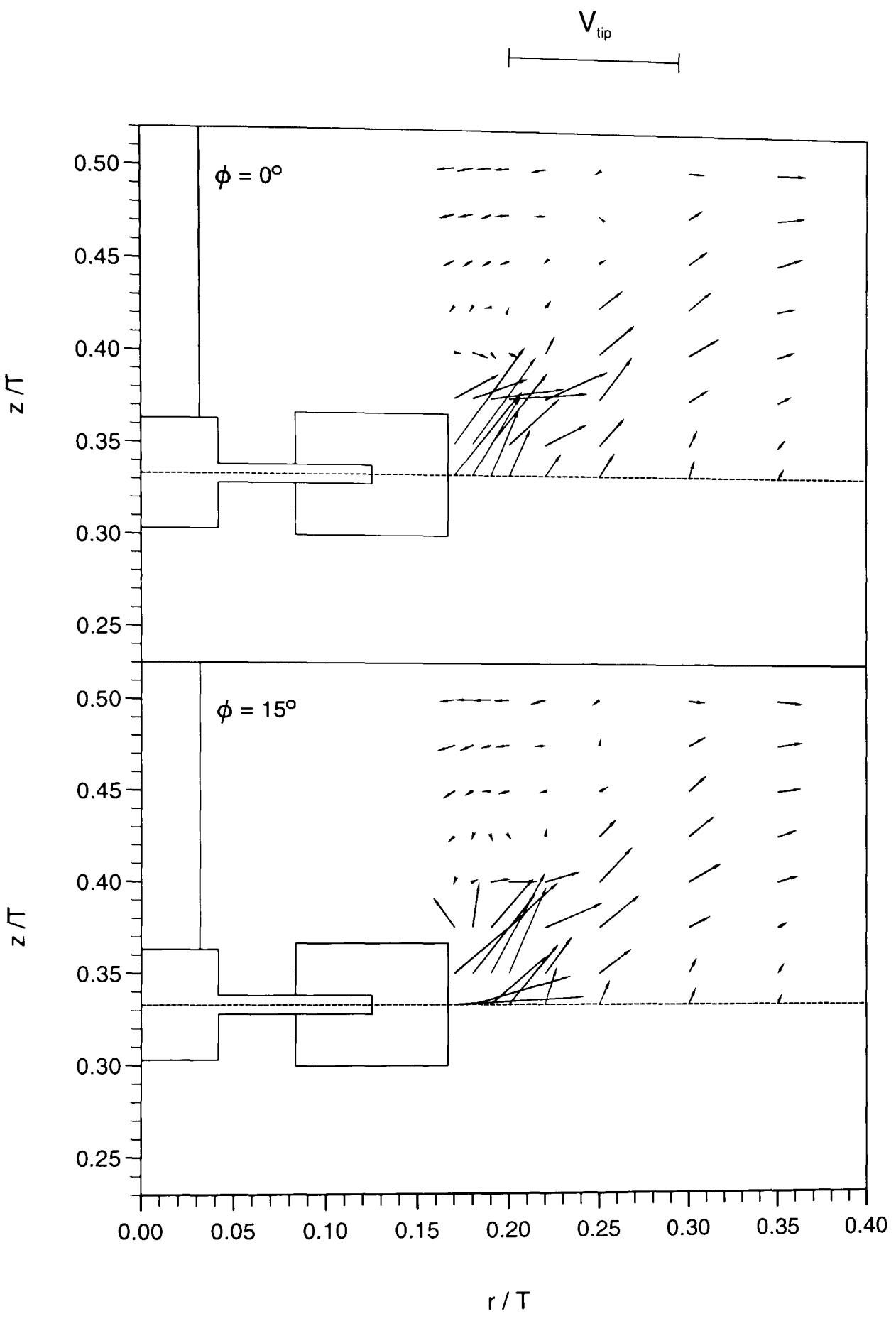


**Figure 5.5(a)** Double Rushton impeller configuration: velocity vectors in the $\phi = 0°$ and $15°$ planes.

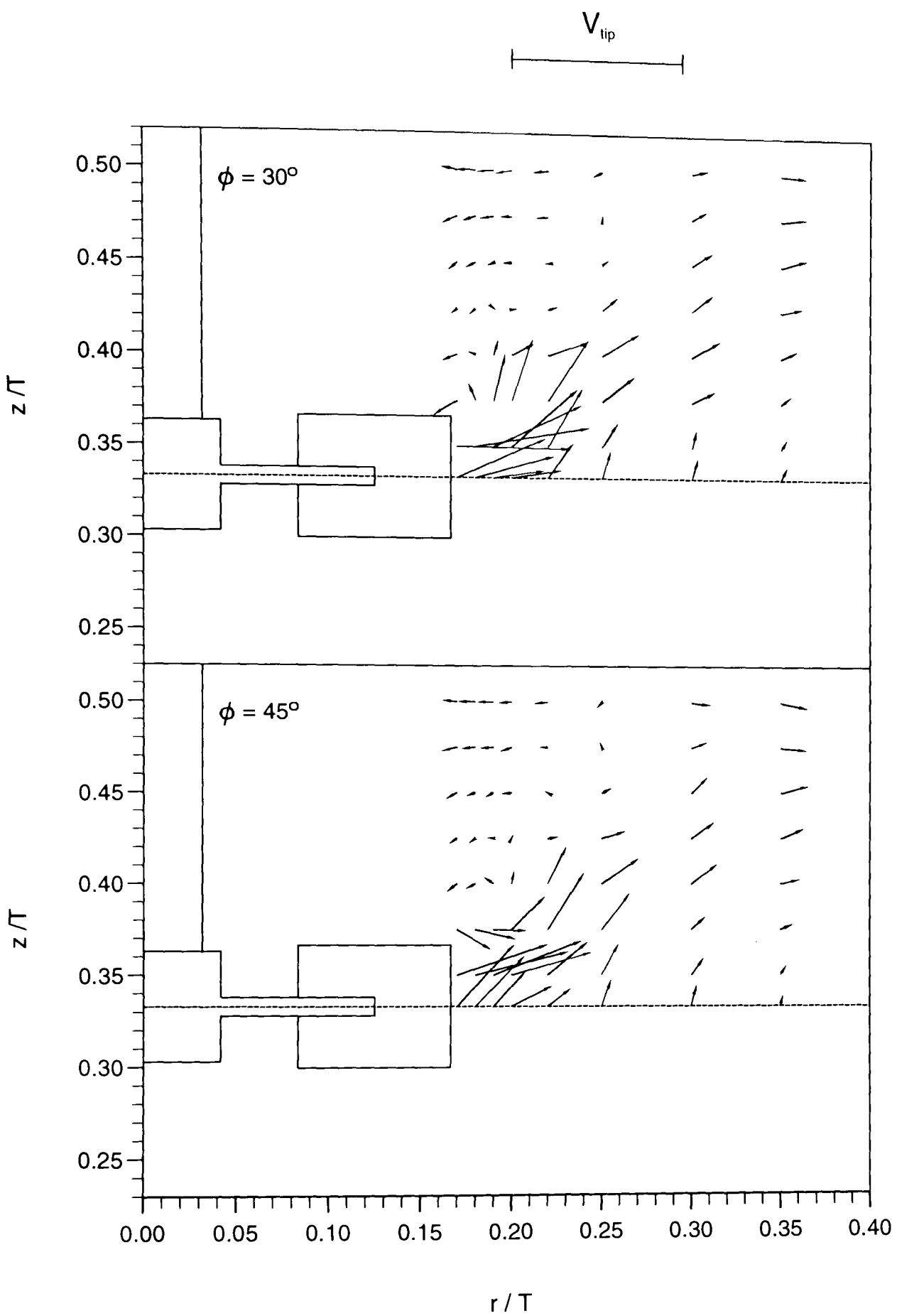


**Figure 5.5(b)** Double Rushton impeller configuration: velocity vectors in the $\phi$ = 30° and 45° planes.

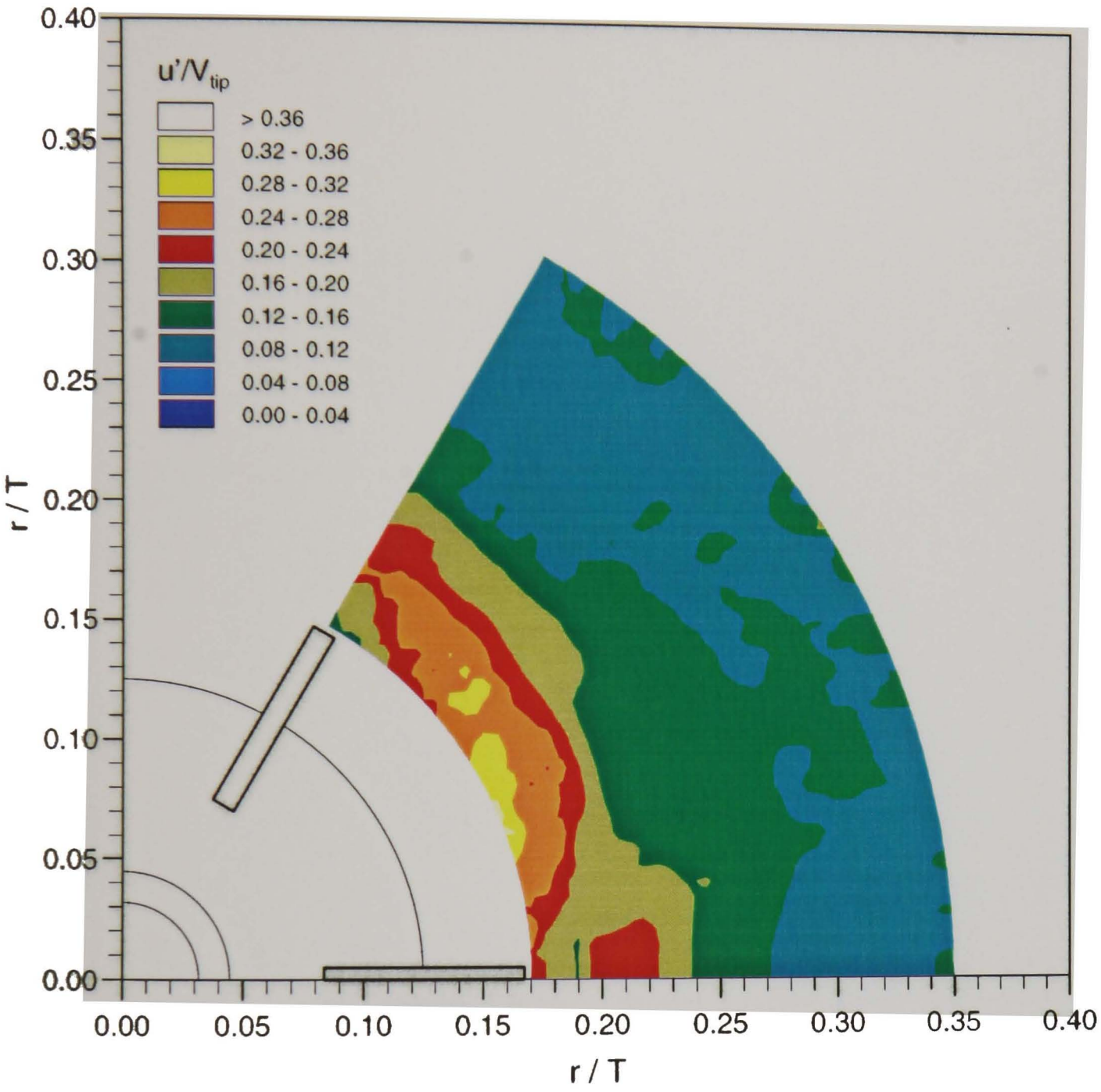


**Figure 5.6** Double Rushton impeller configuration: axial turbulence level contours in the z/T = 0.33 plane.

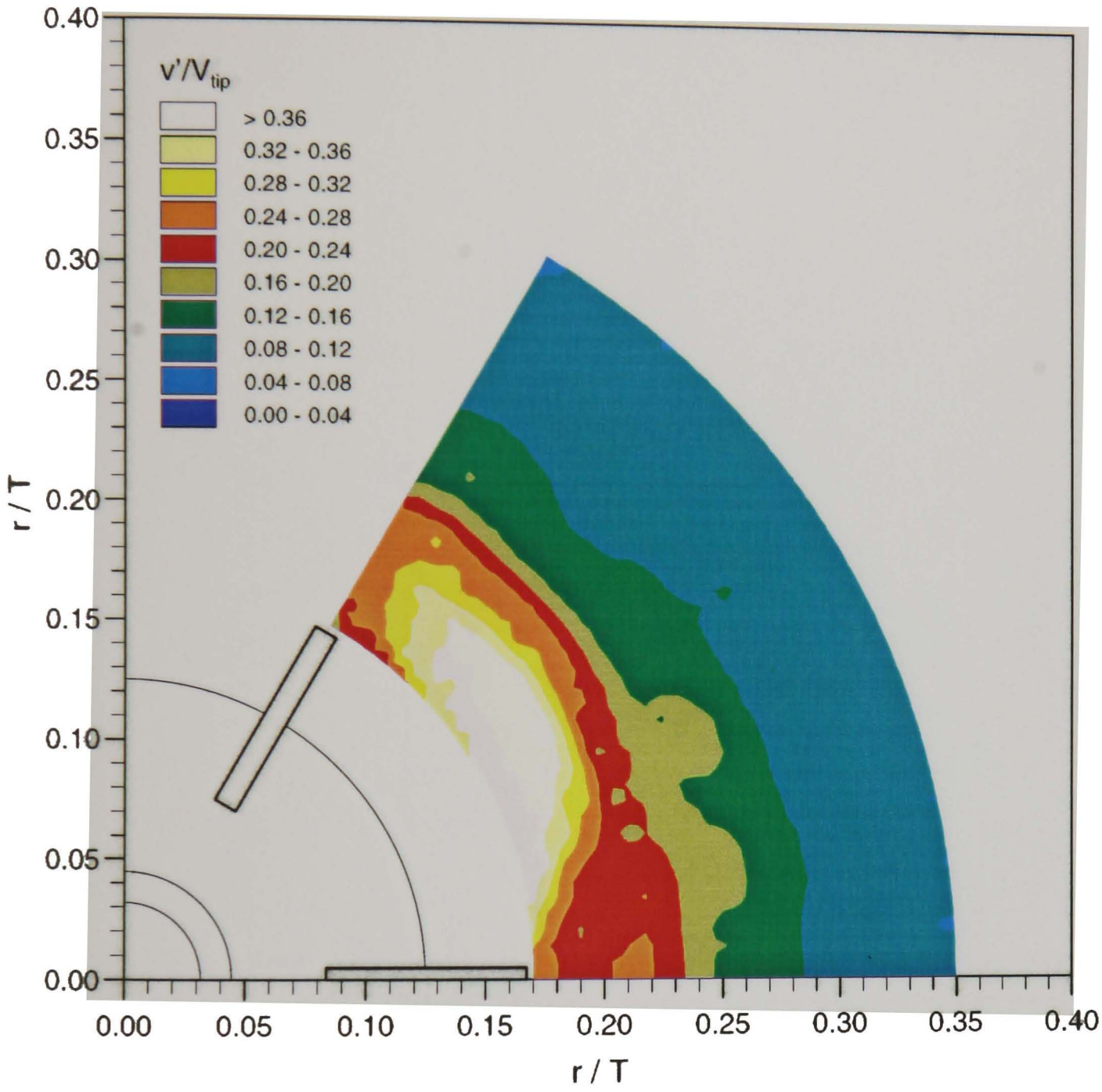


**Figure 5.7** Double Rushton impeller configuration: radial turbulence level contours in the z/T = 0.33 plane.

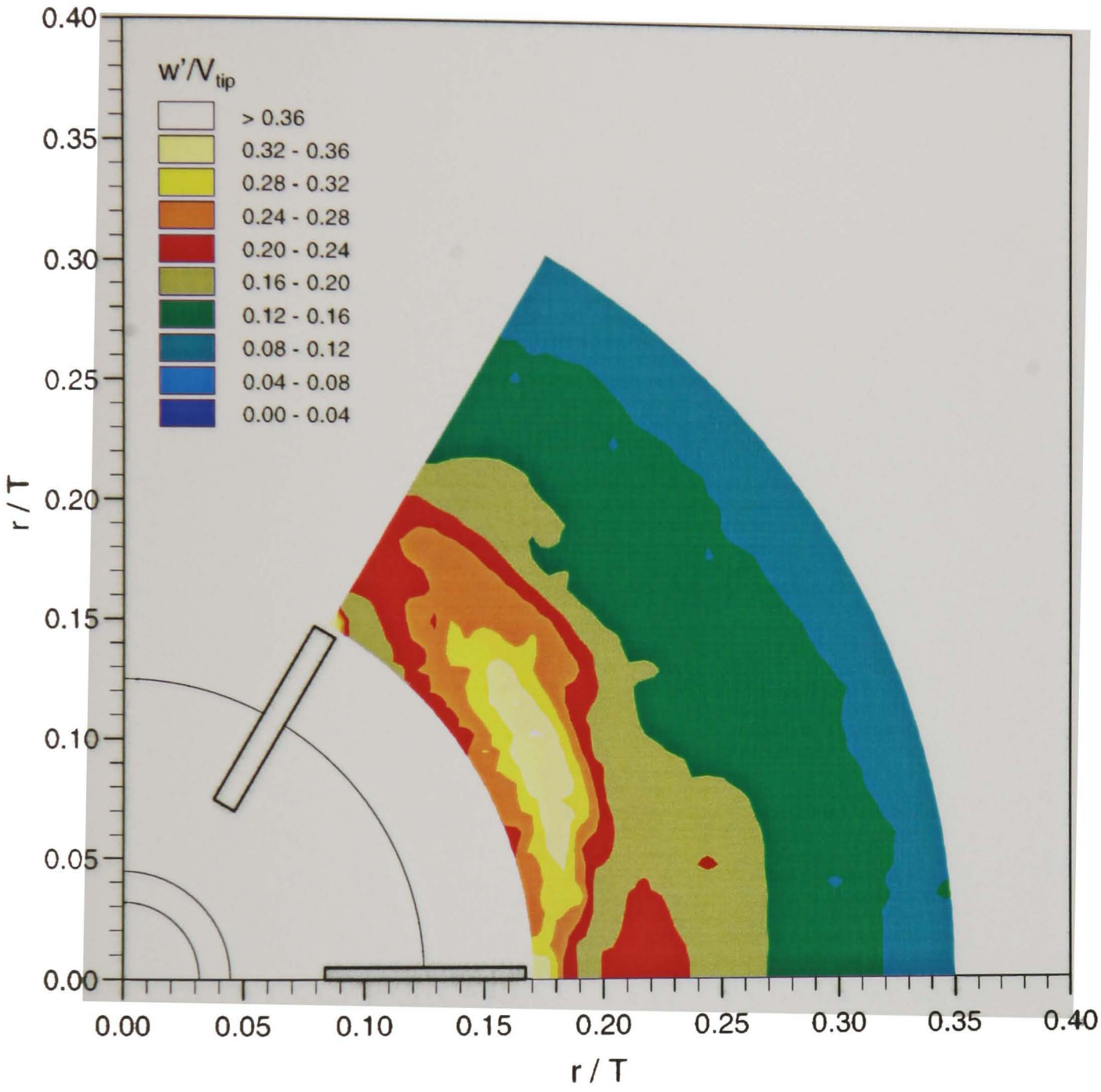


**Figure 5.8** Double Rushton impeller configuration: tangential turbulence level contours in the z/T = 0.33 plane.

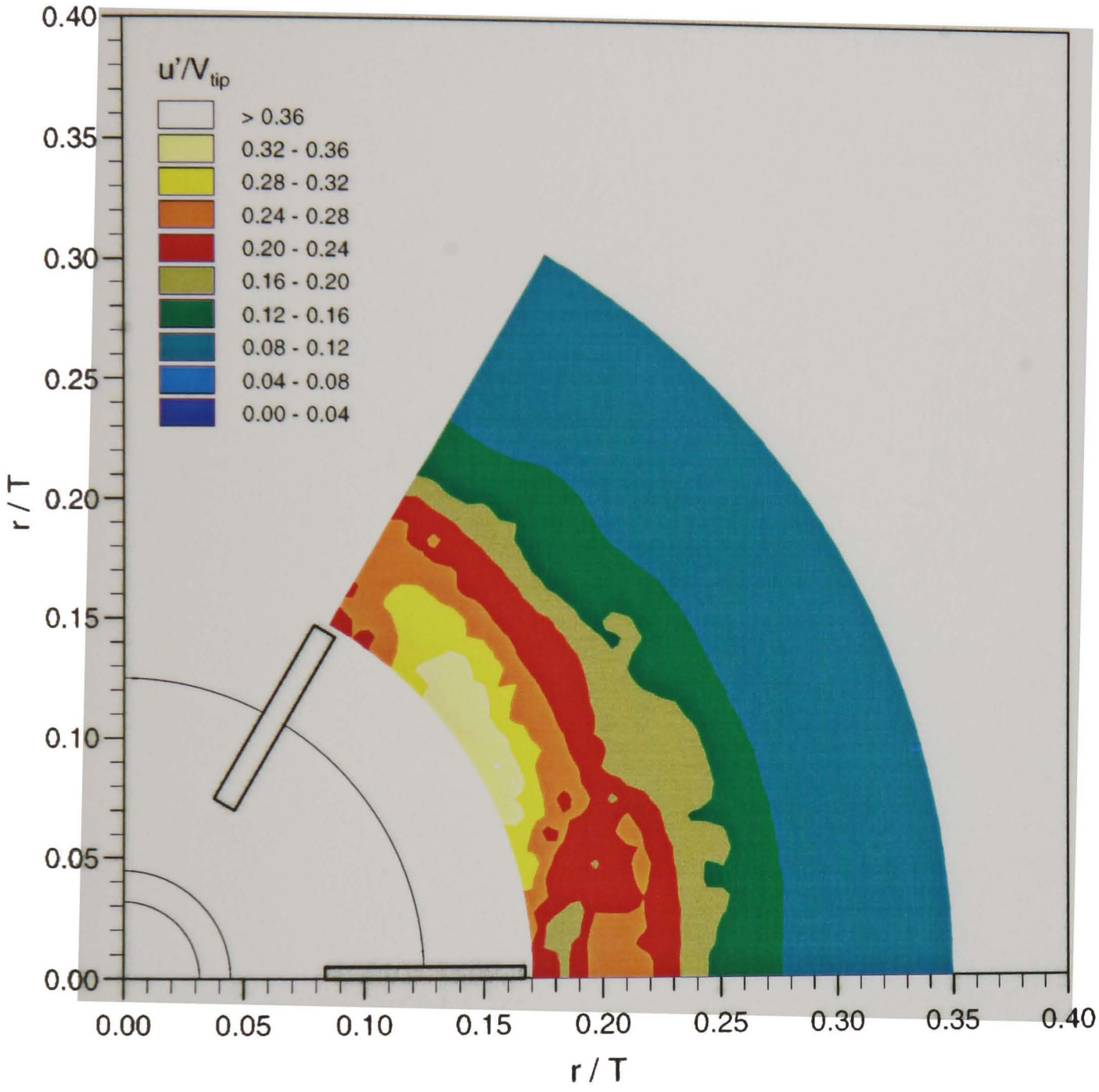


**Figure 5.9** Double Rushton impeller configuration: axial turbulence level contours in the z/T = 0.35 plane.

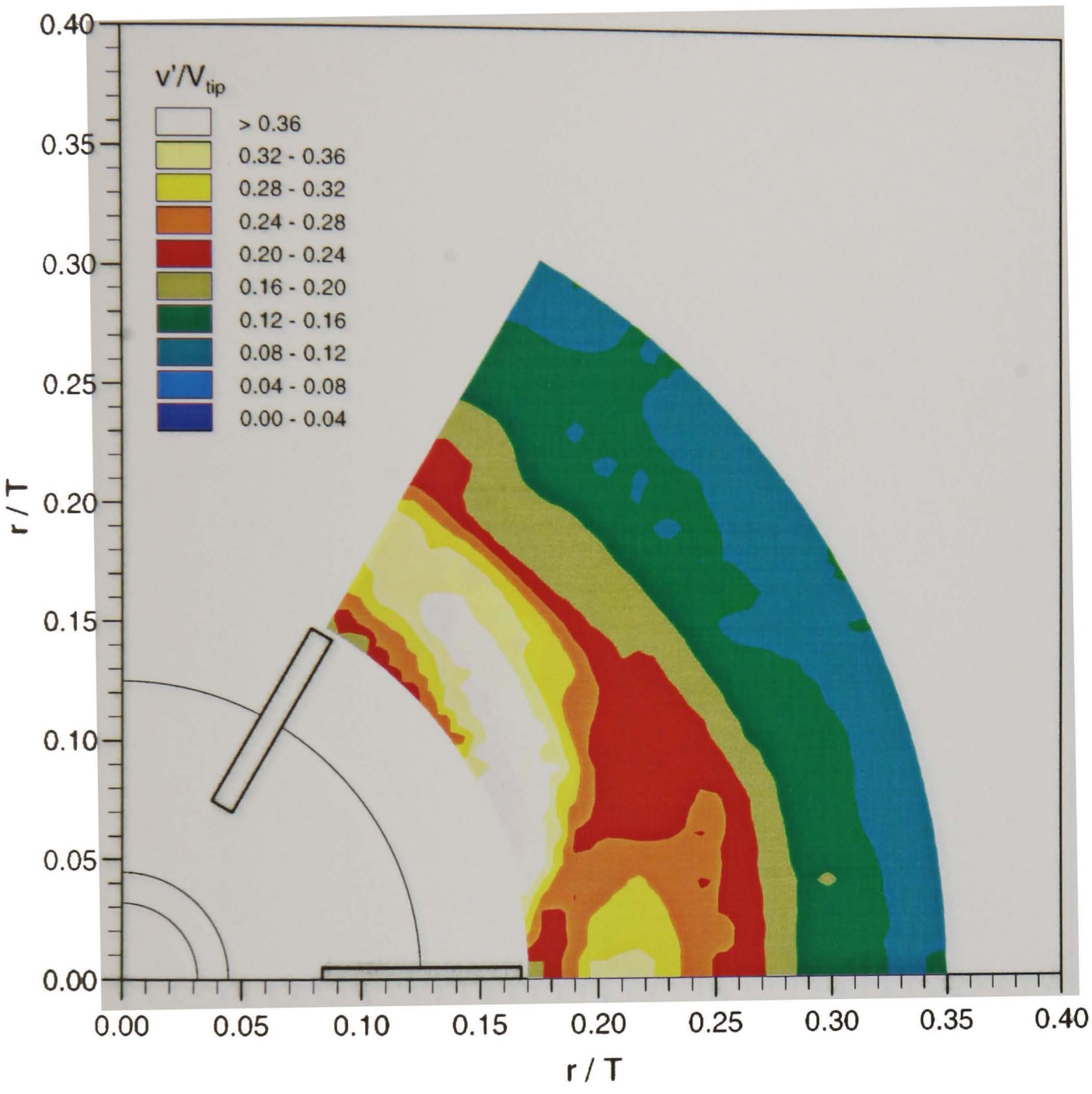


**Figure 5.10** Double Rushton impeller configuration: radial turbulence level contours in the z/T = 0.35 plane.

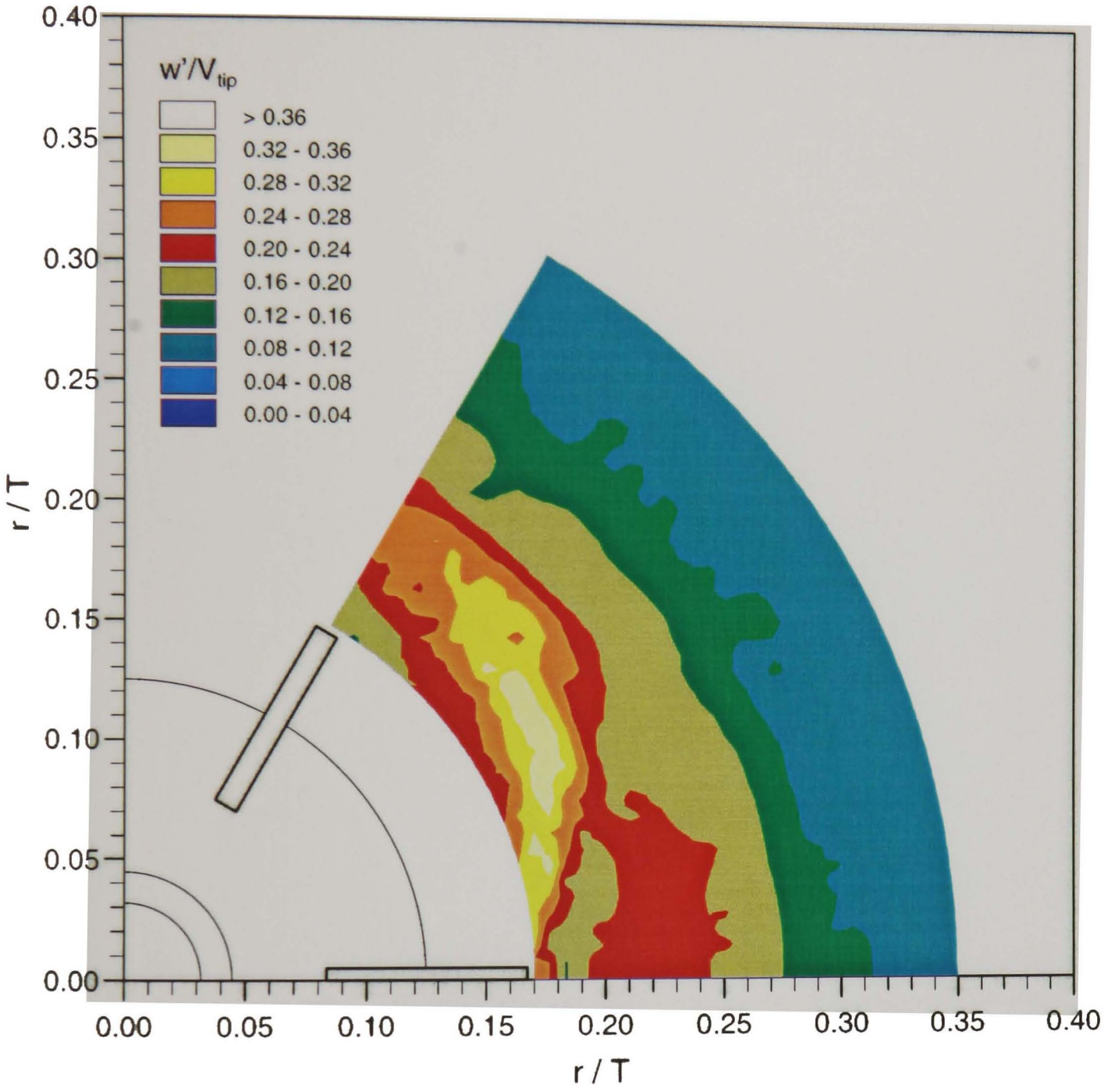


**Figure 5.11** Double Rushton impeller configuration: tangential turbulence level contours in the z/T = 0.35 plane.

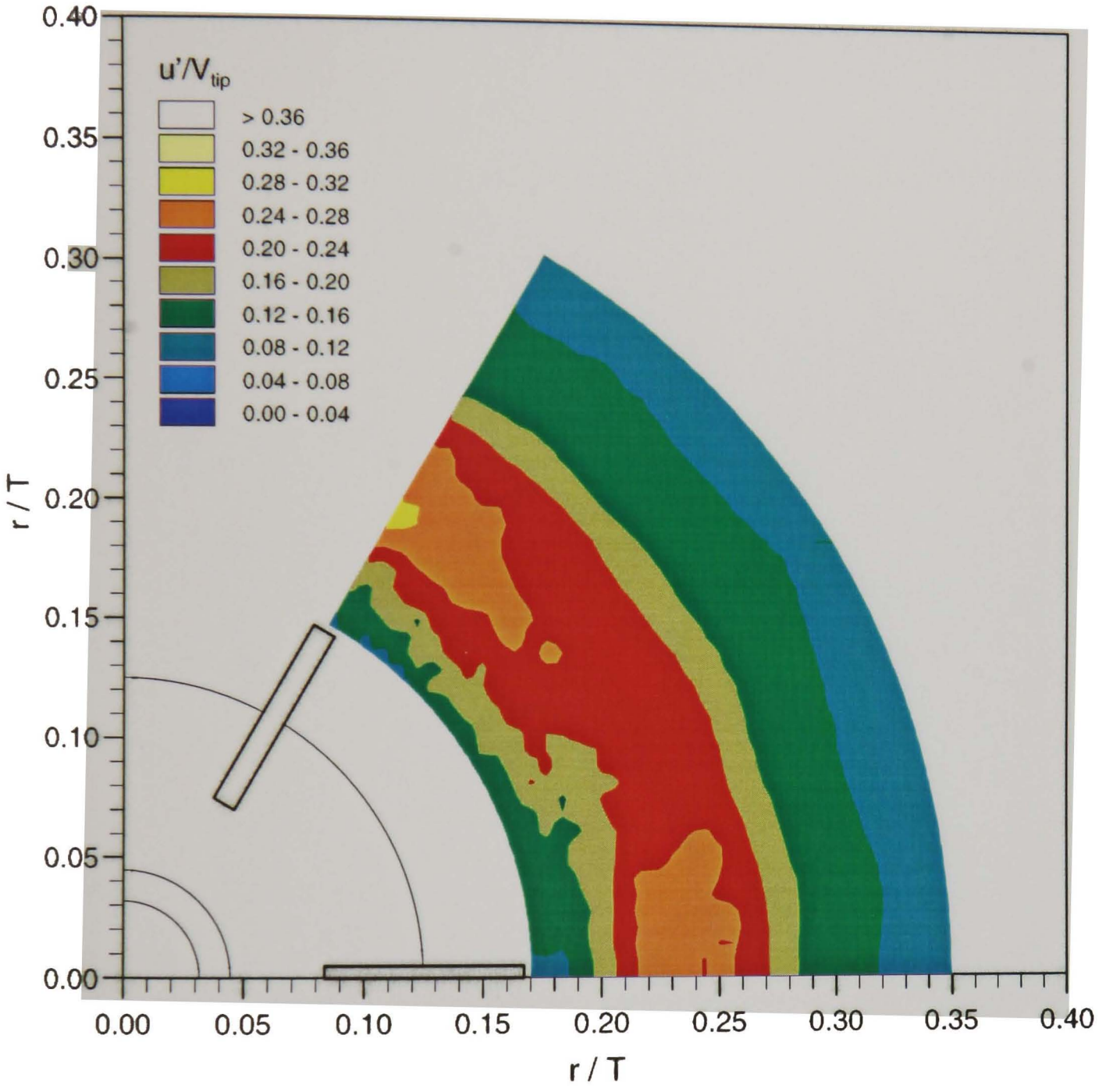


**Figure 5.12** Double Rushton impeller configuration: axial turbulence level contours in the z/T = 0.40 plane.

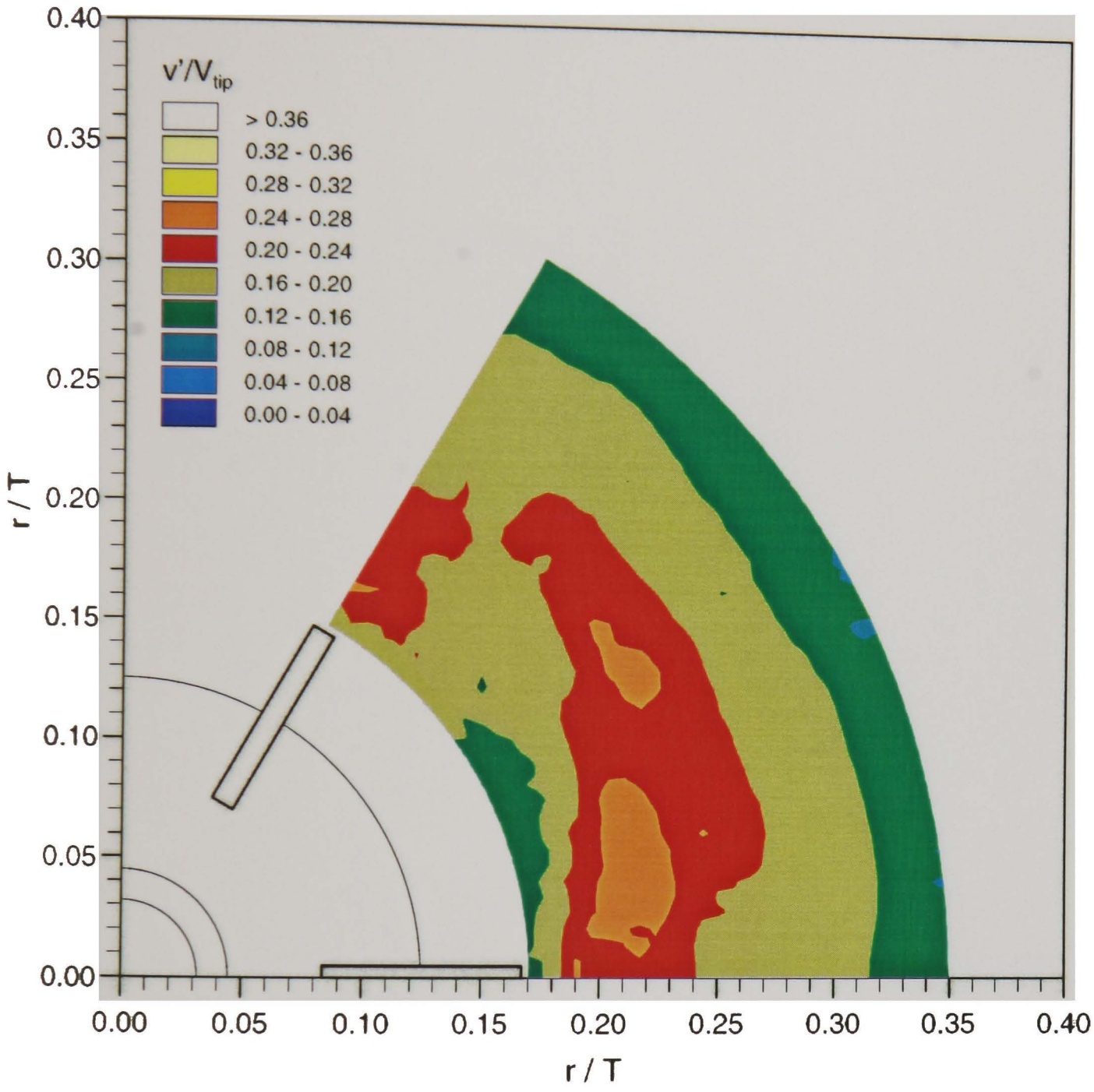


**Figure 5.13** Double Rushton impeller configuration: radial turbulence level contours in the z/T = 0.40 plane.

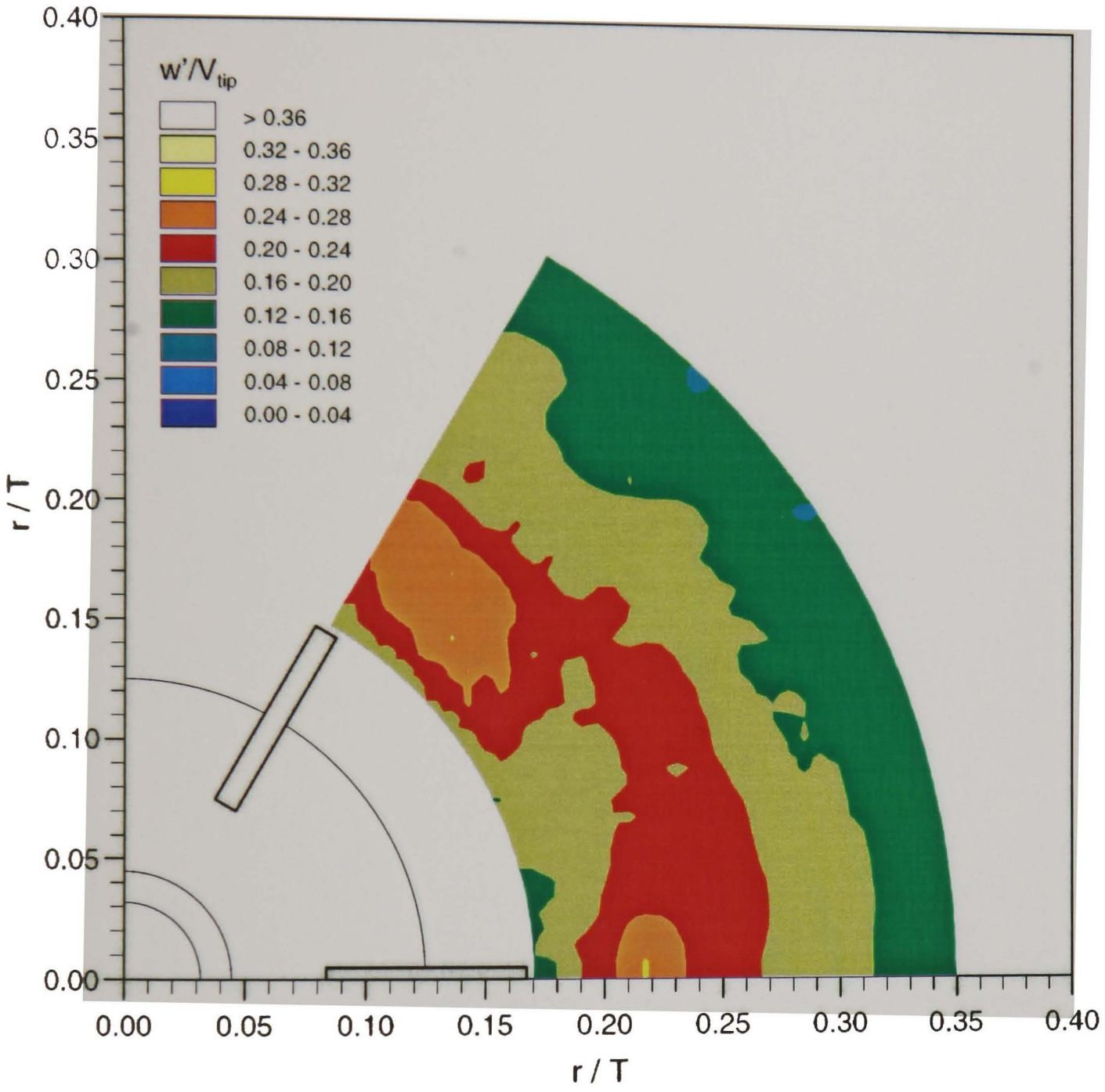


**Figure 5.14** Double Rushton impeller configuration: tangential turbulence level contours in the z/T = 0.40 plane.

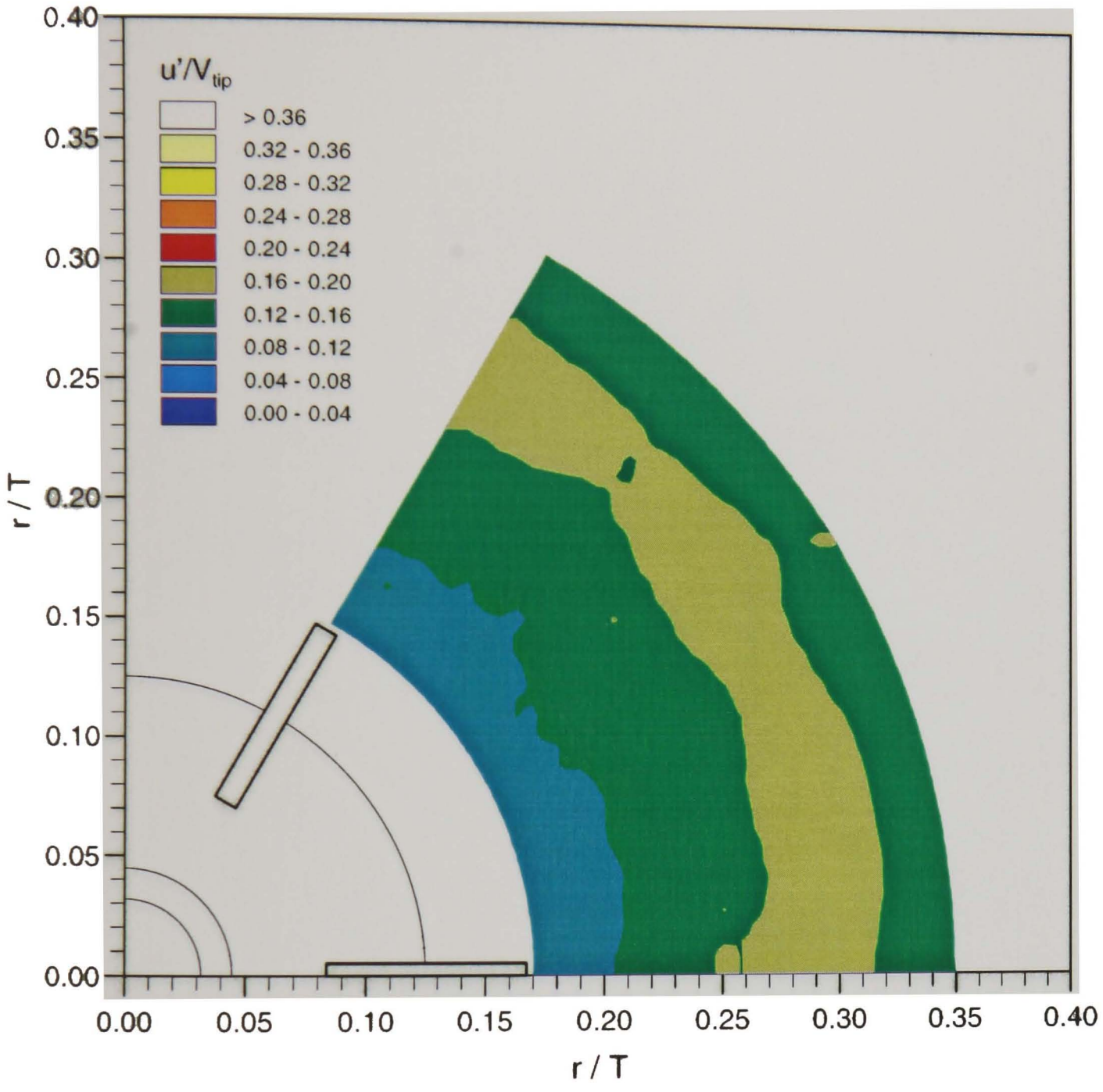


**Figure 5.15** Double Rushton impeller configuration: axial turbulence level contours in the z/T = 0.50 plane.

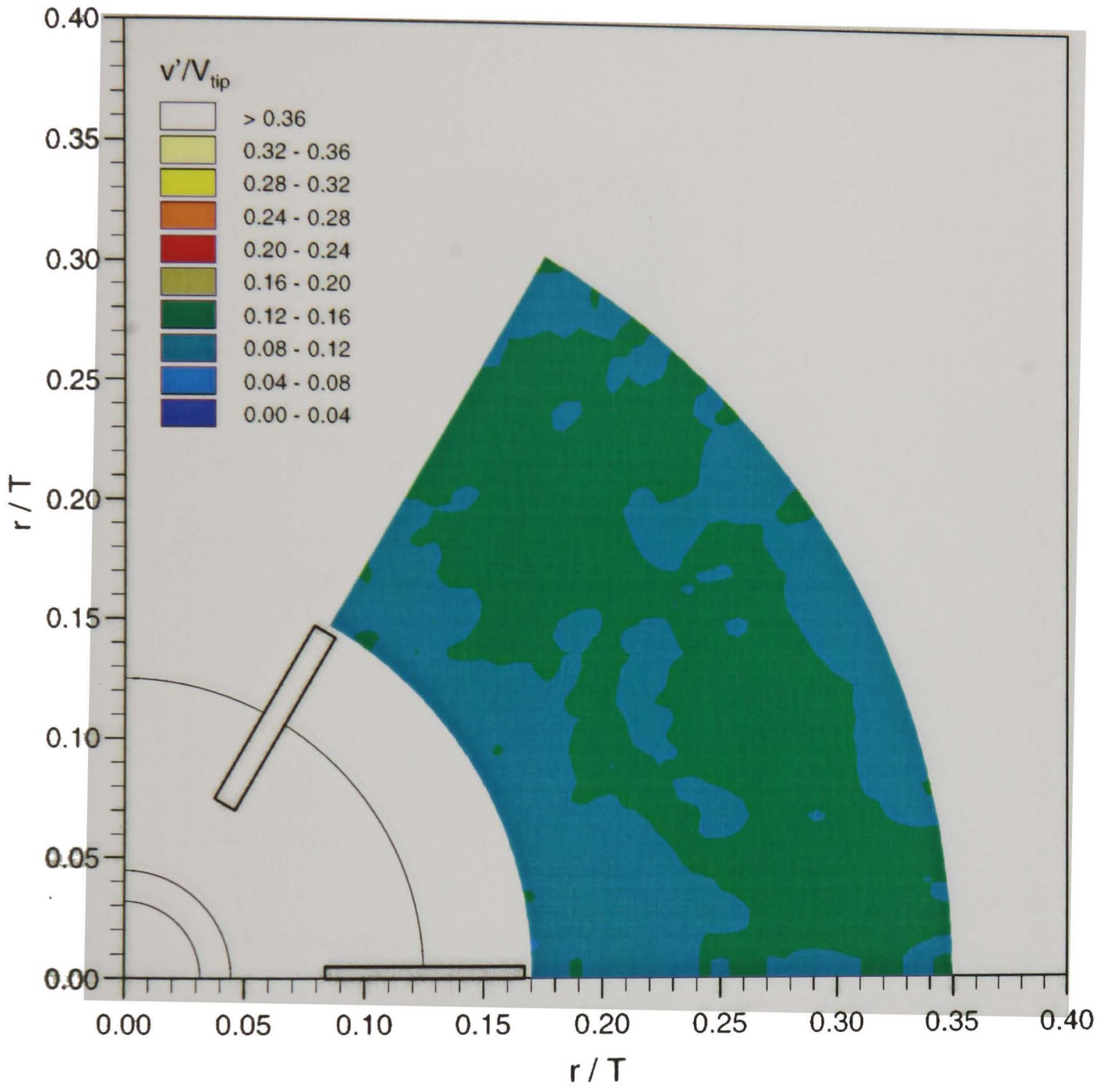


**Figure 5.16** Double Rushton impeller configuration: radial turbulence level contours in the z/T = 0.50 plane.

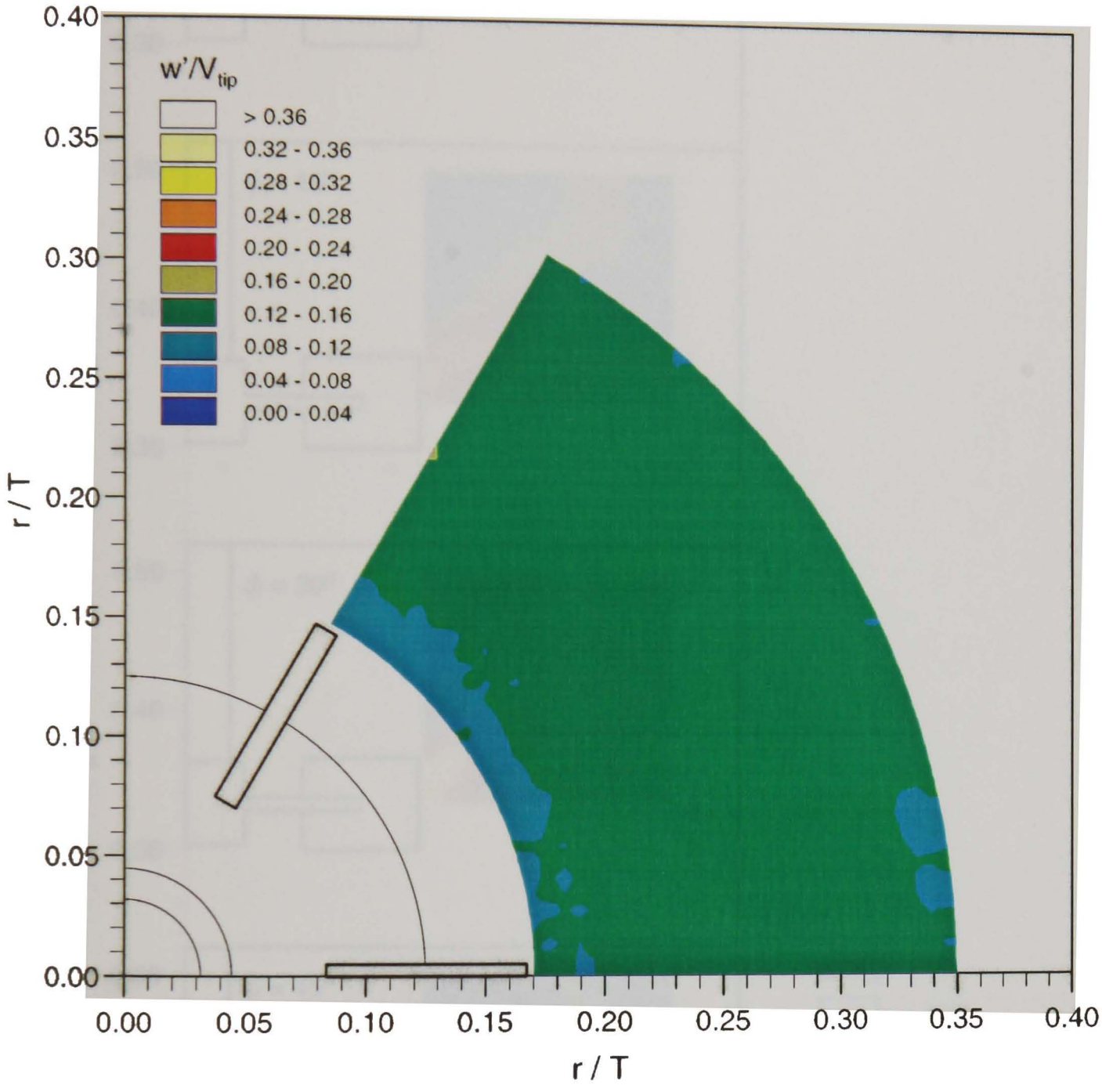


**Figure 5.17** Double Rushton impeller configuration: tangential turbulence level contours in the z/T = 0.50 plane.

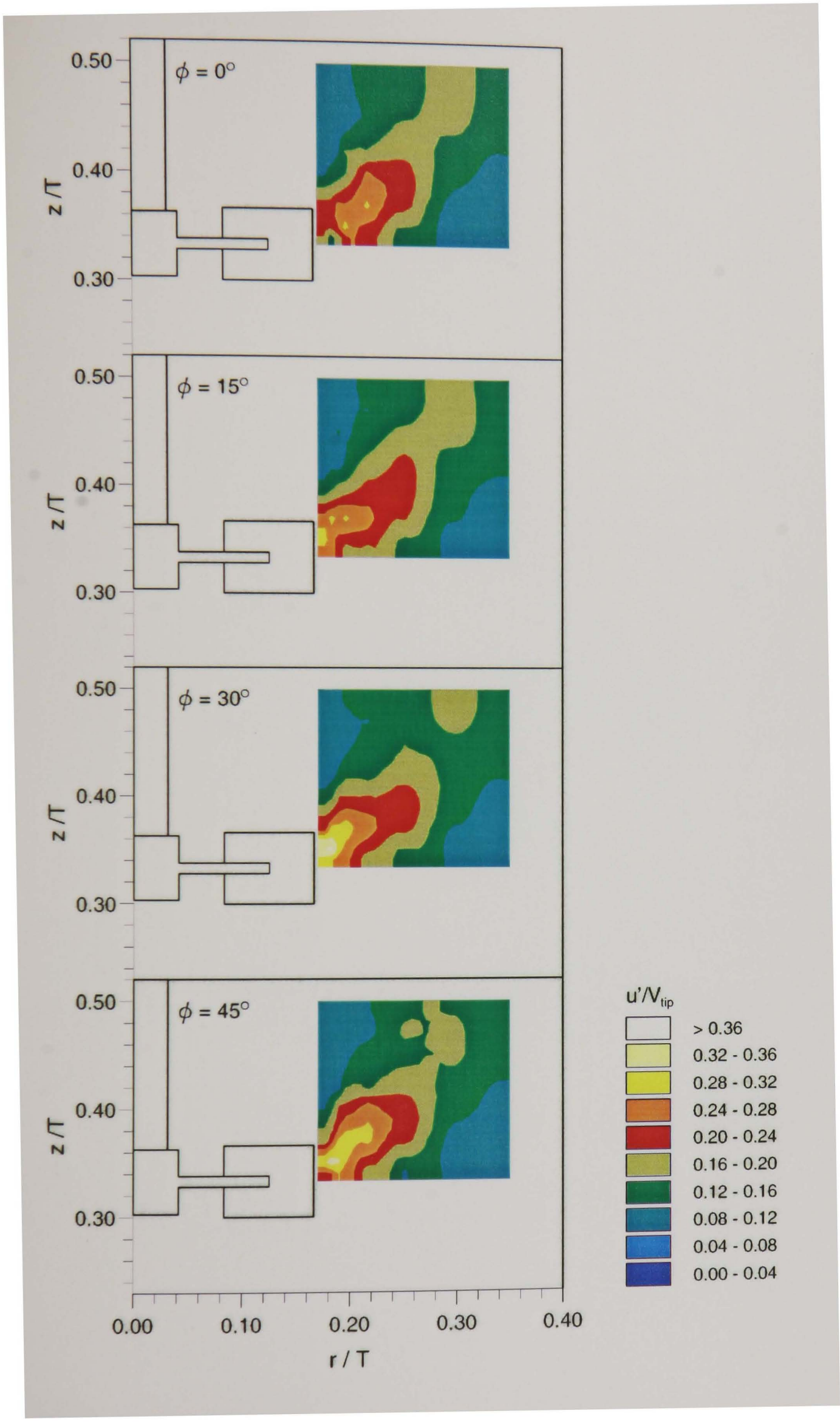


**Figure 5.18** Double Rushton impeller configuration: axial turbulence level contours in the $\phi = 0°$, 15°, 30° and 45° planes.

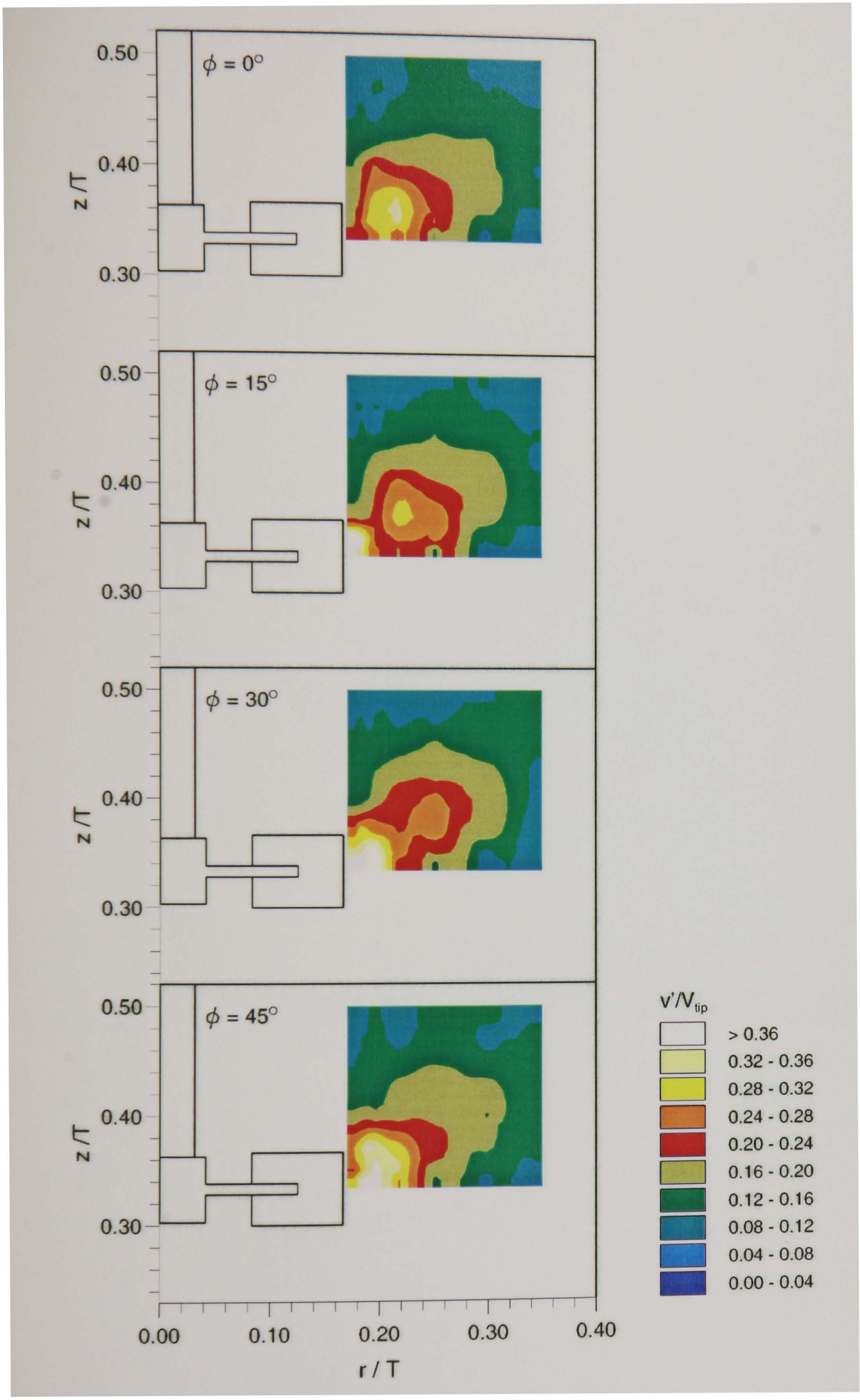


**Figure 5.19** Double Rushton impeller configuration: radial turbulence level contours in the $\phi$ = 0°, 15°, 30° and 45° planes.

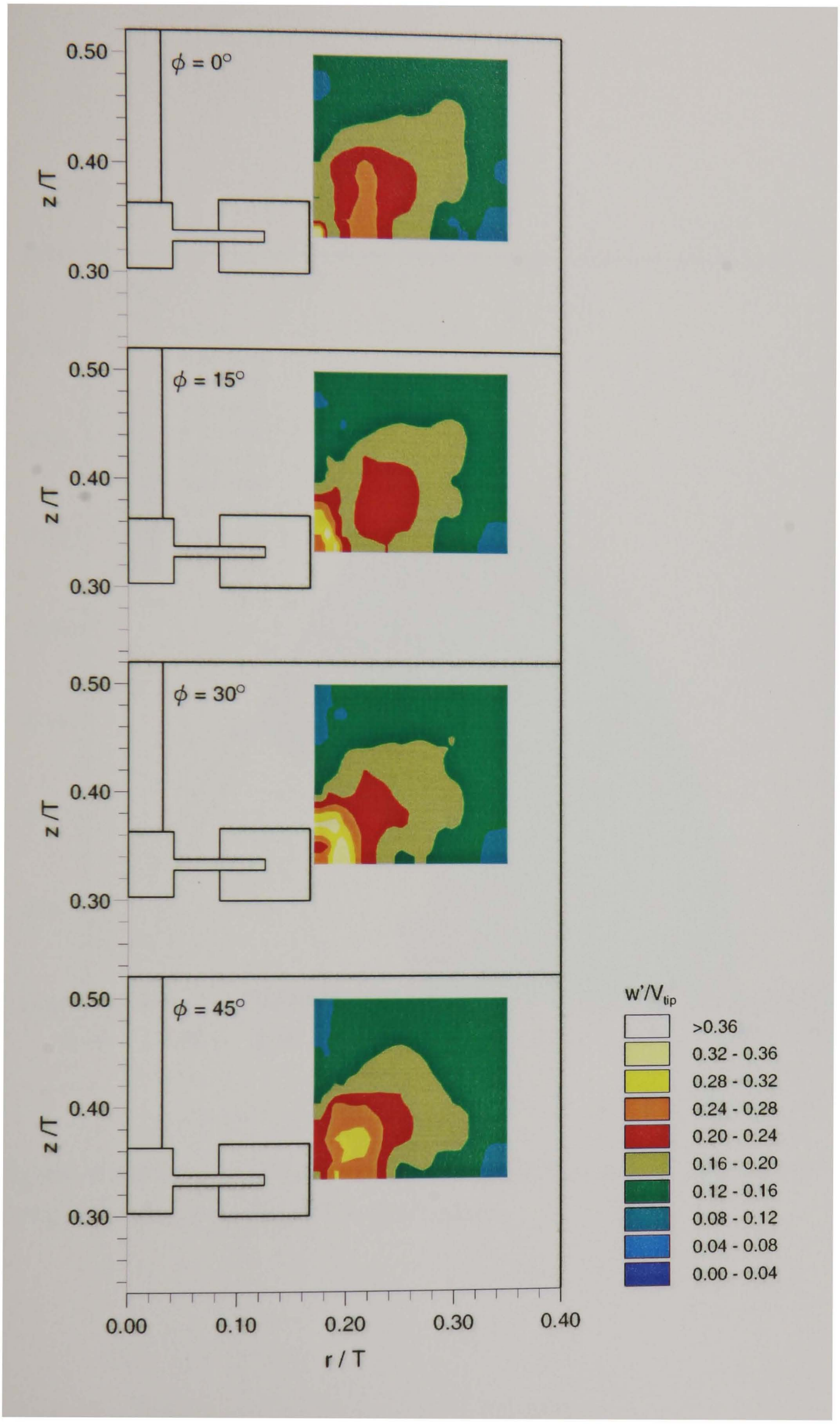


**Figure 5.20** Double Rushton impeller configuration: tangential turbulence level contours in the $\phi$ = 0°, 15°, 30° and 45° planes.

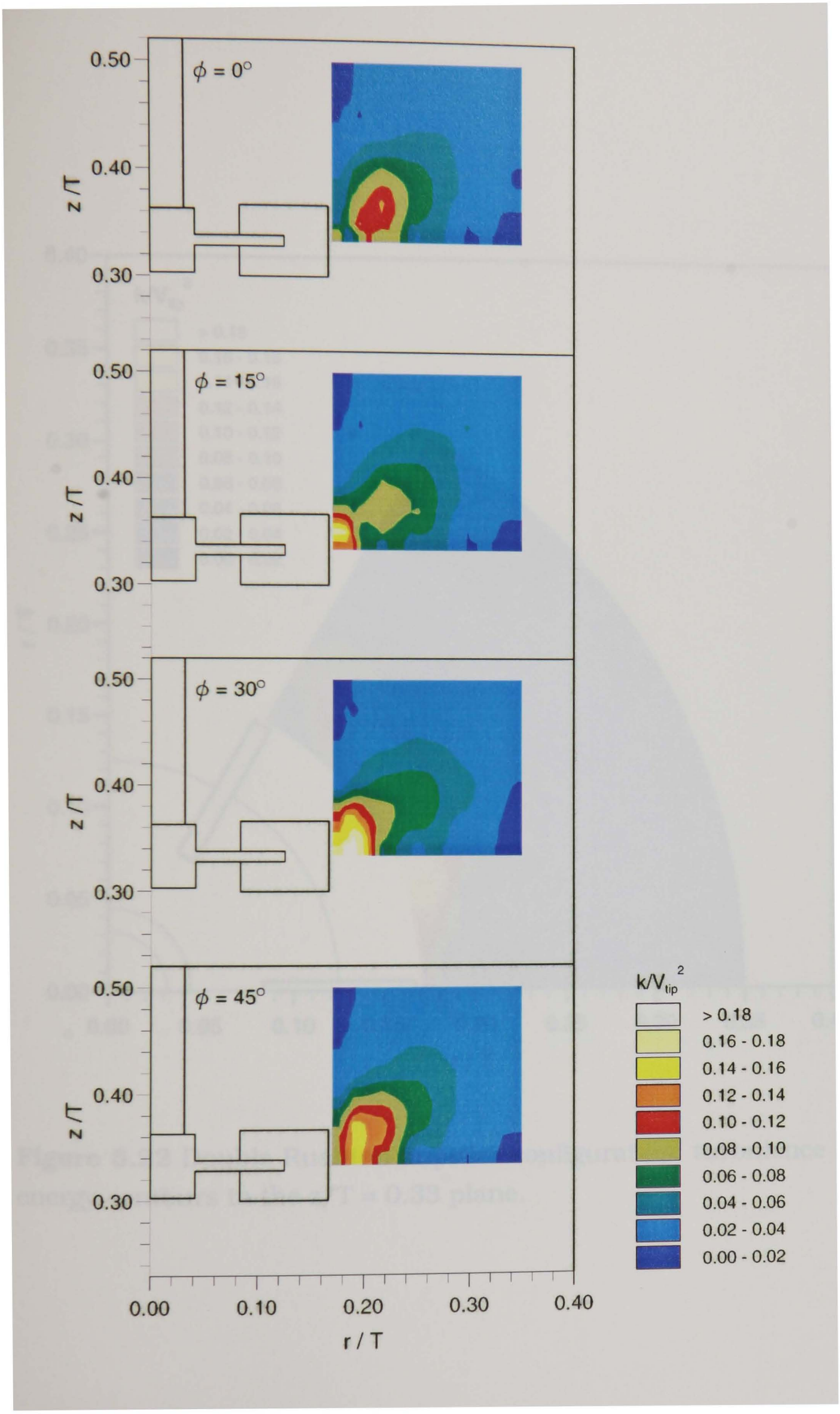


**Figure 5.21** Double Rushton impeller configuration: turbulence kinetic energy contours in the $\phi$ = 0°, 15°, 30° and 45° planes.

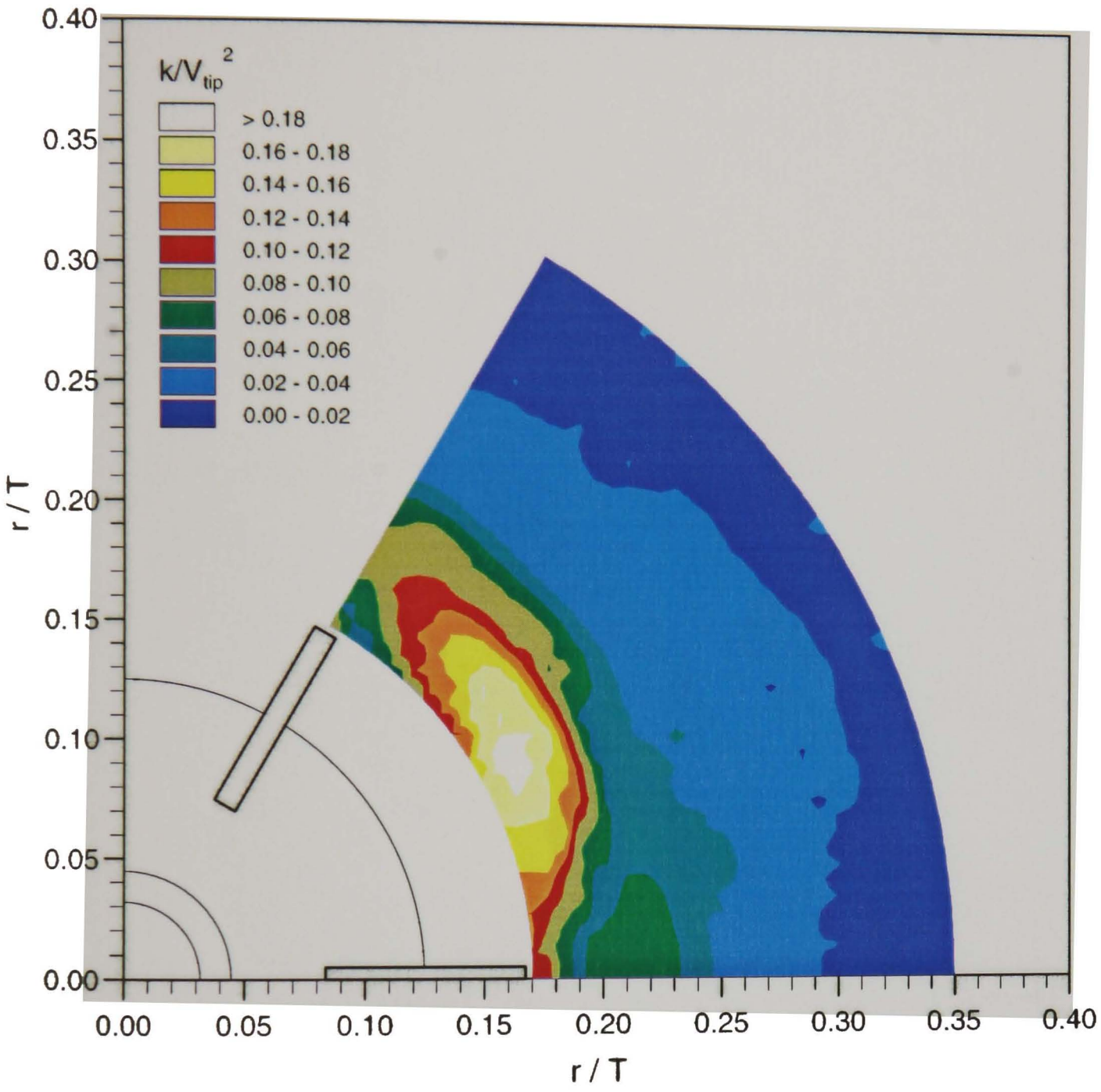


**Figure 5.22** Double Rushton impeller configuration: turbulence kinetic energy contours in the z/T = 0.33 plane.

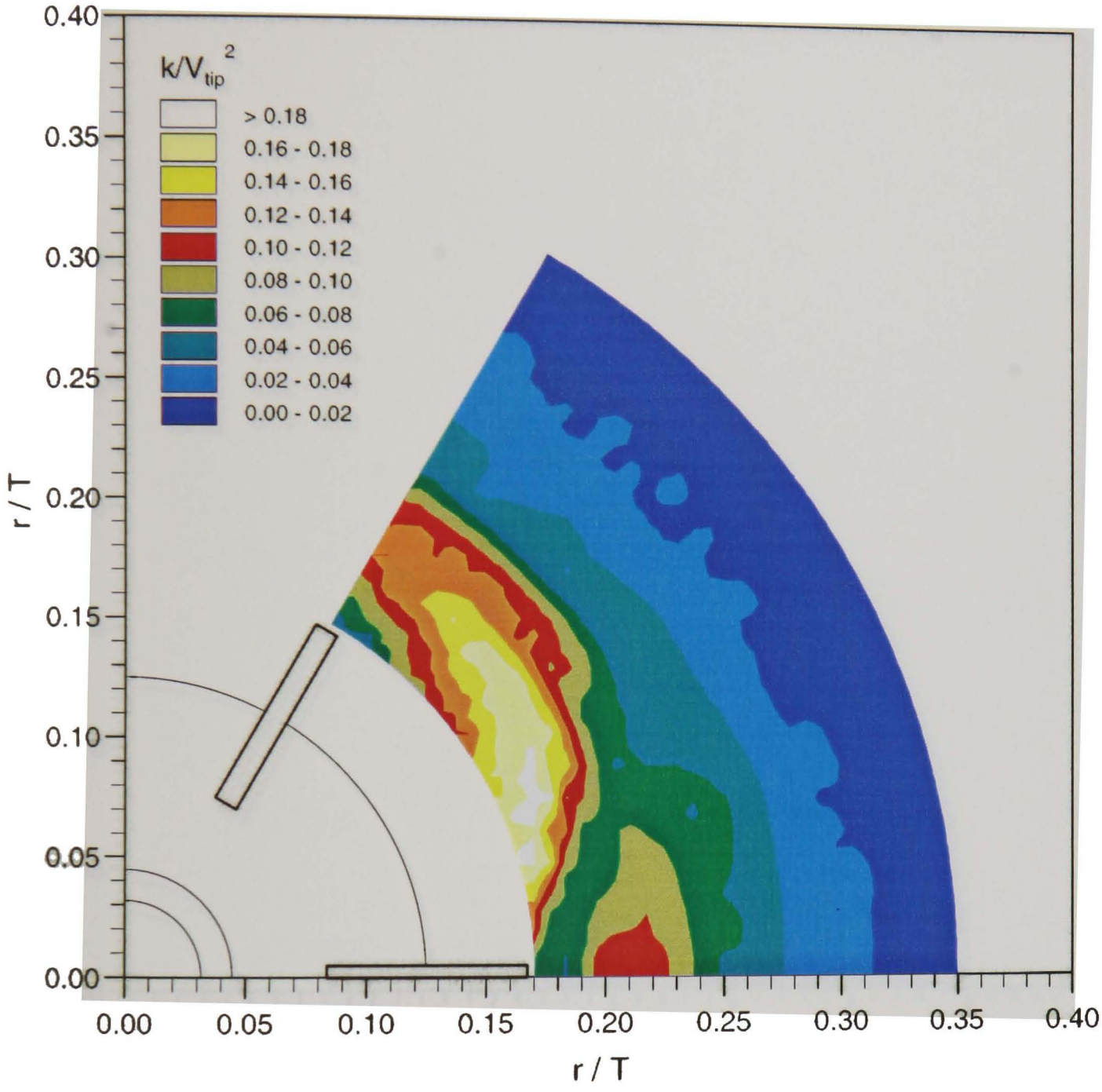


**Figure 5.23** Double Rushton impeller configuration: turbulence kinetic energy contours in the z/T = 0.35 plane.

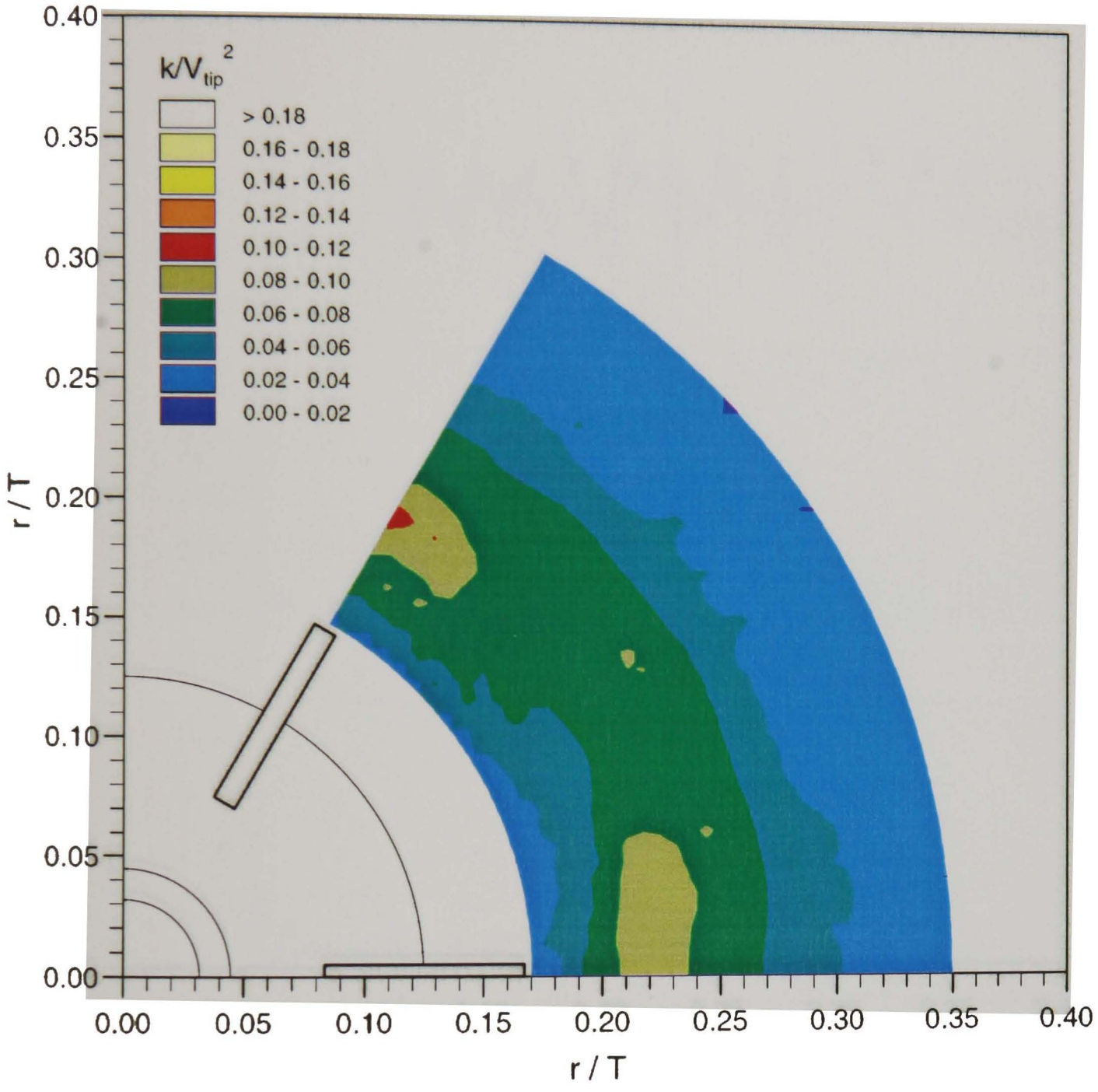


**Figure 5.24** Double Rushton impeller configuration: turbulence kinetic energy contours in the z/T = 0.40 plane.

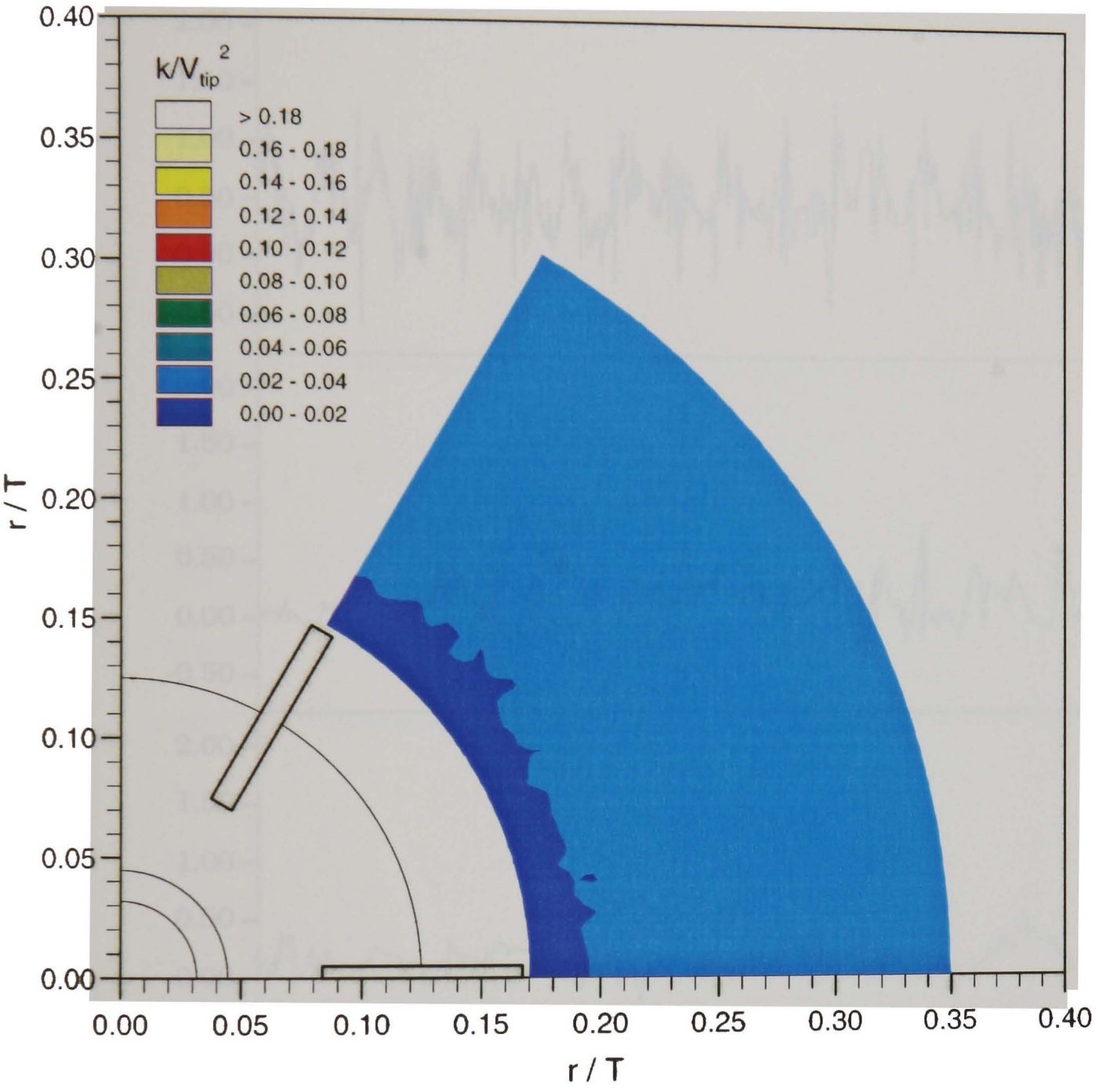


**Figure 5.25** Double Rushton impeller configuration: turbulence kinetic energy contours in the z/T = 0.50 plane.

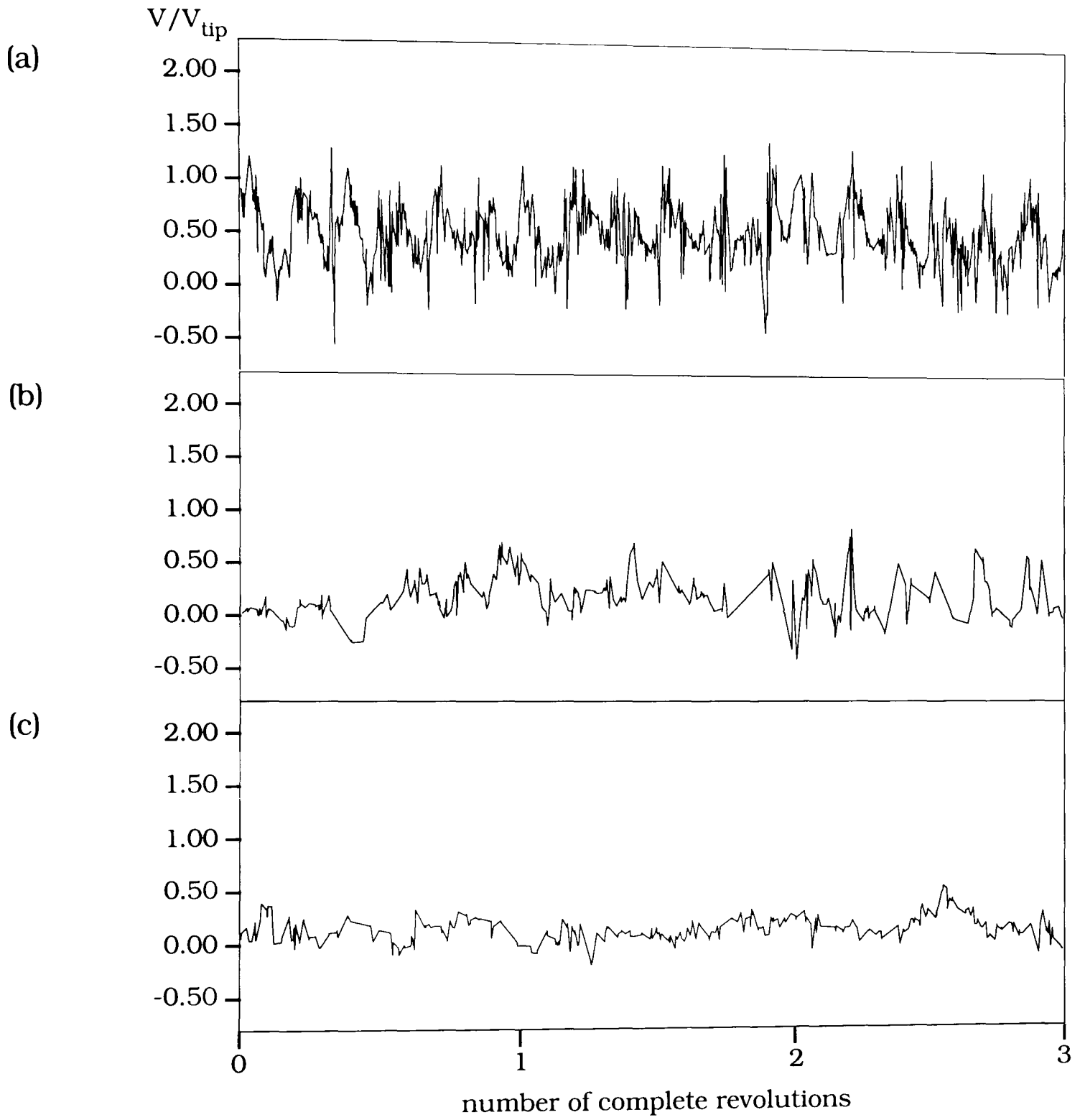


**Figure 5.26** Normalised instantaneous radial velocity recordings made at (a) r/T = 0.17, z/T = 0.33; (b) r/T = 0.25, z/T = 0.41 and (c) r/T = 0.30, z/T = 0.50.

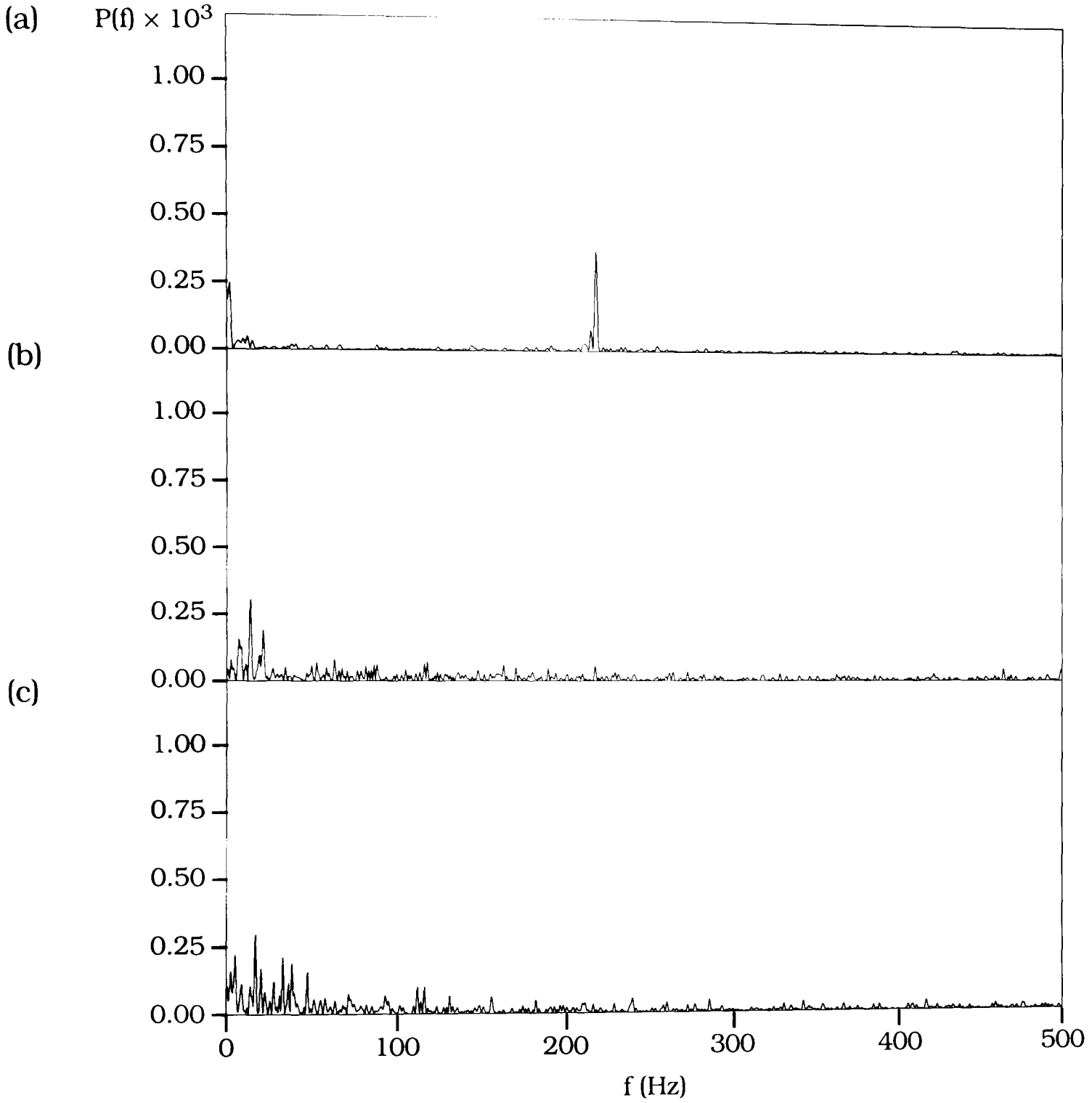


**Figure 5.27** Normalised energy spectra at (a) r/T = 0.17, z/T = 0.33; (b) r/T = 0.25, z/T = 0.41 and (c) r/T = 0.30, z/T = 0.50.

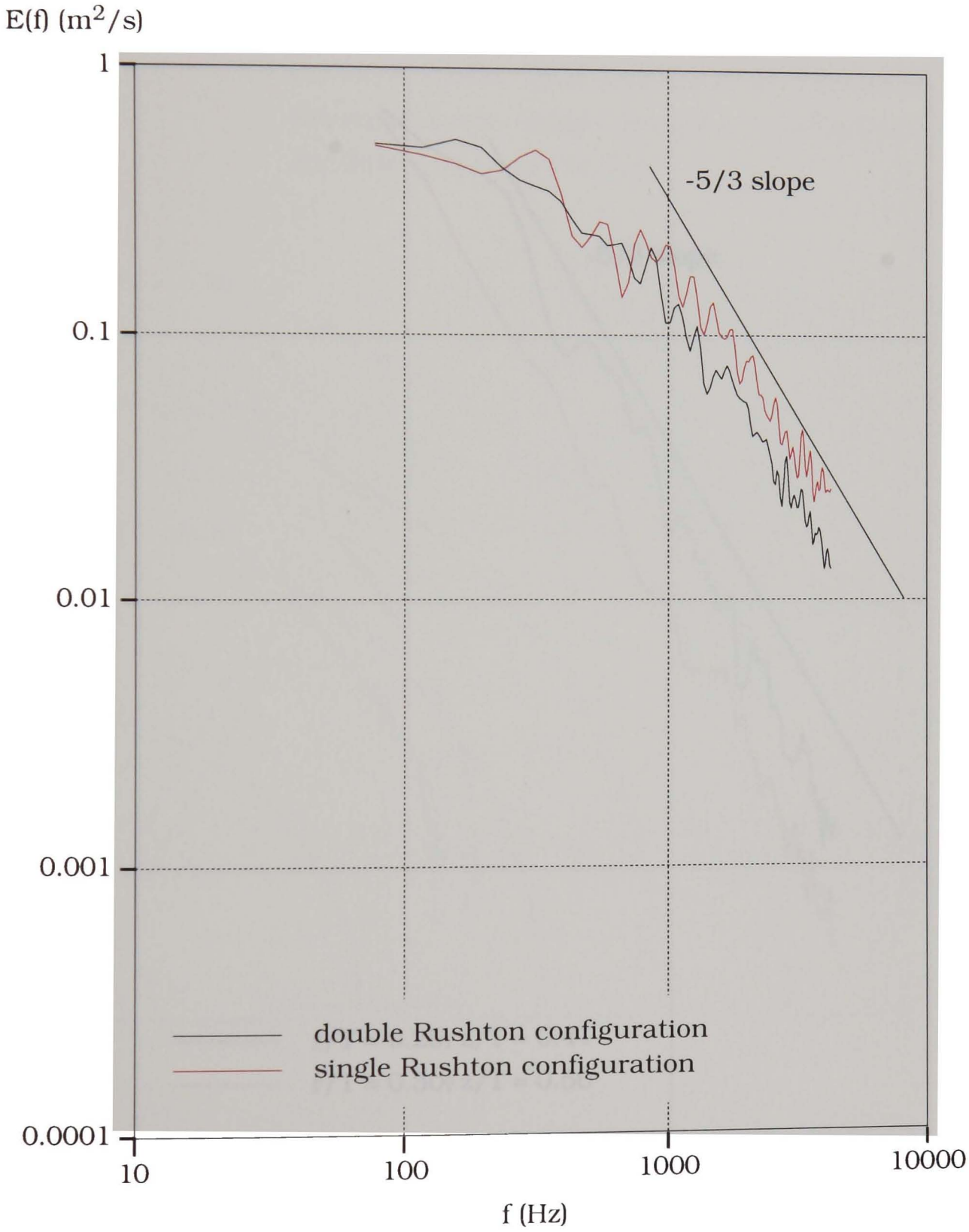


**Figure 5.28** Energy spectra of the radial velocity with the periodic component removed, at r/T = 0.17, z/T = 0.33 with single and double Rushton impeller configurations.

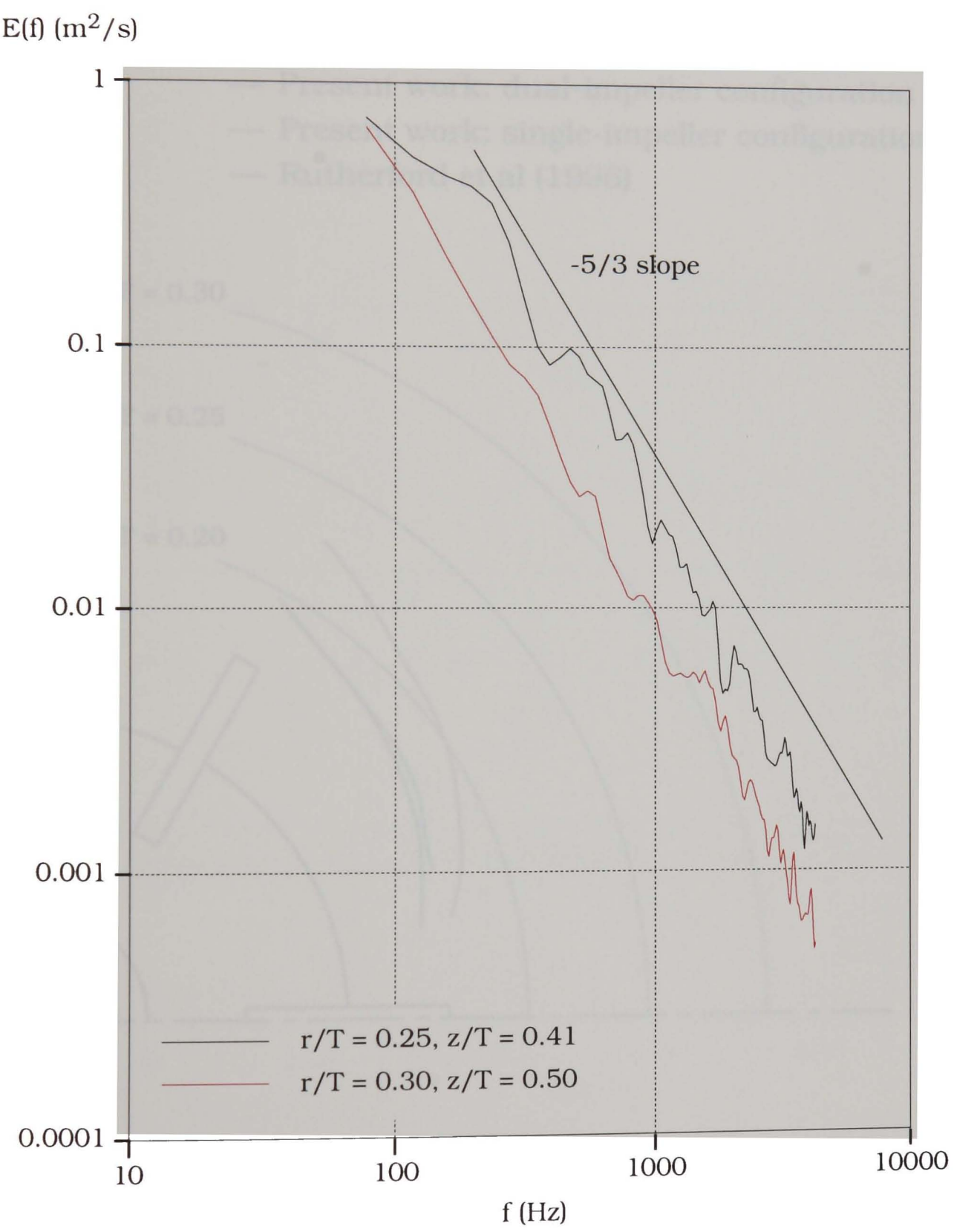


**Figure 5.29** Energy spectra of the radial velocity with the periodic component removed, at r/T = 0.25, z/T = 0.41 and r/T = 0.30, z/T = 0.50 with double Rushton impeller.

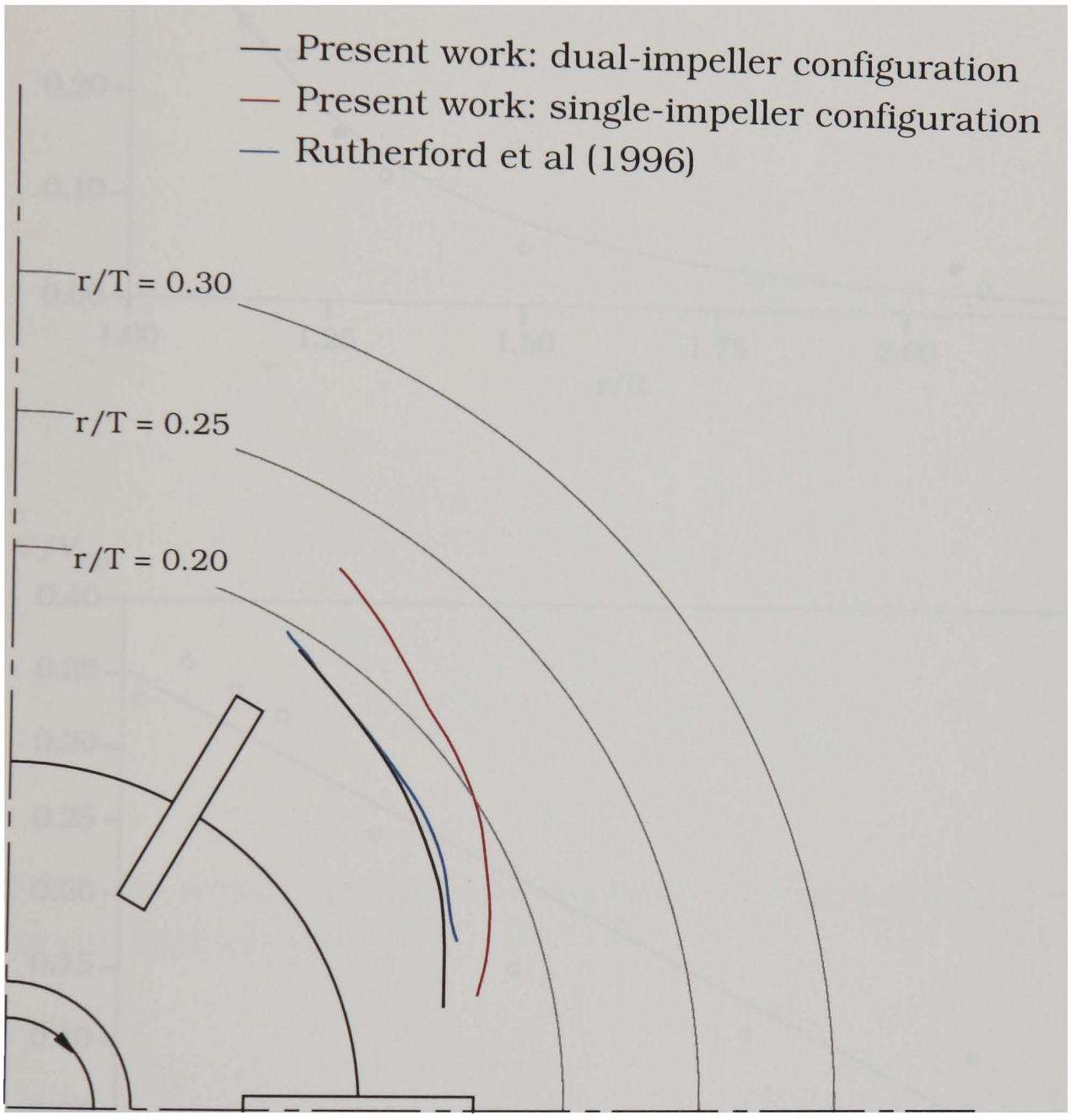


**Figure 5.30** The axis of the trailing vortex shed from the lower Rushton impeller as viewed from above the vessel.

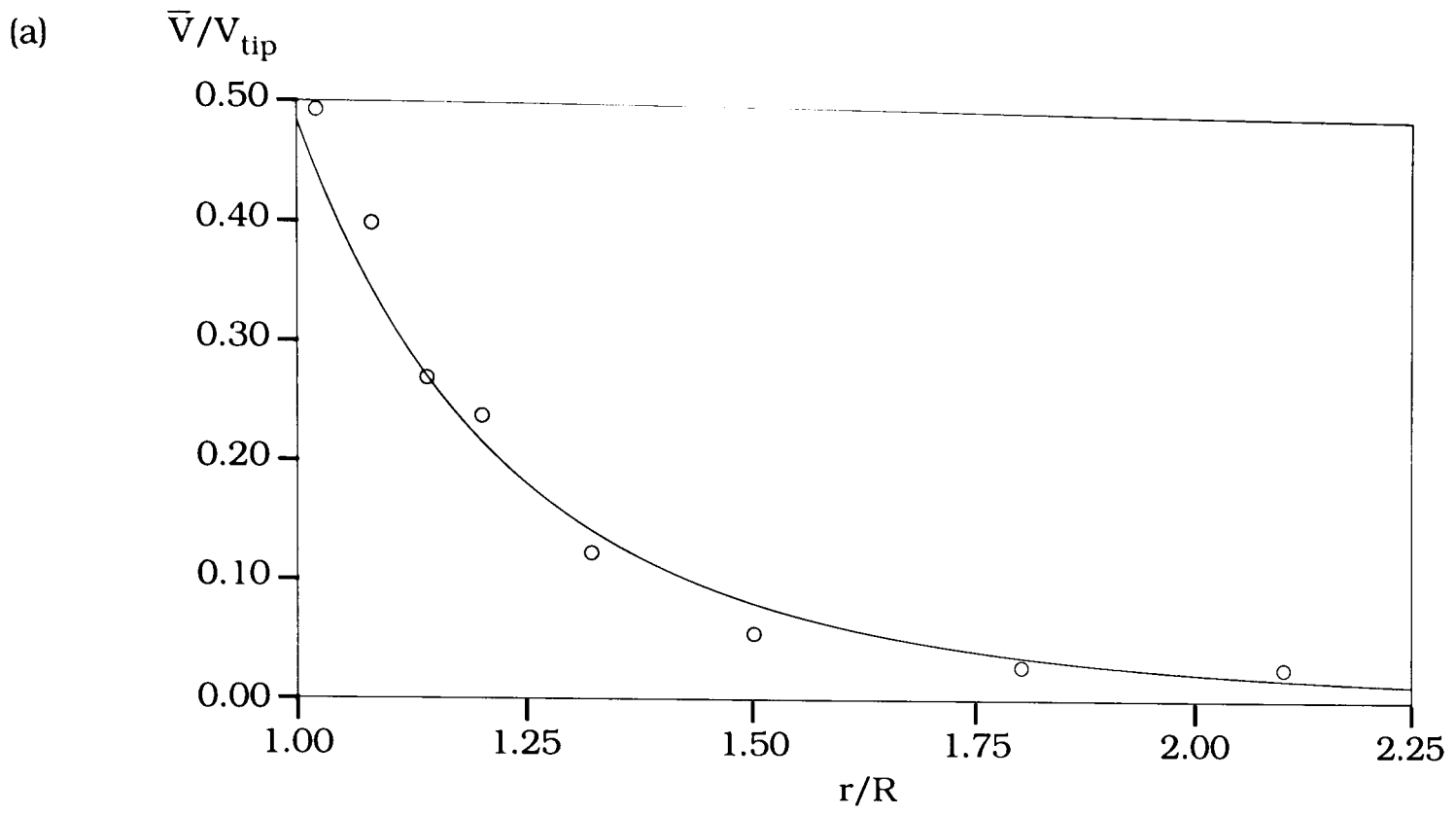


**Figure 5.31** The variation of (a) 360° ensemble-averaged mean velocities and (b) 360° ensemble-averaged turbulence levels with r/R in the z/T = 0.33 plane.

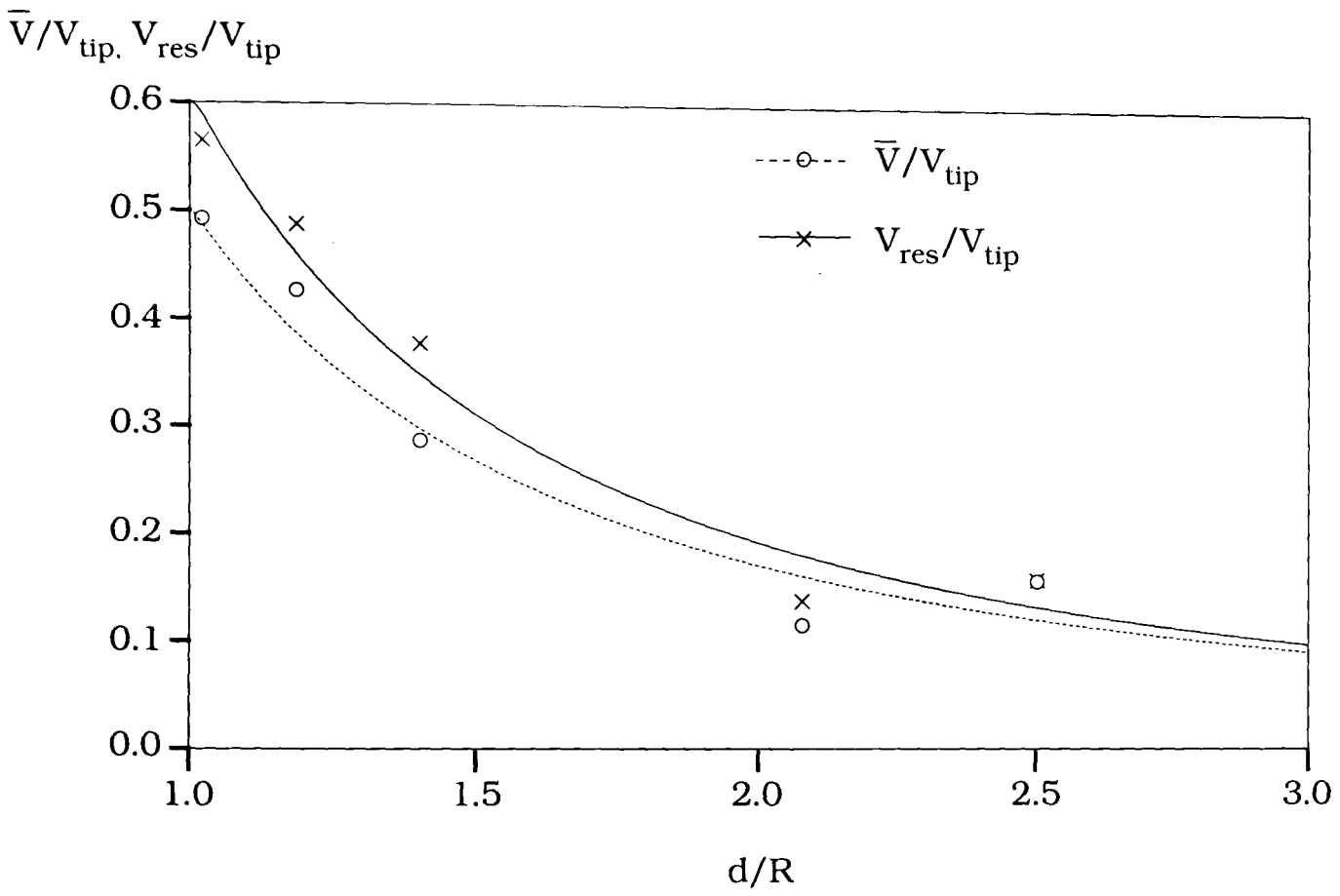


**Figure 5.32** The variation of the 360° ensemble-averaged resultant mean velocity in the impeller stream.

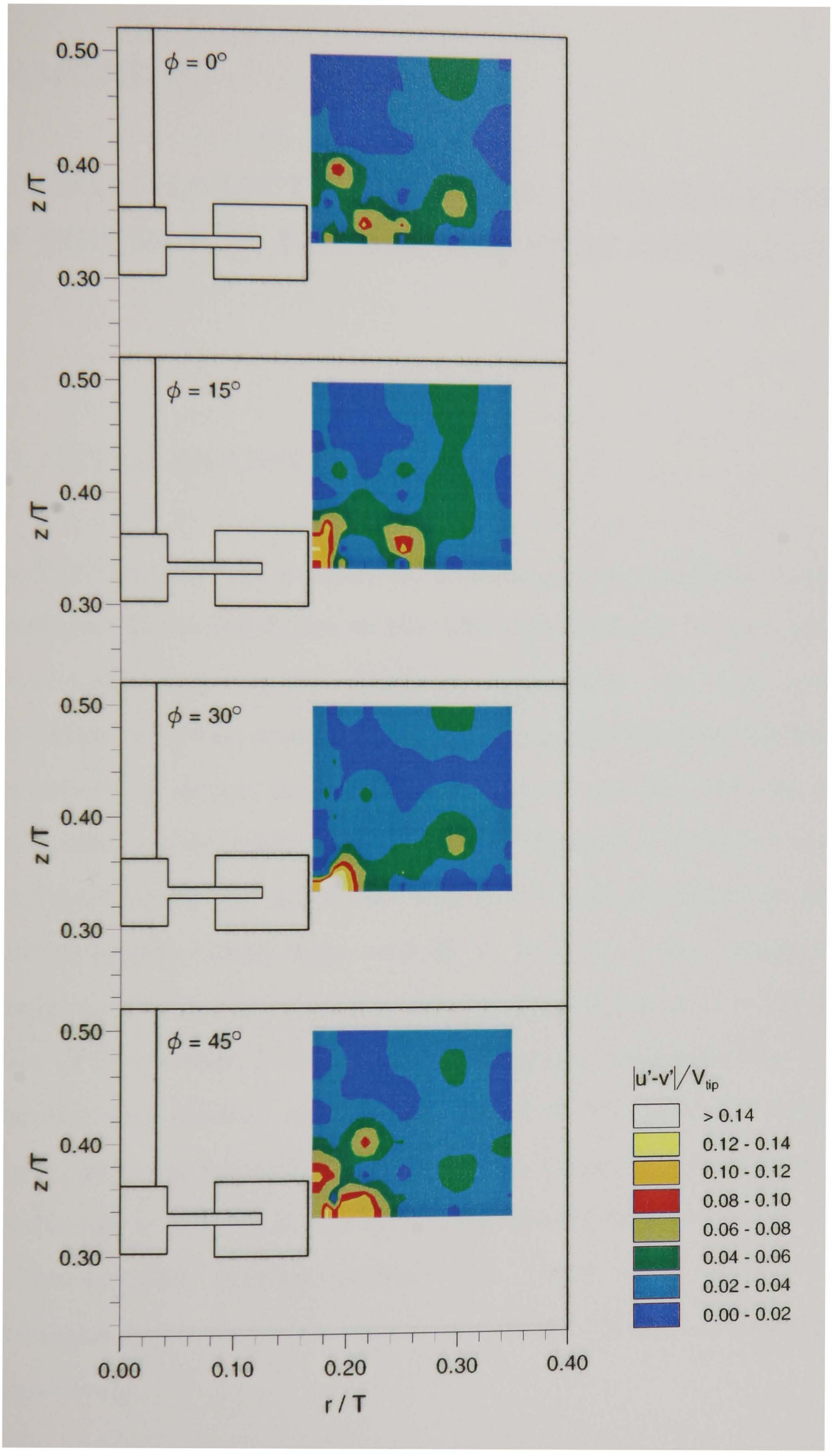


**Figure 5.33** Double Rushton impeller configuration: $|u' - v'|/V_{tip}$ contours in the $\phi = 0°$, 15°, 30° and 45° planes.

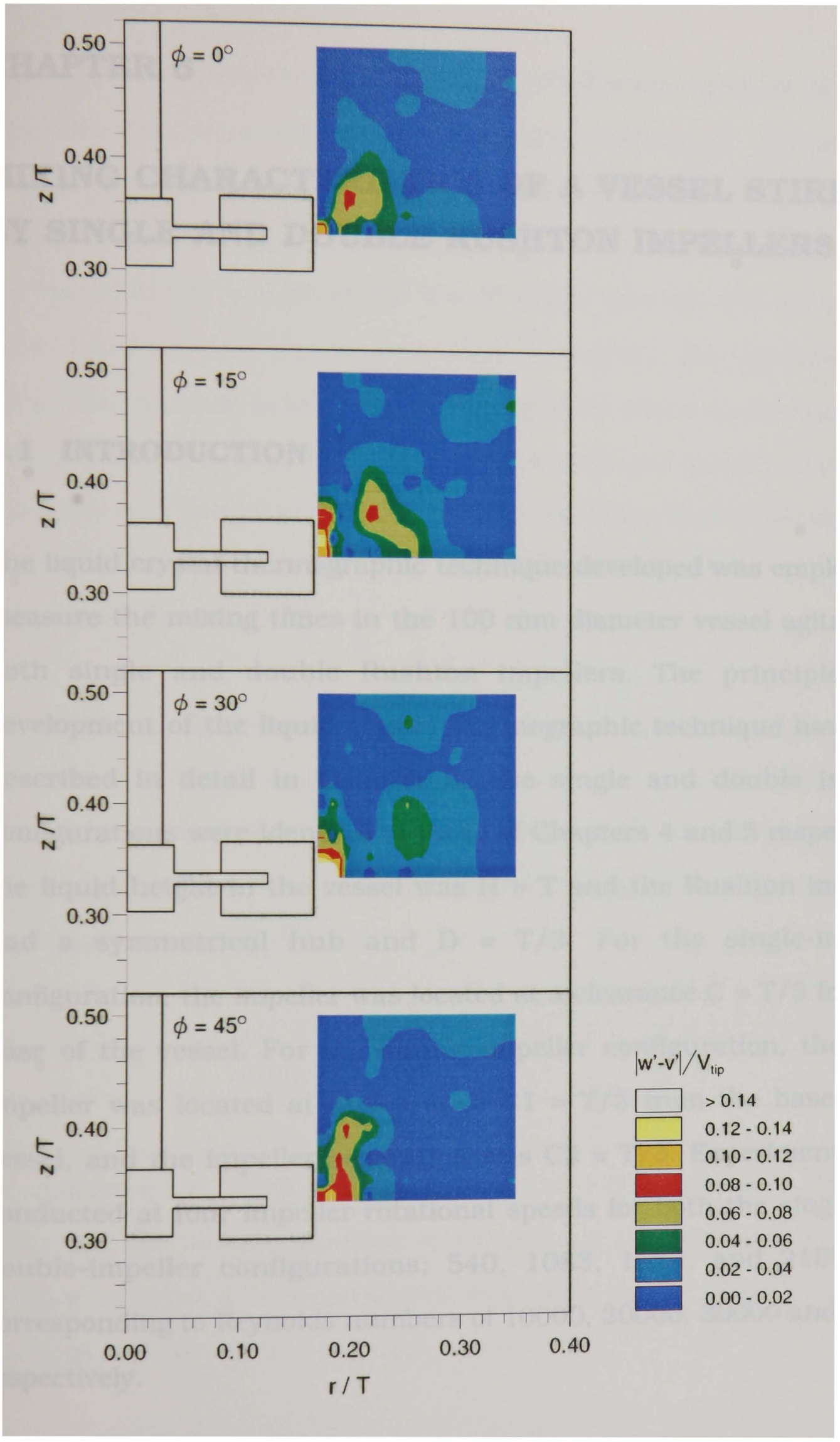


**Figure 5.34** Double Rushton impeller configuration: $|w' - v'|/V_{tip}$ contours in the $\phi = 0°$, 15°, 30° and 45° planes.

# CHAPTER 6

# MIXING CHARACTERISTICS OF A VESSEL STIRRED BY SINGLE AND DOUBLE RUSHTON IMPELLERS

## 6.1 INTRODUCTION

The liquid crystal thermographic technique developed was employed to measure the mixing times in the 100 mm diameter vessel agitated by both single and double Rushton impellers. The principles and development of the liquid crystal thermographic technique have been described in detail in Chapter 3. The single and double impeller configurations were identical to those of Chapters 4 and 5 respectively: the liquid height in the vessel was H = T and the Rushton impellers had a symmetrical hub and D = T/3. For the single-impeller configuration, the impeller was located at a clearance C = T/3 from the base of the vessel. For the double-impeller configuration, the lower impeller was located at a clearance C1 = T/3 from the base of the vessel, and the impeller separation was C2 = T/3. Experiments were conducted at four impeller rotational speeds for both the single- and double-impeller configurations: 540, 1083, 1624, and 2165 rpm, corresponding to Reynolds numbers of 10000, 20000, 30000 and 40000 respectively.

The temperature of the fluid inside the vessel and of the tracer used in the experiments were 25.2°C and 27°C respectively. Thermochromic

liquid crystals encapsulated as gelatine-shell micro-spheres of 20 μm mean diameter were suspended in the fluid in the vessel. A 5 ml tracer of liquid crystals suspended in distilled water, having the same liquid crystal concentration as the fluid inside the vessel was inserted into the vessel at $r/T = 0.25$ in the $\theta = 0°$ plane through the lid and the tracer insertion time was kept constant throughout the experiments at 0.4 s. The transient process of the mixing of the tracer in the vessel was recorded onto video tape at a rate of 25 frames per second. The tracer insertion was performed after the video recording had commenced so that the time of the start of the insertion could be accurately ascertained.

The video recording of each of the processes was subsequently subjected to a frame-by-frame analysis to determine the time between the frame at which the insertion of the tracer commenced ($n_i$) and the frame at which the process was fully-mixed ($n_m$). The mixing time of the process ($\theta_m$) was then obtained from:

$$\theta_m = \frac{n_m - n_i}{\text{frame rate}} \qquad (6.1)$$

As mentioned in Chapter 3, mixing time was determined by means of analysing the hue distribution of the colours displayed by the liquid crystals. A process was considered to be fully-mixed when 95% of the pixels in each image had the same value of hue.

The colours displayed by the liquid crystals depend on the lighting condition as well as on the image collection angle. Therefore these

conditions were optimised so that during the calibration experiments the values of hue of all pixels were within ±5 of the mean value of hue at any particular temperature. Although the impellers and the shaft were painted matt black in order to minimise reflections, strong scatter of light was observed in the vicinity of the impellers and shaft as well as near the vessel wall, lid and base. Therefore, analysis of the hue of the images obtained was not carried out in these regions.

## 6.2 RESULTS WITH SINGLE-RUSHTON IMPELLER CONFIGURATION

Characteristic unprocessed (colour) images obtained from a recording made with the flow stirred by a single impeller at a speed of 540 rpm are shown in Figures 6.1 – 6.6. Only half of the vessel cross-section at the $\theta = 0°$ plane is shown.

Figure 6.1 shows the image obtained 160 ms after the start of the insertion of the tracer. The tracer jet, which was at a higher temperature than the fluid in the vessel, is indicated by the blue region of the figure. It can be seen that 160 ms after the insertion the jet has penetrated as far as the impeller region. The tracer jet path is affected by the impeller stream, curving slightly towards the vessel wall.

280 ms after the insertion of the tracer (Figure 6.2), the jet of the tracer has moved further towards the vessel wall under the influence of the impeller stream, and has reached the bottom of the vessel.

Figures 6.3 and 6.4 show the images obtained at 400 ms and 480 ms after the insertion of the tracer respectively. The greenish-blue regions underneath the impeller that can be observed in these two figures, indicate that the temperature in these regions is between the temperature of the tracer and the temperature of the cooler fluid of the vessel, and indicate vigorous mixing of the tracer with the cooler fluid.

Figure 6.5 shows the image obtained at 720 ms after the insertion of the tracer. Greenish-blue regions can still be observed near the bottom of the vessel, indicating that the fluid in the vessel is not fully-mixed yet. In contrast, the nearly uniform colour observed in the image obtained at 1.80 s after the start of the insertion of the tracer (Figure 6.6) indicates that the fluid in the vessel is nearly fully-mixed.†

Though the colour exhibited by the images presented above can provide a visual indication of the local temperature, in order to determine the mixing time, the images obtained were subjected to a pixel-by-pixel analysis to obtain the hue distribution of the image. The hue contours of the images shown in Figures 6.1 – 6.6 are presented in Figures 6.7 – 6.12 respectively.

The hue contour map of the image obtained 160 ms after the start of the insertion of the tracer is shown in Figure 6.7. The jet of the tracer, which was at a higher temperature than the fluid in the vessel, is indicated by the region of hue values between 120 and 150 (shown in brown and red).

---

† It should be noted that, as the velocity of tracer insertion was relatively high, the mixing time measurements could be affected. This could result in an underestimation of $\theta_m$ in the

Figure 6.8 shows the hue contour map of the image obtained 280 ms after the start of the insertion of the tracer. The region of hue values higher than 120 again indicate the jet of the tracer, which has moved further towards the vessel wall under the influence of the impeller stream and has reached the bottom of the vessel. As in Figure 6.7, locally high hue values (above 135) can be observed in the core of the tracer jet.

Figure 6.9 shows the hue contour map of the image obtained 400 ms after the start of the insertion of the tracer. The region with hue values between 120 and 135 observed between the bottom the vessel and z/T = 0.20, indicates that the tracer jet has been deflected by the bottom of the vessel and is moving upwards. The contour map shown in Figure 6.10, 480 ms after the start of the insertion, indicates that most of the tracer is located now below z/T = 0.50. Again, locally high hue values (above 150) can be observed in the core of the tracer jet in both Figures 6.9 and 6.10.

Figure 6.11 shows the hue map of the image obtained 720 ms after the start of the insertion of the tracer. Regions of high hue values can be observed only below the impeller. At 1.80 s after the start of the insertion of the tracer (Figure 6.12), the hue values in most regions are between 105 and 120, indicating that the fluid inside the vessel is nearly fully-mixed.

Images obtained from the recordings obtained with higher impeller speeds showed similar mixing behaviour to that described above. Hue analysis was performed on the images obtained with all impeller speeds

investigated to determine the mixing times. The mixing times found were 1.92 s, 1.04 s, 0.68 s and 0.60 s for impeller speeds of 540, 1083, 1624 and 2165 rpm respectively.

## 6.3 RESULTS WITH DOUBLE-RUSHTON IMPELLER CONFIGURATION

Unprocessed (colour) images obtained from a recording made with the flow stirred by two Rushton impellers at a speed of 540 rpm are shown in Figures 6.13 – 6.18. As for the single-Rushton configuration, they show only half of the entire flow field. For comparison purposes, Figures 6.13 – 6.17 correspond to the same time intervals as Figures 6.1 – 6.5 presented in the previous section.

Figure 6.13 shows the image obtained 160 ms after the start of the insertion of the tracer. The tracer which has a higher temperature than the fluid inside the vessel is again indicated by the blue colour region in the figure. Figure 6.14 shows the image obtained 280 ms after the start of the insertion of the tracer. It can be observed that the tracer has reached the bottom of the vessel. At 400 ms after the start of the insertion (Figure 6.15), the tracer jet has spread along the base of the vessel to $r/T \approx 0.10$, while 80 ms later (Figure 6.16) it has reached the vessel axis.

Figures 6.13 – 6.16 indicate that the tracer jet is affected relatively slightly by the stream of the upper impeller which is also flowing downwards. The jet is more strongly affected by the counter-flowing

(upward) stream of the lower impeller. As a result of the combined influence of both impeller streams, the jet is curved away from the vessel axis and impinges on the wall at around z/T = 0.45. The tip of the tracer jet can be clearly observed in Figures 6.14 – 6.17 to move under the influence of the lower ring vortex (see Chapter 5) from r/T = 0.25 and z/T = 0.05 at 280 ms to r/T = 0.10 and z/T = 0.20 at 480 ms. It should be noted that the propagation of the tip of the tracer jet (e.g. around 20 mm in 120 ms between Figures 6.14 and 6.15) is consistent with the flow velocities of around 0.05 – 0.1 $V_{tip}$ that have been previously reported (Mahmoudi, 1994).

By 720 ms after the start of the insertion (Figure 6.17) the tracer can be distinguished only below the lower impeller. Finally, Figure 6.18 shows the image obtained 1.12 s after the start of the insertion of the tracer. The greenish-blue colour observed over the entire flow field in this figure indicates that the fluid inside the vessel is almost fully-mixed. The time taken to reach this state is shorter than with the single-impeller configuration (1.80 s). The time to reach fully-mixed conditions was 1.68 s, as described below.

Images obtained for impeller speeds of 1083,1624 and 2165 rpm revealed mixing patterns similar to that observed for 540 rpm. It should be noted however that as the impeller speed is increased, more rigorous mixing takes place in the vessel, mixing times are shorter, and consequently the tracer jet is dispersed progressively more in the upper part of the vessel. Although this was also observed in the single impeller experiments, it is more pronounced in this case due to the more rigorous mixing achieved by the two impellers.

Hue analysis of the images obtained for all the impeller speeds investigated were performed using the calibration data, to determine the mixing times. The average mixing times found were 1.68 s, 0.88 s, 0.56 s and 0.48 s for impeller speeds of 540, 1083, 1624 and 2165 rpm respectively.

## 6.4 DISCUSSION

Since the number of revolutions required to achieve fully mixing in an agitated tank is essentially a constant for a particular geometry (Tatterson, 1991), N and $\theta_m$ can be related by :

$$N\theta_m = K \tag{6.2}$$

where N is the impeller speed in rev/s, $\theta_m$ is the mixing time in seconds, and K is a constant. The values of $N\theta_m$ obtained for both the single- and double-impeller configurations are listed in Table 6.1.

**Table 6.1** $\theta_m$ and $N\theta_m$ at various impeller speeds with single- and double-impellers.

| | | Single-impeller configuration | | Double-impeller configuration | |
|---|---|---|---|---|---|
| N (rev/s) | Re | $\theta_m$ (s) | $N\theta_m$ | $\theta_m$ (s) | $N\theta_m$ |
| 9 | 10000 | 1.92 | 17.28 | 1.68 | 15.12 |
| 18 | 20000 | 1.04 | 18.72 | 0.88 | 15.84 |
| 27 | 30000 | 0.68 | 18.36 | 0.56 | 15.12 |
| 36 | 40000 | 0.60 | 21.60 | 0.48 | 17.28 |

The average values of $\theta_m$ were obtained from 4 experiments, with the exception of the case of N = 2165 rpm with double-impeller configuration, which was obtained from 3 experiments. For each experimental condition, the $\theta_m$ values were repeatable to within ±80 ms.

It can be seen from Table 6.1 that the values of $N\theta_m$ for both the single- and double-impeller configurations are approximately constant up to a Reynolds number of 30000. At the higher Re (40000), the values of $N\theta_m$ for both configurations are higher. These higher values can be partly attributed the comparatively long tracer insertion time. The insertion time was 0.40 s in all cases, corresponding to nearly 67% and 83% of the mixing times at 2165 rpm for the single- and double-impeller configurations respectively. Clearly, shorter insertion times cannot be achieved in practice and most studies to-date have employed pulse injections of tracer lasting around 0.5 – 1.0 s (for example, Armstrong and Ruszkowski, (1988) and Mahmoudi (1994)). Although this represents a limitation of mixing times studies carried out in small vessels and with high impeller speeds to achieve dynamic similarity, the average $N\theta_m$ values are not strongly affected. For example, the average values of $N\theta_m$ determined from the experiments at all four Reynolds numbers are 18.99 and 15.84 for the single- and double-impeller configurations respectively. The corresponding average values for the three lower Reynolds number are 17.97 and 15.36 respectively, i.e. they are smaller by only 5.4% and 3.1% respectively.

The average $N\theta_m$ values obtained were compared with those reported in the literature for single Rushton turbines. Prochazka and Landau (1961) developed a mixing time correlation for a Rushton impeller in a baffled tank in the standard configuration above Re = $10^4$:

$$N\theta_m = 0.905 \left(\frac{T}{D}\right)^{2.57} \log\left(\frac{X_0}{X_c}\right) \qquad (6.3)$$

where $X_0$ was an initial value at which fluctuated between 1.0 and 3.0, and the other symbols have their usual meanings. A value of 2.0 was recommended for $X_0$ and the quantity $X_c$ was the integral mean value of the local degree of inhomogeneity defined as:

$$X_c = \left[ \frac{C(t) - C_x}{C_x - C_i} \right] \tag{6.3a}$$

where $C_i$ and $C_x$ were the initial and final concentrations respectively, and $X_c$ was considered to be 0.05 for most configurations. Using the recommended values for $X_0$ and $X_c$, and substituting the values of T and D used in the present work into Equation 6.3, $N\theta_m$ was found to be 24.4, which is 22% higher than the value obtained for the single-impeller configuration in the present work.

Moo-Young et al (1972) correlated their mixing time results using:

$$N\theta_m = K\ Re^a \tag{6.4}$$

where K = 36 and a = 0 for turbines in baffled tanks for $10^3 < Re < 10^5$. Substituting these values into Equation 6.4, the value of $N\theta_m$ is found to be 36. A similar value of $N\theta_m$ was reported by Shiue and Wong (1984). They found $N\theta_m$ = 34 for a Rushton impeller located at a clearance of C = 0.325H. Again these values are both higher than that obtained in the present study for the single-impeller configuration.

Sano and Usui (1985) provided an expression for mixing times of tracer injection for turbines:

$$N\theta_m = 3.8 \left(\frac{D}{T}\right)^{-1.80} \left(\frac{W}{T}\right)^{-0.51} n_p^{-0.47} \qquad (6.5)$$

where $n_p$ is the number of blades and the other symbols have their usual meanings. Using Equation 6.5 for the single-impeller configuration of the present work, the value of $N\theta_m$ was 38.34. For the double-impeller configuration, considering the addition of an impeller as increasing the number of blades from 6 to 12, the value of $N\theta_m$ obtained using Equation 6.6 was found to be 27.68. These two values are both higher than those obtained in the present study. For continuous flow systems, values of $N\theta_m$ up to 50 have been reported (Biggs, 1963).

There are four likely reasons for the differences between the $N\theta_m$ values determined in this work and those reported in the literature. First, the wide variation in $N\theta_m$ values obtained with the different published correlations (24.4, 34, 36 and 38.34) may be due to differences in experimental procedure and/or the definition of when the 'fully-mixed' state is achieved (e.g. 90% or 95% of the final concentration of tracer). Second, tracer insertion times have not been reported in some of the aforementioned studies, but they may affect the $N\theta_m$ value determined. Evidence for this is provided in the work of Mahmoudi (1994) who employed a single Rushton impeller in a 294 mm diameter vessel which was otherwise identical to the 100 mm vessel used in the present study. He reported an average mixing time of 12.8 s with an insertion time of 6.5 s. The corresponding $N\theta_m$ values are around 45 – 50 compared with the values of up to 38 reported by other investigators. Mahmoudi's

results indicate, as might be expected, that comparatively longer insertion times will result in larger $N\theta_m$ values. This is in agreement with the findings at Re = 40000 compared with those at lower Re's in the present work.

A third, and more likely, reason might be the vessel size. Kramers et al (1953) reported that mixing times are affected by scale: a larger tank required a larger number of revolutions (i.e. a higher value of $N\theta_m$) to achieve the same degree of mixing. Fourth, impeller blade width and thickness could also affect $N\theta_m$. It has been established (Rutherford et al, 1996a) that smaller blade thicknesses result in higher flow numbers and this might be expected to affect mixing times as well. There is also a substantial effect of blade width on mixing times (Tatterson, 1991), but as relevant values are not quoted by many investigators, it is difficult to ascertain how large this effect is.

Although $\theta_m$ values in the transition regime are different (Norwood and Metzner, 1960) the flows in all Re's studied in this work are expected to be fully-turbulent: this is indicated by the similarity of the $N\theta_m$ values determined.

## 6.5 EPILOGUE

The above discussion indicates that, clearly, standardisation of procedures used to measure mixing time is required, if differences in the results obtained are to be resolved. Similarly, differences in impeller geometry (blade width, thickness etc) and vessel size must be accounted

for in the mixing time correlations, as such parameters may affect the value of $N\theta_m$ for a particular impeller design.

The work presented above has shown that the liquid crystal thermographic technique developed can be used to characterise the transient mixing state in a stirred vessel with considerable accuracy and in greater detail than it has been possible hereto. Although hue values were used to describe the mixing process here, the corresponding temperature values can be readily obtained and consequently temperature measurements can also be made.

Mixing times obtained with the double impeller configuration were on average 20% lower than with the single Rushton turbine. However, in practice this more rapid mixing must be assessed against the higher power draw of the two-impeller system (Mahmoudi, 1994).

The work has also shown that more detailed studies of mixing are required, with an aim to formulate more accurate prediction of $N\theta_m$ by taking better account the effects of impeller and vessel geometry. The rapid acquisition of data across the vessel which is possible with the present technique should prove very useful for such studies.

**Figure 6.1** Image of half of the flow field stirred by a single Rushton impeller at 540 rpm, 160 ms after the start of the insertion of the tracer.

**Figure 6.2** Image of half of the flow field stirred by a single Rushton impeller at 540 rpm, 280 ms after the start of the insertion of the tracer.

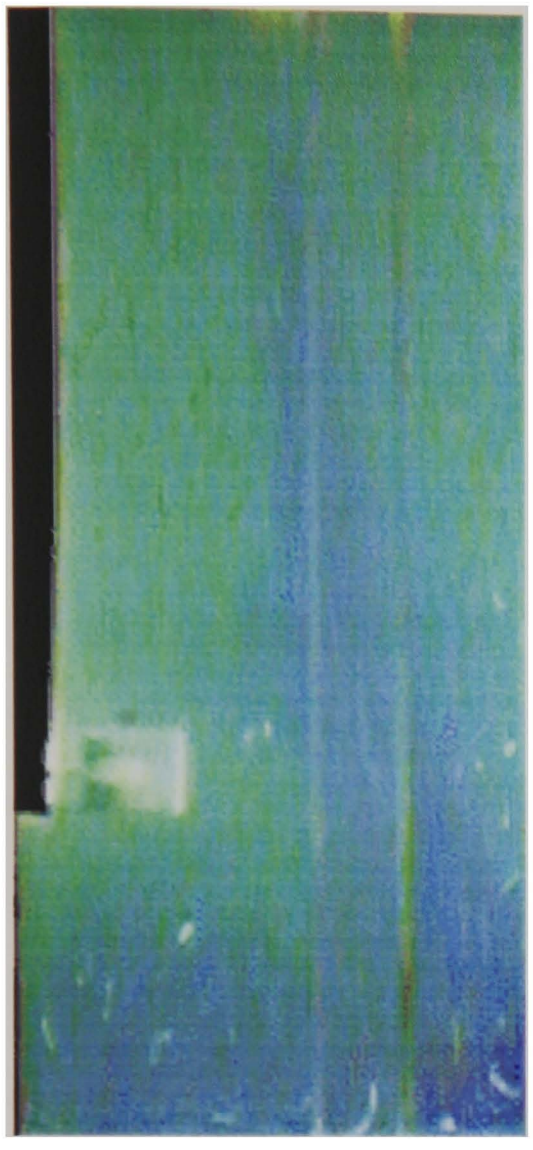

**Figure 6.3** Image of half of the flow field stirred by a single Rushton impeller at 540 rpm, 400 ms after the start of the insertion of the tracer.

**Figure 6.4** Image of half of the flow field stirred by a single Rushton impeller at 540 rpm, 480 ms after the start of the insertion of the tracer.

**Figure 6.5** Image of half of the flow field stirred by a single Rushton impeller at 540 rpm, 720 ms after the start of the insertion of the tracer.

**Figure 6.6** Image of half of the flow field stirred by a single Rushton impeller at 540 rpm, 1.80 s after the start of the insertion of the tracer.

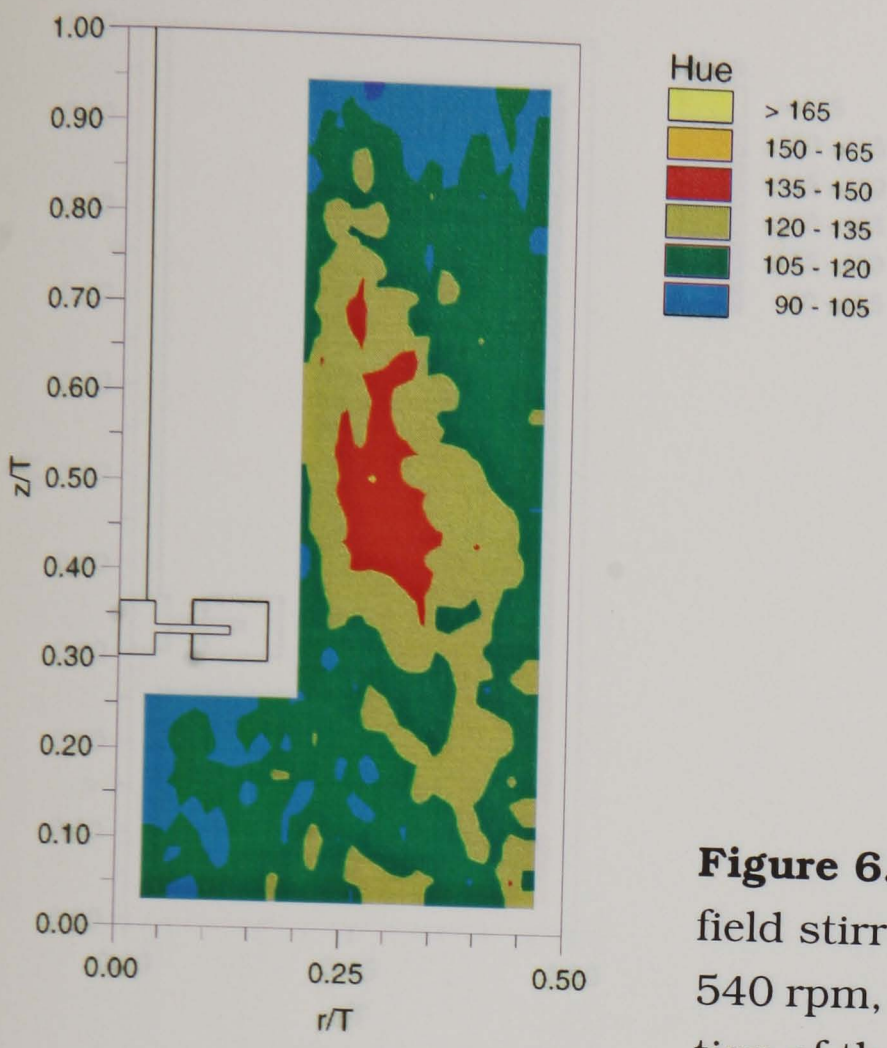


**Figure 6.7** Hue contours of half of the flow field stirred by a single Rushton impeller at 540 rpm, 160 ms after the start of the insertion of the tracer.

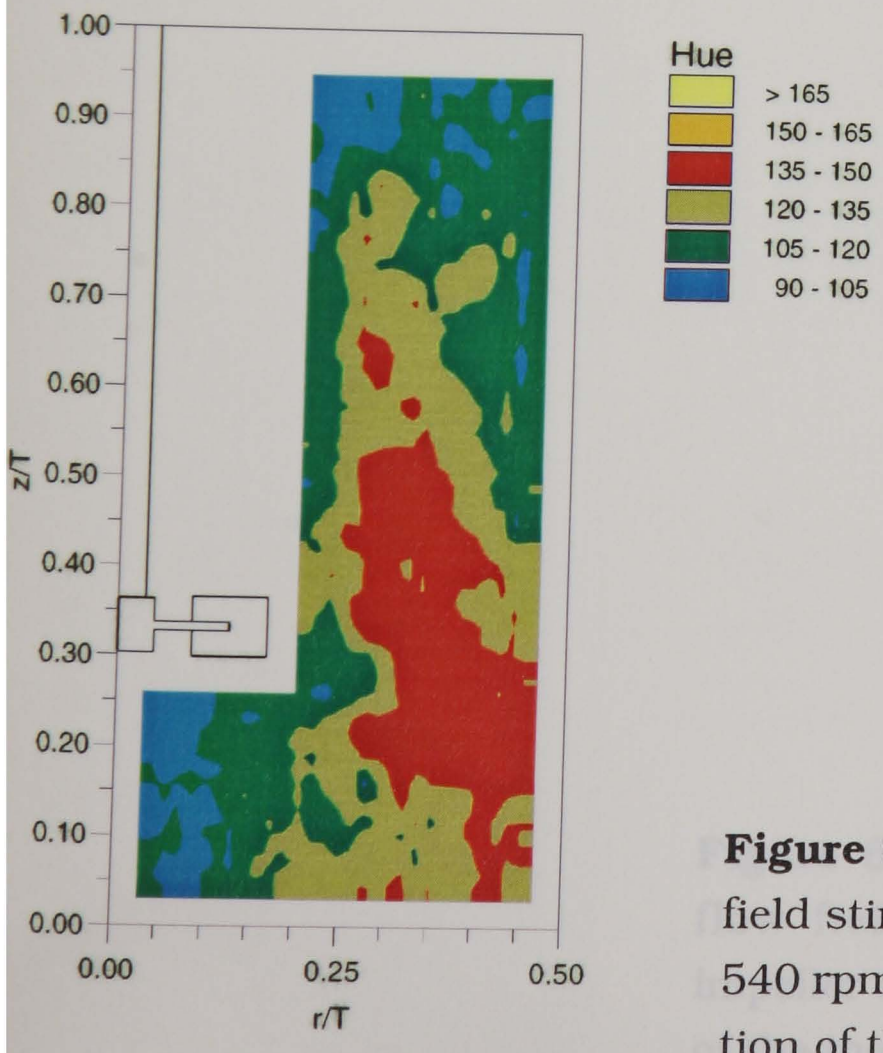


**Figure 6.8** Hue contours of half of the flow field stirred by a single Rushton impeller at 540 rpm, 280 ms after the start of the insertion of the tracer.

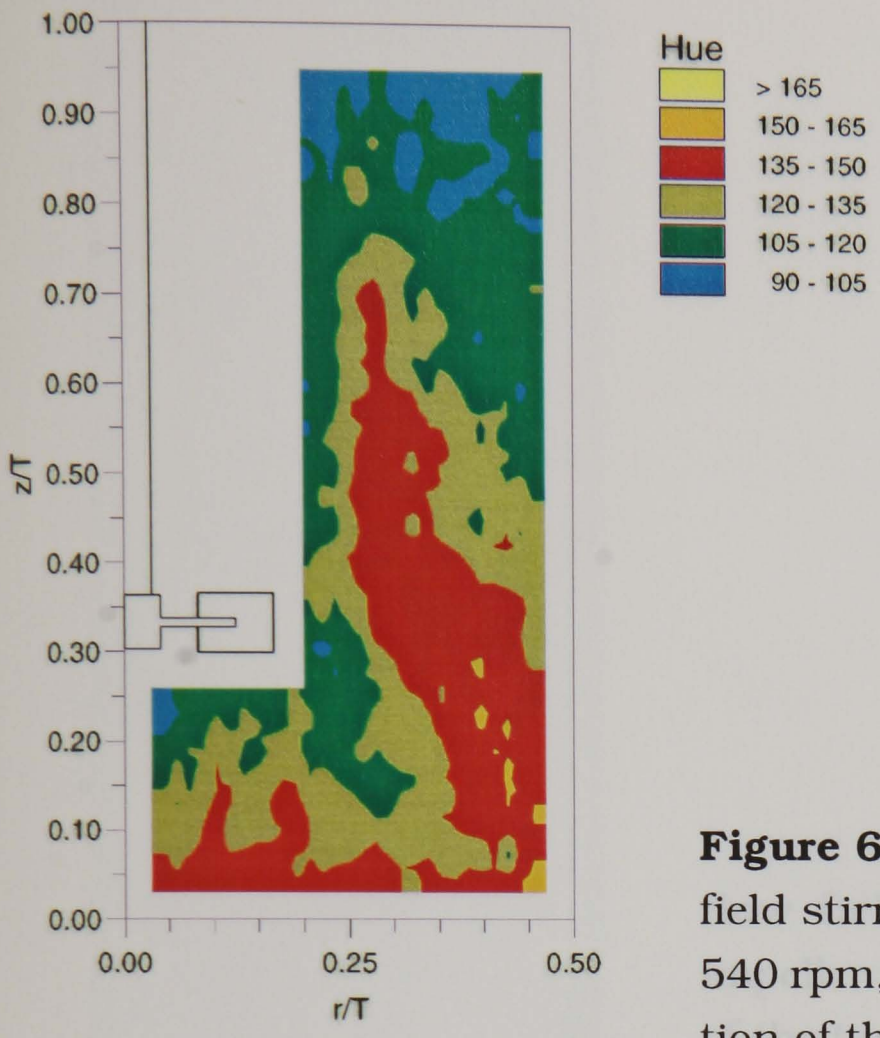


**Figure 6.9** Hue contours of half of the flow field stirred by a single Rushton impeller at 540 rpm, 400 ms after the start of the insertion of the tracer.

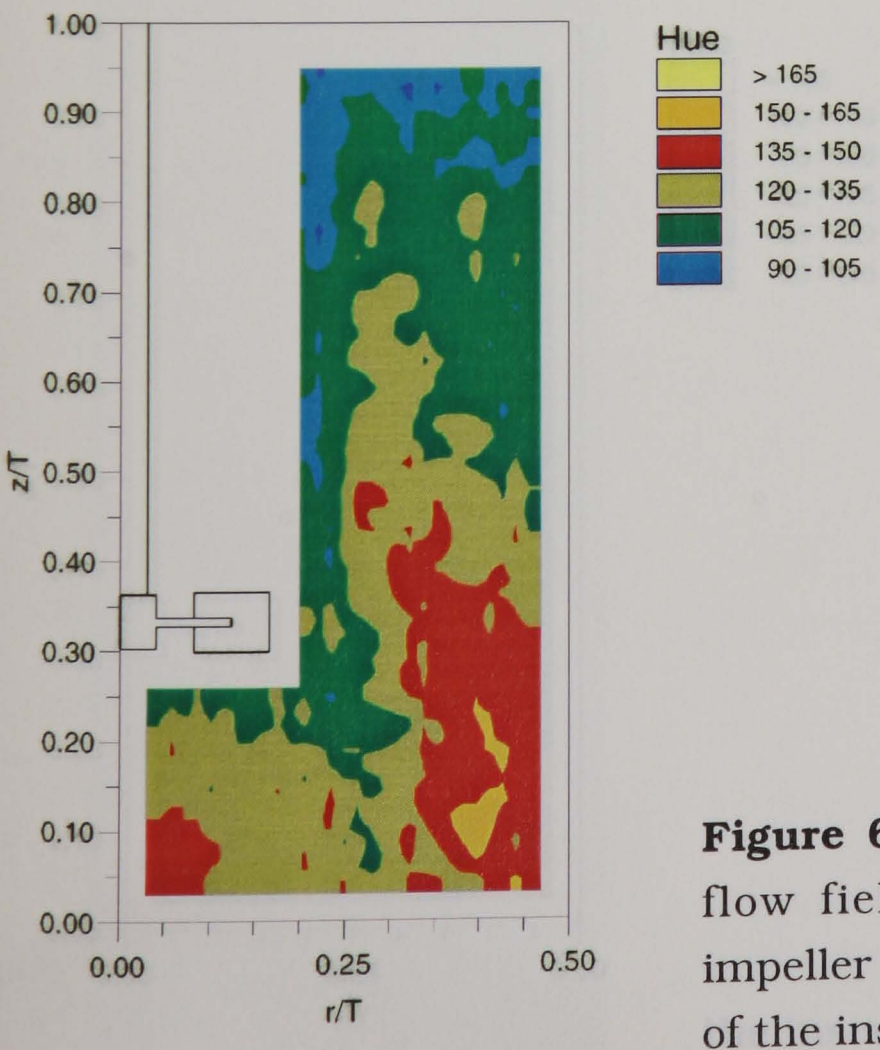


**Figure 6.10** Hue contours of half of the flow field stirred by a single Rushton impeller at 540 rpm, 480 ms after the start of the insertion of the tracer.

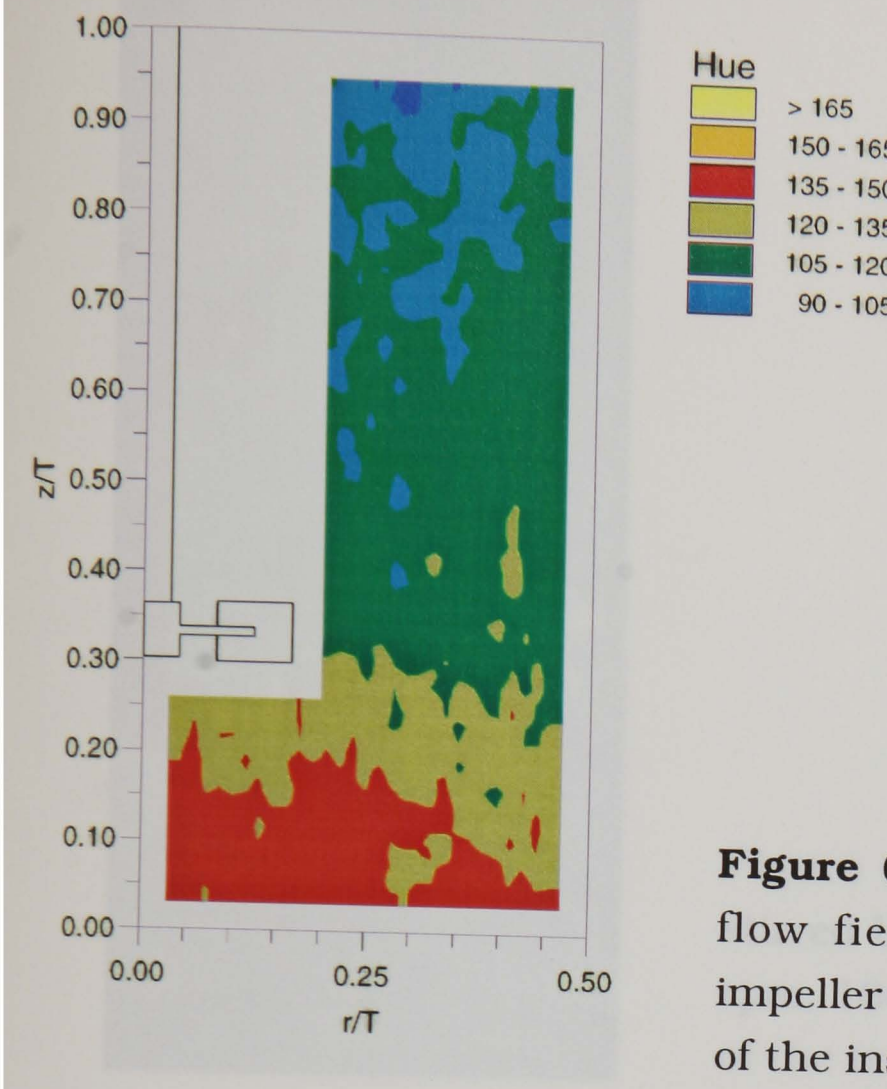


**Figure 6.11** Hue contours of half of the flow field stirred by a single Rushton impeller at 540 rpm, 720 ms after the start of the insertion of the tracer.

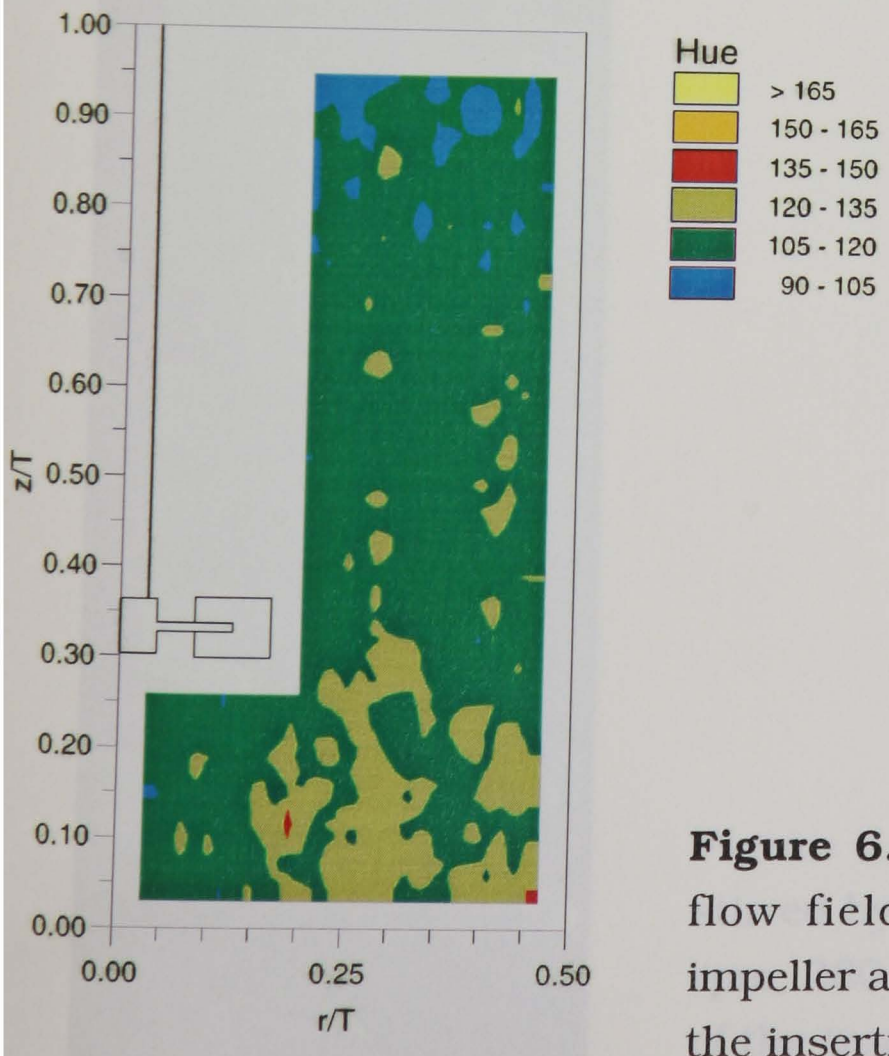


**Figure 6.12** Hue contours of half of the flow field stirred by a single Rushton impeller at 540 rpm, 1.80 s after the start of the insertion of the tracer.

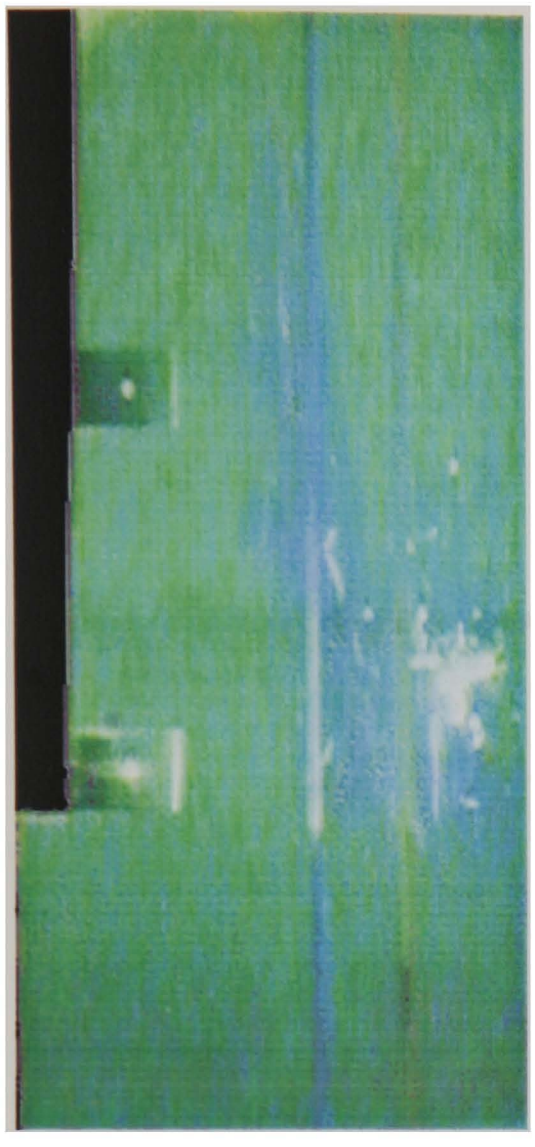

**Figure 6.13** Image of half of the flow field stirred by double Rushton impellers at 540 rpm, 160 ms after the start of the insertion of the tracer.

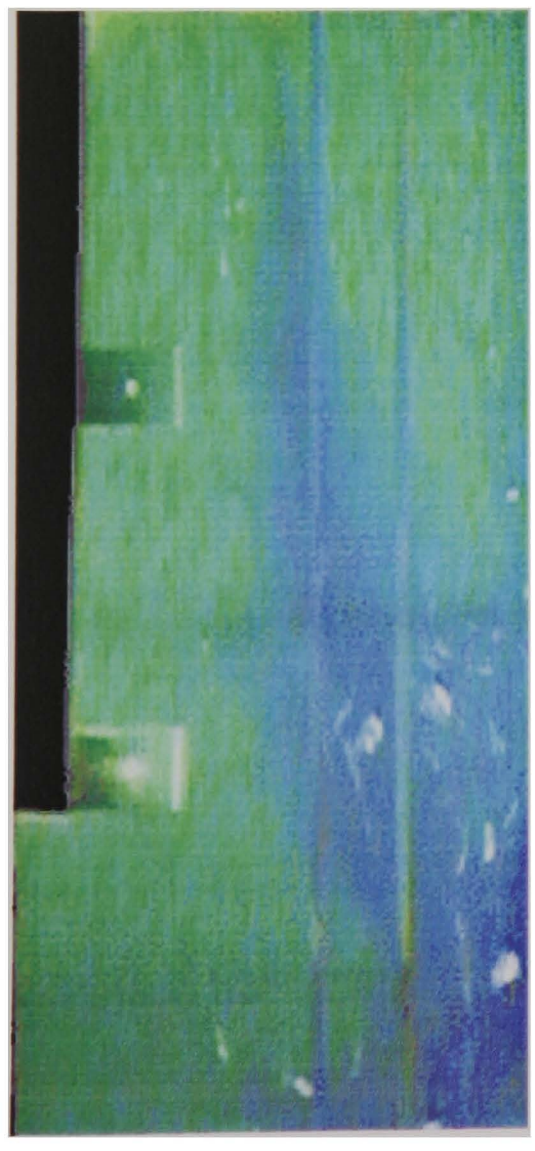

**Figure 6.14** Image of half of the flow field stirred by double Rushton impellers at 540 rpm, 280 ms after the start of the insertion of the tracer.

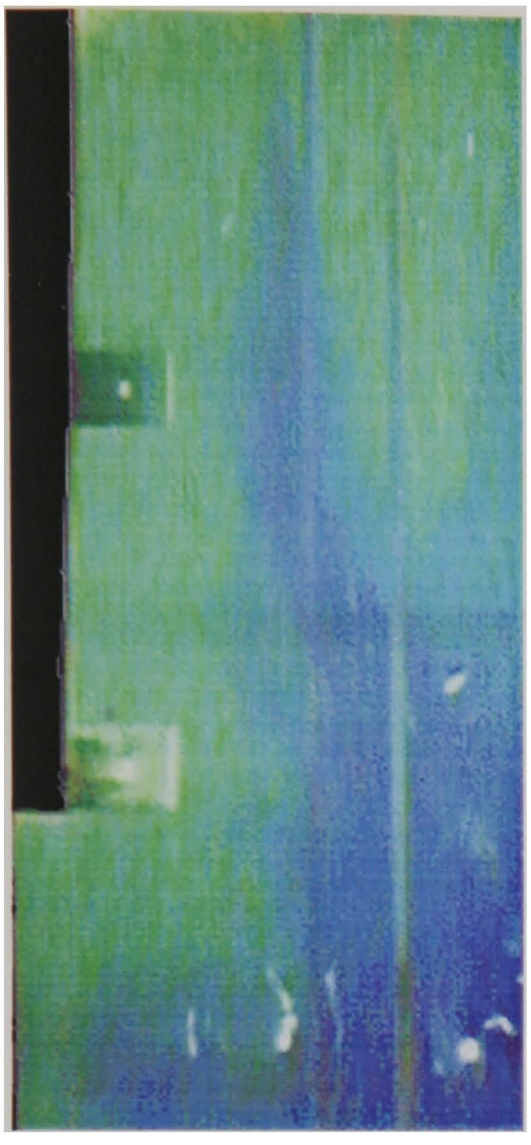

**Figure 6.15** Image of half of the flow field stirred by double Rushton impellers at 540 rpm, 400 ms after the start of the insertion of the tracer.

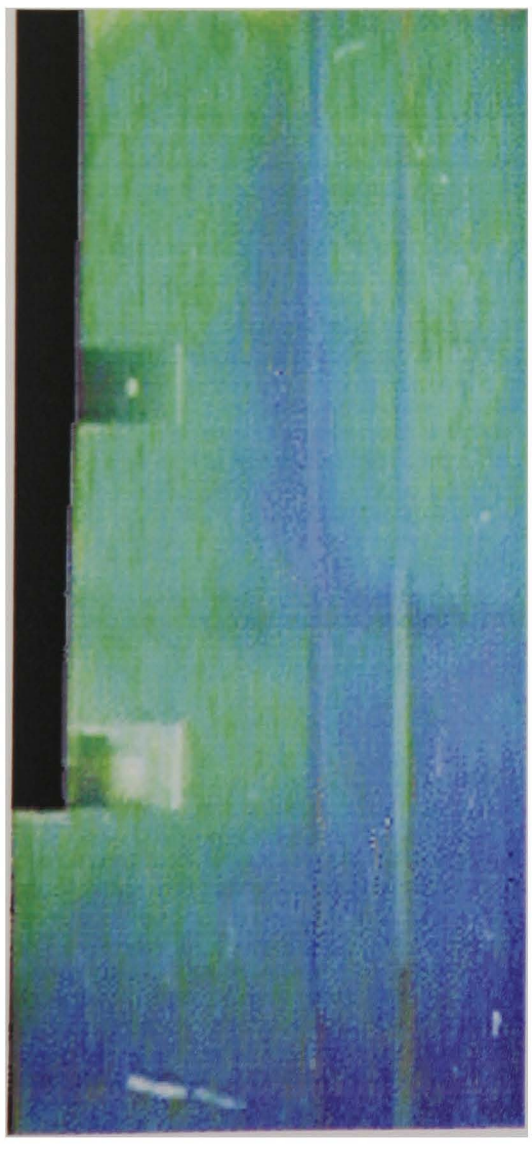

**Figure 6.16** Image of half of the flow field stirred by double Rushton impellers at 540 rpm, 480 ms after the start of the insertion of the tracer.

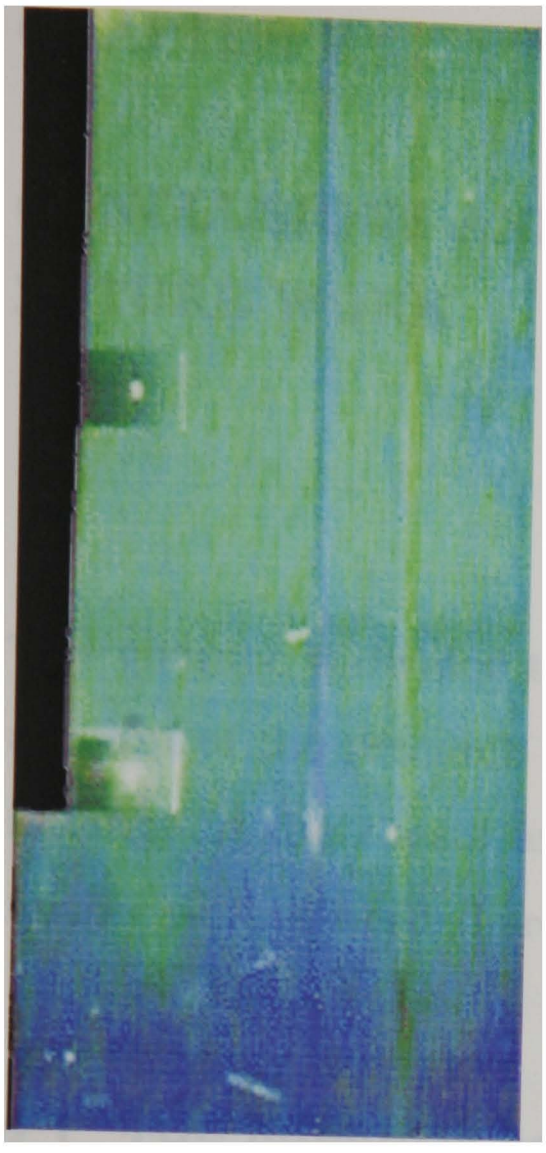

**Figure 6.17** Image of half of the flow field stirred by double Rushton impellers at 540 rpm, 720 ms after the start of the insertion of the tracer.

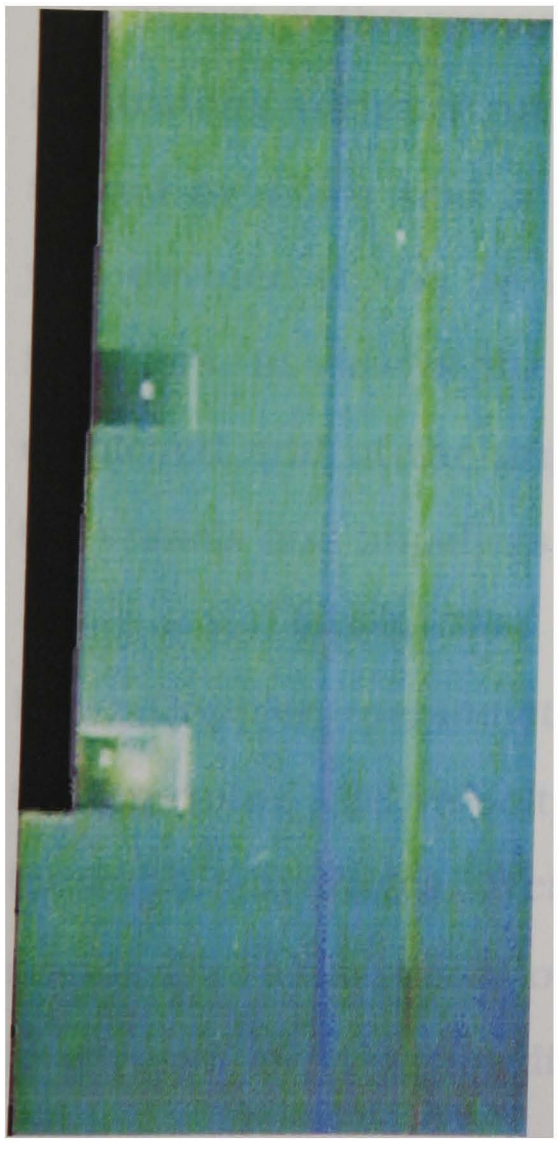

**Figure 6.18** Image of half of the flow field stirred by double Rushton impellers at 540 rpm, 1.52 s after the start of the insertion of the tracer.

# CHAPTER 7

# CONCLUSIONS AND RECOMMENDATIONS FOR FUTURE WORK

This chapter is divided into three sections. In the first section, a brief account of the research carried out is given. In the second, the main findings of the thesis are outlined and in the third areas in which further work is needed are identified.

## 7.1 THE PRESENT CONTRIBUTION

The object of the research presented in this thesis was to investigate the trailing vortex structure and the mixing characteristics in vessels stirred by either one or two Rushton impellers. A considerable effort was devoted to the design of the mixing vessels and of the Rushton impellers, in view of the requirements of the measurement techniques employed and of the importance of the geometrical characteristics of the vessels and impellers indicated by the literature survey.

Laser-Doppler anemometry was chosen as the measurement technique to determine the velocity characteristics of the flow. Angle-resolved (ensemble-averages over 1° of impeller shaft revolution) and time-resolved measurements of the velocity variations were obtained by LDA in a vessel of 100 mm diameter stirred by either one or two Rushton

impellers. Ensemble-averaged velocity measurements were also made and compared with those obtained in a larger vessel (T = 294 mm) of similar geometry to assess the effect of vessel size.

From the time-resolved measurements, the auto-correlation functions, energy spectra and temporal and spatial scales of turbulence of the flows induced by both impeller configurations were also obtained. Attempts were also made to estimate the values of the rate of dissipation of kinetic energy of turbulence in the impeller stream for the single-impeller configuration.

A considerable effort was also devoted to the development of the liquid crystal thermographic technique for the measurement of mixing time. The technique made use of temperature as a passive scalar to determine the transient temperature/concentration field in the vessel. This technique was developed in three stages. During the first two stages, the technique was applied in a specially-built vessel to study free convection and forced convection flows in order to establish the feasibility of its application for the measurement of mixing time. Subsequently, the technique was employed to measure mixing times in the 100 mm diameter vessel for flows agitated by one and two Rushton impellers. The technique enabled unobtrusive measurements of mixing time across the whole vessel to be made.

## 7.2 MAIN FINDINGS OF THE INVESTIGATION

Detailed LDA measurements were made which provided an extensive quantification of the flow fields around the impeller for both the single-

and double-impeller configurations. The flows in the vicinity of the impeller(s) were found to be predominantly periodic. In the single-Rushton case, periodicity was pronounced over a region of approximately cylindrical shape centred on the impeller disk and contained within a radius of 1.0 D and a height of 0.6 D. With two impellers, there was a corresponding cylindrical region where flow periodicity was predominant; this region was centred around the vessel axis and had a radius of 1.0 D and a height of 1.2 D.

The location of the trailing vortex axis was determined from the LDA measurements. It was found to be very similar to those determined in previous investigations with similar impeller and vessel geometries. For the double-impeller configuration, the axis is curved more towards the axis of the vessel due to the stronger tangential flow induced by the presence of the second impeller.

Comparisons of the mean velocity and turbulence level distributions in the vicinity of the single Rushton impeller and of the location and shape of the axes of the trailing vortices generated by both the single and double impellers, showed excellent scaling of the mean flows and turbulence in the 100 and 294 mm vessels. However, comparisons with previously published results showed clearly that all geometrical characteristics of the impeller(s) and vessel must be precisely scaled if accurate conclusions on scale-up are to be drawn. It should be emphasised that this finding has very important implications for stirred reactor design and precise scaling of the stirred reactor geometry must be ensured in practice if comparisons of the results obtained in vessels of different sizes are to be meaningful.

The turbulence in the vicinity of the impeller blades was shown to be anisotropic. This was indicated both through comparisons of the relative magnitudes of the three rms velocity components, as well as from the slopes exhibited by the corrected (non-periodic velocity) energy spectra for both the single- and double-impeller configurations. The turbulence becomes less anisotropic with increasing distance from the impeller blade. The three rms velocity components were similar at distances of r/T = 0.25 from the axis for both configurations.

The results have also shown that 360° ensemble-averaged measurements may significantly overestimate the turbulence levels near the impeller blades and 1° angle-resolved and/or time-resolved measurements should be used to characterise the flows within the regions specified earlier.

The number of velocity realisations near the impeller blades was found to vary considerably with blade angle $\phi$. This finding has important implications for the correct characterisation of mean velocities and turbulence levels. This data rate variation has not been identified before but should be taken into account in future work.

The temporal and spatial scales of turbulence in the impeller streams were estimated from time-resolved measurements of the radial velocity, for both the single- and double-impeller configurations. With one impeller, integral time scales varied from 0.25 ms near the blade to 1.20 ms at r/T = 0.35; the corresponding values of the micro time scales were 0.11 ms and 0.20 ms respectively. The length scales were estimated using the local mean velocity as the characteristic convective velocity;

the integral length scales varied from 0.6 mm near the blade to 1.5 mm at r/T = 0.35, while the micro length scales were nearly constant, approximately 0.25 mm. The dissipation of the kinetic energy of turbulence was calculated from the integral length estimates; its values, normalised by $N^3D^2$, were 38 near the blade and 3 at r/T = 0.35 The corresponding results obtained with two impellers showed that it may be more appropriate to calculate turbulent scales and $\varepsilon$ from time-resolved measurements of the velocity component at 45° to the horizontal due to the inclination of the impeller stream. However, it is expected that the assumptions and approximations involved in the calculation of the length scales and $\varepsilon$, although widely adopted in many earlier investigations (e.g. Kresta (1991), Ruszkowski (1992)), are not appropriate for many parts of the flow studied. For this reason, no attempt was made in this thesis to formulate an energy balance around the impeller based on the power input and the $\varepsilon$ values calculated using the length scale estimates.

The LCT technique was successfully applied to measure the mixing times in the single- and double-impeller configurations for four rotational speeds. The $N\theta_m$ values for the single- and double-impeller configurations were found to be, on average, 19 and 16, respectively. Comparison of the above $N\theta_m$ value for the single impeller with those of earlier investigations indicates that mixing time might be affected by vessel size.

## 7.3 RECOMMENDATIONS FOR FUTURE WORK

The results of the present investigation have shown that there are two main areas for further work: improvements in the measurement techniques employed should be investigated in order to improve their accuracy and further studies of stirred reactor flows are required to improve the understanding of mixing processes.

Due to the approximations involved in the determination of the length scales and therefore of the rate of dissipation of the kinetic energy of turbulence, a more appropriate technique is necessary. For more accurate measurements of $\lambda_x$, $\Lambda_x$ and $\varepsilon$, a two-measurement volume laser anemometer could be promising and should be investigated in future work.

The mixing time measurements showed that although the method developed is very suitable for such work, better illumination of the flow field is necessary for the LCT experiments. To this end a collimated sheet of light from a white light laser may provide a significantly more uniform means of illumination and such an arrangement should be tested. The white light of such a laser is however produced by the mixing of three (red, green and blue) beams; therefore it must be ascertained first whether the crystals will display colours other than those corresponding to the wavelengths of the three beams.

The non-uniformities of the illumination in the present LCT experiment prevented more detailed local mixing information being obtained. This is evident from the scatter in the hue distributions presented in

Chapter 6. Provided the illumination can be improved, for example in the manner described above, LCT data could be analysed further to quantify the degree of mixing at locations throughout the vessel.

The present LCT technique allows only the mixing time to be obtained and separate experiments must be made to determine the velocity characteristics. It would be interesting to determine whether LCT could be employed simultaneously with Particle Tracking Velocimetry (PTV) to determine both the mixing time and the mean velocity.

The literature review indicated that there is little information on flows produced by more than one impeller. The work presented in Chapters 5 and 6 in this thesis has gone some way to bridge the gap, but clearly further studies of multi-impeller flows are required, especially where impeller interaction is important: for example, the diverging flow pattern produced with two Rushton turbines (Mahmoudi and Yianneskis (1991, 1992)) shows promise for lifting solids off the bottom of the vessel and deserves further study. The work should also be extended to solid-liquid flows in stirred tanks. At present LDA data can only be obtained for very dilute particle concentrations due to laser beam blockage by the particles. This limitation could be overcome by applying the refractive-index matching technique employed by Nouri et al (1987b) for dense solid-liquid flows in pipes to stirred tanks to allow beam penetration with high solids concentrations.

The velocity measurements showed good scaling between the two vessel sizes. Scaling effects must however be further investigated through measurements in larger vessels to verify the scaling of the flow and

turbulence described above. Similarly, the LCT technique should be applied to measure mixing times in larger vessels, as previous work has shown that vessel size may affect the mixing characteristics. Clearly, the illumination problems mentioned above will be more significant in larger vessels and this work cannot proceed until a suitable means of providing uniform illumination across the whole vessel has been identified. Scaling rules should also be established for Newtonian fluids of different viscosities.

Finally, this investigation concentrated on the Rushton impeller due to its wide use in practice and its acceptance as a 'baseline' case for mixing studies. There are further aspects of Rushton impeller flows that deserve study: For example, in view of the findings of Kusters (1991), Rutherford et al (1996a) and this thesis, the effect of impeller disk thickness on the mean flow and turbulence must be established. In addition, LDA and LCT measurements similar to those presented here are urgently required for other impeller geometries not only to aid both the understanding of the flows and optimisation of mixing processes, but also to provide much-needed data for the validation of CFD predictions of the flows.

As the present work and that of Rutherford et al (1996) has shown in relation to blade thickness effects and scale-up, a major barrier to the improvement of the understanding of fluid mixing processes is the lack of fundamental knowledge in many areas. For example, there is conflicting evidence on the effect of hub size and shape on the flow (Stoots and Calabrese (1994), Mahmoudi (1994), Ruszkowski (1992)), and on the most appropriate method for the calculation of energy

dissipation in stirred tanks (Kresta (1991), Wu and Patterson (1989)). Therefore, it is necessary to undertake further small-scale work and investigate systematically fundamental aspects of the mixing process before useful conclusions can be drawn from studies carried out in industrially-relevant, large-scale and complex-geometry stirred reactors.

# REFERENCES

N. **Akino**, T. **Kunugi**, K. **Ichimiya**, K. **Mitsushiro** and M. **Ueda (1986)**
"Improved liquid-crystal thermometry excluding human colour sensation: Part 2. Application to the determination of wall temperature distributions", in Pressure and Temperature Measurements, Ed. J.H. Kim and R.J. Moffat, pp. 63-68.

S.G. **Armstrong** and S. **Ruszkowski (1986)**
"Measurement and comparison of flows generated by different types of impeller in a stirred tank" in Colloque Agitation Mecanique, Toulouse, pp. 1.9-1.16.

S.G. **Armstrong** and S. **Ruszkowski (1988)**
"The flow field in the discharge stream of disk turbines", *Proc 6th Eur Conf on Mixing*, Pavia, Italy, pp. 1-6.

R.L. **Bates**, P.L. **Fondy** and R.R. **Corpstein (1963)**
"An examination of some geometric parameters of impeller power", *Ind Eng Chem Proc Des Dev*, **2**, pp. 311-314.

H. **Benkreira** (Ed) **(1990)**
Fluid Mixing 4, Institution of Chemical Engineers, Rugby, UK.

R.D. **Biggs (1963)**
*AIChE J*, **9**, 5, p. 636.

C.M. **Bloomer (1990)**
Principles of Visual Perception, Herbert Press, London.

W. **Bujalski**, A.W. **Nienow**, S. **Chatwin** and M. **Cooke (1986)**
"Power consumption with aerated Rushton turbines", *Trans Inst Chem Engrs*, **52**, pp. 88-104.

R. **Calabrese** and C.M. **Stoots (1989)**
"Flow in the impeller region of a stirred tank", *Chem Eng Prog*, May 1989, p.43.

S. **Chandrasekhar (1992)**
Liquid Crystals, 2nd Ed, Cambridge University Press.

R.G. **Cooper** and D. **Wolf (1968)**
"Velocity profiles and pumping capacities for turbine type impellers", *Can J Chem Eng* , **46**, pp. 94-100.

T.E. **Cooper**, R.J. **Woolf** and J.F. **Meyer (1975)**
"Liquid crystal thermography and its application to the study of convective heat transfer", *Trans ASME J Heat Transfer*, August 1975, pp. 442-450.

J. **Costes** and J.P. **Couderc (1982)**
*Proc 4th European Conf on Mixing*, Noordwijkerhout, The Netherlands, p. 25.

D.B.A. **Crozier (1989)**
"A detailed study of the flow characteristics in a tall sirred tank", *Proc 3rd Int Conf on Laser Anemometry - Advances and Applications*, Wales, pp. 16.1-16.10.

L.A. **Cutter (1966)**
"Flow and turbulence in a stirred tank", *AIChE J*, **12**, pp. 35-45.

D. **Dabiri** and M. **Gharib (1991)**
"Digital particle image thermometry: The method and implementation", *Exp in Fluids*, **11**, pp. 77-86.

**Desoutter Limited** and **King's College London (1995)**
"Torque - capacitance transducers", United Kingdom Patent Application No. 9515779.8, 1 August 1995.

A. **DeSouza** and R.W. **Pike (1972)**
"Fluid dynamics and flow patterns in stirred tanks with a turbine impeller", *Can J Chem Eng*, **50**, pp. 15-23.

L.E. **Drain (1980)**
The Laser Doppler Technique, John Wiley and Sons, Chichester.

J. **Drbohlav**, I. **Fort** and J. **Kratky (1978a)**
Coll Czech Chem Commun, **43**, p. 696.

J. **Drbohlav**, I. **Fort** and J. **Kratky (1978b)**
Coll Czech Chem Commun, **43**, p. 3148.

D.F.G. **Durao** and J.H. **Whitelaw (1975)**
"The influence of sampling procedures on the velocity bias in turbulent flows", *Proc LDA Symp on The Accuracy of Flow Measurements by Laser Doppler Methods*, Copenhagen.

D.F.G. **Durao**, J. **Laker** and J.H. **Whitelaw (1980)**
"Bias effects in laser Doppler anemometry", *J Phys E: Sci Instrum*, **13**, p. 442.

F. **Durst**, A. **Melling** and J.H. **Whitelaw (1981)**
Principles and Practice of Laser Doppler Anemometry, 2nd Ed, Academic Press, London.

K.N. **Dyster**, E. **Koutsakos**, Z. **Jaworski** and A.W. **Nienow (1993)**
"An LDA study of the radial discharge velocities generated by a Rushton turbine: Newtonian fluids, Re ≥ 5", *Trans IChemE*, **71**, Part A, pp.11-23.

I. **Fort**, J. **Drbohlav**, J. **Kratky**, M. **Grospicora** and K. **Kronzilova (1972)**
Coll Czech Chem Commun, **37**, p. 222.

W.K. **George** and J.L. **Lumley (1973)**
"The laser-Doppler velocimetry and its application to the measurement of turbulence", *J Fluid Mech*, 60, 2, pp. 321-362.

R.J. **Goldstein** and J.F. **Timmers (1982)**
"Visualization of heat transfer from arrays of impinging jets", *Int J Heat Mass Transfer*, **25**, 12, pp. 1857-1868.

A.A. **Günkel** and M.E. **Weber (1975)**
"Flow phenomena in stirred tanks, part I. The impeller stream", *AIChE J*, **21**, 5, pp. 931-948.

G. **Heskestad (1965)**
"A generalized Taylor's hypothesis with application for high Reynolds number turbulent shear flows", *Trans ASME J Applied Mech*, **32**, pp. 735-739.

J.O. **Hinze (1975)**
Turbulence, McGraw Hill, London.

W. **Hoesel** and W. **Rodi (1977)**
"New biasing elimination method for laser-Doppler velocimeter counter processing", *Rev Sci Instrum*, **48**, 7.

D.B. **Holmes**, R.M. **Voncken** and J.A. **Dekker (1964)**
"Fluid flow in turbine stirred, baffled tank-I: Circulation time", *Chem Eng Sci*, **19**, pp. 201-208.

R.W.G. **Hunt (1991)**
Measuring Color, Ellis Horwood, London.

Y. **Iritani**, N.**Kasagi** and M. **Hirata (1984)**
"Heat transfer mechanism and associated turbulence structure in a near-wall region of a turbulence boundary layer", in Turbulent Shear Flow 4, Ed. L.J.S. Bradbury and others, pp. 223-234, Springer-Verlag, Berlin.

**Judd** and **Wyszecki (1975)**
Color in Business Science and Industry, 3rd ed, Wiley, New York.

N. **Kasagi**, R.J. **Moffat** and M. **Hirata (1989)**
"Liquid Crystals", Chapter 8 in Handbook of Visualization, Ed W. Yang, Hemisphere Publishing, New York.

S.J. **Khang** and T.J. **Fitzgerald (1975)**
"New scale-up and design method for stirred agitated batch mixing vessels", *Chem Eng Sci*, **31**, pp. 569-577.

I. **Komasawa**, R. **Kuboi** and T. **Otake (1974)**
"Fluid and particle motion in turbulent dispersion - I. Measurement of turbulence of liquid by continual pursuit of tracer particle motion', *Chem Eng Sci*, 29, pp. 641-650.

H. **Kramers**, G.M. **Baars** and W.H. **Knoll (1953)**
"A comparative study on the rate of mixing in stirred tanks", *Chem Eng Sci*, **2**, pp. 35-42.

J. **Kratky**, I. **Fort** and J. **Drbohlav (1974)**
Coll Czech Commun, **39**, p. 3238.

S.M. **Kresta (1991)**
Characterization, Measurement and Prediction of the Turbulent Flow in Stirred Tanks, PhD Thesis, McMaster University, Canada.

R. **Kuboi** and A.W. **Nienow (1982)**
"The power drawn by dual impeller systems under gassed and ungassed condition", *Proc 4th Eur Conf on Mixing*, Noordwijkerhout, The Netherlands, pp. 247-261.

M. **Kuriyama**, M. **Ohta**, M. **Yanagawa**, K. **Aria** and S. **Saito (1981)**
"Heat transfer and temperature distributions in an agitated tank equipped with helical ribbon impeller", *J Chem Eng Japan*, **14**, pp. 323-330.

K.A. **Kusters (1991)**
The Influence of Turbulence on Aggregation of Small Particles in Agitated Vessels, PhD Thesis, Eindhoven University of Technology, The Netherlands.

D.R. **Lancaster (1976)**
"Effects of engine variables on turbulence in a spark-ignition engine", SAE paper No. 760159.

M.T. **Landahl** and E. **Mollo-Christensen (1986)**
Turbulence and Random Processes in Fluid Mechanics, Cambridge University Press.

H.D. **Laufhütte** and A.B. **Mersmann (1985)**
"Dissi;ation of power in stirred vessels", *Proc 5th European Conf on Mixing*, BHRA Fluid Engineering, Wurzburg, West Germany, pp. 331-340.

K.C. **Lee** and M. **Yianneskis (1993)**
"An image processing technique for the analysis of thermotic distributions utilising liquid crystals", Chapter 16 in Imaging in Transport Processes, Ed S. Sideman and K. HijiKata, Begell House Inc, New York.

S.M.S. **Mahmoudi (1994)**
Velocity and Mixing Characteristics of Stirred Vessels with Two Rushton Impellers, PhD Thesis, King's College London, University of London.

S.M.S. **Mahmoudi** and M. **Yianneskis (1991)**
"The variation of flow pattern and mixing time with impeller spacing in stirred vessels with two Rushton impellers", *Proc 7th Eur Conf on Mixing*, pp. 17-24.

S.M.S. **Mahmoudi** and M. **Yianneskis (1992)**
"The effect of impeller spacing on the mean flow and turbulence in stirred vessels with two Rushton impellers", *Proc IChemE Research Event*, Manchester, pp. 380-382.

M. **Mahouast**, G. **Cognet** and R. **David (1989)**
"Two-component LDV measurements in a stirred tank", *AIChE J*, **35**, 11, pp. 1770-1778.

A.J. **Marquis (1995)**
Personal communication.

D.K. **McLaughlin** and W.G. **Tiederman (1973)**
"Biasing correction for individual realisation of laser anemometry measurements in turbulent flows", *Physics of Fluids*, **6**, p.2082.

A. **Melling (1975)**
Investigation of Flows in Non-Circular Ducts and Other Configuartions by Laser Doppler Anemometry, PhD Thesis, Imperial College, University of London.

A. **Melling (1977)**
"Axisymmetric, turbulent flow in a motored reciprocating engine", Imperial College Mech Eng Dept Report CHT/77/4, 1977.

A. **Melling** and J.H. **Whitelaw (1976)**
"Turbulent flow in a rectangular duct", *J Fluid Mech*, **78**, 2, pp. 289-315.

R.J. **Moffat (1990)**
"Experimental heat transfer", *Proc 9th Internation Heat Transfer Conf*, Jerusalem, 19-24 August.

K. **van der Molen** and H.R.E. **van Maanen (1978)**
"Laser-Doppler measurements of the turbulent flow in stirred vessels to establish scaling rules", *Chem Eng Sci*, **33**, pp. 1161-1168.

M. **Moo-Young**, K. **Tichar** and F.A.L. **Takahashi (1972)**
*AIChE J*, 18, 1, p. 178.

A.S.**Mujumdar**, B.**Huang**,D.**Wolf**, M.E.**Weer** and W.S.M.**Douglas (1970)**
"Turbulence parameters in stirred tank, *Can J Chem Eng*, **48**, pp. 475-483.

S. **Nagata**, K. **Yamamoto**, T. **Hashimoto** and Y. **Naruse (1960)**
*Mem Fac Engng*, Kyoto University, **22**, p. 68.

S. **Nadarajah (1991)**
"A rotating grating unit designed for Reynolds stress measurements", King's College London Report EM/91/05.

S. **Nadarajah (1992)**
An Experimental Investigation of Flows Through Inlet Ports and Valves, PhD Thesis, King's College London, University of London.

M. **Nishikawa**, Y. **Okamoto**, K. **Hasimoto** and S **Nagata (1976)**
"Turbulence energy spectra in baffled mixing vessels", *J Chem Eng Japan*, **9**, 6, pp.493.

K.W. **Norwood** and A.B. **Metzner (1960)**
*AIChE J*, **6**, 3, p. 432.

J.M. **Nouri** and J.H. **Whitelaw (1990)**
"Effect of size and confinement on the flow characteristics in stirred reactors", *Proc 5th Int Symposium on Application of Laser Techniques to Fluid Mechanics*, Lisbon, Portugal, paper 23.2.

J.M. **Nouri**, J.H. **Whitelaw** and M. **Yianneskis (1987a)**
"The scaling of the flow field with impeller size and rotational speed in a stirred reactor", *Proc 2nd Int Conf on Laser Anemometry - Advances and Applications*, Strathclyde, Scotland, September 1987, pp. 489-500.

J.M. **Nouri**, J.H. **Whitelaw** and M. **Yianneskis (1987b)**
"Particle motion and turbulence in dense two-phase flows", *Int J Multiphase Flow*, **13**, 6, pp. 792-739.

G.K. **Patterson** and H. **Wu (1985)**
"Distribution of turbulence energy dissipation rates in mixers", *Proc 5th Eur Conf on Mixing*, BHRA Fluid Engineering, Wurzburg, West Germany.

W.H. **Press**, B.P. **Flannery**, S.A. **Teukolsky** and W.T **Vetterling (1986)**
Numerical Recipes, the Art of Scientific Computing, Cambridge University Press.

J. **Prochazka** and J. **Landau (1961)**
Coll Czech Chem Cummun, **26**, p. 2961.

N.B. **Reed**, M. **Princz** and S. **Hartland (1977)**
"Laser Doppler measurements of turbulence in a standard stirred tank", *Proc 2nd Eur Conf on Mixing*, paper B1, pp. B1.1 - B1.26.

K. **van't Riet** and J.M. **Smith (1973)**
"The behaviour of gas-liquid mixtures near Rushton turbine blades", *Chem Eng Sci*, **28**, pp. 1031-1037.

K. **van't Riet** and J.M. **Smith (1975)**
"The trailing vortex system produced by Rushton turbine agitators", *Chem Eng Sci*, **30**, pp. 1093-1105.

K. **van't Riet**, W. **Bruijn** and J.M. **Smith (1976)**
"Real and pseudo-turbulence in the discharge stream from a Rushton turbine", *Chem Eng Sci*, **31**, pp. 407-412.

B.K. **Revill (1982)**
"Pumping capacity of disc turbine agitators - A literature review", *Proc 4th Eur Conf on Mixing*, paper B1, pp. 11-24.

H.S. **Rhee**, J.R. **Koseff** and R.L. **Street (1984)**
"Flow visualization of a recirculating flow by rheoscopic liquid and liquid crystal techniques", *Exp Fluids*, **2**, pp. 57-64.

J. **Rojas**, J.H. **Whitelaw** and M. **Yianneskis (1987)**
"Forced convective heat transfer in curved diffusers", *Trans ASME J Heat Transfer*, **109**, pp. 866-871.

J.H. **Rushton**, E.W. **Costich** and H.J. **Everett (1950)**
"Power characteristics of mixing impeller, Part I", *Chem Eng Prog*, **46**, 8, pp. 395-404.

S.W. **Ruszkowski (1992)**
Impeller Discharge Flow Characteristics and Their Effect on Mixing Processes in Tanks, PhD Thesis, Cranfield Institute of Technology.

K. **Rutherford**, S.M.S. **Mahmoudi**, K.C. **Lee** and M. **Yianneskis (1996a)**
"The influence of Rushton impeller blade and disk thickness on the mixing characteristics of stirred vessels", *Tran IChemE Chem Eng Res Des*, (To appear in March 1996).

K. **Rutherford**, K.C. **Lee**, S.M.S. **Mahmoudi** and M. **Yianneskis (1996b)**
"The hydrodynamic characteristics of dual Rushton impeller stirred vessels", *AIChE J.* (To appear in January 1996).

Y. **Sano** and H. **Usui (1985)**
*J Chem Eng Japan*, **18**, p. 47.

J.P. **Sachs** and J.H. **Rushton (1954)**
"Discharge flow from turbine-type mixing impellers", *Chem Eng Prog*, **50**, 2, pp. 597-603.

C. **Schofield (1974)**
"The definition and assessment of mixing quality in liquids and pastes", *Proc 1st Eur Conf on Mixing and Centrifugal Separation*, pp. C1-1 - C1-13.

S.J. **Shiue** and C.W. **Wong (1984)**
*Can J Chem Eng*, **62**, p. 602.

C.M. **Stoots** and R.V. **Calabrese (1994)**
"The mean velocity field relative to a Rushton turbine blade", *AIChE J.*

K.O. **Suen (1992)**
Investigation of Gas Flow in a Motored High Speed Diesel Engine by Laser-Doppler Anemometry, PhD thesis, King's College London, University of London.

G.B. **Tatterson (1991)**
Fluid Mixing and Gas Disperson in Agitated Tanks, McGraw Hill.

J. **Thyn**, V. **Novak** and P. **Pock (1976)**
"Effect of measured volume size on the homogenization time", *Chem Eng Sci*, **12**, pp. 211-217.

V.W. **Uhl** and J.B. **Gray (1966)**
Mixing, Theory and Practice, Academic Press, London.

R.M. **Voncken**, D.B. **Holmes** and H.V. **Den Hartog (1964)**
"Fluid flow in turbine-stirred, baffled tanks - II: Dispersion during circulation", *Chem Eng Sci*, **31**, pp. 407-412.

H. **Wu** and G.K. **Patterson (1989)**
"Laser-Doppler measurements of turbulent-flow parameters in a stirred mixer", *Chem Eng Sci*, **44**, 10, pp. 2207-2221.

W.J. **Yanta (1973)**
"Turbulence measurements with a laser-Doppler velocimeter", Naval Ordnance Labs, White Oak, Silver Spring, Report NOLTR 73-94.

M. **Yianneskis (1982)**
Flow in Reciprocating Engine Cylinders and Curved Ducts, PhD thesis, Imperial College, University of London.

M. **Yianneskis (1988)**
"Thermal monitoring by liquid crystals", *J Condition Monitoring*, **2**, pp.139-151.

M. **Yianneskis** and J.H. **Whitelaw (1993)**
"On the structure of the trailing vortices around Rushton turbine blades", *Tran IChemE*, **17**, Part A, pp. 543 - 550.

M. **Yianneskis**, Z. **Popiolek** and J.H. **Whitelaw (1987)**
"An experimental study of the steady and unsteady flow characteristics of stirred reactors", *J Fluid Mech*, **175**, pp. 537-555.

M.**Yianneskis**, M.J. **Tindal** and S. **Nadarajah (1991)**
"Measurement of turbulence scales, moments and spectra in engine flows", *Proc IMechE, Exp Methods in Engine Research and Development*, pp. 127-133.